PIEZOELECTRIC MATERIALS AND ENERGY HARVESTING USING A NOVEL TRANSDUCER DESIGN

By

GREGORY YESNER

A dissertation submitted to the

School of Graduate Studies

Rutgers, The State University of New Jersey

In partial fulfillment of the requirements

For the degree of

Doctor of Philosophy

Graduate Program in Materials Science and Engineering

Written under the direction of

Prof. Ahmad Safari

And approved by

_____

_____

_____

_____

New Brunswick, New Jersey

January, 2018

ABSTRACT OF THE DISSERTATION

Piezoelectric Materials and Energy Harvesting Using a Novel Transducer Design

By GREGORY YESNER

Dissertation Director:

Professor Ahmad Safari

Bismuth based piezoelectric ceramics such as $0.88Bi_{1/2}Na_{1/2}TiO_3 - 0.08Bi_{1/2}K_{1/2}TiO_3 - 0.04BaTiO_3$ (BNKBT88) are a promising lead-free candidate with moderate piezoelectric properties for use in in transducers, multilayer actuators (MLA), and piezoelectric transformers. This dissertation focuses on three areas of piezoelectric research: i) development of a BNT-based co-fired actuator with copper metal electrodes sintered at low temperature and in controlled oxygen atmosphere, ii) study the effect of A-site non-stoichiometry in BNKBT ceramics and improvement of the electrical resistivity in Bi-deficient composition for a high power transducer application, and iii)

development of a prototype bridge transducer with a novel electrode pattern utilizing d_{33} for enhanced energy generation.

i) Compatibility of Bi-based ceramics and copper electrodes was demonstrated by co-firing BNKBT88 ceramics with copper electrodes at 900ºC in controlled atmosphere with an oxygen partial pressure of 6.1×10^{-8} atm. A combination of additives for low temperature sintering was used for firing at 900ºC in air or controlled atmosphere with minimal effect on the piezoelectric properties of BNKBT88 compared to sintering at 1150ºC. The oxygen atmosphere was controlled during sintering by mixing carbon dioxide and a hydrogen-nitrogen mixture. To keep the concentration of oxygen within the narrow range necessary for the coexistence of Cu metal and Bi_2O_3, the BNKBT88 samples were placed inside of a rectangular alumina boat and covered with a custom drilled alumina plate. A mixture of copper metal powder and cuprous oxide (Cu_2O) were placed adjacent to the samples inside of the alumina boat to release or absorb excess O_2. BNKBT88 ceramics were successfully co-fired with internal and surface Cu metal electrodes.

ii) The effect of non-stoichiometry of A-site cations in BNKBT88 was studied. Hardening and softening of piezoelectric properties has been observed. The most notable effect is that the mechanical quality factor, which is an essential figure of merit for high power application, is as high as 1200 for the Bi-deficient composition compared to 150 for the unmodified composition. Multilayer bismuth deficient BNKBT88 with co-fired copper metal electrodes is candidate for use in a lead-free piezoelectric transformer.

iii) A prototype novel lead zirconate titanate (PZT) bridge transducer based on the cymbal design has been developed for energy harvesting from impact loading by vehicle-induced deformations on pavement. Efficient transfer of mechanical energy from the road to the piezoelectric transducers embedded beneath the surface is achieved through mechanical coupling of the transducer and the pavement. A busy highway can be used as a source of electrical power where the harvested energy can be transmitted to the electrical grid or used to power streetlights.

The novel transducer is also a highly sensitive detector that has the potential to be used to monitor vehicles on a roadway. The novel transducers generate energy to power electronic circuitry, including wireless transmitters for real-time traffic monitoring, without requiring external cables. A network of self-powered piezoelectric sensors could be installed in any roadway to control the flow of traffic on a highway or enable the communication of autonomous vehicles with the road.

A novel electrode design is used to polarize the piezoelectric ceramic along its length, effectively utilizing d_{33} mode for enhanced energy generation. The effective piezoelectric coefficient d_{33}^{ef} was measured to be 19,000pC/N using a modified Berlincourt method. Horizontal poling increases energy and output voltage considerably. A prototype module with 64 bridge transducers was fabricated and loaded repeatedly with a pneumatic piston to simulate vehicle loading on a busy highway. Each loading of 600 lbs on the prototype transducer module generates 0.83 mJ of energy. Loading under simulated traffic conditions with 500 lbs at 5 Hz generated 2.1 mW at a resistive load of 330 kOhm. An impedance matching circuit utilizing a step down switch-mode DC-DC "buck" converter was used to power a series of LEDs.

Acknowledgements

I am grateful for the encouragement, guidance, and support of my advisor Prof. Ahmad Safari.

I would like to thank my thesis committee, Dr. Glenn Amatucci, Dr. Dunbar Birnie, and Dr. Ali Maher who monitored my work and took effort in reading and providing valuable comments and questions which improved the quality of my thesis.

Dr. David Spang provided me with very valuable advice to design and build my laboratory furnace. I am particular grateful for the assistance given by Abbas Jasim, whose work in simulations assisted in the design of the piezoelectric transducer.

I would like to thank past and present members of the electroceramics group Dr. Medhi Hejazi, Dr. Rut Rivera, and Elaheh Taghaddos. I would like to acknowledge the help provided by Patrick Urbankowski and Max Kuciej, who spent many hours with me in the lab. I am grateful for the opportunity to train hard working students to conduct research and I wish you the best of luck in graduate school.

I am grateful to the Shoei Chemical Inc. who provided the oxidation resistant copper powered used in my research.

My special thanks are extended to Dr. Ali Maher and the staff of the Center for Advanced Infrastructure and Transportation (CAIT), as well as the United States Federal Highway Administration (FHA) for their support of research in piezoelectric energy harvesting.

I would like to thank the Glenn Howatt Electroceramics Foundation for their generous financial support that made my research possible.

Table of contents

List of Tables

List of illustrations

1. Research Objectives and Scope of the Dissertation

1.1 Statement of the problem

Lead based piezoelectric materials are used extensively for applications as sensors, actuators, resonators, and transducers. Lead zirconate titanate (PZT) has a piezoelectric charge coefficient up to 700 pC/N and can operate over a wide temperature range of temperature due to a high Curie temperature. Despite the high piezoelectric properties of PZT, the manufacture of lead-based ceramics causes environmental contamination due to the high vapor pressure of lead oxide (PbO). The toxic effects of lead on the environment and human health are well known, and have resulted in efforts to restrict the use of lead-containing materials.

In the European Union, The Restriction of Hazardous Substances Directive (RoHS) aims to eliminate the use of hazardous materials such as lead from electronic devices, while the Waste Electrical and Electronic Equipment Directive (WEEE) and the End of Life Vehicles Directive (ELV) require manufacturers to be responsible for the recovery and recycling of their waste products. Co-fired PZT multilayer actuators (MLA) with copper electrodes have been extensively used as fuel injectors in diesel engines. Copper is used as a low cost electrode material in MLA. Co-firing with copper requires low temperature sintering in controlled oxygen atmosphere. One of the possible lead-free alternatives for use in piezoelectric MLA is $Bi_{0.5}Na_{0.5}TiO_3$ (BNT) based ceramics. Co-firing PZT with copper requires low temperature sintering and controlled oxygen atmosphere. While it is possible to co-fire bismuth based ceramics with copper electrodes, the process must be carried out at low temperature of around 900ºC and

within an extremely narrow range of oxygen partial pressure to avoid oxidation of copper or reduction of bismuth oxide.

Donor or accepter doping in piezoelectric ceramics is used to obtain desired properties for specific applications. A-site non-stoichiometry in BNT-based ceramics such as bismuth excess or deficiency, has been found to modify properties similar to acceptor or donor doping. Defects induced by non-stoichiometry may result in piezoelectric ceramics with properties comparable to those of hard PZT. Lead free ceramics including Bi-based compositions may have a good chance to replace PZT in the future for many applications including high power transducers and energy harvesting. However, these compositions are unlikely to match or exceed the high d_{33} and relative permittivity of soft PZT that is necessary for energy generation. Lead zirconate titanate will continue to be used due to the lack of a high d_{33} lead free alternative in the immediate future. Lead free piezoelectric ceramics will enjoy advantages for high power applications. They have been shown to be effective for transducers for medical use such as high intensity focused ultrasound transducers due to their high coercive field and efficiency at higher vibration velocity.

Another area of piezoelectric research involves the conversion of mechanical energy into useable electrical power from environmental sources. A source of mechanical energy is the elastic deformation of a road surface as a vehicle drives over the road. This energy is an untapped source of renewable and clean power that is currently wasted and dissipated as heat. Stacks of PZT ceramics have been used harvest energy from a roadway, however a piezoelectric transducer must be designed to match the stiffness of the road for efficient conversion from mechanical to electrical energy. The cymbal

transducer and the rectangular version of the cymbal, the bridge transducer, can be designed not only to match the stiffness of asphalt pavement, but will also provide higher power. These transducers utilize a combination of the lateral and longitudinal piezoelectric coefficients. A novel electrode design facilitates an increased energy density and enhanced effective piezoelectric coefficient d_{33}^{eff}.

1.2 Research Objectives

The scope of this dissertation covers three areas of piezoelectric research:

Low temperature sintering and atmospheric control for the development of a lead-free multilayer actuator with co-fired copper electrodes.

1- Develop a composition of additives to sinter morphotropic phase boundary $0.88Bi_{1/2}Na_{1/2}TiO_3 – 0.08Bi_{1/2}K_{1/2}TiO_3 – 0.04BaTiO_3$ (BNKBT88) ceramics at 900ºC with minimal effect on the electromechanical properties compared to ceramics fired at 1150ºC.

2- Co-fire BNKBT88 ceramics with copper metal electrodes in controlled oxygen atmosphere to demonstrate the feasibility of BNT-based multilayer actuators.

Piezoelectric, ferroelectric, and dielectric properties of non-stoichiometric BNKBT88 ceramics.

3- Evaluate the effects of A-site non-stoichiometry in BNKBT88 ceramics on electromechanical properties.

4- Study the effect of bismuth deficiency on the hardening of electromechanical properties.

5- Study the effect of bismuth oxide addition to improve the resistivity in Bi-deficient BNKBT88 ceramics.

Fabrication of a novel piezoelectric transducer for a road-based piezoelectric energy harvesting application.

6- Design and prototype a bridge transducer using a novel electrode pattern and surface poling for enhanced energy generation.
7- Simulate vehicle loading in traffic conditions and evaluate the output power and energy.
8- Build a DC-DC step down converter to enable the generated power to be used to illuminate LEDs.
9- Develop measurement method and evaluate the effective piezoelectric d_{33} coefficient of the piezoelectric bridge transducer.

1.3 Outline of dissertation

In Chapter 2, the fundamentals of piezoelectricity are discussed. Chapter 3 presents low temperature additives for sintering BNKBT88 ceramics at 900ºC. In Chapter 4, BNKBT88 ceramics are sintered in controlled oxygen atmosphere at 900ºC in a modified laboratory furnace to demonstrate the compatibility of using copper co-fired electrodes. Chapter 5 presents the effects of A-site non-stoichiometry on the electromechanical properties of BNKBT88 and further studies electromechanical

properties resulting from bismuth deficiency. In Chapter 6, a novel piezoelectric bridge transducer is designed, fabricated, and evaluated for a road-based energy harvesting application and tested under simulated vehicle loading.

2. Introduction

2.1 Piezoelectricity

The piezoelectric effect is used to convert mechanical energy into electrical energy and is given by the equation:

$$D_i = d_{ijk}T_{jk}, \quad i,j,k = 1,2,3$$

where D is the dielectric displacement with units of charge per area, d is the piezoelectric coefficient in pC/N, and T is stress [1][2]. The piezoelectric coefficient involves 27 components in 3 directions that can be reduced to 18 independent components represented by a 6x3 matrix. In the matrix notation, the equation for dielectric displacement by the direct piezoelectric effect can be written as:

$$D_i = d_{ij}T_j \qquad i = 1,2,3 \;\; j = 1,2,3,\ldots,6$$

Piezoelectricity is determined by symmetry in a point group. All 11 centrosymmetric point groups have zero piezoelectric coefficients due to symmetry, while all of the remaining non-centrosymmetric point groups all exhibit the piezoelectric effect with the exception of point group 432. Examples of piezoelectric ceramics are quartz (SiO_2), zinc oxide, and lead titanate.

Poled lead titanate, $PbTiO_3$ is a piezoelectric material with the polar, non-centrosymmetric point group 4mm [2]. The symmetry of the 4mm point group results in three piezoelectric coefficients: the transverse d_{31} and d_{32}, longitudinal d_{33}, and the shear d_{15} coefficients. The transverse d_{31} and d_{32} coefficients are equal with negative value.

$$d_{ij} = \begin{bmatrix} 0 & 0 & 0 & 0 & d_{15} & 0 \\ 0 & 0 & 0 & d_{15} & 0 & 0 \\ d_{31} & d_{31} & d_{33} & 0 & 0 & 0 \end{bmatrix}$$

These different piezoelectric modes are shown in Figure 2.1. By convention, the direction 3 is the direction that the ceramic is poled. The polarization resulting from stress is given by the equation:

$$D_3 = d_{31}T_1 + d_{31}T_2 + d_{33}T_3$$

For stress applied in the 3-direction only, the polarization simplifies to:

$$D_3 = d_{33}T_3$$

Piezoelectric transducers can be operated in the d_{31}, d_{33}, and d_{15} or a combination of piezoelectric modes depending on their design and the applied stress.

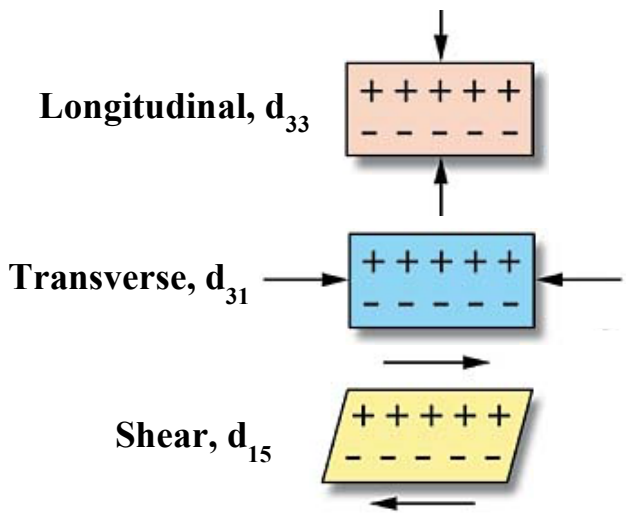

Figure 2.1. Stress direction resulting in longitudinal, transverse, or shear piezoelectric coefficient.

2.2 Ferroelectricity

A group of piezoelectric materials show spontaneous polarization in the absence of an electric field. Unlike other polar materials, the direction of the spontaneous polarization can be switched by the application of an external electric field. Ten of the twenty piezoelectric point groups are ferroelectric, including lead titanate with the

perovskite crystal structure shown in Figure 2.2. The perovskite crystal structure has the general formula ABO_3. The A-site is occupied by large, low valence cation such as Pb^{2+}, Na^{+}, K^{+}, Bi^{3+}, and Ba^{2+}. The B-site is occupied by small, high valence cation such as Ti^{4+}, Zr^{4+}, and Nb^{5+}.

At high temperature, lead titanate is paraelectric. The high temperature structure is from a cubic centrosymmetric point group so there are no piezoelectric properties. Upon cooling, the material transforms to a ferroelectric point group at a certain temperature with the development of spontaneous polarization. Figure 2.2 shows two phases of $PbTiO_3$ and spontaneous polarization only occurs in the tetragonal ferroelectric phase. The temperature where the ferroelectric transformation occurs is the Curie temperature, T_C. Below T_C, the ferroelectric domains form with spontaneous polarization.

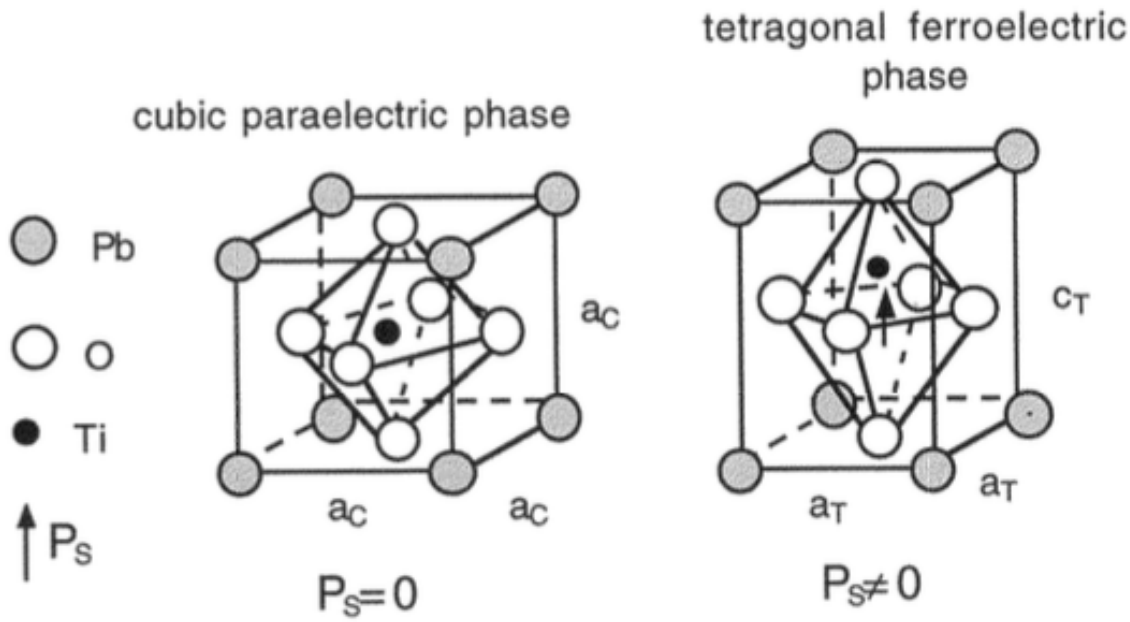

Figure 2.2. Lead titanate $PbTiO_3$ has perovskite crystal structure. At high temperature, $PbTiO_3$ has a paraelectric cubic phase. As it cools from high temperature, there is a transformation to tetragonal phase at the Curie temperature and becomes ferroelectric [3].

Ferroelectric domains are randomly orientated when a material is cooled from T_C. An electric field is applied to the ferroelectric material in a process called poling that aligns spontaneous polarization in the direction of the electric field. Figure 2.3 shows random orientation of ferroelectric domains before poling when the net polarization is zero. After poling, the polarization direction is aligned with the applied electric field. The ferroelectric domains are separated by boundaries called domain walls. The angle of rotation between the polarization direction of the ferroelectric domain and adjacent domains may be 180º, 90º, 71º, and 109º.

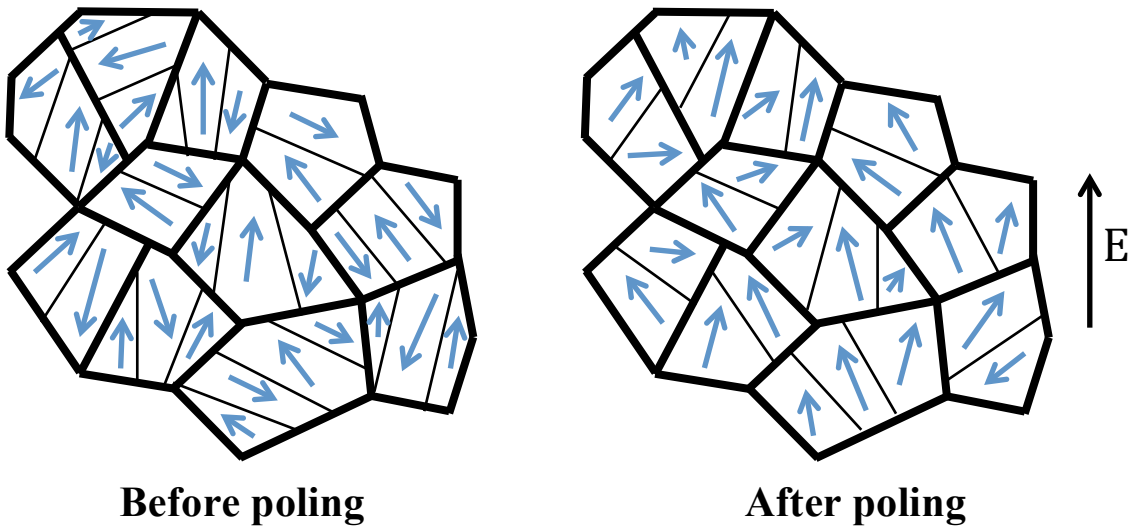

Figure 2.3. Polarization direction of ferroelectric domains before and after poling. Before poling, the domains are randomly oriented. Poling aligns the domains in the direction of the applied electric field.

The polarization in ferroelectric materials is reversible. Polarization is measured over an AC electric field and the polarization–electric field hysteresis is shown in Figure 2.4. Initially the polarization is at point A due to the random orientation of the ferroelectric domains. As the electric field increases, the polarization follows along the path from A-B-C-D. Point D is the maximum or saturated polarization, P_S, when the ferroelectric domains are all aligned due to the external electric field. As the electric field returns to zero, the polarization slightly decreases to the remnant polarization, P_r, because some of the ferroelectric domains do not keep their orientation once the electric field is removed. As negative electric field is applied, the polarization direction switches at point F. The electric field needed to switch the polarization direction of the ferroelectric domains is called the coercive field E_C. As the magnitude of the negative electric field is increased, the saturation polarization, $-P_S$, is achieved and returns to the remnant polarization $-P_r$ when the electric field is removed. The polarization does not return to

zero unless the ferroelectric material is heated to the Curie temperature or extreme pressure is applied.

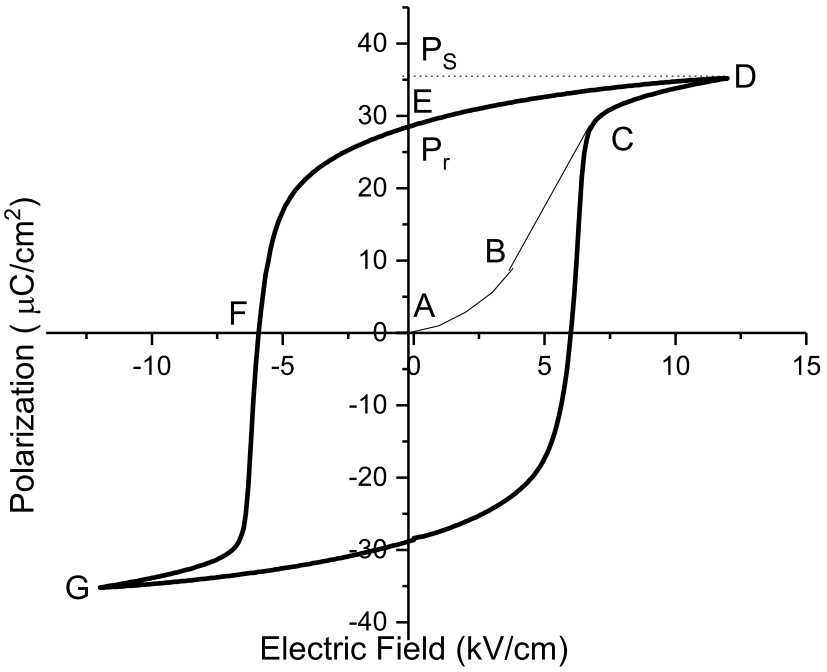

Figure 2.4. Polarization–electric field hysteresis loop.

The strain–electric field hysteresis occurs simultaneously with the polarization–electric field hysteresis. Due to the converse piezoelectric effect, the lattice expands when an electric field is applied in the same direction as the polarization, and the lattice contracts when an electric field is applied in the opposite direction. Figure 2.5 shows the strain–electric field hysteresis loop and Figure 2.6 shows the electric field and stain measured over time. At the starting point A, the poling direction is down and there is no electric field. A positive electric field is applied, which is opposite to the direction of

spontaneous polarization, and the lattice contracts to point B. At point B, the electric field is equal to the coercive field and the spontaneous polarization becomes aligned with the electric field. The magnitude of the electric field continues to increase and the lattice expands since the domains are not aligned in the same direction. A maximum strain is achieved when the highest electric field is applied at point C. As the magnitude of the electric field is reduced, strain decreases to zero. The application of an electric field in the opposite direction of the polarization direction causes the lattice to contract. At point D, the electric field is equal to the coercive field and polarization switching of the ferroelectric domains occurs. After switching, the polarization direction is now in the same direction as the applied electric field and the strain becomes positive. Further increasing the magnitude of the negative electric field causes strain to reach the maximum at point E. The strain–electric field behavior results in a butterfly shape due to the switching of ferroelectric domains from an applied AC electric field.

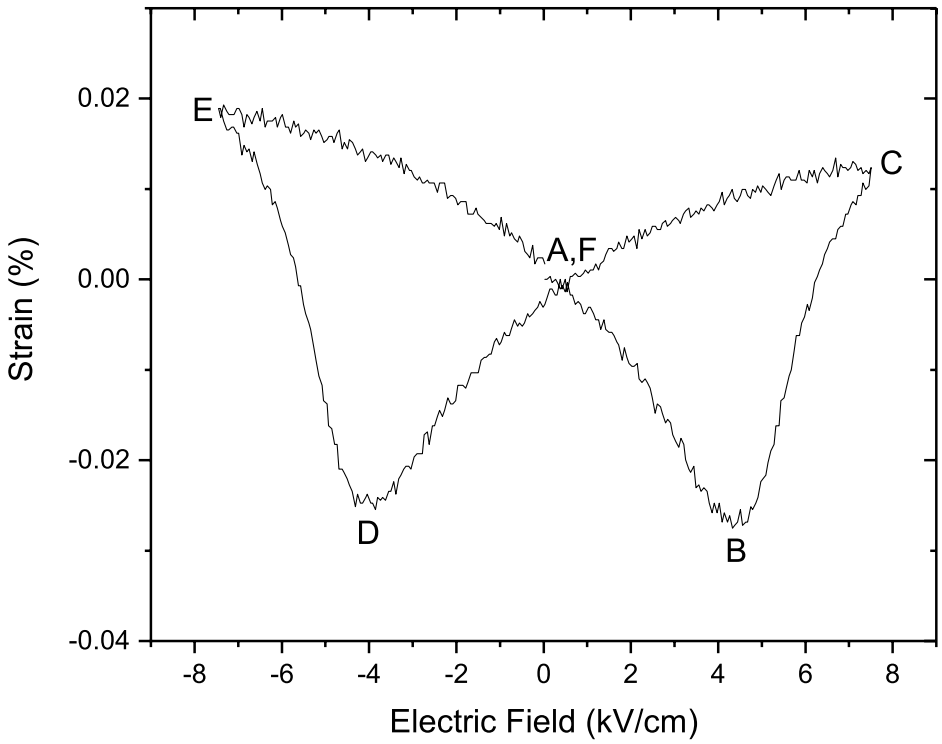

Figure 2.5. Strain–electric field hysteresis.

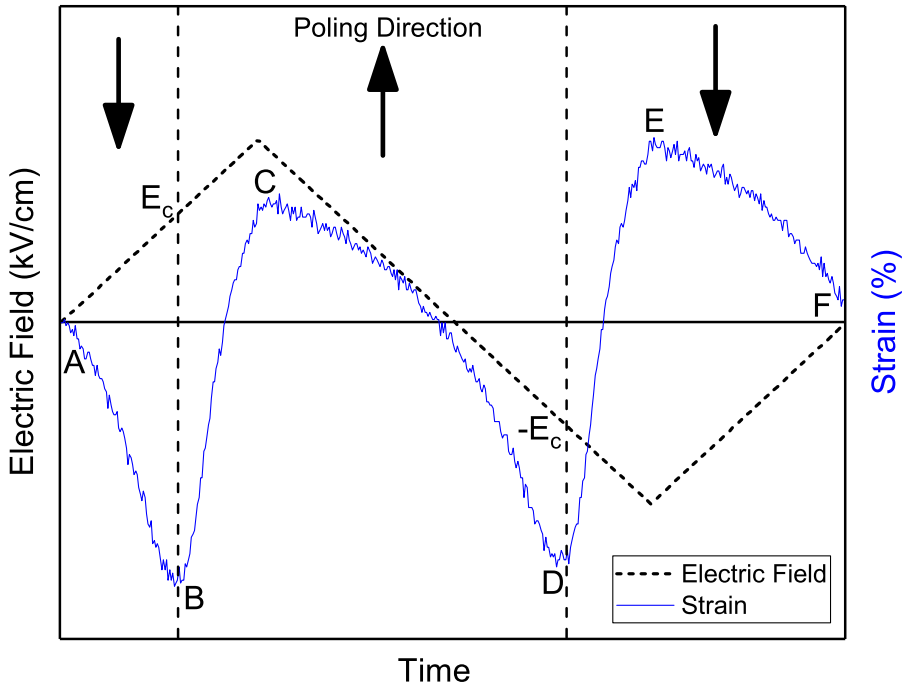

Figure 2.6. Strain and electric field measured with time for the hysteresis shown in Figure 2.5. The arrows indicate the poling direction.

The number of polarization directions is determined by the crystal structure of the ferroelectric material. Figure 2.7 shows the possible polar directions in rhombohedral, orthorhombic, and tetragonal crystal systems. Tetragonal crystal systems have six possible polar directions along the <001> direction. The polar directions in rhombohedral are along the diagonals of the crystal for a total of eight polar directions along the <111> direction. Orthorhombic systems have a total of 12 polar directions. The monoclinic phase has a total of 24 possible polar directions shown in Figure 2.8. Polarization is free to rotate along the <111>, <110>, and <100> directions in M_A, M_B, and M_C respectively [4].

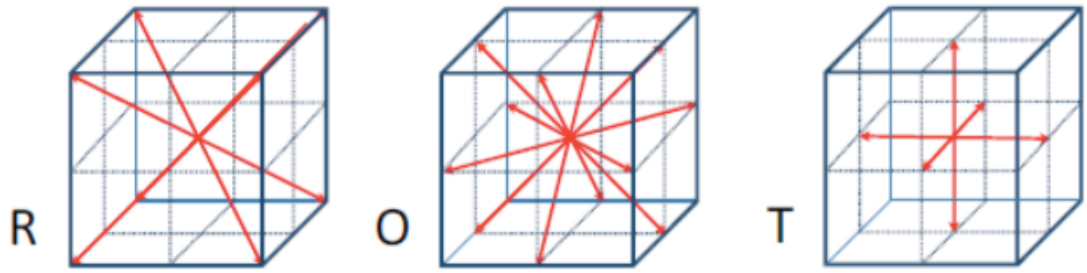

Figure 2.7. Possible polar directions in rhombohedral R, orthorhombic O, and tetragonal T phases. In each crystal system, the polarization directions for rhombohedral, orthorhombic, and tetragonal are along the <111>, <110>, and <001> directions respectively [4].

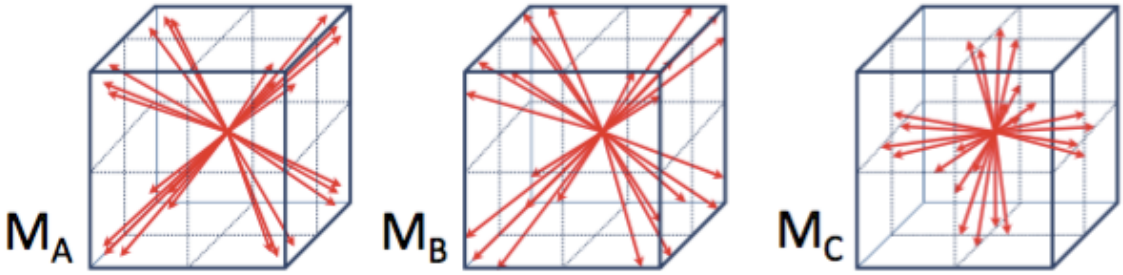

Figure 2.8. The monoclinic phase has a total of 24 possible polar directions. Polarization is free to rotate along the <111>, <110>, and <100> directions in M_A, M_B, and M_C respectively [4].

In the lead zirconate ($PbZrO_3$) – lead titanate ($PbTiO_3$) system shown in Figure 2.9, a morphotropic phase boundary (MPB) occurs for the composition $Pb(Zr_{0.52},Ti_{0.48})O_3$. At the morphotropic phase boundary between tetragonal and rhombohedral phases, the six possible polarization directions from the tetragonal phase combine with the eight directions of the rhombohedral phase to give a possible 14 polarization directions and domains are easily polarized in the direction of an applied electric field. A vertical phase boundary between tetragonal and rhombohedral phases is important because the MPB compositions is stable with temperature. PZT remains at the MPB composition as it is heated up to the Curie temperature at 350ºC. A monoclinic

phase occurs in PZT for morphotropic phase boundary compositions at low temperature [5].

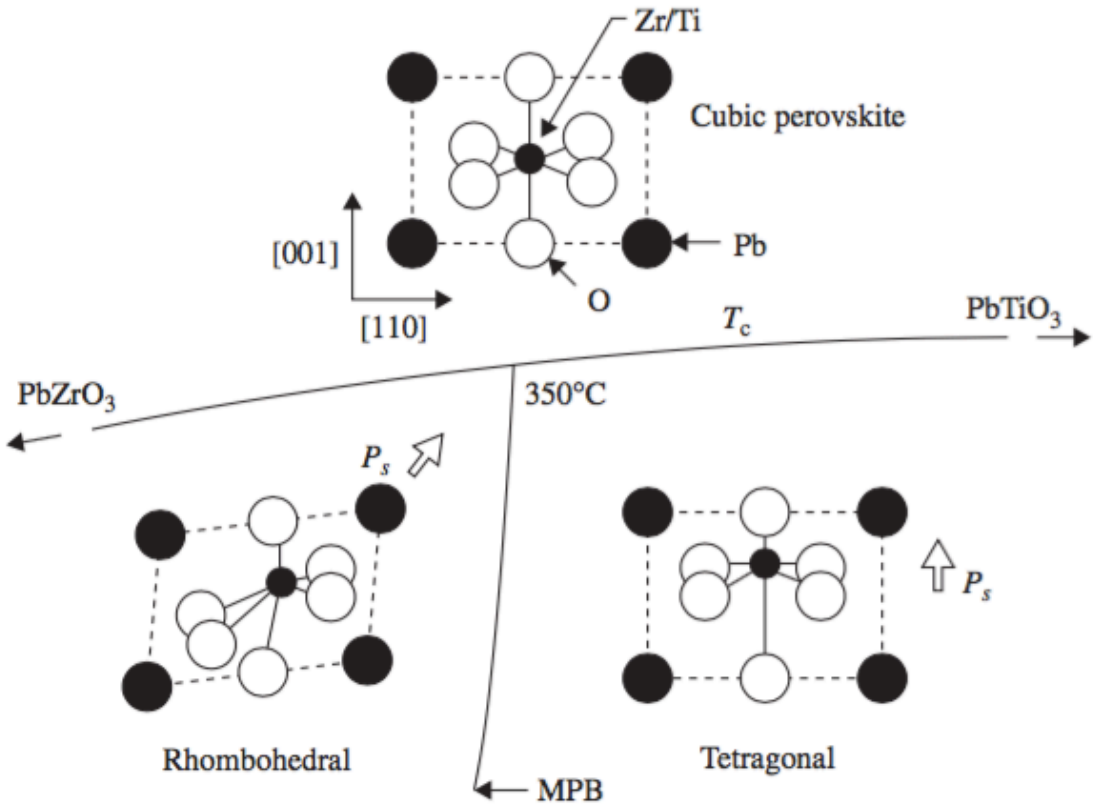

Figure 2.9. The morphotropic phase boundary occurs between rhombohedral $PbZrO_3$ and tetragonal $PbTiO_3$ compositions. The MPB composition has a total of 14 possible polar directions resulting in superior piezoelectric properties [2].

2.3 Applications of piezoelectric and ferroelectric materials

The piezoelectric material PZT has been extensively studied and used in many applications such as hydrophones, acoustic devices, medical imaging, micro-electromechanical systems (MEMS), ferroelectric dynamic random access memory (Fe-DRAM), as well as piezoelectric actuators and motors [6][7][8][9]. Many of these devices utilize the resonant frequency of the piezoelectric device. Depending on the

geometry of the ceramic and the location of the electrodes, different vibrational modes occur as shown in Figure 2.10. The longitudinally poled ceramic utilizes the d_{33} mode while the transversely poled ceramics utilizes the d_{31} mode. The disc uses a combination of d_{33} and d_{31} and has two vibrational modes, planar and thickness mode, depending on the frequency range.

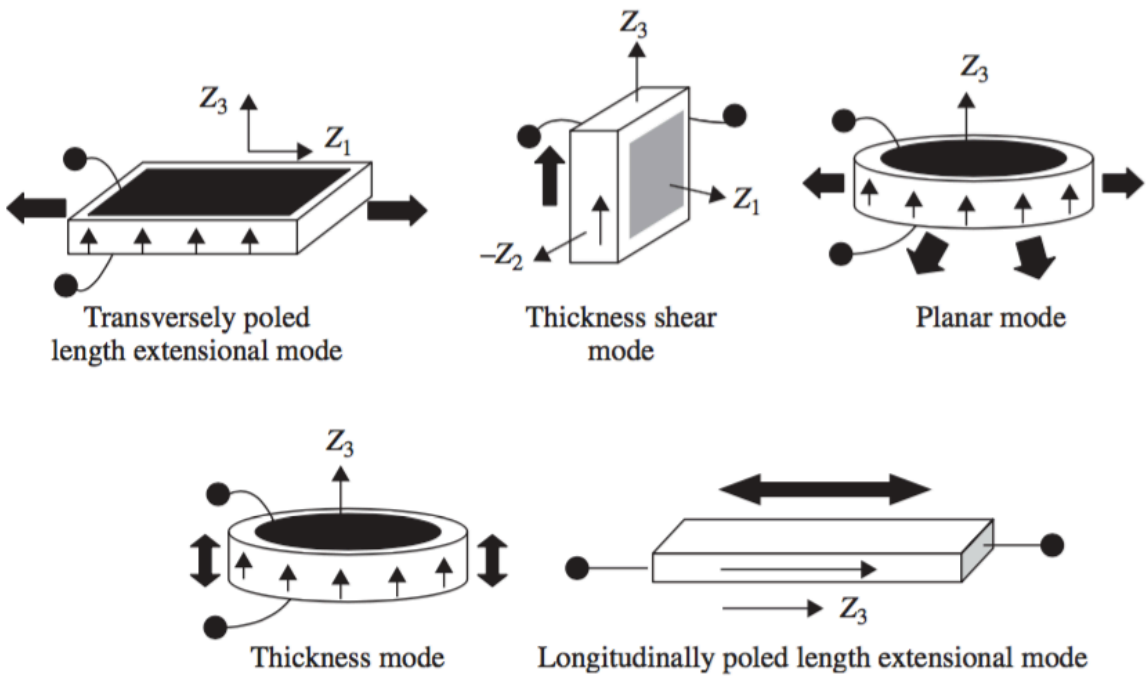

Figure 2.10. Different vibrational modes in piezoelectric devices [2].

The perovskite structure has the general structure ABO_3 where the sum of the charges on the A-site and B-site add up to six. Perovskite materials can have the form $A^{+}B^{5+}O_3$, $A^{2+}B^{4+}O_3$, or $A^{3+}B^{3+}O_3$ [3]. Elements used to dope the perovskite structure on either the A-site or B-site can have various effects that alter the piezoelectric properties. The terms “hard” and “soft” are used to describe the properties. Acceptor doping the A-site or B-site by substitution with a lower valence cation produces hard properties.

Acceptor doped piezoelectric materials have square shaped hysteresis loops, decreased dielectric loss and improved mechanical quality factor, but have decreased dielectric constant. Hard piezoelectric materials are ideal for high power application due to their low loss. Oxygen vacancies form to counter the increased charge in the structure. The oxygen vacancies pin domain walls resulting in an internal bias field, which opposes motion of the domain walls, making hard piezoelectric compositions difficult to pole and depole [1]. The pinning of domain walls inhibits their movement when an electric field is applied, reducing mechanical losses [3].

Donor doping the A-site or B-site with a higher valence cation results in "soft" piezoelectric properties. Donor-doped piezoelectric materials are easy to pole, as well as depole and have reduced Curie temperature. They have high coupling coefficients, high d_{33}, improved dielectric constant, but poor mechanical quality factor and increased dielectric loss [1]. Soft materials are used for low power medical imaging devices, acoustic sensors, and ferroelectric random access memory (FeRAM) [6].

The use of an element as a dopant depends on the ionic radius and valance. Large, low valence cations are possible A-site dopants and their ionic radius is given in Table 2.1. These include the alkali and alkaline earth metals, as well as many of the rare earth elements. Small, high valence cations are used as B-site dopants are shown in Table 2.2, including many of the transition metals, which can have multiple valence states and corresponding ionic radii [10].

Table 2.1. A-site dopants and their ionic radii [10].

Cation	Ionic radius (Å)
Na^{1+}	1.39
K^{1+}	1.64
Ca^{2+}	1.34
Sr^{2+}	1.44
Ba^{2+}	1.61
Pb^{2+}	1.49
Bi^{3+}	1.4
La^{3+}	1.36
Ce^{3+}	1.34
Nd^{3+}	1.27
Sm^{3+}	1.24

Table 2.2. B-site dopants and their ionic radii [10].

Cation	Ionic radius (Å)
Ti^{4+}	0.605
Fe^{3+}	0.645
Ni^{2+}	0.69
Mn^{2+}	0.83
Mn^{3+}	0.645
Mn^{4+}	0.53
Cu^{2+}	0.73
Zn^{2+}	0.74
Zr^{4+}	0.72
Nb^{4+}	0.68
Nb^{5+}	0.64
Sn^{4+}	0.69

The stability of any combination of A-site and B-site cations for forming a perovskite structure can be estimated using the tolerance factor τ:

$$\tau = \frac{r_A + r_O}{\sqrt{2}\,(r_B + r_O)}$$

where r_A and r_B are the ionic radii of the 12-coordinated A-site and 6 coordinated B-site cations respectively and r_O is the ionic radius of oxygen [11]. Perovskite structures are stable for τ ranging from about 0.88 to 1.09 with increasing stability as τ increases. At lower values of τ, the structure becomes distorted due to the tilting of oxygen octahedra [11]. For compositions with multiple A-site or B-site cations, the weighted average of their ionic radii are used to calculate tolerance factor.

2.4 Lead-free piezoceramics

The toxicity of lead to human health is well documented and the effects of past lead use are persistent today. Lead paint, which was banned in 1978, is the leading cause of lead exposure to children [12]. Human exposure to lead has decreased dramatically since it was phased out as an automotive gasoline additive in 1979, but lead has accumulated in soils in urban areas from its use in gasoline and paint [12][13].

In the United States, government regulations of lead have been implemented slowly. The switch to unleaded gasoline in 1974 was not due to concerns over lead, but because new cars were equipped with catalytic converters that would be damaged by lead. Lead was phased out as a gasoline additive between 1979 and 1988 but refiners were using low levels of lead until 1996 [13].

In Europe, toxic substances in electronic devices and waste including vehicles is regulated to limit their impact on the environment and health. The Restriction of Hazardous Substances Directive (RoHS), the Waste Electrical and Electronic Equipment Directive (WEEE Directive), and the End of Life Vehicles Directive (ELV) is the legislation used to restrict hazardous substances. Lead in piezoelectric ceramics has been exempt from the RoHS directive since it was adopted in 2003 because a suitable lead-free alternative has not been found [14]. The current RoHS exemption of lead-based ceramics expires in 2019.

The alternatives to lead based piezoelectric ceramics are $BaTiO_3$ (BT), $K_{0.5}Na_{0.5}NbO_3$ (KNN) and $(Bi_{0.50}Na_{0.50})TiO_3$ (BNT) based compositions. However the piezoelectric properties of these compositions cannot match PZT. The piezoelectric coefficient as a function of Curie temperature is shown in Figure 2.11 for PZT and lead free materials. For the different PZT and lead-based compositions, there is an inverse relationship between d_{33} and Curie temperature. BNT, BT, and KNN compositions cannot match the high piezoelectric coefficient of lead-based ceramics. Replacements for PZT will need to be suited for their specific applications rather than overall piezoelectric properties [14].

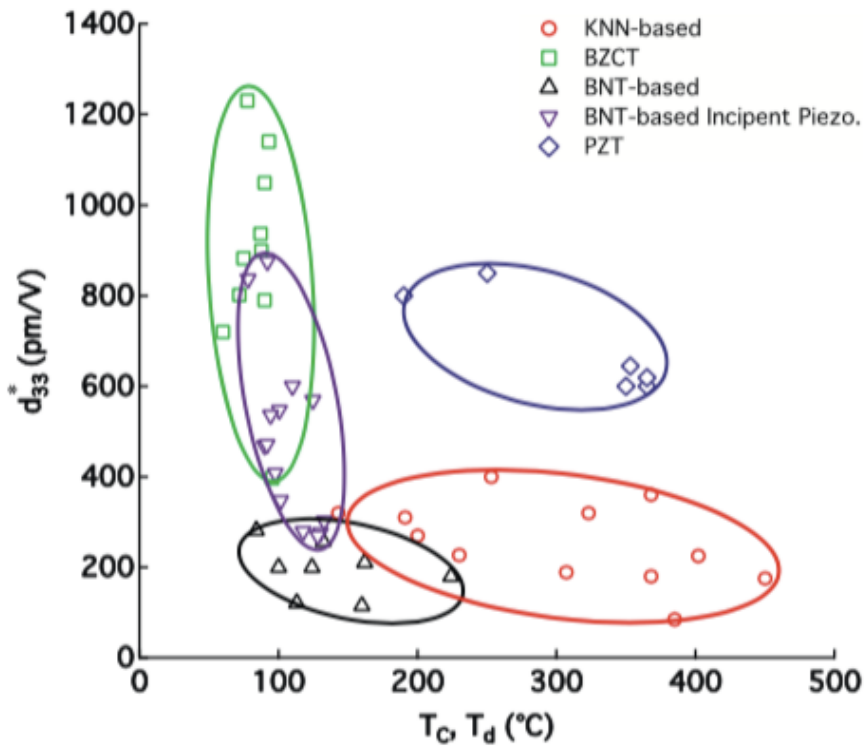

Figure 2.11. d_{33} values for different piezoelectric compositions as a function of Curie temperature [14].

2.5 BNT-based piezoceramics

Rhombohedral BNT forms solid solutions with tetragonal $BaTiO_3$ (BT) and has a morphotropic phase boundary near the composition 0.94BNT-0.06BT (BNBT-6). The electromechanical properties of BNBT-6 are higher than those of BNT [15]. The BNT-BT phase diagram shown in Figure 2.12 has an antiferroelectric phase that occurs at 130ºC for the MPB composition [15]. The transition to the antiferroelectric phase causes depolarization of the ferroelectric composition [16]. Above depolarization temperature, T_d, there is a transition to an intermediate antiferroelectric state, and for MPB compositions there is a coexistence of ferroelectric and antiferroelectric states [17][18]. BNT based piezoelectric materials have a Curie temperature of about 300°C where the

crystal structure becomes cubic, however the transition to an antiferroelectric phase causes depolarization to occur at lower temperature [17].

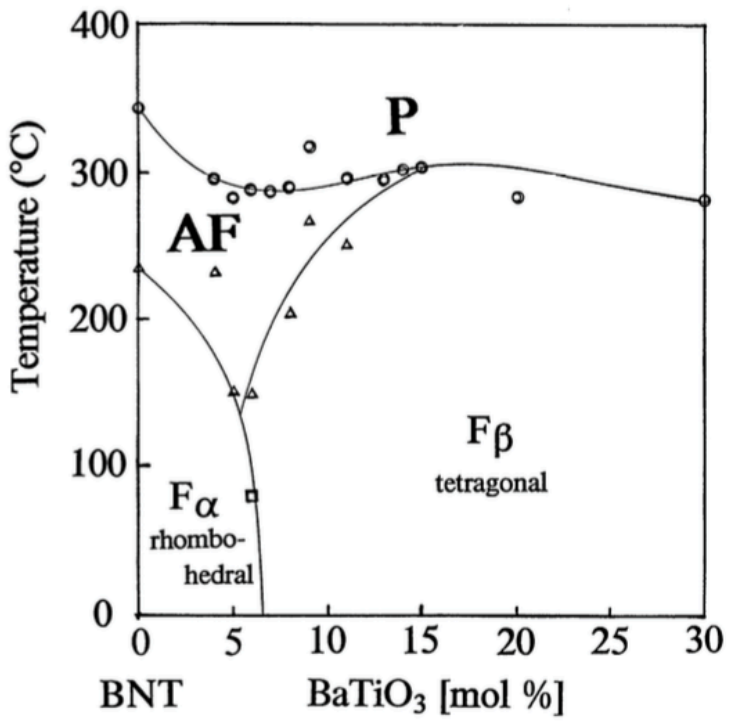

Figure 2.12. BNT-BT system has a morphotropic phase boundary near 7% $BaTiO_3$ [15].

The X-ray diffraction pattern for the (1-x)BNT-xBT system is shown in Figure 2.13. The BNT rich phase has a rhombohedral structure which transitions to tetragonal phase with increasing BT. The composition with x=0.50 shows mixed rhombohedral and tetragonal phases. The structure can not be resolved by X-ray diffraction and requires synchrotron radiation source or neutron diffraction for further analysis [19].

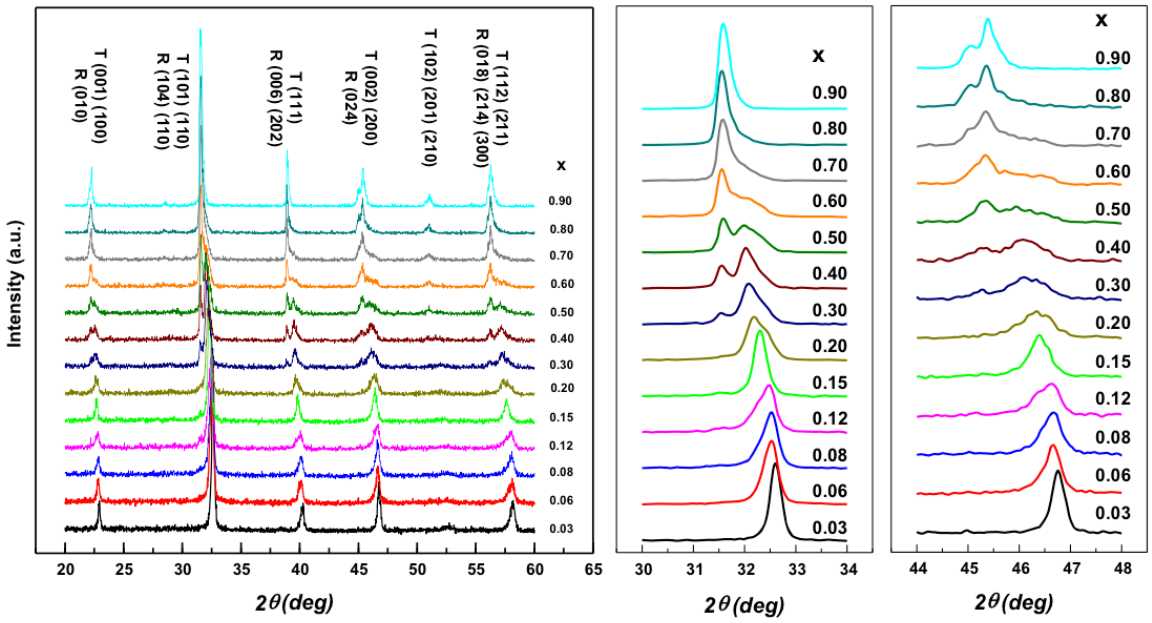

Figure 2.13. X-ray diffraction pattern of (1-x)BNT-xBT. The BNT rich phase has a rhombohedral structure which transitions to tetragonal phase with increasing BT[19].

The electromechanical properties of BNT-BT system can be improved by modification with $(Bi_{0.50}K_{0.50})TiO_3$ (BKT) or $(Bi_{0.50}Li_{0.50})TiO_3$ (BLT). In the ternary system BNT-BKT-BT, the morphotropic phase boundary occurs at the region shown in **Figure 2.14** [20][17]. Compositions near the MPB are can be written in the form $x[(Bi_{0.5}Na_{0.5})TiO_3] – y[(Bi_{0.5}K_{0.5})TiO_3] – z[BaTiO_3]$ where x+y+z=1 and the ratio of y:z is 2:1, abbreviated as BNKBTx [21]. Using this notation, BNKBT-x phase diagram is shown in Figure 2.15 and the MPB occurs for the composition BNKBT88. Similar to the BNT-BT system, there is an antiferroelectric phase that occurs at the MPB composition in the BNT-BKT-BT ternary system.

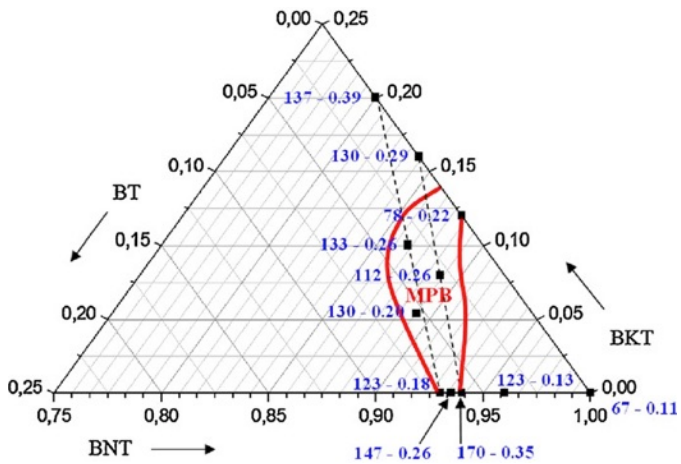

Figure 2.14. d_{33} and k_p for various compositions along the MPB in the BNT-BKT-BT system [20].

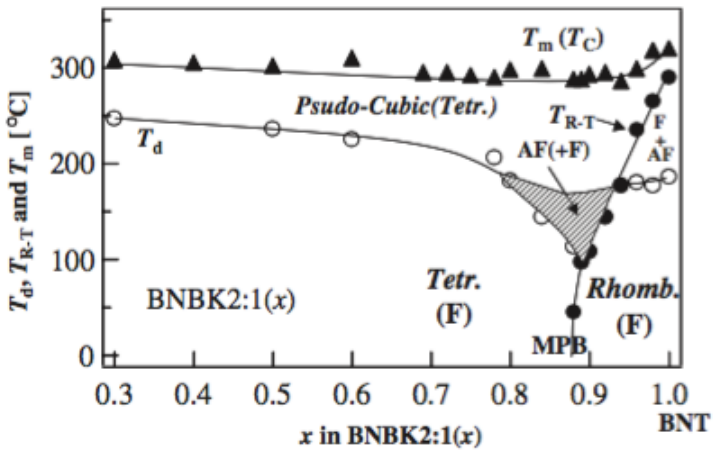

Figure 2.15. Phase diagram of the BNBK2:1. (x)BNT–(y)BKT–(z)BT [x+y+z=1; y:2=2:1]. The morphotropic phase boundary occurs at BNBK88 composition. Depolarization occurs at lower temperature for compositions near the MPB. [17].

The piezoelectric properties and phases of various BNT-based compositions are given in Table 2.3. The morphotropic phase boundary composition has the highest d_{33} and coupling coefficients but also the lowest depolarization temperature [17]. In the x(BNT)-y(BLT)-z(BKT) system the morphotropic phase boundary occurs from 0-8% BLT and 18-20% BKT [22]. This composition is abbreviated BNLKTy-z. BLT increases d_{33} while reducing depolarization temperature. The optimal composition has the formula 0.76BNT-

0.04BLT-0.20BKT with d_{33} of 176 pC/N and T_d of 171°C [22]. The composition with 0.08BLT has d_{33} of 231pC/N although T_d would be below 100°C.

Rhombehedral 0.88BNT-0.08BKT-0.04BLT has depolarization temperature of 220ºC, which is suitable for use in high power application but has lower d_{33} compared to the morphotropic phase boundary composition [23]. Acceptor doping by substitution of manganese for titanium on the B-site in rhombehedral BNKLT piezoceramics has achieved a coercive field of 50kV/cm and mechanical quality factor up to 974 making these ceramics a potential in alternative to hard PZT in high power application [24][25].

Table 2.3. Properties of BNT based compositions near the morphotropic phase boundary

Material	Phase	d_{33} (pC/N)	T_d (°C)	T_C (°C)	ε_r	k_p	k_{33}	Q
BNBK94 [17]	Rh.	92	185		493	0.253	0.476	
BNBK88 [17]	MPB	181	113		999	0.319	0.56	
BNBK88 [21]	MPB	170		262	810	0.36		150
BNBK80 [17]	Tetr.	128	182		1058	0.17	0.455	
BNBT-6 [26]	MPB	125		288	580		0.55	81
BNKT-20 [26]	MPB	151		317	1030	0.27	0.49	109
BNLKT4-20 [22]	MPB	176	171		800			
BNLKT8-20 [22]	MPB	190	115		1000			

References

[1] B. Jaffe, W. R. Cook, and H. Jaffe, *Piezoelectric Ceramics*. New York: Academic Press, 1971.

[2] R. E. Newnham, *Properties of Materials Anisotropy, Symmetry, Structure*. Oxford University Press, 2005.

[3] D. Damjanovic, "Ferroelectric, dielectric and piezoelectric properties of ferroelectric thin films and ceramics," *Rep. Prog. Phys.*, vol. 61, pp. 1267–1324, 1998.

[4] J. Perantie, "Electric-field-induced dielectric and caloric effects in relaxor ferroelectrics," University of Oulu, Oulu, 2014.

[5] B. Noheda *et al.*, "The monoclinic phase in PZT: New light on morphotropic phase boundaries," *AIP Conf Proc*, vol. 535, p. 304, 2000.

[6] G. H. Haertling, "Ferroelectric Ceramics: History and Technology," *J. Am. Ceram. Soc.*, vol. 82, no. 4, pp. 797–818, 1999.

[7] Department of Defense, "Piezoelectric Ceramic for Sonar Transducers," *DOD-STD-1376ASH*, 1988.

[8] N. Setter, Ed., *ELECTROCERAMIC-BASED MEMS Fabrication-Technology and Applications*. Springer Science, 2005.

[9] K. Uchino, *Piezoelectric Actuators and Ultrasonic Motors*. 1997.

[10] R. D. Shannon, "Revised Effective Ionic Radii and Systematic Studies of Interatomic Distances in Halides and Chaleogenides," *Acta. Cryst.*, vol. 32, p. 751, 1976.

[11] A. Kumar, A. S. Verma, and S. R. Bhardwaj, "Prediction of Formability in Perovskite-Type Oxides," *Open Appl. Phys. J.*, vol. 1, pp. 11–19, 2008.

[12] B. Lanphear *et al.*, "Prevention of Childhood Lead Toxicity," *Pediatrics*, vol. 138, no. 1, p. 1493, 2016.

[13] H. Mielke, "Nature and extent of metal-contaminated soils in urban environments," *Env. Geochem Health*, vol. 38, no. 4, pp. 987–999, 2016.

[14] J. Rodel, K. G. Webber, R. Dittmer, W. Jo, M. Kimura, and D. Damjanovic, "Transferring lead-free piezoelectric ceramics into application," *J. Eur. Ceram. Soc.*, vol. 35, pp. 1659–1681, 2015.

[15] T. Takenaka, K. Maruyama, and K. Sakata, "(Bi1/2Na1/2)TiO3–BaTiO3 System for Lead-Free Piezoelectric Ceramics," *Jpn. J. Appl. Phys.*, vol. 30, no. 9B, pp. 2236–2239, 1991.

[16] E.-M. Anton, W. Jo, D. Damjanovic, and J. Rodel, "Determination of depolarization temperature of (Bi1/2Na1/2)TiO3-based lead-free piezoceramics," *J. Appl. Phys.*, vol. 110, p. 094108, 2011.

[17] Y. Hiruma, H. Nagata, and T. Takenaka, "Phase Transition Temperatures and Piezoelectric Properties of (Bi1/2Na1/2)TiO3–(Bi1/2K1/2)TiO3–BaTiO3 Lead-Free Piezoelectric Ceramics," *Jpn. J. Appl. Phys.*, vol. 45, pp. 7409–7412, 2006.

[18] Y. Guo, Y. Liu, R. L. Withers, F. Brink, and H. Chen, "Large Electric Field-Induced Strain and Antiferroelectric Behavior in (1-x)(Na0.5Bi0.5)TiO3-xBaTiO3 Ceramics," *Chem. Mater.*, vol. 23, pp. 219–228, 2011.

[19] J.-H. Cho, Y.-H. Jeong, J.-H. Nam, J.-S. Yun, and Y.-J. Park, "Phase transition and piezoelectric properties of lead-free (Bi1/2Na1/2)TiO3–BaTiO3 ceramics," *Ceram. Int.*, vol. 40, pp. 8419–8425, 2014.

[20] J.-F. Trelcat, C. Courtois, M. Rguiti, A. Leriche, P.-H. Duvigneaud, and T. Segato, "Morphotropic phase boundary in the BNT–BT–BKT system," *Ceram. Int.*, vol. 38, pp. 2823–2827, 2012.
[21] S. Zhang, T. R. Shrout, H. Nagata, Y. Hiruma, and T. Takenaka, "Piezoelectric Properties in (K0.5Bi0.5)TiO3-(Na0.5Bi0.5)TiO3-BaTiO3 Lead-Free Ceramics," *Ieee Trans. Ultrason. Ferroelectr. Freq. Control*, vol. 54, no. 5, pp. 910–917, 2007.
[22] Y. Hiruma, H. Nagata, and T. Takenaka, "Depolarization temperature and piezoelectric properties of (Bi1/2Na1/2)TiO3–(Bi1/2Li1/2)TiO3–(Bi1/2K1/2)TiO3 lead-free piezoelectric ceramics," *Ceram. Int.*, vol. 35, pp. 117–120, 2009.
[23] Y. Hiruma, T. Watanabe, H. Nagata, and T. Takenaka, "Piezoelectric Properties of (Bi1/2Na1/2)TiO3-Based Solid Solution for Lead-Free High-Power Applications," *Jpn. J. Appl. Phys.*, vol. 47, no. 9, pp. 7659–7663, 2008.
[24] E. Taghaddos, M. Hejazi, and A. Safari, "Electromechanical Properties of Acceptor-Doped Lead-Free Piezoelectric Ceramics," *J. Am. Ceram. Soc.*, vol. 97, no. 6, pp. 1756–1762, 2014.
[25] M. Hejazi, E. Taghaddos, E. Gurdal, K. Uchino, and A. Safari, "High Power Performance of Manganese-Doped BNT-Based Pb-Free Piezoelectric Ceramics," *J Am Ceram Soc*, vol. 97, no. 10, pp. 3192–3196, 2014.
[26] H. Nagata, M. Yoshida, Y. Makiuchi, and T. Takenaka, "Large Piezoelectric Constant and High Curie Temperature of Lead-Free Piezoelectric Ceramic Ternary System Based on Bismuth Sodium Titanate-Bismuth Potassium Titanate-Barium Titanate near the Morphotropic Phase Boundary," *Jpn. J. Appl. Phys.*, vol. 42, pp. 7401–7403, 2003.

3. Low temperature sintering of BNKBT88 ceramics

In this chapter, the development of additives for the low temperature sintering of BNT-based piezoceramics is discussed. The combination of Bi_2O_3, Li_2CO_3, CuO, ZnO and B_2O_3 oxides or carbonate additives are used to sinter BNKBT88 ceramics at 900ºC in air and controlled oxygen atmosphere for co-firing with copper electrodes. The composition of additive is based on the research and development for the low temperature sintering of piezoelectric ceramics.

3.1 Introduction

Co-fired ceramics and electrode materials are used to make microelectronic devices such as accelerometers, actuators, sensors, and acoustic wave devices. Co-firing reduces cost by incorporating the electrodes into the fabrication process [1]. Decreasing the sintering temperature of the ceramic enables the use of lower cost electrode materials such as silver. Other low cost electrode materials such as copper or nickel can be used, but require controlled oxygen atmosphere and low temperature for sintering copper around 900ºC [2][3].

The thermodynamic driving force for sintering is the reduction of surface free energy. Sintering occurs via diffusion and must be carried out at high temperature due to high activation energy. Sintering temperatures are typically 70% of the melting temperature of the ceramic [4]. Sintering is considered a solid state phenomena, but there is often a liquid present due to small quantities of impurities in the ceramic composition [5][6]. The liquid phase lowers the activation energy of sintering by providing the ceramic a pathway for diffusion through the liquid. Smaller ceramic particles dissolve in

the liquid and recrystallize onto larger grains [7]. In ceramics that contain a volatile component such as PZT, lead oxide enhances sintering through the vapor phase transport of lead oxide [8].

Additives that are used to enhance sintering by lowering the activation energy are known as sintering aids, sintering additives, or fluxes. The additives lower the activation energy of sintering by forming a liquid phase. The liquid phase consolidates the ceramic particles through capillary forces and enhances diffusion. A list of additives used for sintering lead-based piezoceramics is given in Table 3.1. Ceramic oxides with low melting temperature, such as V_2O_5 that melts at 690ºC, can be used to sinter PZT below 975ºC [9]. The additive does not need to have a low melting temperature if it forms a eutectic with an oxide from the ceramic composition. The phase diagram of the PbO-CuO system, shown in Figure 3.1, has a low temperature eutectic of about 800ºC [10][11]. When copper oxide, which melts at 1326ºC is added to PZT, PbO from the ceramic particles melts with the CuO to form a liquid. The liquid will begin to form at the eutectic temperature of 800ºC even if the CuO-PbO mixture is not at the eutectic composition. Above the eutectic temperature, the liquid is present with either PbO or CuO, which continues to melt as temperature is increased. Lead oxide can diffuse through the CuO-PbO liquid to form the liquid phase that lowers sintering temperature by enhancing diffusion of the PbO [7].

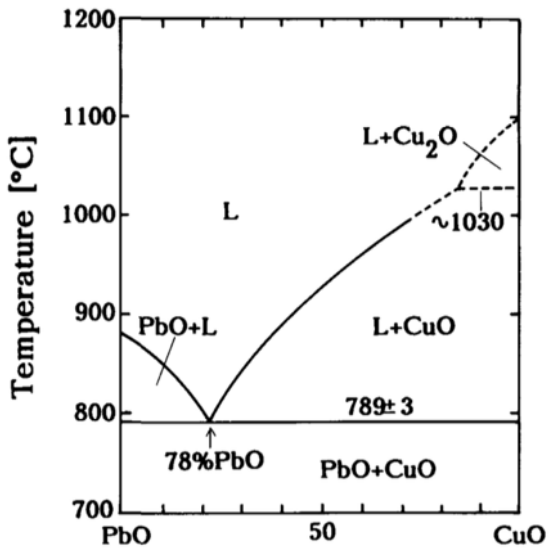

Figure 3.1. PbO–CuO phase diagram [10].

Table 3.1. Additives used for sintering of PZT based ceramics at low temperature.

Ceramic	Additive	Sintering temperature (ºC)	Reference
PZT	1.0 wt% $LiBiO_2^*$ + 0.06 wt% CuO	880	[12]
PZT	0.2wt% $4PbO•B_2O_3$	1150	[13]
PZT (Pz26)[1]	$PbO•Cu_2O$	1100	[14]
PZT	1.2 wt% $PbO•WO_3$	1075	[15]
PZT	2.0 wt% P_2O_5	1050	[16]
PZT	1.0 wt% V_2O_5	975	[9]
PZT (APC 841)[2]	0.2 wt% CuO + 1.1 wt% ZnO	950	[17]
PNN-PT-PZ[3]	3 mol% ZnO + 1 mol% CuO	900	[18]
PLZT[4]	6.0 wt% $LiBiO_2^*$	950	[19]
PMN-PZT[5]	0.1wt% Li_2CO_3 + 0.3wt% Bi_2O_3 + 0.3wt% CuO	940	[20]
PZT-SKN[6]	1.0 wt% $LiBiO_2^*$ + 1.0 wt% CuO	900	[21]

[1]Ferroperm standard PZT. [2]American Piezoceramics 841, hard PZT for high power application. [3]$Pb(Ni_{1/3}Nb_{2/3})O_3$-$PbTiO_3$-$PbZrO_3$. [4]$(Pb,La)(Zr,Ti)O_3$. [5]$Pb(Mn_{1/3}Nb_{2/3})O_3$-$Pb(Zr,Ti)O_3$. [6]$Pb(Zr,Ti)O_3$–$Sr(K_{0.25}Nb_{0.75})O_3$. *$LiBiO_2$ is 1:1 molar ratio mixture of Li_2O and Bi_2O_3.

The liquid phase must have good adhesion to the ceramic particles and fully wet the surface. If there is poor adhesion to the ceramic particles, the liquid will not wet the ceramic and can leak out of the ceramic. The surface tension is measured by the contact angle between the liquid and the ceramic particles. A low contact angle indicates that there is strong adhesion to the ceramic [22]. However, the contact angle has to be measured at the sintering temperature where the liquid phase forms and requires a unique and difficult experimental setup [23].

In ideal conditions, the liquid phase completely wets all of the ceramic particles forming a 3D network. Driven by the reduction of surface free energy, smaller ceramic particles dissolve in the liquid and crystallize onto larger particles. Capillary forces pull the particles together; larger particles grow and begin to contact each other forming grain boundaries, and the liquid phase is expelled [7].

After densification, the components of the sintering aid remain in the ceramic. Crystallization of the sintering aid as a secondary phase may affect electrical or mechanical properties of the low temperature sintered ceramics. Diffusion of the sintering aids into the grains of the ceramic can have a negative effect on the properties [1]. To limit diffusion into the ceramic, the concentration of additives is kept as low as possible and is often below the detection limits of X-ray diffraction. The inclusion of glass forming oxides in the additive composition or the use of a pulverized multicomponent glass mixed with the ceramic may prevent crystallization of a secondary phase [1]. The glassy flux will remain at the grain boundaries as an amorphous film.

Removal of the liquid phase by evaporation enhances densification and prevents the formation of a secondary phase. Oxides such as lead oxide and bismuth oxide have

relatively high vapor pressure and will evaporate during sintering, even at a low temperature of 900ºC. Densification is enhanced as the liquid is removed and the ceramic particles are drawn closer together by capillary forces. Through evaporation, it is possible to remove the volatile components from the liquid composition.

The principles of liquid phase sintering have been refined into a new process called "Cold Sintering". Consolidation of ceramics can be accomplished at temperatures as low as 180ºC [24]. Cold sintered $BaTiO_3$ is prepared from $BaTiO_3$ nanoparticles mixed with and a suspension of $Ba(OH)_2/TiO_2$ dissolved in water. The slurry is placed in a die with a heated jacket and compacted under uniaxial pressure while heated to 180ºC [24]. Heating causes the Ba^{2+} ions and TiO_2 to become supersaturated in the liquid, and the ions precipitate onto the ceramic particles. The supersaturated ions are driven towards the surface of the $BaTiO_3$ particles by a compositional gradient [25]. Cold sintering is not possible for all piezoceramics compositions such as bismuth based ceramics where precursor have limited solubility in water. Cold sintering can consolidate compositions such as PZT; however high temperature annealing is required to achieve higher piezoelectric properties [26]. A requirement for this process is that the components of the ceramic are soluble in water. Cold sintering of bismuth containing ceramics may not be possible due to relative insolubility and instability of the Bi^{3+} ion in water [27].

3.2 Experimental procedure

The sintering additives Bi_2O_3 (Acros Organics, 99.9%), Na_2CO_3 (Acros Organics, 99.95%), Li_2CO_3 (Aldrich, 99.99%), CuO (Fischer Scientific, 99%), ZnO (Alfa Aesar, 99.99%), $BaCO_3$ (Alfa Aesar, 99.8%), and B_2O_3 (Alfa Aesar, 99.98%) were chosen as potential additives for sintering of BNT-based ceramics. The additives are weighed and combined with calcined BNKBT88 powder followed by ball milling in acetone for 12hr. After milling, the powders are dried in an oven. A solution of 10wt% polyvinyl alcohol (PVA) in water was used as binder in the unmodified BNKBT composition. The addition of binder is necessary to create plastic flow of the powder to assist in pressing [6]. The use of binder prevents flaws that occur during uniaxial pressing such as delamination. Due to the hygroscopic nature of some of the sintering additives such as lithium carbonate, water based binders could not be used. Initially, binder was not used and additional care during sieving to break up all agglomerates was necessary. Pellets were inspected following pressing and were discarded if flaws were found. Internal defects could only be discovered after sintering when the ceramics were polished. High green body density was achieved regardless of binder addition to the powder.

A non-aqueous binder of 10wt% polyvinyl butyral (PVB) in ethanol was ultimately made for compositions with hygroscopic additives where aqueous binders could not be used. The unmodified composition was prepared using PVA and PVB binders for comparison and no difference in densification or piezoelectric properties were found when using these two binders.

After the amount and composition of sintering additives was determined that could achieve higher density, the effects of the additives on the electromechanical properties were studied.

3.3 Results and Discussion

3.3.1 Sintering at 1050–1065ºC

Initially, sintering at 1065ºC was carried out using a combination of bismuth oxide and copper oxide. The phase diagram for the Bi_2O_3–CuO system is shown in Figure 3.2. The Bi_2O_3–CuO system has a eutectic at 770ºC for the composition with a CuO concentration of approximately 12 molar percent. The sintering additive composition that forms a eutectic is 4.2wt% Bi_2O_3 and 0.085wt% CuO, shown as the line I. A relative density of approximately 92% was achieved at 1065ºC for 4 hours using the eutectic sintering aid composition. The amount of CuO was increased to 0.17wt%, which is in the hypereutectic region of the Bi_2O_3–CuO system, shown by line II in Figure 3.2. The relative density increased to 94% for the composition with 4.2wt% Bi_2O_3 and 0.17wt% CuO.

The addition of an alkali element such as Na or Li to Bi_2O_3–CuO composition further improved densification. An addition of 0.1wt% of Na_2CO_3 was added to both the eutectic and hypereutectic Bi_2O_3–CuO compositions, increasing the relative density by 2% when sintered at 1065ºC. A relative density of 96% was achieved in the hypereutectic Bi_2O_3–CuO composition with the addition of Na_2CO_3. Lithium carbonate was found to be more effective than sodium carbonate when an equivalent molar quantity was substituted.

The composition with 0.07wt% Li_2CO_3, 4.2wt% Bi_2O_3, and 0.17wt% CuO could be sintered to 94% relative density at lower temperature of 1050ºC.

3.3.2 Sintering at 1000ºC

As sintering temperature was lowered to 1000ºC, longer sintering time was required to compensate for the decrease in temperature in order to achieve high density. Longer sintering time revealed that the liquid phase would "leak" out of the ceramic and remain on the alumina substrate. The liquid phase did not consolidate the ceramic particles. At 1050ºC the liquid phase, which is mostly Bi_2O_3, would evaporate at 1050ºC and did not remain on the substrate. At 1000ºC, evaporation of Bi_2O_3 is too slow and the low viscosity of the liquid phase results in poor densification.

The amount of Bi_2O_3 in the sintering aid composition was decreased from 4.2wt% to 0.8wt% due to the lower evaporation rate at 1000ºC. The composition consists of 0.8wt% Bi_2O_3, 0.3wt% CuO, and 0.15wt% Li_2CO_3, which corresponds to approximately 70 molar percent CuO in the Bi_2O_3–CuO phase diagram, shown by line III in Figure 3.2. According to the phase diagram, the solid melts incongruently at about 840ºC to form a liquid and copper oxide. At 1000ºC, the sintering aid is liquid.

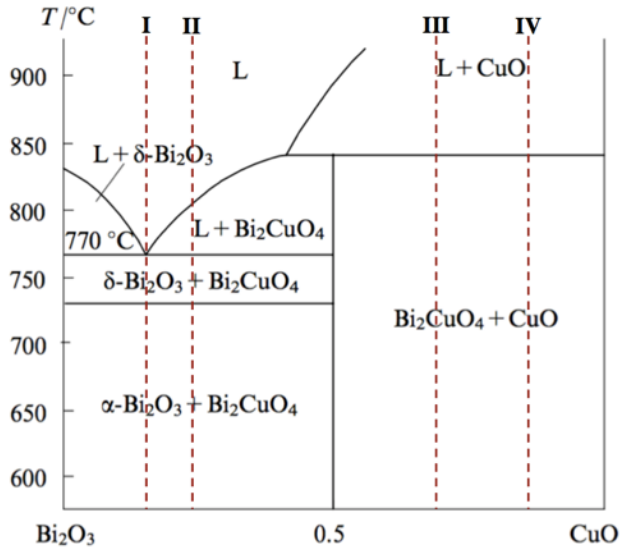

Figure 3.2. Phase diagram for the Bi_2O_3–CuO system [28][29]. The lines I, II, III and IV correspond to different compositions used for sintering.

3.3.3 Sintering at 900ºC

The dynamics of sintering change when the temperature is reduced to 900ºC from 1000ºC. The volatility of Bi_2O_3 is significantly lowered at 900ºC and the evaporation rate decreases considerably. The liquid phase stuck to the alumina crucible with the sintering aid composition 0.8wt% Bi_2O_3, 0.3wt% CuO, and 0.15wt% Li_2CO_3 at 900ºC

The amount of CuO and Li_2CO_3 in the composition was increased and Bi_2O_3 was decreased to sinter to a relative density of about 94–96%. The sintering aid composition initially used at 900ºC has 0.4wt% CuO, 0.2wt% Li_2CO_3 and the amount of Bi_2O_3 ranged from 0–0.4wt%. The ceramic could be sintered to high density without addition of Bi_2O_3. The piezoelectric properties of the compositions using 0.2 and 0.4wt% Bi_2O_3 was nearly identical. With no addition of Bi_2O_3, Cu^{2+} diffuses into the lattice. The evaluation of electromechanical properties show increased mechanical quality factor and decreased

loss, typical of hard piezoelectric properties resulting from acceptor doping. Copper is likely substituting for Ti^{4+} in the perovskite structure

Overall, the piezoelectric properties are decreased when using only Bi_2O_3, CuO, and Li_2CO_3 as seen by the low d_{33} and coupling coefficients. The low piezoelectric properties of the ceramics sintered with Bi_2O_3, CuO, and Li_2CO_3 could be the result of poor densification, but diffusion of Bi^{3+} or Li^{+} cannot be ruled out. Bi^{3+} would increase d_{33} and permittivity but the properties are not easily predictable.

Table 3.2. Piezoelectric properties of BNKBT88 sintered using Bi_2O_3, CuO, Li_2CO_3 additives.

Sintering Temperature (ºC) and additives	Relative density	d_{33} (pC/N)	k_p	Q_m	tanδ(%)	ε_r
BNKBT88	97	164	0.265	145	1.2	825
0.8wt% Bi_2O_3, 0.3wt% CuO, and 0.15wt% Li_2CO_3.1000ºC	95.8	148	0.223	155	1.98	840
0.2–0.4wt% Bi_2O_3, 0.4wt% CuO, and 0.2wt% Li_2CO_3. 900ºC	95	140	0.200	145	2.74	1000
0.4wt% CuO, and 0.2wt% Li_2CO_3. 900ºC	96	110	0.140	350	1.03	900

Additional oxides are incorporated into the sintering aid composition to improve piezoelectric properties. The effect of boron oxide on the solubility, diffusion, or surface tension of the liquid phase on BNKBT88 ceramic particles during sintering is investigated. Boron oxide is a glass former and reduces the viscosity and melting temperature of the liquid phase. The ternary phase diagram for the Bi_2O_3–CuO–B_2O_3 system is shown in Figure 3.3. As a network former, boron oxide may cause the liquid to remain in an amorphous state after sintering rather than crystallize along grain boundaries. The addition of boron oxide improves the piezoelectric properties, however its effect on sintering or its role in the combinations of is difficult to study. The optimal

composition of sintering additives for sintering in air is 0.2–0.4wt% Bi_2O_3, 0.4wt% CuO, and 0.15wt% Li_2CO_3.

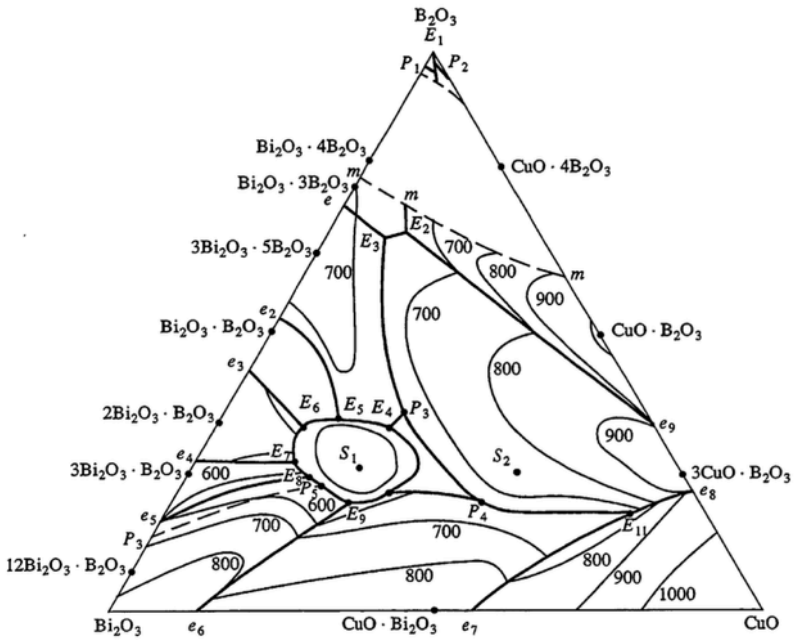

Figure 3.3. Bi_2O_3–CuO–B_2O_3 phase diagram [30]. Boron oxide lowers the melting temperature when added to Bi_2O_3–CuO.

3.3.4 Sintering in controlled oxygen atmosphere

The development of co-fired Bi-based ceramics with copper electrodes requires the ceramic to be sintered at low temperature and in controlled oxygen atmosphere. The ceramics were sintered in controlled oxygen atmosphere of 10^{-8} atm O_2 and 900ºC. Atmospheric control is discussed in depth in a later chapter.

Controlled oxygen atmosphere sintering requires a replacement for cupric oxide. When fired in air, the copper is in the form of Cu^{2+} and turns the ceramics black. In controlled oxygen atmosphere, Cu^{2+} is reduced to Cu^{+} in the form of Cu_2O, which gives the ceramics a red-brown color shown in Figure 3.4. Cu_2O is not as effective for sintering as CuO and a replacement for the CuO sintering aid is needed.

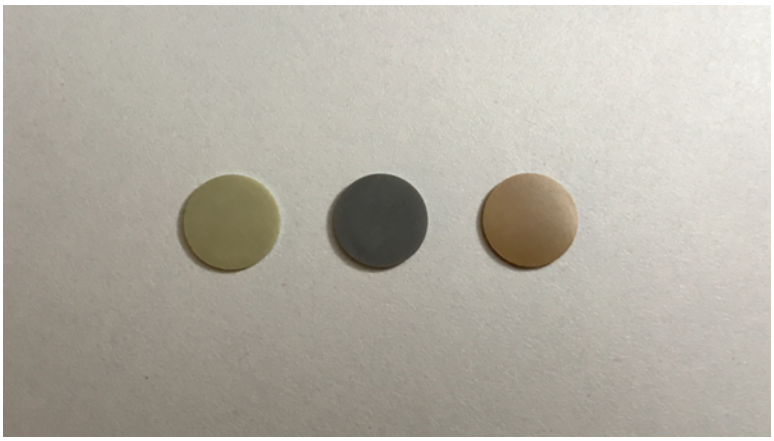

Figure 3.4. BNKBT88 sintered at 1150ºC with no additives (left), BNKBT88 with sintering aids fired at 900ºC in air (middle) and in controlled atmosphere (right). The sample sintered in air is dark from CuO. In controlled atmosphere, the CuO turns into Cu_2O which has a red-brown color.

Zinc oxide has been used as a sintering aid in combination with CuO in many lead-based compounds [18][17]. The Bi_2O_3–ZnO phase diagram, shown in Figure 3.5, is similar to the Bi_2O_3–CuO and has a eutectic at 738ºC [31][28]. Compositions that are rich in zinc will form a liquid with zinc oxide particles above the eutectic temperature, similar to CuO in the Bi_2O_3–CuO system. BNKBT88 could not be sintered at when CuO was completely removed from the sintering additives.

The optimal composition of additives for sintering in controlled oxygen atmosphere at 900ºC is 0.2–0.4wt% Bi_2O_3, 0.2wt% CuO, 0.4 wt% ZnO and 0.15wt% Li_2CO_3 and 0.07wt% B_2O_3. This composition could also be sintered in air with similar properties to the composition without ZnO. Small changes to the sintering additives do not have a considerable effect on the piezoelectric properties of low temperature sintered BNKBT88. This suggests that there is limited diffusion of the components of the liquid phase into the ceramic.

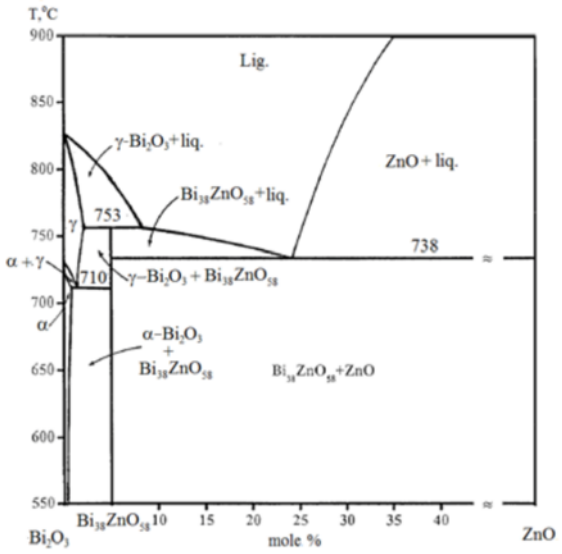

Figure 3.5. Bi_2O_3–ZnO phase diagram [31]. For compositions rich in ZnO, the solid phase melts incongruently at the eutectic temperature of 738ºC. ZnO particles and a liquid phase are present at the sintering temperature of 900ºC.

In low oxygen atmosphere conditions, Bi_2O_3 can be reduced to metallic bismuth. Bismuth metal has a high vapor pressure and will quickly evaporate. This develops a white ring along the edge of the ceramic and can be seen in Figure 3.6. This is caused by brief exposure to reducing conditions. If the oxygen atmosphere becomes too reducing, the bismuth oxide in the sintering aid composition is reduced to metallic bismuth, which quickly evaporated from the surface of the sample and densification does not occur. The samples shown in Figure 3.7 are heavily reduced. The interior is black from metal bismuth but the surface has a pale grey color where the metal bismuth evaporated from the surface.

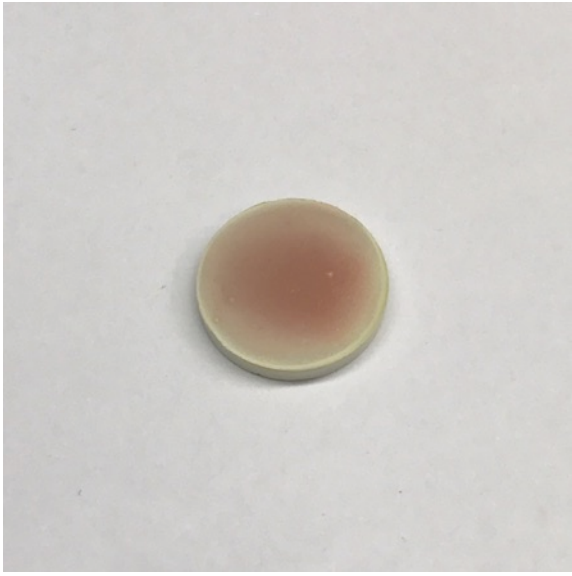

Figure 3.6. Ceramic exposed to slightly reducing conditions during sintering. Densification does not occur in the outer edges of the ceramic due to removal of bismuth oxide.

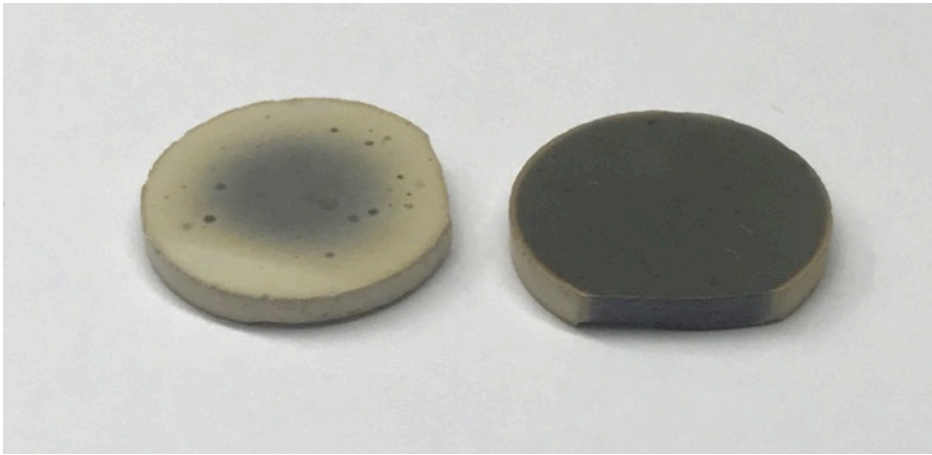

Figure 3.7. BNKBT88 ceramics exposed to reducing atmosphere during sintering. The metal bismuth evaporated from the surface of the ceramic on the left. The polished section of the ceramic on the right reveals that the metal bismuth remains in the interior.

The sample location inside of the covered alumina boat within the hot zone is influence by the atmosphere. The sample located on left is the first to enter the hot zone and be exposed to the oncoming gases of the furnace atmosphere. The surface of the ceramics at the left side of the boat is reduced more than other ceramics when sintered at

1000ºC in controlled atmosphere, shown in Figure 3.8. Yellow colored bismuth oxide can be seen deposited on the right half of the boat. The samples located on the left have the highest mass loss and can be considered as sacrificial samples in order to suppress the volatilization of bismuth oxide and avoid reduction in the other samples in the boat.

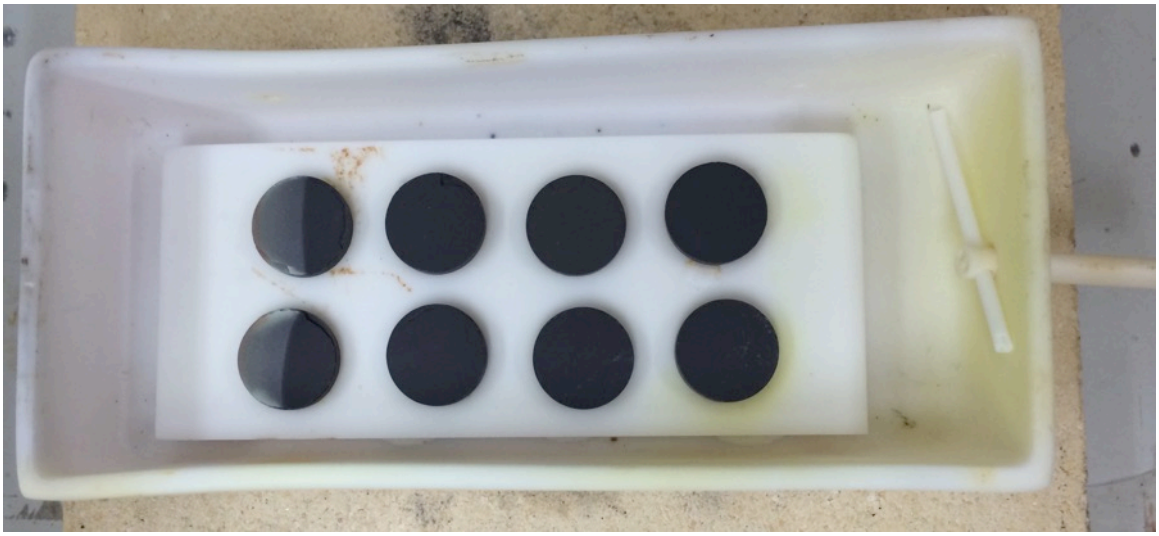

Figure 3.8. BNKBT88 sintered at 1000ºC. The leftmost samples have been reduced on one half of the ceramic.

3.3.5 Piezoelectric properties of low temperature sintered BNKBT88 ceramics

The effects of individual components of the sintering aid composition on densification and piezoelectric properties were studied by altering the additive composition. The optimal sintering aid compositions for different temperatures and atmospheres are given in Table 3.3, and the corresponding piezoelectric properties are listed in Table 3.4. The piezoelectric coefficient, planar coupling coefficient, and mechanical quality factor are similar for BNKBT88 sintered at different temperatures. The largest change is in depolarization temperature, which is decreased.

Table 3.3. Optimal sintering additive composition for sintering at various conditions

	Sintering aid composition (wt. %)				
Sintering Conditions	Bi_2O_3	Li_2CO_3	CuO	ZnO	B_2O_3
1000ºC, air	0.8	0.15	0.3	0	0
900ºC, air	0.2-0.4	0.15	0.4	0	0.07
900ºC, low PO_2	0.2-0.4	0.15	0.2	0.4	0.07

Table 3.4. Properties of BNKBT88 sintered at 1150ºC and low temperature using the optimal additive composition for each condition.

Sintering Temperature (ºC)	d_{33} (pC/N)	k_p	Q_m	ε_r	T_d (ºC)
1150	164	0.265	145	825	152
1000	148	0.223	155	840	150
900 (air)	160	0.288	150	880	130
900 (low PO_2)	154	0.265	125	940	125

The depolarization temperature is determined by measuring relative permittivity during heating cycle, shown in Figure 3.9. The depolarization temperature for BNKBT88 sintered at 1150ºC is indicated by the rapid increase in relative permittivity with heating. Depolarization is not seen during cooling of the sample. Depolarization occurs rapidly within a few degrees of T_d for the unmodified BNKBT88. The compositions sintered at 900ºC in air and controlled atmosphere had T_d of 130ºC and 125ºC respectively. The increase in relative permittivity at T_d is gradual compared to the sample sintered at 1150ºC. The depolarization behavior is characterized by the room temperature d_{33} after heating the sample. Typically, piezoceramics do not gradually lose piezoelectric properties when heated to temperatures T_d. The piezoelectric d_{33} coefficient of BNKBT88 ceramics sintered at 900ºC in air or controlled oxygen atmosphere depolarized, shown in Figure 3.10. Although depolarization occurs at about 130ºC in the ceramics sintered at low temperature depolarization occurs over a wider range from about 75–130ºC,

compared 150–155ºC for unmodified BNKBT88. The temperature where maximum permittivity occurs, which corresponds to transformation to cubic phase is also decreased for the samples sintered at low temperature.

The effect of each individual component of the sintering additives on the depolarization behavior is difficult to determine. Small modifications on the amount of each component do not affect physical and electromechanical properties. Sintering duration at 900ºC in air or in reducing atmosphere has been observed to effect T_d. When sintered for 2 h in air, depolarization temperature is 105ºC. Sintering for longer than 4 h does not improve T_d above 130ºC.

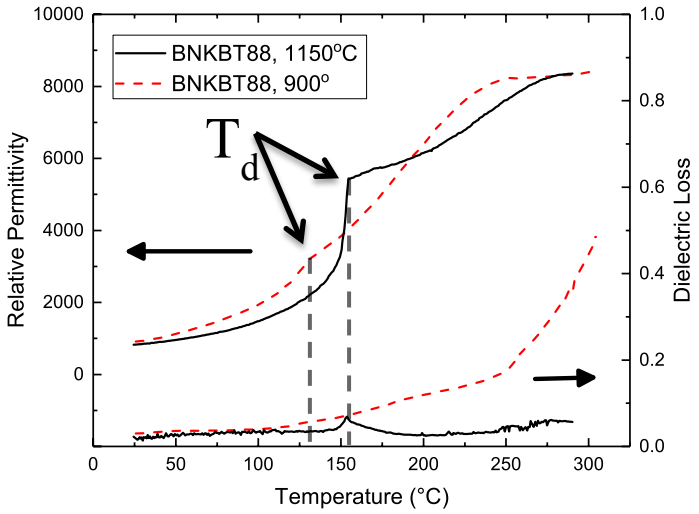

Figure 3.9. Relative permittivity measured with temperature during heating of BNKBT88 ceramics sintered at 900ºC and 1150ºC. The depolarization temperature, T_d, occurs at the sharp change in permittivity and marked by the dashed lines. The depolarization transition occurs at lower temperature and is broader in BNKBT88 sintered at 900ºC compared to the unmodified composition.

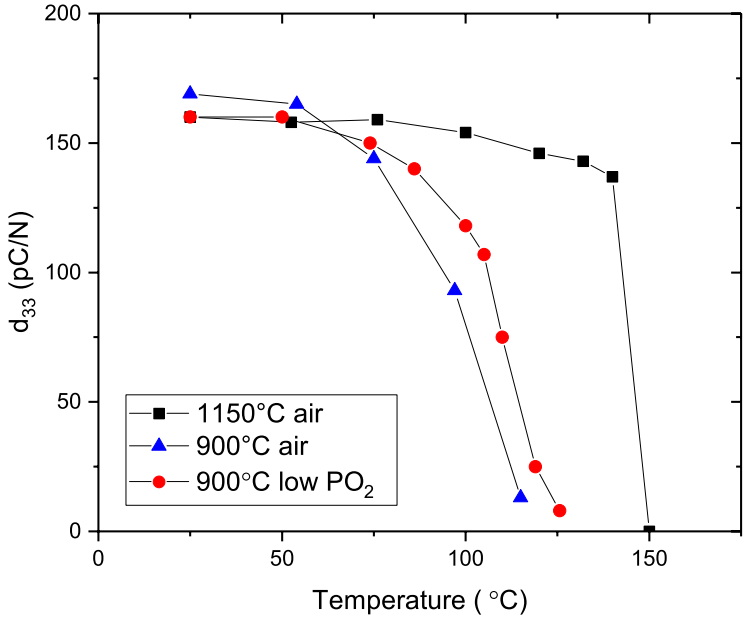

Figure 3.10. Depolarization behavior of BNKBT88 ceramics. Sintering additives for 900ºC are 0.2wt% Bi_2O_3, 0.2wt% CuO, 0.4wt%ZnO, 0.15wt% Li_2CO_3, and 0.07wt% B_2O_3 The d_{33} is measured at room temperature after heat to higher temperature. The compositions sintered at 900ºC begin to depolarize at lower temperature than unmodified BNKBT88.

The samples sintered at 900ºC in air or controlled atmosphere both show a reduction in coercive field, which indicates softening of the piezoelectric properties. This could result from the combination of additives at low temperature sintering in 0.88BNT-0.08BKT-0.04BT. The polarization-electric field hysteresis shown in Figure 3.11 for sintering in air at 900ºC results in an increase in remnant polarization to 34 μC/cm^2 compared to 28 μC/cm^2 for sintering at 1150ºC. The remnant polarization was slightly increased for samples sintered in controlled atmosphere with a reduction in coercive field. The polarization-electric field plot shown in Figure 3.12 for the BNKBT88 samples sintered at 900ºC in controlled atmosphere. The remnant polarization and coercive field are slightly lower than the BNKBT88 samples sintered at 1150ºC.

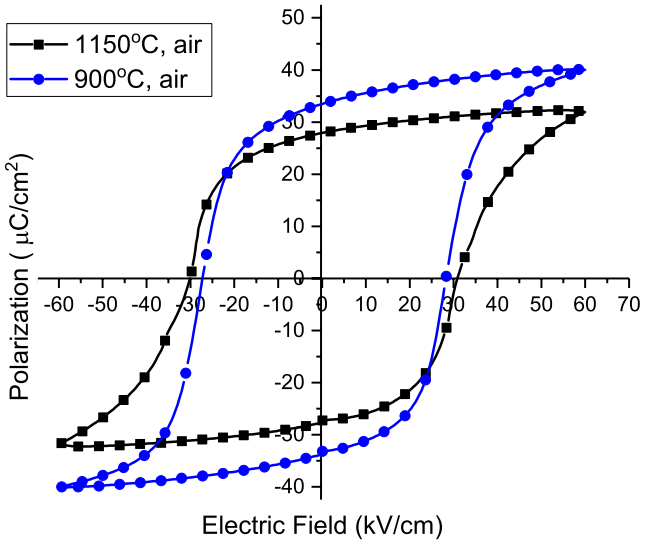

Figure 3.11. Polarization–electric field hysteresis of BNKBT88 sintered at low temperature in air at 900ºC using additives and unmodified BNKBT88 sintered at 1150ºC. The polarization is increased for low temperature sintered BNKBT88. The coercive field is similar to the unmodified composition.

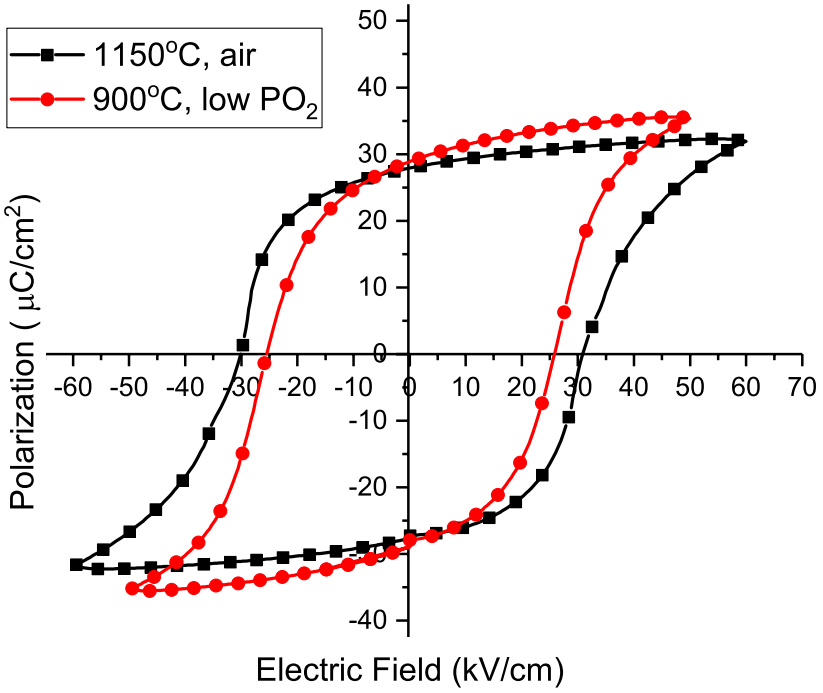

Figure 3.12. Polarization–electric field hysteresis of BNKBT88 sintered at low temperature in controlled oxygen atmosphere at 900ºC using additives and unmodified BNKBT88 sintered at 1150ºC. The saturation polarization is increased for low temperature sintered BNKBT88. However, the coercive field is slightly decreased.

The addition of 0.4wt% ZnO was necessary for sintering in controlled atmosphere at 900ºC. To study the effect of the addition of zinc oxide component on sintering behavior in air and controlled oxygen atmosphere, a range of 0.2–0.8wt% of ZnO was added along with the sintering additives 0.2wt% Bi_2O_3, 0.2wt% CuO, 0.15wt% Li_2CO_3, and 0.07wt% B_2O_3. When sintered in air, the amount of zinc oxide did not have a significant effect on the relative density of the ceramics, as shown in Figure 3.13. The composition could be effectively sintered in air at 900ºC; however, in controlled atmosphere 0.4wt% ZnO was the minimum amount needed to sinter.

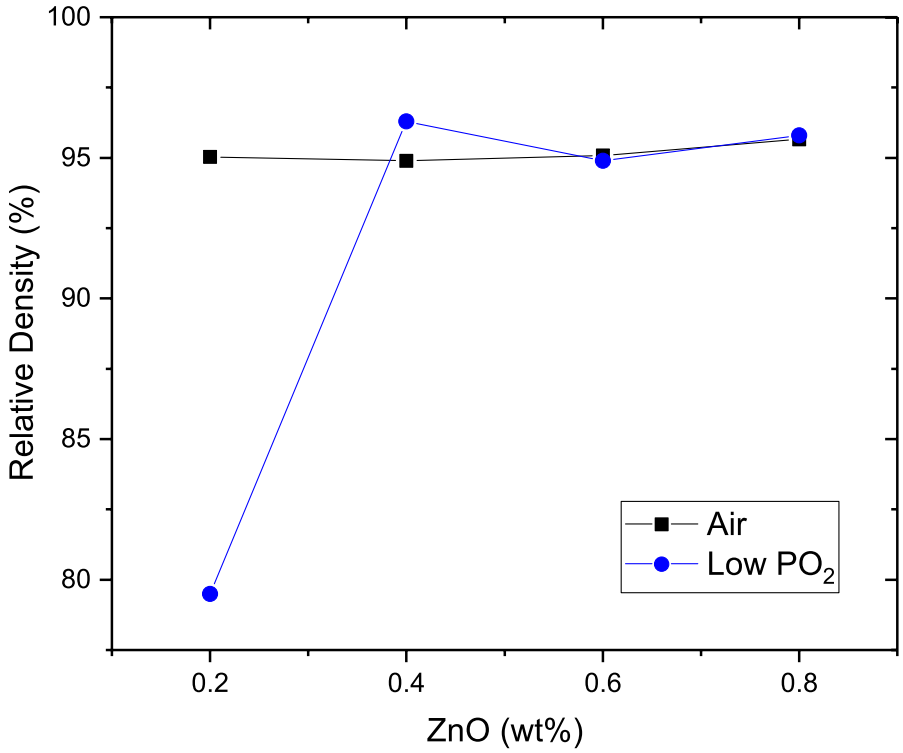

Figure 3.13. The effect of zinc oxide on the densification of BNKBT88 ceramics sintered at 900ºC in air and controlled oxygen atmosphere. The sintering additives are 0.2wt% Bi_2O_3, 0.2wt% CuO, and 0.15wt% Li_2CO_3, 0.07wt% B_2O_3 and 0.2-0.8 wt% ZnO. The amount of zinc oxide does not affect the densification in air; however, 0.4wt% ZnO is the minimum to sinter in low oxygen.

The d_{33} of the low temperature sintered ceramics with different amount of ZnO are shown in Figure 3.14. As zinc oxide content increases, d_{33} increases for the ceramics sintered in low oxygen atmosphere at 900ºC. A high d_{33} of 180pC/N is measured for the air fired BNKBT88 with 0.2wt% ZnO in the sintering additive, which is higher than the d_{33} of the unmodified composition, but could not be sintered to full density in low oxygen. The BNKBT88 sintered at 900ºC with 0.4wt% ZnO had higher density, lower dielectric loss, and slightly lower d_{33} compared to BNKBT88 with increased amount of ZnO added.

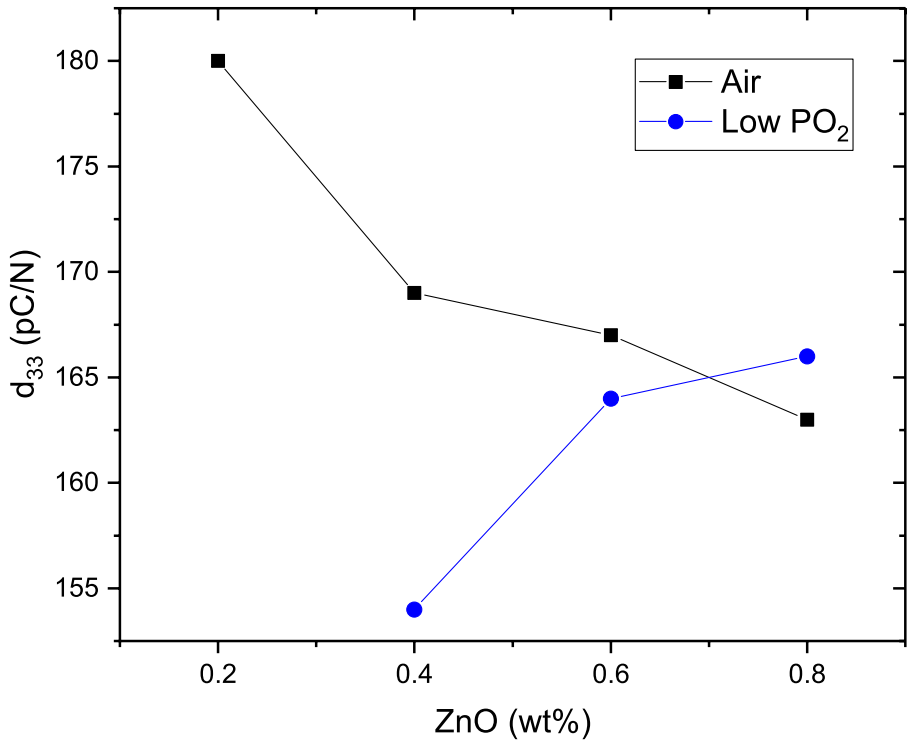

Figure 3.14. The d_{33} for different amount of zinc oxide in the sintering additive for BNKBT88 ceramics sintered at 900ºC in air and controlled oxygen atmosphere. As zinc oxide content increases, d_{33} increases for the ceramics sintered in low oxygen conditions although the opposite occurs in the air fired ceramics.

Effect of Li_2CO_3

Lithium carbonate is an essential component of the sintering additives. Without Li_2CO_3, the ceramics could not be sintered at 900ºC in air or controlled atmosphere. The BNKBT88 ceramic was sintered using additives 0.2wt% Bi_2O_3, 0.2wt% CuO, 0.4wt%ZnO 0.07wt% B_2O_3 and 0–0.15wt% Li_2CO_3. The ceramic could not be sintered to full density with less than 0.15wt% of Li_2CO_3. The relative density of BNKBT88 ceramics with different amounts of lithium carbonate added is shown in Figure 3.15. The ceramics fired in air with 0.075wt% Li_2CO_3 could be poled but the piezoelectric properties were moderately lower compared to 0.15wt% Li_2CO_3 addition.

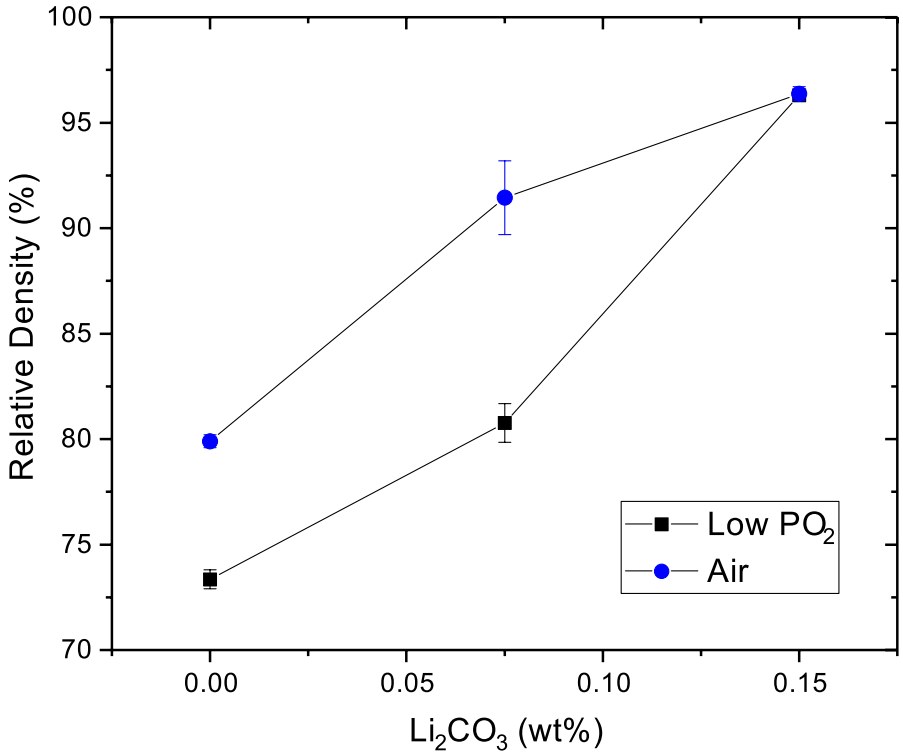

Figure 3.15. Relative density of BNKBT88 ceramics with different amount of Li_2CO_3 sintered at 900ºC in air and controlled oxygen atmosphere. The sintering additives are 0.2wt% Bi_2O_3, 0.2wt% CuO, 0.4wt%ZnO 0.07wt% B_2O_3 and 0–0.15wt% Li_2CO_3. The ceramic could not be sintered to full density with less than 0.15wt% of Li_2CO_3.

3.4 Conclusion

BNT-based piezoelectric ceramics with morphotropic phase boundary composition $0.88Bi_{1/2}Na_{1/2}TiO_3 – 0.08Bi_{1/2}K_{1/2}TiO_3 – 0.04BaTiO_3$ can be sintered at 900ºC, 250ºC below their normal sintering temperature in air or in controlled atmosphere using a combination of Bi_2O_3, CuO, Li_2CO_3, ZnO, and B_2O_3 as sintering additives. The room temperature piezoelectric properties are maintained when sintered at 900ºC for 2-4hr. The depolarization temperature is reduced from 155ºC for BNKBT sintered at 1150ºC to approximately 130ºC when sintered at 900ºC with additives. Overall, it is

difficult to determine the individual effect of each component of the additives on the densification and piezoelectric properties.

Bismuth-based ceramics can be sintered at 900ºC in controlled atmosphere with an oxygen partial pressure of 10^{-8} atm for 2-4hr. The reduction of the sintering temperature and compatibility in low oxygen conditions enables development of cost effective BNKBT88 ceramics with copper internal and external electrodes to be developed.

References

[1] C. A. Randall, A. Kelnberger, G. Y. Yang, R. E. Eitel, and T. R. Shrout, "High Strain Piezoelectric Multilayer Actuators—A Material Science and Engineering Challenge," *J. Electroceramics*, vol. 14, pp. 177–191, 2005.

[2] W. Zhang and R. E. Eitel, "Sintering Behavior, Properties, and Applications of Co-Fired Piezoelectric/Low Temperature Co-Fired Ceramic (PZT-SKN/LTCC) Multilayer Ceramics," *Int J Appl Ceram Technol*, vol. 10, no. 2, pp. 354–364, 2013.

[3] R. Castro, "Overview of Conventional Sintering," in *Sintering Mechanisms of Convention Nanodensification and Field Assisted Processes*, vol. 35, Springer, 2013.

[4] A. E. McHale, *Phase Diagrams and Ceramic Processes*. Springer Science, 1998.

[5] D. J. Shanefield, *Organic Additives and Ceramic Porcessing*. Springer Science, 1995.

[6] M. Kondo and K. Kurihara, "Sintering Behavior and Surface Microstructure of PbO-Rich PbNi1/3Nb2/3O3–PbTiO3–PbZrO3 Ceramics," *J Am Ceram Soc*, vol. 84, no. 11, pp. 2469–74, 2001.

[7] B. Jaffe, W. R. Cook, and H. Jaffe, *Piezoelectric Ceramics*. New York: Academic Press, 1971.

[8] D. E. Wittmer and R. C. Buchanan, "Low-Temperature Densification of Lead Zirconate-Titanate with Vanadium Pentoxide Additive," *J Am Ceram Soc*, vol. 64, no. 8, pp. 485–490, 1981.

[9] H. Kitaguchi, J. Takada, K. Oda, and Y. Miura, "Equilibrium phase diagram for the system PbO-CaO-CuO.pdf," *J. Mater. Res.*, vol. 5, no. 5, pp. 929–931, 1990.

[10] D. L. Corker, R. W. Whatmore, E. Ringgaard, and W. W. Wolny, "Liquid-phase sintering of PZT ceramics," *J. Eur. Ceram. Soc.*, vol. 20, pp. 2039–2045, 2000.

[11] X. X. Wang, K. Murakami, O. Sugiyama, and S. Kaneko, "Piezoelectric properties, densification behavior and microstructural evolution of low temperature sintered PZT ceramics with sintering aids," *J. Eur. Ceram. Soc.*, vol. 21, pp. 1367–1370, 2001.

[12] C.-H. Wang and L. Wu, "4PbO•B2O3—A New Sintering Agent for Pb(Zr,Ti)O3 Ceramics," *Jpn. J. Appl. Phys.*, vol. 32, pp. 3209–3213, 1993.

[13] E. Ringgaard, E. R. Nielsen, and W. W. Wolny, "Optimisation of new liquid-phase sintering aid for PZT," in *Proceedings of the 12th IEEE International Symposium on Applications of Ferroelectrics*, Honolulu, HI, 2000.

[14] E. R. Nielsen, E. Ringgaard, and M. Kosec, "Liquid-phase sintering of Pb(Zr,Ti)O3 using PbO–WO3 additive," *J. Eur. Ceram. Soc.*, vol. 22, pp. 1847–1855, 2002.

[15] A. K. Saha, D. Kumar, O. Parkash, A. Sen, and H. S. Maiti, "Effect of phosphorous addition on the sintering and dielectric properties of Pb(Zr0.52Ti0.48)O3," *Mater. Reasearch Bull.*, vol. 38, pp. 1165–1174, 2003.

[16] C.-W. Ahn *et al.*, "Effect of ZnO and CuO on the Sintering Temperature and Piezoelectric Properties of a Hard Piezoelectric Ceramic," *J Am Ceram Soc*, vol. 89, no. 3, pp. 921–925, 2006.

[17] C.-W. Ahn *et al.*, "Effects of CuO and ZnO Additives on Sintering Temperature and Piezoelectric Properties of 0.41Pb(Ni1/3Nb2/3)O3-0.36PbTiO3-0.23PbZrO3 Ceramics," *Jpn. J. Appl. Phys.*, vol. 43, no. 1, pp. 205–210, 2004.

[18] R. Liang, W. Zhang, M. Gao, L. Wang, and X. Dong, “Excellent electrostrictive properties of low temperature sintered PZT ceramics with high concentration LiBiO2 sintering aid,” *Ceram. Int.*, vol. 39, pp. 563–569, 2013.
[19] J. Yoo, C. Lee, Y. Jeong, K. Chung, D. Lee, and D. Paik, “Microstructural and piezoelectric properties of low temperature sintering PMN-PZT ceramics with the amount of Li2CO3 addition,” *Mater. Chem. Phys.*, vol. 90, pp. 386–390, 2005.
[20] W. Zhang and R. E. Eitel, “Low Temperature Sintering and Properties of 0.98PZT-0.02SKN Ceramics with LiBiO2 and CuO Addition,” *J Am Ceram Soc*, vol. 94, no. 10, pp. 3386–3390, 2011.
[21] R. M. German, P. Suri, and S. J. Park, “Review: liquid phase sintering,” *J. Mater. Sci.*, vol. 44, pp. 1–39, 2009.
[22] M. Humenik and N. M. Parikh, “Cermets: I, Fundamental Concepts Related to Microstructures and Physical Properties of Cermet Systems,” *J Am Ceram Soc*, vol. 39, pp. 60–63, 1956.
[23] Y. Imanaka, *Multilayered Low Temperature Cofired Ceramics (LTCC) Technology*. Springer Science, 2005.
[24] H. Guo, J. Guo, A. Baker, and C. A. Randall, “Hydrothermal-Assisted Cold Sintering Process: A New Guidance for Low-Temperature Ceramic Sintering,” *ACS Appl. Mater. Interfaces*, vol. 8, p. 20909−20915, 2016.
[25] H. Guo, A. Baker, J. Guo, and C. A. Randall, “Cold Sintering Process: A Novel Technique for Low-Temperature Ceramic Processing of Ferroelectrics,” *J Am Ceram Soc*, vol. 99, no. 11, pp. 3489–3507, 2016.
[26] D. Wang, “Hydrothermal Assisted Cold Sintering of Lead Zirconate Titanate (PZT-5A) Powder,” presented at the 2017 Joint IEEE ISAF-IWATMD-PFM, Atlata, GA, 08-May-2017.
[27] J. Kragten, *Atlas of Metal-Ligand Equilibria in Aqueous Solution*. Ellis Horwood Limited, 1978.
[28] V. V. Belousov and A. A. Klimashin, “High-temperature oxidation of copper,” *Russ. Chem. Rev.*, vol. 82, no. 3, pp. 273–288, 2013.
[29] B. Hallstedt, D. Risold, and L. J. Gauckler, “Thermodynamic Evaluation of the Bi-Cu-O System,” *J Am Ceram Soc*, vol. 79, no. 2, pp. 353–58, 1996.
[30] M. I. Zargarova, N. M. Mustafaev, and N. S. Shuster, “CuO-Bi2O3-B2O3 System,” *Inorg. Mater.*, vol. 32, no. 1, pp. 65–70, 1996.
[31] L. A. Irtyugo, N. V. Belousova, V. M. Denisov, L. T. Denisova, S. D. Kirik, and L. G. Chumilina, “High-Temperature Heat Capacity of Bismuth Oxide and Bismuth-Zinc Double Oxide with the Sillenite Structure,” *J. Sib. Fed. Univ. Chem.*, vol. 2, pp. 125–130, 2012.

4. Development of a copper co-fired Pb-free material

4.1 Introduction

In the development of multilayer actuators, the oxidation of the metal electrode and the reduction of one or more ceramic oxide components must be avoided. In order to co-fire a metal electrode and a ceramic oxide, there must be a region of temperature and oxygen partial pressure where oxidation of the electrode will not occur and the ceramic oxide is not reduced. The region of temperature and oxygen partial pressure where the metal and the ceramic oxide coexist is calculated from the Gibbs free energy for each component. The standard Gibbs free energy of formation for select oxides are given in Table 4.1 and used to calculate the oxygen partial pressure for a reaction over a specific temperature range. The reaction's typical form is:

$$xX_{(s)} + yO_{2(g)} \Leftrightarrow zZ_{(s)} \tag{1}$$

where X is a metal and Z is the metal oxide. The Gibbs free energy is equal to:

$$\Delta G^{\circ} = -RT \ln K \tag{2}$$

and the reaction constant K is:

$$K = \left(\frac{a_Z^z}{a_X^x P_{O2}^y}\right) \tag{3}$$

where a is the thermodynamic activity for each species and P_{O2} is the partial pressure of oxygen. The thermodynamic activity is 1 for condensed phases in their pure form. The oxidation of copper metal to form cuprous oxide is given by equation 4.

$$Cu_{(s)} + \frac{1}{2}O_{2(g)} \Leftrightarrow Cu_2O_{(s)} \tag{4}$$

The expression for the Gibbs free energy for the reaction given in equation 4 is:

$$\Delta G^{\circ} = -RT \ln \left(\frac{a_{Cu_2O}}{a_{Cu} P_{O2}^{1/2}}\right) \tag{5}$$

The thermodynamic activity of Cu_2O and Cu are equal to one because they are pure substances and the equation 5 simplifies to equation 6.

$$\Delta G^{\circ} = -RT \ln \left(\frac{1}{P_{O2}^{1/2}}\right) \tag{6}$$

Rearranging equation 6 to solve for oxygen partial pressure gives

$$P_{O2} = \left(e^{-\Delta G^{\circ}/RT}\right)^{-2} \tag{7}$$

where the equilibrium partial of oxygen pressure is a function of temperature. The Ellingham diagram of the Gibbs free energy of formation and equilibrium oxygen partial pressure vs. temperature for the Cu–Cu_2O–CuO phases is shown in Figure 4.1. Copper has 2 oxides that form depending on temperature and oxygen partial pressure. Under low oxygen conditions, copper exists in its metallic form. Increasing the oxygen concentration results in the formation of cuprous oxide, Cu_2O, and eventually forms cupric oxide, CuO. Cupric oxide is the thermodynamically preferred phase at room temperature and standard atmospheric conditions.

Firing of a metal electrode must be done at an oxygen partial pressure below equilibrium to prevent oxidation. For a ceramic to successfully co-fire with metal electrode, the oxygen partial pressure must remain below the metal's equilibrium oxygen partial pressure and above the ceramic oxide's equilibrium oxygen partial pressure. The equilibrium oxygen partial pressure for various electrode materials at 900ºC and 1200ºC are is listed in Table 4.2.

Table 4.1. Standard Gibbs free energy of formation for various compounds.

Reaction	ΔG° (J)	Range (K)	Reference
$Cu_{(s)} + \frac{1}{2}O_{2(g)} \Leftrightarrow CuO_{(s)}$	– 155,600 + 93.0 T	298 - 1356	[1]
$Cu_{(l)} + \frac{1}{2}O_{2(g)} \Leftrightarrow CuO_{(s)}$	– 168,650 + 102.6 T	1356 - 1509	[1]
$2Cu_{(s)} + \frac{1}{2}O_{2(g)} \Leftrightarrow Cu_2O_{(s)}$	– 162,200 + 69.24 T	298-1356	[1]
$2Cu_{(l)} + \frac{1}{2}O_{2(g)} \Leftrightarrow Cu_2O_{(s)}$	– 188,300 + 88.48 T	1356 - 1509	[1]
$2Ni_{(s)} + O_{2(g)} \Leftrightarrow 2NiO_{(s)}$	– 471,200 + 172 T	298-1726	[1]
$Pb_{(l)} + \frac{1}{2}O_{2(g)} \Leftrightarrow PbO_{(s)}$	– 208,700 + 91.75 T	600-1158	[1]
$Pb_{(l)} + \frac{1}{2}O_{2(g)} \Leftrightarrow PbO_{(l)}$	– 181,200 + 68.03 T	1158-1808	[1]
$2Bi_{(l)} + \frac{3}{2}O_{2(g)} \Leftrightarrow Bi_2O_{3(s)}$	– 583,400 + 293.8 T	572-988	[2]
$2Bi_{(l)} + \frac{3}{2}O_{2(g)} \Leftrightarrow Bi_2O_{3(s)}$	– 543,900 + 253.8 T	988-1098	[2]
$2Bi_{(l)} + \frac{3}{2}O_{2(g)} \Leftrightarrow Bi_2O_{3(l)}$	– 492,400 + 207.0 T	1098-1127	[2]
$C_{(s)} + \frac{1}{2}O_{2(g)} \Leftrightarrow CO_{(g)}$	– 111,700 – 87.65 T	298-2000	[1]
$C_{(s)} + O_{2(g)} \Leftrightarrow CO_{2(g)}$	– 394,100 – 0.84 T	298-2000	[1]
$H_{2(g)} + \frac{1}{2}O_{2(g)} \Leftrightarrow H_2O_{(g)}$	– 247,500 + 55.85 T	298-1726	[1]

Table 4.2. The equilibrium oxygen partial pressure for various electrode materials and ceramic oxides at 900 and 1200ºC. Silver and palladium are noble metals and can be fired in air. Copper and nickel require the furnace oxygen partial pressure to be below the values listed in order to prevent oxidation.

	$\log PO_2$	
	900ºC	1200ºC
Ag/AgO	4.2	4.7
Pd/PdO	0.04	2.0
Cu/Cu_2O	-7.2	-4.3
Ni/NiO	-12.0	-7.7
Bi/Bi_2O_3	-7.4	-4.0
Pb/PbO	-9.0	-5.7
Na/Na_2O	-22.8	-12.3
Ti/TiO_2	-32.6	-24.1
Ba/BaO	-38.6	-28.8
Zr/ZrO_2	-39.0	-29.1

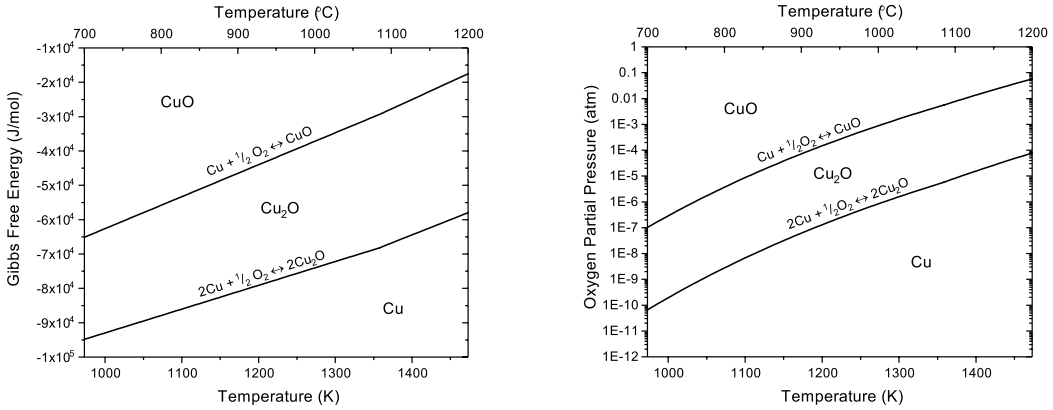

Figure 4.1. Standard Gibbs free energy (a) and the equilibrium oxygen partial pressure (b) for the oxidation of copper.

Silver and palladium are precious metals that are used extensively as electrodes for multilayer actuators fired in air. Palladium is alloyed with silver to increase it low melting point of 962ºC. Higher firing temperatures require increased content of palladium, increasing the cost of the electrode material. Palladium readily deoxidizes above 850ºC and can be easily fired in air [3]. The BKT multilayer actuator with Ag/Pd electrodes was fabricated by Nagata et al [4]. Interaction of the BKT with silver ions caused the ceramic to decompose, adversely affecting properties [4].

Attempts have been made to utilize less expensive metals such as copper and nickel, which are an attractive alternative to Ag and Ag/Pd electrodes due to the lower cost but cannot be fired in air [5]. The oxygen partial pressure during sintering must be compatible with both the metal electrode and the ceramic. Nickel requires more reducing atmospheric conditions than copper and is suitable for use in multilayer devices such as $BaTiO_3$ capacitors and KNN-based piezoceramics [6][7]. Both KNN and $BaTiO_3$ can withstand the reducing atmosphere required to prevent oxidation of copper or nickel [8][9][10][11].

Unlike KNN and $BaTiO_3$, compounds containing Pb or Bi cannot be co-fired with Ni electrodes [12]. Figure 4.2 shows the equilibrium oxygen partial pressure curve for nickel is under the curve for lead. Therefore, there is no combination of temperature and oxygen partial pressure where Ni metal and PbO coexist. The nickel metal has a stronger affinity for oxygen than lead oxide and will be reduced to metallic lead and nickel oxide.

Nickel foil is used as a substrate for PZT films and requires rapid heat treatment to prevent oxidation. A layer of HfO_2 was deposited on the foil to prevent oxidation during heat treatment. Oriented PZT films prepared by chemical solution deposition were annealed at 700ºC for 60 seconds without oxidizing of the nickel [13]. However, it is not possible to fabricate Pb or Bi based ceramic multilayer actuators with Ni metal electrodes that require higher temperatures and longer sintering duration.

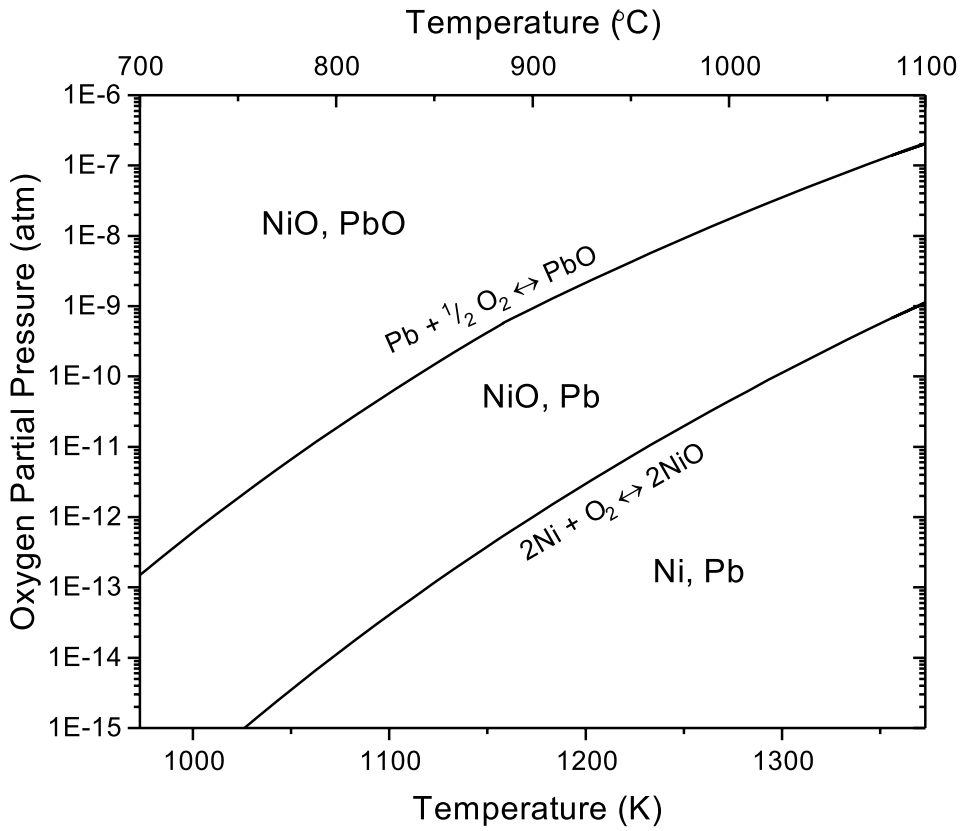

Figure 4.2. Equilibrium oxygen partial pressure for Pb and Ni. The curve for the oxidation of nickel occurs below that of Pb. There is no region where lead oxide and nickel metal coexist. Nickel is not suitable as an electrode material for compounds containing lead oxide.

PZT MLA with Cu electrodes

PZT multilayer actuators with copper internal electrodes have been extensively used in fuel injectors for diesel engines by Epcos and have exceeded the performance of air-fired PZT actuators with Ag-Pd electrodes. In the co-fired MLA containing silver, the Ag^+ ions react with the PZT at the electrode interface creating a local region with hard piezoelectric properties, reducing performance [14]. The migration of Ag ions results in fatigue of the PZT which does not occur when using copper electrodes [15]. Co-firing should be carried out at temperatures of about 1000ºC or less due to the low melting point of copper (1083ºC), which is 100-300ºC below the typical sintering temperatures of the ceramic compositions [16]. Additives are used to reduce the sintering temperature. The equilibrium oxygen partial pressure for Cu and PbO are shown in Figure 4.3. Atmospheric control during sintering of PZT multilayer actuators is accomplished by mixing water vapor and hydrogen [15]. Different mixtures of hydrogen and water vapor are used to keep the oxygen partial pressure within the region of coexistence of Cu metal and PbO. Firing MLA within the region of coexistence of Cu and PbO can be accomplished with careful control of the sintering atmosphere.

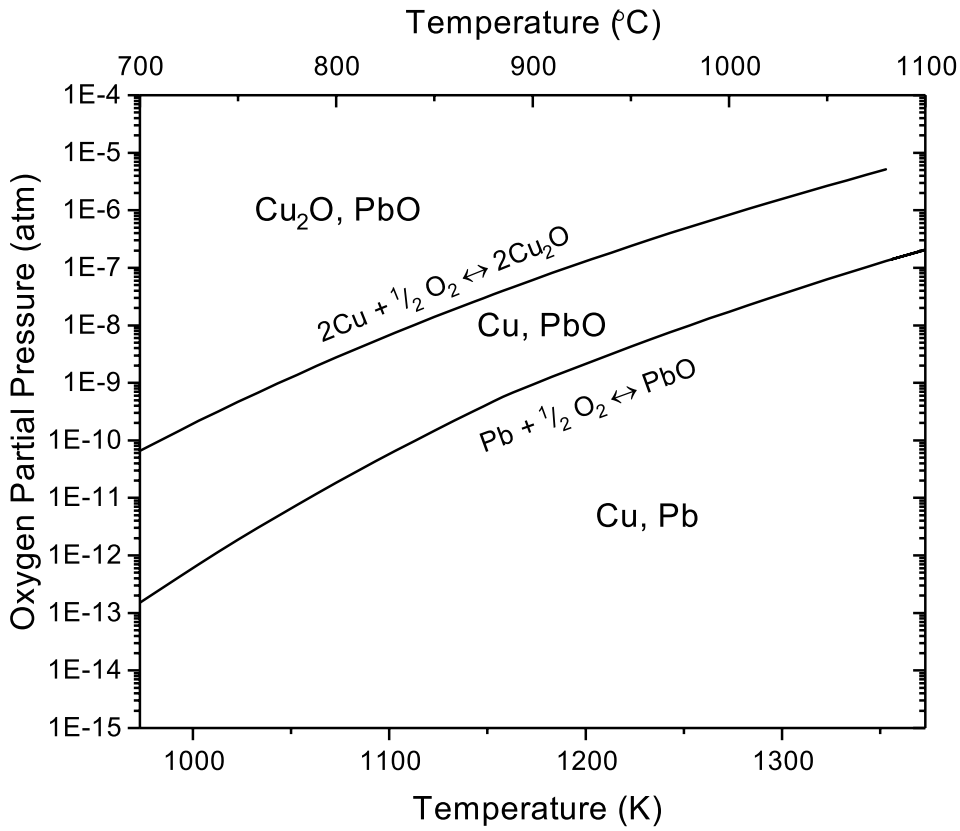

Figure 4.3. Equilibrium oxygen partial pressure for Pb and Cu. The curve for the oxidation of copper occurs above that of Pb. Lead oxide and copper metal can coexist in the region between the 2 curves. The oxygen partial pressure must be carefully controlled during sintering to co-fire lead oxide based ceramics with copper electrodes.

Bi_2O_3 compatibility with Cu

Bismuth oxide based piezoceramics have not been previously co-fired with copper electrodes due to the narrow region of coexistence for bismuth oxide and copper metal. The Gibbs free energy of bismuth oxide is used to calculate the oxygen partial pressure. Bismuth oxide melts at 825ºC (1098K) so the liquid phase is used in calculations.

$$2\,Bi_l + \frac{3}{2}O_{2(g)} \Leftrightarrow Bi_2O_{3(l)} \tag{8}$$

$$\Delta G^{\circ} = -RT\ln\left(\frac{a_{Bi2O3}}{a_{Bi}^2 P_{O2}^{3/2}}\right) \tag{9}$$

$$\Delta G^{\circ} = -RT\ln\left(\frac{a_{Bi2O3}}{P_{O2}^{3/2}}\right) \tag{10}$$

$$P_{O2} = \left(\frac{a_{Bi2O3}}{e^{-\frac{\Delta G^{\circ}}{RT}}}\right)^{2/3} \tag{11}$$

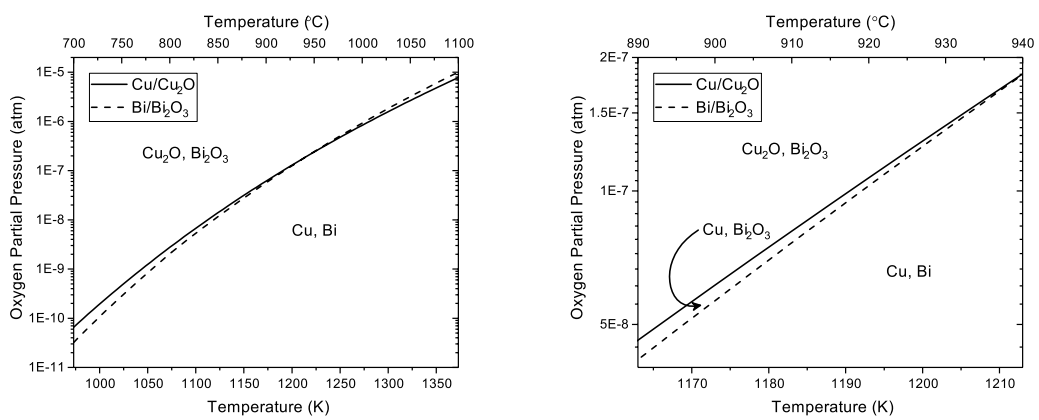

Figure 4.4. Equilibrium oxygen partial pressure for Bi and Cu. The curve for the oxidation of copper occurs above that of Bi, however the region of coexistence is extremely narrow compared to the PbO-Cu system. The two curves intersect at 1213K (940ºC) so bismuth oxide containing ceramics with copper electrodes must be co-fired at lower temperature.

The equilibrium oxygen partial pressure for copper and bismuth is shown in Figure 4.4a over the temperature range from 973-1373K (700-1100ºC). The region of coexistence of copper metal and bismuth oxide is extremely narrow. Figure 4.4b expands the region on the temperature scale 1163-1213K (890ºC – 940ºC). According to the thermodynamic Gibbs free energy reported by Itoh and Azakami, Cu metal and Bi_2O_3 coexist for the oxygen partial pressure range $5.5\text{-}6.1\text{x}10^{-8}$ atm at 900ºC [2]. The oxygen partial pressure curves intersect at 940ºC, suggesting there is an upper limit to the compatibility of Cu and Bi_2O_3. However, this is not the case for all of the reported thermodynamic data determined by EMF method for bismuth oxide. There is a range of values reported for the enthalpy and entropy of bismuth oxide in the literature [2][17][18].

In BNKBT88, bismuth oxide exists in the perovskite structure as a solid solution, so the thermodynamic activity is less than one. However, the thermodynamic activity of bismuth oxide in BNKBT88 can only be determined experimentally and has not been reported previously. According to equation 11, a thermodynamic activity of bismuth oxide less than one will decrease the oxygen partial pressure where reduction occurs and slightly increases the range of coexistence for Bi_2O_3 and Cu. Until the thermodynamic activity of Bi_2O_3 in BNKBT88 can be determined, a value of 1 will be assumed for the purpose of calculating the equilibrium oxygen partial pressure. For bismuth metal, the activity is considered to be 1 since it would exist as its pure form if reduced from the oxide form.

The oxygen partial pressure during sintering is controlled by a chemical reaction of the gases inside the furnace, which produce a constant equilibrium oxygen partial pressure. The reaction of hydrogen gas can is used to control the oxygen partial pressure. At room temperature hydrogen reacts explosively with oxygen. However, when mixed with steam and heated to high temperature, equilibrium of hydrogen, oxygen, and water vapor is achieved. The chemical reaction for the combustion of hydrogen is:

$$H_{2(g)} + {}^{1}/_{2}\, O_{2(g)} \Leftrightarrow H_2O_{(g)} \tag{12}$$

The Gibbs free energy of formation and reaction constant K for the reaction are:

$$\Delta G° = -RT \ln K \qquad K = \left(\frac{P_{H2O}}{P_{H2}P_{O2}^{1/2}}\right) \tag{13}$$

The equilibrium oxygen partial pressure is determined by temperature and the ratio of hydrogen to water vapor.

$$P_{O2} = \left(e^{-\Delta G^{\circ}/RT} \cdot \frac{P_{H2}}{P_{H2O}}\right)^{-2} \tag{14}$$

Percolating hydrogen gas through water makes a mixture of hydrogen and water vapor known as wet hydrogen. Temperature determines the vapor pressure of water in the gas mixture. However, it can be difficult to accurately control because the water bath for percolation must be kept at a constant temperature. The vapor pressure of water is also dependent on atmospheric pressure, which varies with weather and ambient temperature. Condensation of the water vapor may occur in the tubes as it is delivered to the furnace, and this must be avoided in order to maintain the correct ratio of hydrogen to steam. Forming gas is a mixture of hydrogen with an inert gas such as argon or nitrogen and is used as a source of hydrogen. These mixtures can contain less than 10% hydrogen, which is below the explosive limit.

Another method for controlling oxygen partial pressure uses the decomposition of carbon dioxide into carbon monoxide and oxygen.

$$CO_{2(g)} \Leftrightarrow CO_{(g)} + {}^{1}/_{2}\, O_{2(g)} \tag{15}$$

$$\Delta G = -RT \ln K \qquad K = \left(\frac{P_{O2}^{1/2} P_{CO}}{P_{CO_2}}\right) \tag{16}$$

$$P_{O2} = \left(e^{-\Delta G^{\circ}/RT} \cdot \frac{P_{CO_2}}{P_{CO}}\right)^2 \tag{17}$$

The Gibbs free energy for the decomposition of CO_2 can be calculated from the reaction of formation of carbon monoxide and carbon dioxide listed in Table 4.3. Carbon dioxide decomposes into equilibrium with oxygen and carbon monoxide at high temperatures. However, CO_2 does not have a buffering capacity to react with oxygen present from leaks or impurities to remove excess oxygen from the furnace atmosphere. This would require CO_2 to be mixed with carbon monoxide gas, which is poisonous and explosive.

Table 4.3. Chemical reactions used to calculate the Gibbs free energy for the decomposition of carbon dioxide into carbon monoxide and oxygen.

Reaction	ΔG° (J)
$C_{(s)} + \frac{1}{2} O_{2(g)} \Leftrightarrow CO_{(g)}$	– 111,700 – 87.65 T
$CO_{2(g)} \Leftrightarrow C_{(s)} + O_{2(g)}$	394,100 + 0.84 T
$CO_{2(g)} \Leftrightarrow CO_{(g)} + \frac{1}{2} O_{2(g)}$	282,400 – 86.81 T

A third method to control sintering atmosphere used a mixture of hydrogen and carbon dioxide gases. Hydrogen and carbon dioxide react at high temperature to produce carbon monoxide and water vapor shown by the chemical reaction:

$$H_{2(g)} + CO_{2(g)} \Leftrightarrow H_2O_{(g)} + CO_{(g)} \tag{18}$$

Water vapor is a product of the reaction so it is not required to percolate the gas through a water bath. Carbon monoxide is a minority component of the equilibrium at high

temperature and all of the gases can be used below their explosive limits. Hydrogen can react with excess oxygen from leaks or impurities. Although oxygen does not appear in equation 18, it can be calculated using the decomposition of CO_2 and combustion of H_2, as shown in Table 4.4. First, the equilibrium constant, K, for the overall reaction is calculated from the standard Gibbs free energy for the reaction.

$$K = e^{-\Delta G_f^o / RT} \tag{19}$$

Then, the CO_2/CO ratio that produces the desired oxygen partial pressure is calculated by rearranging equation 17.

$$x = \frac{P_{CO_2}}{P_{CO}} = \frac{P_{O_2}^{1/2}}{e^{-\Delta G_f^o / RT}} \tag{20}$$

Finally, the CO_2/H_2 ratio needed to achieve the desired oxygen partial pressure is calculated by the CO_2/CO ratio from equation 20 and the equilibrium constant form equation 19 [19].

$$\frac{P_{CO_2}}{P_{H_2}} = \frac{x\,(1+x)}{(x+1/K)} \tag{21}$$

Table 4.4. Chemical reactions used to calculate the Gibbs free energy for the reaction of carbon dioxide and hydrogen [1].

Reaction	ΔG° (J)
$CO_{2(g)} \Leftrightarrow CO_{(g)} + \frac{1}{2}O_{2(g)}$	282,400 – 86.81 T
$H_{2(g)} + \frac{1}{2}O_{2(g)} \Leftrightarrow H_2O_{(g)}$	– 247,500 + 55.85 T
$H_{2(g)} + CO_{2(g)} \Leftrightarrow H_2O_{(g)} + CO_{(g)}$	34,900 – 30.96 T

The concentration of oxygen is measured by a galvanic cell using the electrochemical potential between 2 concentrations of oxygen separated by an electrolyte. Yttria stabilized zirconia (YSZ) can be used as the electrolyte because it conducts oxygen

at temperatures above 800ºC [20]. Platinum is used as the electrodes that are exposed to the oxygen on either side of the YSZ electrolyte. The concentration gradient between oxygen at pressures separated by the electrolyte produces an electrical voltage E, given by the Nernst equation:

$$E = \frac{RT}{4F} \ln \left({P_{O_2}^1}/{P_{O_2}^2} \right) \tag{22}$$

where R is the gas constant, T is temperature in K, and F is the Faraday constant 96,485 coulombs per mol [19]. A reference concentration of oxygen is used. Pure oxygen can be used, which has a pressure of 1 atm. If air is used as a reference, which has an oxygen partial pressure of 0.2 atm, the Nernst equation can be simplified to:

$$E = -4.96\times10^{-5}\ \mathrm{T} \log \left({P_{O_2}}/{0.2} \right) \tag{23}$$

Binder, organic burnout

A challenge to co-firing multilayer devices in low oxygen atmosphere is removing organic binders. Binder is typically removed through combustion with oxygen when heated to 550ºC in air [21]. However, heating base metal electrodes in air would result in oxidation. Incomplete binder removal leaves behind residual carbon, which degrades properties and reduces reliability of the actuator [22]. Acrylic based binders are preferred when using base metal electrodes because they depolymerize and evaporate instead of burning. This can be done in wet hydrogen to avoid oxidizing the electrode [21].

Shoei Chemical inc. has developed oxidation resistant copper power [23]. The Shoei Cu-505 is micron sized copper powder with an amorphous silica coating. The TEM

image in Figure 4.5 shows a silica coating of approximately 20nm on a copper particle. It can be heated in air up to 300ºC without oxidation of the copper, which is sufficient to remove acrylic based binders as well as ethyl cellulose.

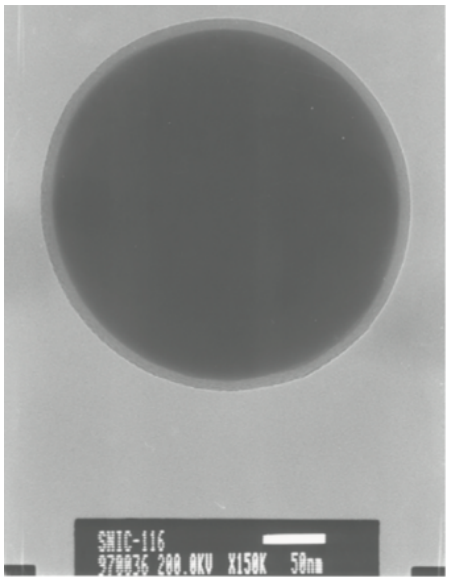

Figure 4.5. TEM image of Shoei-505 oxidation resistant copper powder [23]. The copper particle is coated in approximately 20nm of silica to prevent oxidation when heated.

4.2 Experimental procedure

4.2.1 Furnace setup

A CM model tube furnace was used for controlled oxygen sintering with a 36” long alumina tube with a diameter of 2.5”. Water-cooled steel endcaps closed the ends of the tube. Nitrogen (99.9%), carbon dioxide (bone dry grade), and a mixture of 5% hydrogen in 95% nitrogen was used to control the furnace atmosphere. The gasses were mixed together using a multi-tube flow system, which allowed the flow rate of each gas to be viewed individually on its own Matheson flow tube.

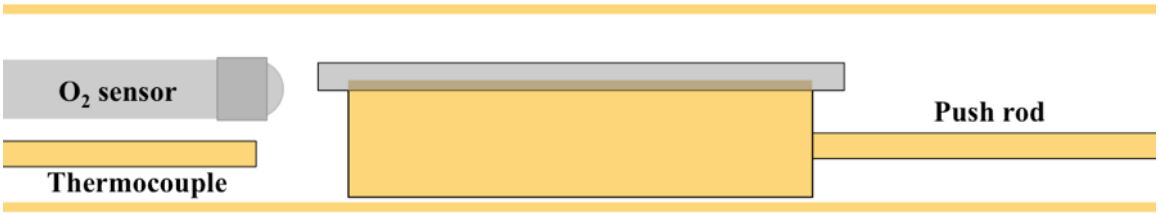

Figure 4.6. Diagram showing the cross section of the furnace hot zone during sintering. The samples are inside of the covered alumina boat that is connected to the push rod. The oxygen sensor and a thermocouple inside of a protection tube monitor the oxygen partial pressure inside of the hot zone.

The ends of the tube are closed with water-cooled steel end caps which were modified to accommodate an oxygen sensor, a protection tube for a thermocouple to monitor the hot zone, and an alumina push rod for pushing and pulling a boat into the hot zone. The oxygen sensor, thermocouple, and push rod are shown in Figure 4.6. The temperature profile has a bell-shape and is shown in Figure 4.7. The hot zone is approximately 6” wide and the tube is offset by 0.75”, so the center is 18.75” from the left end cap.

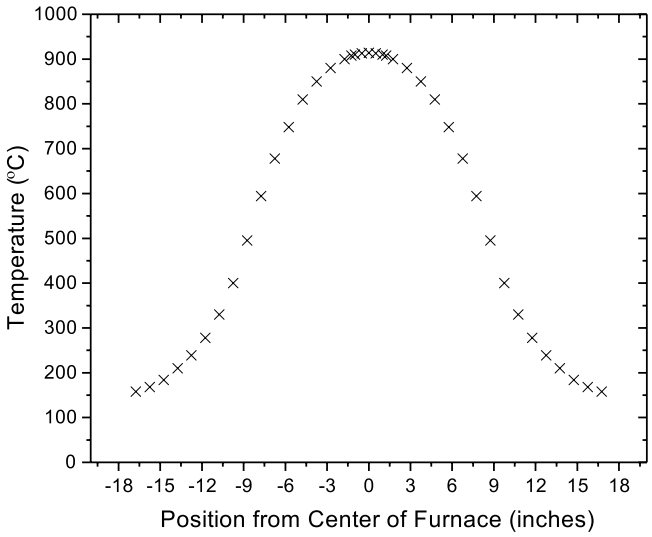

Figure 4.7. The temperature profile of the tube furnace shows a typical bell shaped curve. The hot zone of the furnace has a width of about 6 inches. The ends of the tube have a temperature greater than 150ºC. The alumina boat is pushed into the furnace at a rate of 0.5" per minute.

The alumina rod is used to push the boat into the hot zone of the furnace at a rate of 0.5"/minute. After sintering, it is then used to pull the boat out of the hot zone at the same rate. To connect the push-rod to the boat, a hole was drilled into the end of the rod to fit a smaller ⅛" diameter alumina rod inside. A hole was drilled into the both sides of the ⅛" rod to fit a 1/16" diameter ceramic used as a dowel pin. A hole was drilled in the side of the boat to fit the ⅛" ceramic rod, and another dowel pin secured it in place, shown in Figure 4.8.

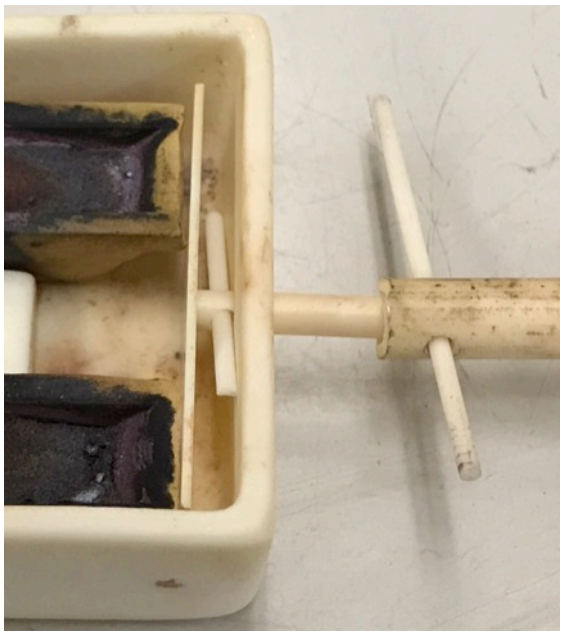

Figure 4.8. The rod is used to push the samples into the hot zone as well as pull them out after sintering. The rod is connected to the boat by an alumina rod. 1/16" ceramic rods are used as dowel pins that fit through drilled holes.

It is necessary to be able to push the rod into the furnace and maintain a leak-tight seal. This is accomplished using compression fittings and O-rings to make an airtight seal around the alumina rod shown in Figure 4.9. Swagelok compression fittings are typically used for making leak-tight connections for gas or water lines. The fittings use a front and a back ferrule that grips onto the tubing. When the hex nut is tightened, the back ferrule forces the front ferrule inward, pinching the tubing and making a seal. In standard use, the ferrule becomes permanently attached to the pinched tube and cannot be used to make an airtight seal around the alumina rod. The alumina push rod fits inside of a ⅜" steel tube that is screwed into the furnace's water-cooled end cap. Swagelok compression fittings on the end of the tube are used to squeeze rubber O-rings around rod, shown in Figure 4.9. The ¼" alumina rod fits tightly inside of a Swagelok ⅜" compression fitting. When the hex nut is tightened, the front and back ferrules squeeze the O-rings in between

the steel walls and the alumina rod, creating a leak-tight seal. The hex nut is loosened to allow the rod to push into and pull out of the furnace. The steel tube is attached to the water-cooled end cap and is sufficient to cool the alumina rod as it comes out of the furnace.

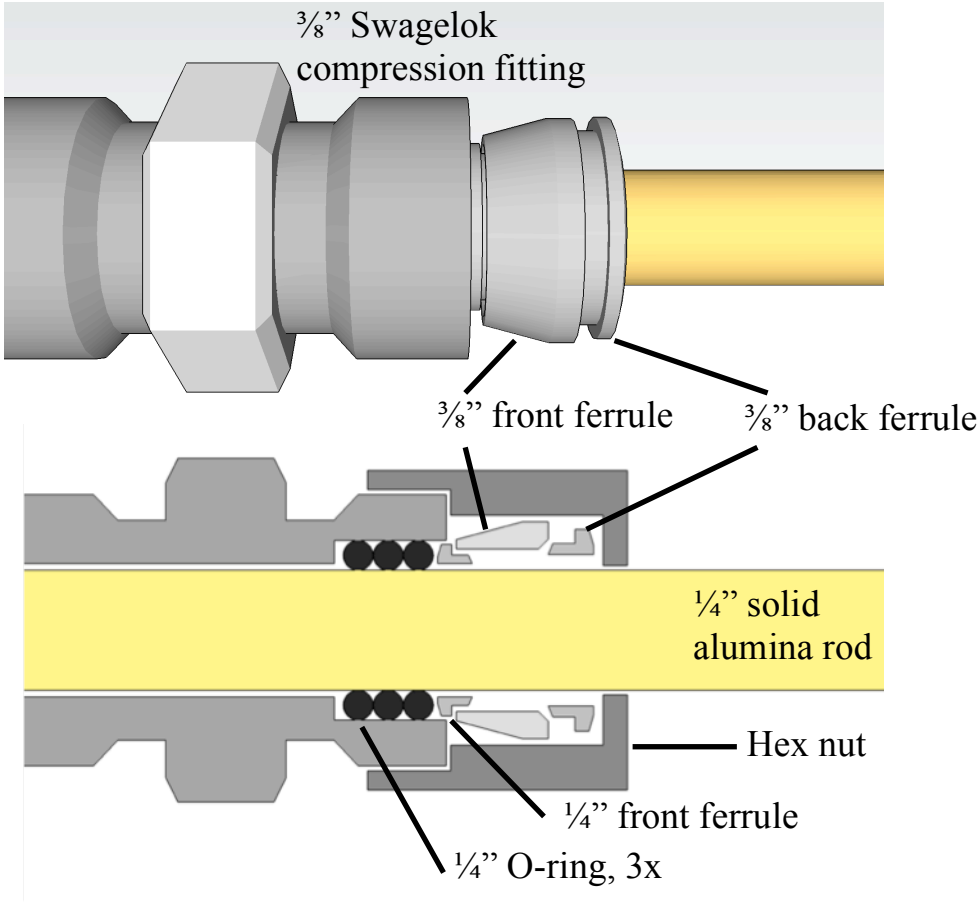

Figure 4.9. Schematic and cross section of the compression fittings used to make a leak-tight seal around the alumina push-rod. The ¼” alumina rod fits inside of a Swagelok ⅜” compression fitting. When the hex nut is tightened, the ferrules compress three O-rings to make a leak-tight seal.

4.2.2 Oxygen sensor

The oxygen sensor was built using a yttria stabilized zirconia tube with platinum foil and wire. The benefits of the laboratory built oxygen sensor are that it can be repaired

in the lab while a commercial sensor would be required to ship back to the manufacturer, which is not cost effective. The sensor is made using a 22” long zirconia tube that is closed on one end. The tube has an outer diameter of 0.5” and inner diameter of 0.375”.

The outer electrode is made from platinum foil that is wrapped around the closed end of the zirconia tube and welded together with a spot welder, shown in Figure 4.10. Platinum foil is difficult to weld, so small pieces of platinum wire are placed between the 2 layers of foil. A long platinum wire is welded to the outer platinum foil electrode, which extends outside of the furnace and is connected to the high impedance voltmeter. The wire must be electrically insulated from the steel end cap. To do this, the platinum wire was placed around the zirconia tube and wrapped with Teflon tape for electrical insulation. Then a ½ ” compression fitting was tightened around the zirconia tube, such that it would extend 15” into the furnace.

Figure 4.10. Oxygen sensor made using a yttria stabilized zirconia tube with a platinum foil external electrode.

The inner electrode was made by welding 3 strips of platinum foil into a 6-pointed star pattern shown in Figure 4.11. This is welded to a long platinum wire, which is threaded through one hole of a 30” long double bored 0.25” alumina rod, and is then inserted into the zirconia tube, shown schematically in Figure 4.12. The star shaped platinum foil folds back as it is inserted into the YSZ tube, making good electrical contact with the walls as the inner electrode. Compressed air is blown through the open hole of the double bored alumina rod to maintain constant reference oxygen partial pressure [19].

Figure 4.11. The inner electrode of the oxygen sensor is made by welding 3 strips of platinum foil into a star pattern. It is attached to a platinum lead wire and inserted into the furnace. The foil folds backwards and makes contact with the inner walls of the zirconia tube.

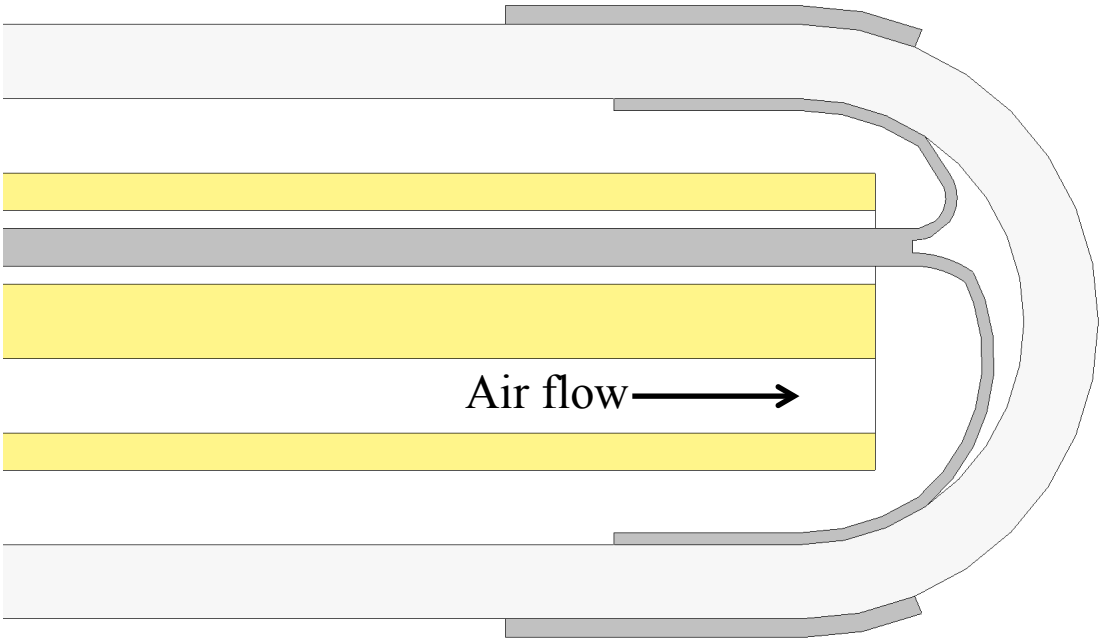

Figure 4.12. Cross section of the oxygen sensor. The oxygen partial pressure inside the furnace is calculated from the voltage generated by the difference in oxygen concentration across the zirconia electrolyte. Compressed air is used as a reference and flows through the open hole of the double bore alumina rod.

4.2.3 Gettering crucible

The control of the gases during sintering is critical to maintain the oxygen partial pressure with the precision necessary for co-firing Cu and Bi_2O_3. A modified boat was used to control the oxygen partial pressure at the Cu/Cu_2O equilibrium. Copper metal powder was placed inside to absorb excess oxygen while isolated with a custom fit cover to protect from the direct flow of the furnace gases. The alumina boat is 4” long and 1.75” wide. Grooves were carefully cut into an alumina plate, shown in Figure 4.13, using a high-speed rotary tool and diamond embedded engravers. The cover plate was placed into a shallow bath of water to cool the bits during drilling. The shape of the grooves were checked by comparing to the alumina boat’s shape. The long and narrow

crucibles were slightly shortened in order to fit inside of the alumina boat and were filled with copper metal powder and cuprous oxide, shown in Figure 4.13. The unfired ceramic samples were placed on top of platinum foil between the copper filled crucibles. Crucibles filled with Cu metal powder and Cu_2O are on either side of the samples as shown in Figure 4.13 and Figure 4.14.

Figure 4.13. Samples for controlled atmosphere sintering are placed on top of platinum foil inside of an alumina boat with crucibles filled with Cu metal power on either side. The alumina cover plate is drilled to fit the alumina boat.

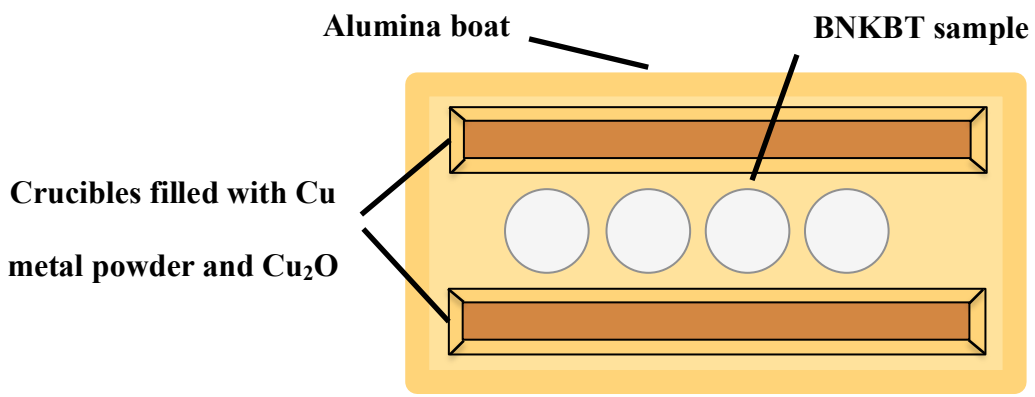

Figure 4.14. Cu metal and Cu_2O is used to keep the atmosphere at the equilibrium pO_2 for co-firing BNKBT88 and copper.

4.2.4 Sample preparation and electroding

Samples were prepared via conventional powder processing and low temperature sintering aids were added after calcination as described in the previous chapter. Removal of the PVB binder requires a minimum temperature of 500ºC in air, which is not compatible with the copper electrodes. Binder was removed from all of the pressed ceramic discs at 550ºC in air to ensure the complete elimination of carbon prior to electroding with copper.

The first method for electroding the unfired ceramics utilized copper powder that is pressed between two unfired ceramic discs. Binder was removed from the ceramic prior to pressing with copper powder and the unfired ceramic discs developed internal cracks.

A second method for preparing the copper electrode used a paste that was made from Shoei Cu-505 oxidation resistant copper powder, ethyl cellulose, terpineol, and ethanol. First, 1.0g of ethyl cellulose is dissolved in 10mL of ethanol. Then 2.0g of Cu-505 powder was added to 2.0g of terpineol. Then 4mL of the ethyl cellulose solution in

ethanol was added to the copper powder and terpineol. As the mixture is stirred, ethanol evaporates and the mixture thickens into a paste that is applied to the unfired ceramics using a paintbrush. The unfired ceramics and the electrode paste are dried at 100ºC to allow the terpineol to evaporate. Terpineol is a viscous solvent that evaporates with sufficient time at 100ºC. After drying, the ethyl cellulose binder is pyrolized by heating to 300ºC in air [24]. The oxidation resistant copper power is not affected by heating to 300ºC.

The piezoceramic composition used for co-firing with copper electrodes is bismuth deficient BNKBT88-2.0Bi, which is discussed in further detail in the following chapter. The bismuth deficient composition is used here because it sinters faster than the unmodified BNKBT88 and the same sintering aids are used for both compositions. This makes co-firing easier due to the difficulty of maintaining the correct oxygen partial pressure for longer time. The bismuth deficient composition could be sintered at 900ºC in 2hr compared to 4hr for the unmodified composition.

Co-fired ceramics with copper surface electrodes were gently polished with 1200 grit Buehler silicon carbide paper to remove the oxide layer after sintering. Air-dry silver paint was applied to the bottom of the ceramic, and it was poled through the top copper electrode. The samples with internal copper electrodes were polished for microscopy starting with 120-grit silicon carbide and using finer grit paper until finishing with 1200 grit.

4.3 Results and discussion

4.3.1 Furnace performance

The atmospheric composition that produces the desired oxygen partial pressure of 4.1×10^{-8} atm at 900ºC has a CO_2 to H_2 ratio of 22000:1, making the furnace atmosphere mostly CO_2. The hydrogen is diluted to 5% in nitrogen in the forming gas mixture and the ratio of CO_2 to H_2 is reasonably accomplished by keeping the H_2/N_2 flow rate at a minimum. Fine adjustments to the gas composition could be made using the pressure regulators on each gas tanks to increase or decrease pressure. The flow tubes were used only for coarse adjustments because they do not allow for precise changes to the flow rate. The overall rate of flow through the flow tubes is dependent on the pressure on the regulator. The overall flow rate of gas through the tube furnace is approximately 250 SCCM.

At 900ºC, it takes approximately 1 hour for the furnace gasses to reach equilibrium with a stable oxygen partial pressure. However, the furnace atmosphere slowly becomes more reducing over time. During sintering the oxygen partial pressure continues to slowly decrease and has a tendency for the atmosphere to become more reducing over time. Once the samples have been pushed into the hot zone it is difficult to measure small changes in the oxygen partial pressure when in close proximity to the copper filled boat. The copper metal inside the boat influences the nearby atmosphere by removing excess oxygen greater than the equilibrium oxygen partial pressure for Cu/Cu_2O.

The furnace atmosphere often became too reducing for the bismuth oxide. When bismuth oxide is reduced it forms metal bismuth in its liquid phase, due to the low

melting point of 271ºC. Bismuth metal has a low boiling point of 1564ºC and the vapor pressure at 900ºC is sufficient for the metal to evaporate. The metal vapor is deposited outside of the hot zone of the furnace.

Exposure to metallic bismuth vapor causes damages to the exposed components of the oxygen sensor by alloying with platinum. These intermetallic compounds are brittle, causing the platinum wires to break with repeated exposure to bismuth vapor. The embrittled platinum wires were replaced and new wires were welded. This requires the removal of the oxygen sensor from the furnace, which is difficult because contact with the furnace walls could contaminate the platinum electrode. It is also necessary to avoid contact of the platinum wire with skin because contamination with oils from the skin can cause embrittlement when exposed to reducing atmospheres.

The oxygen partial pressure is difficult to control as the furnace cools because the equilibrium of the reaction between the CO_2 and H_2 is dependent on temperature. According to the thermodynamics of the reaction, the atmosphere becomes more reducing as the furnace cools. Figure 4.15 shows that calculated oxygen partial pressure resulting from the mixture ratio of 22000:1 for CO_2:H_2 for temperatures between 900ºC and 400ºC. At 400ºC, the calculated equilibrium oxygen partial pressure is 8.4×10^{-27} atm. Reducing conditions of this magnitude do not occur because the reaction of CO_2 and H_2 is kinetically limited by activation energy. Below 850ºC, the zirconia oxygen sensor cannot be used and the oxygen partial pressure cannot be measured. Hydrogen has the capacity to react with oxygen present from impurities at high temperature. However, the temperature at the end of the tube is about 150ºC, which is too low to remove oxygen

from leaks or impurities. The oxygen partial pressure at the end of the tube is equal to the oxygen impurity of the nitrogen and any leaks.

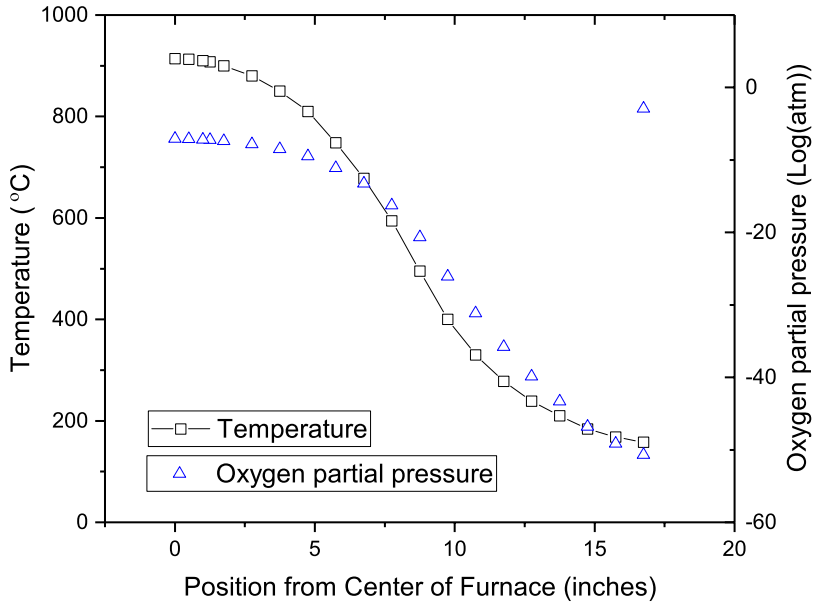

Figure 4.15. Temperature profile and the resulting oxygen partial pressure profile for a fixed CO_2/H_2 ratio of 22000:1. As temperature decreases, the furnace atmosphere becomes more reducing. However at lower temperatures the furnace gases do not have sufficient activation energy to react with oxygen from impurities and leaks.

The furnace seals were sufficient for maintaining constant oxygen atmosphere in the hot zone of the furnace. Exposure to oxygen could not be prevented when the crucible was pulled to the end of the tube during cool down. Air leaks from the end of the tubes cause the exposed copper electrodes to oxidize. The samples are hot as they are pulled from the hot zone and the copper readily absorbs any oxygen leaking from the end caps.

4.3.2 Co-fired base metal electrodes

Copper metal electrodes and the BNKBT88 ceramic were successfully co-fired at 900ºC in controlled oxygen atmosphere. The cross section of an internal copper electrode co-fired with BNKBT88 is show in Figure 4.16. The internal copper electrode has a thickness of 125 microns when pressed copper power was used. The resulting electrode thickness using the copper paste was 12 microns. The copper was also used as a surface electrode shown in Figure 4.16. The copper surface electrode was partially oxidized as the samples cooled in the furnace. The metal at the edges of the ceramic were oxidized to cupric oxide, however the metal electrode remained underneath of a cuprous oxide layer. Polishing revealed a smooth metallic copper surface electrode shown in Figure 4.17. Air-dried silver paint was applied to the bottom of the ceramic, and it was poled through the copper electrode. The d_{33} of the BNKBT88-2.0Bi with the surface Cu electrode was 77pC/N compared to 100pC/N for BNKBT88-2.0Bi sintered at 1150ºC. The polarization-electric field hysteresis for the co-fired BNKBT88-2.0Bi is shown in Figure 4.18. The surface area of the electrode was estimated for calculating the polarization, and therefore the polarization may be inaccurate. The coercive field is consistent with the properties of Bi-deficient BNKBT88

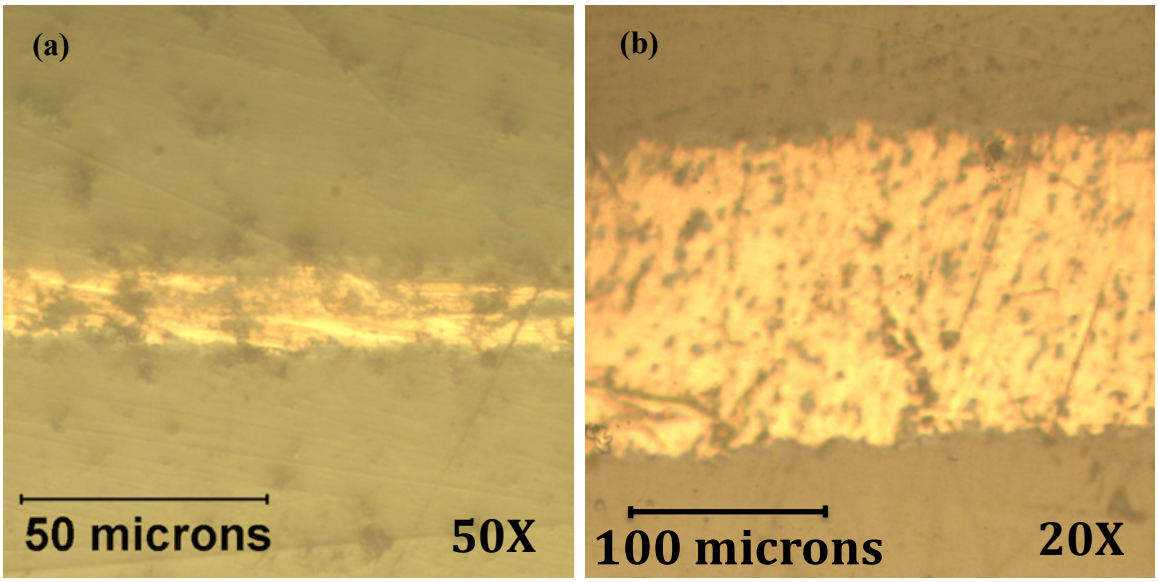

Figure 4.16. Cross section of the internal copper electrode co-fired with BNKBT88. (a) 12 micron thick electrode using Shoei Cu-505 and (b) 120 micron thick electrode using pressed copper power.

Figure 4.17. Bismuth deficient BNKBT88 co-fired with a surface copper electrode. The sides of the electrode reacted with oxygen as the furnace cooled.

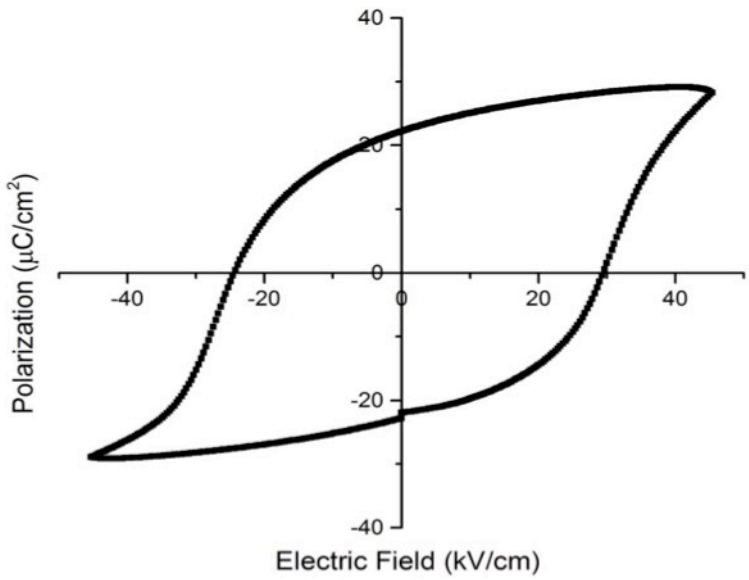

Figure 4.18. Polarization-electric field hysteresis for BNKBT88-2.0Bi measured through the co-fired copper electrode.

4.3.3 Thermodynamic activity of Bi_2O_3 in BNKBT

The thermodynamic activity of Bi_2O_3 in BNKBT88 can be calculated from the temperature and oxygen partial pressure where reduction of bismuth oxide occurs. The exact condition where reduction occurs is not measurable because the samples cannot be observed during sintering. Through recording temperature and oxygen partial pressure during sintering, the conditions where reduction occurs are estimated. Temperature and oxygen partial pressure during sintering for two different runs that resulted in reduction of bismuth oxide in one case and not in the other are shown in Figure 4.19. In both cases, the ranges of oxygen partial pressures are similar. However, in one case bismuth oxide evaporated from the edges of the samples and deposited as bismuth metal on the lid of the boat. The activity of bismuth oxide is calculated from the lowest oxygen partial pressure where reduction did not occur, which is 3.25×10^{-8} atm at 903ºC. Equation 11 can be rearranged to calculate a thermodynamic activity of 0.38.

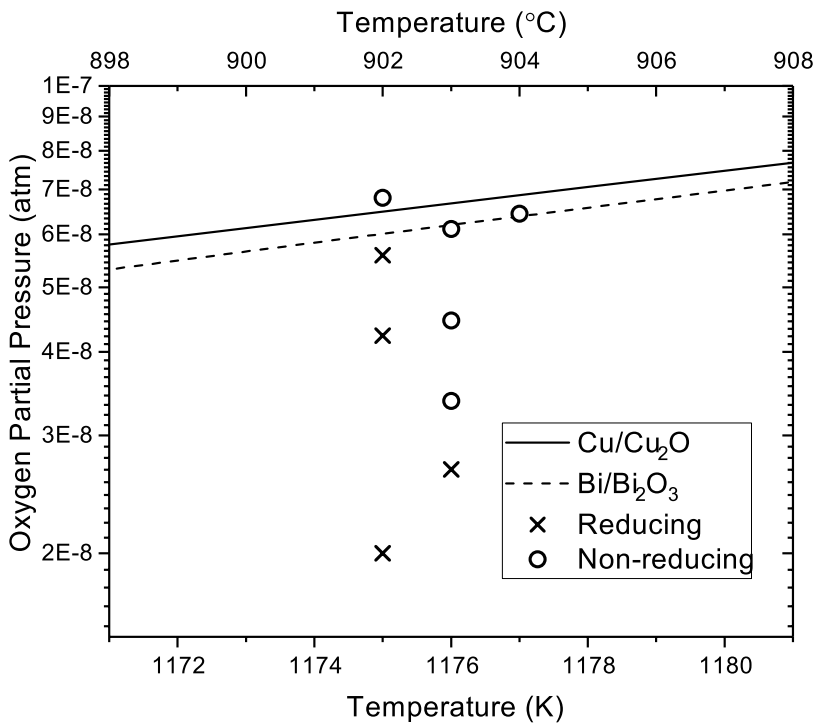

Figure 4.19. Temperature and oxygen partial pressure during sintering for two different runs that resulted in reduction of bismuth oxide in one case and not in the other. The lowest oxygen partial when reduction did not occur is used to calculate the thermodynamic activity of Bi_2O_3 in BNKBT88.

The method for determining the thermodynamic activity has many sources of error that make the measurement difficult. First, temperature and oxygen partial pressure must be measured accurately inside the hot zone of the furnace. Although the R-type thermocouple has minimal error of ±0.5ºC at the sintering temperature, it sits at the edge of the hot zone. The temperature profile was measured without the alumina boat and the profile is expected to change once the alumina boat is pushed into the hot zone. The temperature inside the covered boat could not be measured but is assumed to be constant. While the oxygen sensor measures the atmosphere inside the tube furnace, the oxygen partial pressure inside the covered boat cannot be measured. Reduction did not occur when the oxygen partial pressure dropped below the Bi_2O_3/Bi equilibrium. However, the

crucibles filled with the Cu_2O/Cu mixture inside of the boat were designed to maintain the oxygen partial pressure by decomposing under these conditions to release oxygen.

The Gibbs free energy for the formation of Bi_2O_3 has a wide range of values reported for thermodynamic studies in the literature. Based on the wide range of values reported, the Bi_2O_3/Bi equilibrium oxygen partial pressure could be described as a zone rather than the fine line shown in Figure 4.19.

4.4 Conclusion

The compatibility of copper base metal electrodes and Bi-based ceramics was demonstrated. A suitable sintering aid composition was used to sinter BNKBT88 at 900ºC in air or controlled oxygen atmosphere.

Control of the atmosphere is the greatest challenge for co-firing a copper metal electrode and Bi-based ceramic. An in-situ oxygen sensor and mixing CO_2 and H_2 gases provides the precise control of oxygen inside the tube furnace necessary to avoid reaction of the copper or reduction of the bismuth oxide. The presence of a mixture of Cu metal and Cu_2O next to the samples inside of a covered alumina boat was able to keep the Cu/Cu_2O equilibrium oxygen partial pressure needed to co-fire the ceramic.

A challenge that was not overcome is the absorption of oxygen by the copper electrode as the furnace cooled. The rubber between the furnace tube and the water-cooled end caps cannot provide the seal necessary to prevent air from oxidizing the hot samples during cooling and the zirconia oxygen sensor cannot operate below 850ºC.

References

[1] D. R. Gaskell, *Introduction to the Thermodynamics of Materials*. Taylor & Francis, 2003.

[2] S. Itoh and T. Azakami, "Activity Measurements of Liquid Bi-Sb Alloys by the E.M.F. Method Using Solid Electrolytes," *J. Jpn. Inst. Met. Mater.*, vol. 48, pp. 293–301, 1984.

[3] Y. Imanaka, *Multilayered Low Temperature Cofired Ceramics (LTCC) Technology*. Springer Science, 2005.

[4] H. Nagata, K. Tabuchi, and T. Takenaka, "Fabrication and Electrical Properties of Multilayer Ceramic Actuator Using Lead-Free (Bi1/2K1/2)TiO3," *Jpn. J. Appl. Phys.*, vol. 52, p. 09KD05, 2013.

[5] L. Gao, H. Guo, S. Zhang, and C. A. Randall, "Base Metal Co-Fired Multilayer Piezoelectrics," *Actuators*, vol. 5, no. 1, p. 8, 2016.

[6] H. Hayashi *et al.*, "Reliability of Nickel Inner Electrode Lead-Free Multilayer Piezoelectric Ceramics," *Jpn. J. Appl. Phys.*, vol. 51, p. 09LD01, 2012.

[7] H. Kishi, Y. Mizuno, and H. Chazono, "Base-Metal Electrode-Multilayer Ceramic Capacitors: Past, Present and Future Perspectives," *Jpn. J. Appl. Phys.*, vol. 42, pp. 1–15, 2003.

[8] H. Shimizu, K. Kobayashi, Y. Mizuno, and C. A. Randall, "Advantages of Low Partial Pressure of Oxygen Processing of Alkali Niobate: NaNbO3," *J Am Ceram Soc*, vol. 97, no. 6, pp. 1791–1796, 2014.

[9] C. Lui, P. Lui, K. Kobayashi, and C. A. Randall, "Base metal Co-fired (Na,K)NbO3 structures with enhanced piezoelectric performance," *J. Electroceramics*, vol. 32, pp. 301–306, 2014.

[10] K. Kobayashi, Y. Doshida, Y. Mizuno, and C. A. Randall, "A Route Forwards to Narrow the Performance Gap between PZT and Lead-Free Piezoelectric Ceramic with Low Oxygen Partial Pressure Processed (Na0.5K0.5)NbO3," *J Am Ceram Soc*, vol. 95, no. 9, pp. 2928–2933, 2012.

[11] L. Gao, S.-W. Ko, H. Guo, E. Hennig, and C. A. Randall, "Demonstration of Copper Co-Fired (Na,K)NbO3 Multilayer Structures for Piezoelectric Applications," *J Am Ceram Soc*, vol. 99, no. 6, pp. 2017–2023, 2016.

[12] J. F. Ihlefeld, M. D. Losego, and J.-P. Maria, "Base Metal Bottom Electrodes," in *Chemical Solution Deposition of Functional Oxide Thin Films*, Springer-Verlag, 2013.

[13] H. G. Yeo and S. Trolier-Mckinstry, "{001} Oriented piezoelectric films prepared by chemical solution deposition on Ni foils," *J. Appl. Phys.*, vol. 116, p. 014105, 2014.

[14] C. A. Randall, A. Kelnberger, G. Y. Yang, R. E. Eitel, and T. R. Shrout, "High Strain Piezoelectric Multilayer Actuators—A Material Science and Engineering Challenge," *J. Electroceramics*, vol. 14, pp. 177–191, 2005.

[15] EPCOS AG, "Piezo actuators for fuel injection systems." 2014.

[16] K. Hirakata, S.-I. Sato, F. Uchikoba, Y. Kosaka, and K. Sawamura, "Multilayer Capacitors with Copper Inner Electrodes," *Ferroelectrics*, vol. 133, pp. 139–144, 1992.

[17] H. L. Lukas and S. G. Fires, "The Bismuth-Oxygen System," *J. Phase Equilibria*, vol. 16, no. 3, pp. 223–234, 1995.

[18] R. Ganesan, T. Gnanasekaran, and R. S. Srinivasa, "Determination of standard molar Gibbs free energy of formation of Bi2O3 over a wide temperature range by EMF method," *J. Chem. Thermodyn.*, vol. 35, pp. 1703–1716, 2003.
[19] I. Burn and W. C. Porter, "Processing Multilayer Ceramics with Internal Copper Conductors," in *Materials and Processes for Microelectronic Systems*, vol. 15, K. M. Nair, R. Pohonka, and R. C. Buchanan, Eds. The American Ceramic Society, 1990, pp. 375–390.
[20] M. Sato, "Electrochemical Measurements and Control of Oxygen Fugacity and Other Gaseous Fugacities with Solid Electrolyte Systems," in *Research Techniques for High Pressure and High Temperature*, G. C. Ulmer, Ed. Springer-Verlag, 1971, pp. 43–99.
[21] D. J. Shanefield, *Organic Additives and Ceramic Porcessing*. Springer Science, 1995.
[22] Y. Takayama, N. J. Donnelly, and C. A. Randall, "Piezoelectric Actuators with Cu Inner Electrode," *Appl. Ferroelectr.*, vol. ISAF 2008, 2008.
[23] "Fine Powders and Thick Film Materials." Shoei Chemical inc.
[24] Y. A. Aggour, "Thermal decomposition behaviour of ethyl cellulose grafted copolymers in homogeneous media," *J. Mater. Sci.*, vol. 35, pp. 1623–1627, 2000.

5. Non-stoichiometry in bismuth based piezoceramics

5.1 Introduction

In BNT-based compositions, there is a large variance in piezoelectric properties reported for the same BNT-based compositions, especially at the morphotropic phase boundary where changes in composition can greatly affect properties [1][2][3]. The volatility at sintering temperatures of the starting materials such as bismuth oxide, and the affinity of potassium carbonate to absorb water make stoichiometric control over the composition difficult.

The effect of excess Bi_2O_3 added to BNT in order to compensate for volatilization during sintering has been studied [4]. A small addition of Bi_2O_3 was found to enhance densification during sintering and improve piezoelectric properties. A 1 mol% addition of Bi_2O_3 decreased leakage current which made poling easier and slightly improved piezoelectric properties, but reduced depolarization temperature [4]. Excess bismuth was also found to increase resistivity by 3-4 orders of magnitude in BNT, while sodium excess decreased resistivity [5].

Non-stoichiometry of A-site cations was studied by Sung in BNT ceramics [6]. It was found that the non-stoichiometry of Bi and Na resulted in intrinsic defects, and the piezoelectric and dielectric properties, as well as grain structure were found to be sensitive to the non-stoichiometry [6][7][8]. Bismuth deficiency, as well as sodium excess caused large grain growth, increased depolarization temperature, and decreased d_{33}. Bismuth deficiency induces oxygen vacancies, which pin domain walls [6]. Excess bismuth suppresses the formation of vacancies created from the volatilization of Bi_2O_3

and can diffuse into the lattice and occupy the A-site [6]. In both bismuth excess or alkali deficiency, the depolarization temperature is reduced.

The pinning of domain walls leads to hard piezoelectric properties. These properties are high coercive field, high mechanical quality factor, and low loss that are desirable for high power applications are. In $Pb(Zr,Ti)O_3$ (PZT) based piezoceramics, these properties are achieved by acceptor doping, such as substitution of Mn^{2+} or Fe^{2+} on the titanium site [9]. In lead-free ceramics, acceptor doping by substitution of manganese for titanium on the B-site in rhombehedral BNKLT piezoceramics has achieved a coercive field of 52kV/cm and mechanical quality factor up to 974 [10]. While BNT-based piezoceramics have lower coupling coefficient than PZT, the high mechanical quality factor and high vibration velocity of Mn-doped BNKLT ceramics makes them a potential alternative to hard PZT in high power application [11][12]. Few studies on non-stoichiometric BNT-based ceramics with Bi deficiency or Na excess have reported mechanical quality factor or coercive field. In morphotropic phase boundary BNT-BT composition, increased coercive field and a small increase in mechanical quality factor from Bi deficiency has been reported [13]. However, Bi deficiency was studied in a narrow composition range, from 0 to 0.8mol% deficiency.

The electrical properties of BNT are sensitive to small changes in non-stoichiometry. The thermally activated mobility of the oxygen vacancies in Bi deficient and Na excess BNT greatly increases electrical conductivity at elevated temperatures. Bismuth excess and Na deficiency improve the resistivity. Bismuth deficient and Na

excess BNT have been studied for a possible application as an oxygen conductor in solid oxide fuel cells [14][15].

5.2 Experimental procedure

The conventional mixed oxide method was used to prepare all ceramic compositions. The abbreviations for the non-stoichiometric compositions are listed in Table 5.1. The starting materials are Bi_2O_3 (Acros Organics, 99.9%), Na_2CO_3 (Acros Organics, 99.95%), K_2CO_3 (99.0% Alfa Aesar), $BaCO_3$ (Alfa Aesar, 99.8%), and TiO_2 (99.9% Aldrich). The raw materials were dried overnight at 200°C in an oven overnight. The powders were weighed according to the formula of the composition being prepared. An example of the weighted amounts of raw materials used for preparing a batch of bismuth deficient BNKBT88-2.0Bi is given in Table 5.2. The measured amounts correspond to 100g of BNKBT88-2.0Bi powder after calcination. The weighed powders are milled in acetone for 20hr. After milling, all powders were dried and then calcined at 800°C for 3hr in air. The calcined powders were ball milled again for 10hr. Binder was added using a 10 wt% polyvinyl alcohol solution and pressed into disks of 12.7 mm diameter. The samples were heated to 550°C to remove binder followed by sintering at 1150°C for 2hr in air.

Table 5.1. Abbreviations and compositions for non-stoichiometric BNKBT88.

Stoichiometry	Abbreviation	Composition
Stoichiometric	BNKBT88 :	$0.88(Bi_{0.50}Na_{0.50})TiO_3–0.08(Bi_{0.50}K_{0.50})TiO_3–0.04BaTiO_3$
Bismuth excess	BNKBT88+2.0Bi:	$0.88(Bi_{0.52}Na_{0.50})TiO_3–0.08(Bi_{0.52}K_{0.50})TiO_3–0.04BaTiO_3$
Bismuth deficient	BNKBT88-2.0Bi:	$0.88(Bi_{0.48}Na_{0.50})TiO_3–0.08(Bi_{0.48}K_{0.50})TiO_3–0.04BaTiO_3$
Alkali excess	BNKBT88+2.0Na,K:	$0.88(Bi_{0.50}Na_{0.52})TiO_3–0.08(Bi_{0.50}K_{0.52})TiO_3–0.04BaTiO_3$
Alkali deficient	BNKBT88-2.0Na,K:	$0.88(Bi_{0.50}Na_{0.48})TiO_3–0.08(Bi_{0.50}K_{0.48})TiO_3–0.04BaTiO_3$
A-site excess	BNKBT88+2.0A:	$0.88(Bi_{0.52}Na_{0.52})TiO_3–0.08(Bi_{0.52}K_{0.52})TiO_3–0.04BaTiO_3$
A-site deficient	BNKBT88-2.0A	$0.88(Bi_{0.48}Na_{0.48})TiO_3–0.08(Bi_{0.48}K_{0.48})TiO_3–0.04BaTiO_3$

Table 5.2. Weighted amounts of raw materials for preparing a 100g (after calcination) batch of bismuth deficient BNKBT88-2.0Bi.

Raw material	Mass (g)
Bi_2O_3	51.2845
TiO_2	38.1520
Na_2CO_3	11.1388
$BaCO_3$	3.7707
K_2CO_3	1.3204
Total	105.6664
$0.88(Bi_{0.48}Na_{0.50})TiO_3–0.08(Bi_{0.48}K_{0.50})TiO_3–0.04BaTiO_3$	100.0000

The sintered ceramics are polished to a thickness of 1 mm and electroded using DuPont 7095 air-fired silver conductor. Poling was done with an electric field of 5 kV/mm at 25-90ºC in an oil bath. The piezoelectric coefficient was measured using a Berlincourt d_{33} piezometer. Dielectric properties were measured using a HP4194A impedance analyzer and a HP4248 precision LCR meter. Mechanical quality factor Q_m was calculated at the resonant frequency from the equivalent circuit using the equation 1.

$$Q_m = \frac{1}{R}\sqrt{\frac{L}{C_a}} \qquad (1)$$

Hysteresis measurements were made using a Radiant Technologies Precision LC and High Voltage Interface (HVI). For measurements at elevated temperature, the High Voltage Test Fixture (HVTF) was placed inside of an oven. DC resistivity was measured using a guarded electrode with Keithley 617 electrometer [16]. A DC bias of 100 V/cm was used. The circular pattern for the guard electrode was deposited via sputtering using gold.

All samples for X-ray diffraction were polished to a flat, smooth surface using sand paper and finished using 1200 grit size. In samples that were poled, silver electrode was painted onto the surface. After poling, the electrode was removed using acetone. BNKBT88-2.0(Na,K) could not be poled so the only the unpoled sample was analyzed.

X-ray diffraction was done on a PANalytical X'Pert Pro using CuKα at 45kV and 30mA. A step size of 0.013º and a dwell time of 21.42 seconds per step over a range of 15-80º 2θ were used. Analysis of the XRD pattern was done using the software Jade. The structure was analyzed using rhombohedral $Bi_{0.5}Na_{0.5}TiO_3$ (space group R3c) and

tetragonal $BaTiO_3$ (space group P4mm). The rhombohedral and tetragonal lattice parameters were calculated using the d-spacing of diffraction peaks. Due to the coexistence of both phases and their similar structure, some peaks occur too close together to be resolved. This occurred in nearly all diffraction patterns for the tetragonal (101)/(110) and rhombohedral (104)/(110) reflections. Therefore these peaks could not be used to determine lattice parameters. The rhombohedral structure was calculated using hexagonal lattice parameters and then transferred into the pseudo-cubic unit cell with length a and angle α.

5.3 Results and discussion

5.3.1 Piezoelectric and ferroelectric properties

The piezoelectric and ferroelectric properties of non-stoichiometric BNKBT88 were found to be extremely sensitive to changes in stoichiometry. The properties of all the compositions with 2% non-stoichiometry are given in Table 5.3. The changes in the properties can be grouped into 3 different categories: Bi-deficient and alkali excess became hard with lower d_{33} and increased Q_m, T_d was lower for Bi excess and alkali deficient which decreased coercive field and improved d_{33} in the former while causing relaxor behavior in the later, and an overall decrease in piezoelectric properties for the A-site excess and deficient compositions.

Table 5.3. Properties of Non-stoichiometric BNKBT88 ceramics. The piezoelectric coefficient d_{33}^* for BNKBT88-2.0Na,K was calculated from strain and has units pm/V.

Composition	Density (g/cc)	d_{33} (pC/N)	Q_m	tanδ (%)	ε_{33}	P_r (μC/cm^2)	E_c (kV/cm)	T_d (°C)
BNKBT88	5.80	165	150	1.0	720	28	31	150
BNKBT88+2.0Bi	5.76	170	85	4.7	1200	27	22	75
BNKBT88-2.0Bi	5.72	105	1200	1.1	425	36	47	178
BNKBT88+2.0Na,K	5.50	100	550	1.6	415	41	42	170
BNKBT88-2.0Na,K	5.61	670*	-	9.1	1765	-	-	-
BNKBT88+2.0A	5.69	131	168	2.2	620	40.3	33.6	140
BNKBT88-2.0A	5.44	146	126	2.9	770	34.5	28.8	90

The Bi-deficient and alkali excess compositions had low loss, increased coercive field and mechanical quality factor, which are desired for high power application. The polarization-electric field hysteresis for Bi-deficient and alkali excess are shown in Figure 5.1and there is a substantial increase in the coercive field compared to unmodified BNKBT88. Bismuth excess caused a small increase in d_{33} and decreased coercive field consistent with the effects of donor doping. The properties listed in Table 5.3 are for optimized poling conditions. Poling was difficult at 90ºC due to increasing conductivity during poling. Temperature was slightly reduced and the poling duration had to be carefully adjusted in order to maximize properties. A mechanical quality factor of 1200 was achieved in BNKBT88-2.0Bi when poled at 80ºC with 5kV/mm electric field for 1 minute. After 1 minute of poling, the current limiter of the high voltage amplifier activated, which reduces the voltage when the current exceeds a set threshold. The conductivity of the sample rises during poling so the power supply reduces the voltage in

order to prevent the current from exceeding the set limit of 280μA. Poling was terminated when the power supply indicated that the current limit had been reached. The properties of BNKBT88-2.0Bi resulting from poling were reproducible although the duration of poling at 5kV/mm was dependent on the rate that the electric field was increased. The conductivity of the sample was affected by the total duration and magnitude of the applied electric field. In one case where the electric field was increased slowly, the sample was only held at 5kV/mm for less than 10 seconds before the voltage limiter activated and the piezoelectric properties were the same. The effect of different amount of Bi-deficiency is discussed later in section 4.3.3.

The alkali excess samples were poled at 70ºC for 5 minutes with 5kV/mm electric field. In general, the piezoelectric properties are inferior Bi-deficient composition; the alkali excess had lower d_{33}, Q_m, E_c, and higher loss. The reduced piezoelectric properties are likely due to the lower density of BNKBT88+2.0Na,K. Polishing the alkali excess ceramics to a mirror-like finish with 1200 grit silicon carbide paper revealed internal pores large enough to be seen with the eye. The excess alkali inhibited sintering by leaving closed internal pores in the ceramics. The alkali excess composition was not a good candidate to study hardening of piezoelectric properties due to non-stoichiometry.

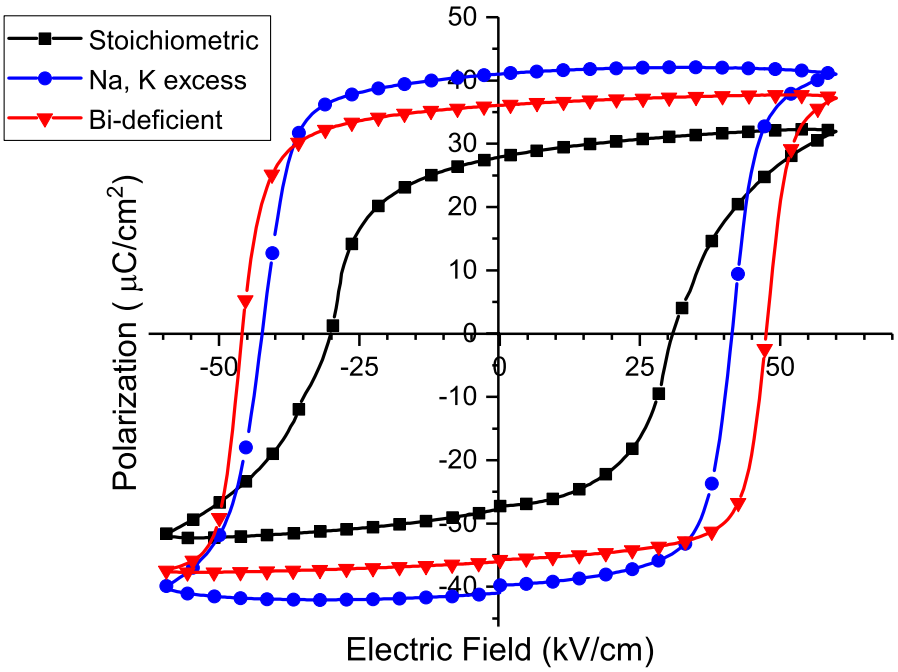

Figure 5.1. Polarization–electric field hysteresis of unmodified BNKBT88, bismuth deficient, and alkali excess BNKBT88 compositions. Bismuth deficiency and alkali excess resulted in hard ferroelectric properties with increased coercive field. The polarization increased as well.

Depolarization is measured from the permittivity during heating, shown in Figure 5.2 for poled Bi excess, Bi deficient, and unmodified BNKBT88, and occurs at 178ºC for bismuth deficient BNKNBT88-2.0Bi. The dielectric loss is low at room temperature. However, the conductivity in bismuth deficient BNKBT88-2.0Bi increases rapidly at elevated temperature, which causes the dielectric loss to be high. The high dielectric loss leads to the rapid increase in permittivity that occurs after depolarization. The high dielectric loss makes poling impossible at 90ºC and the ceramics are unusable at temperatures above 150ºC.

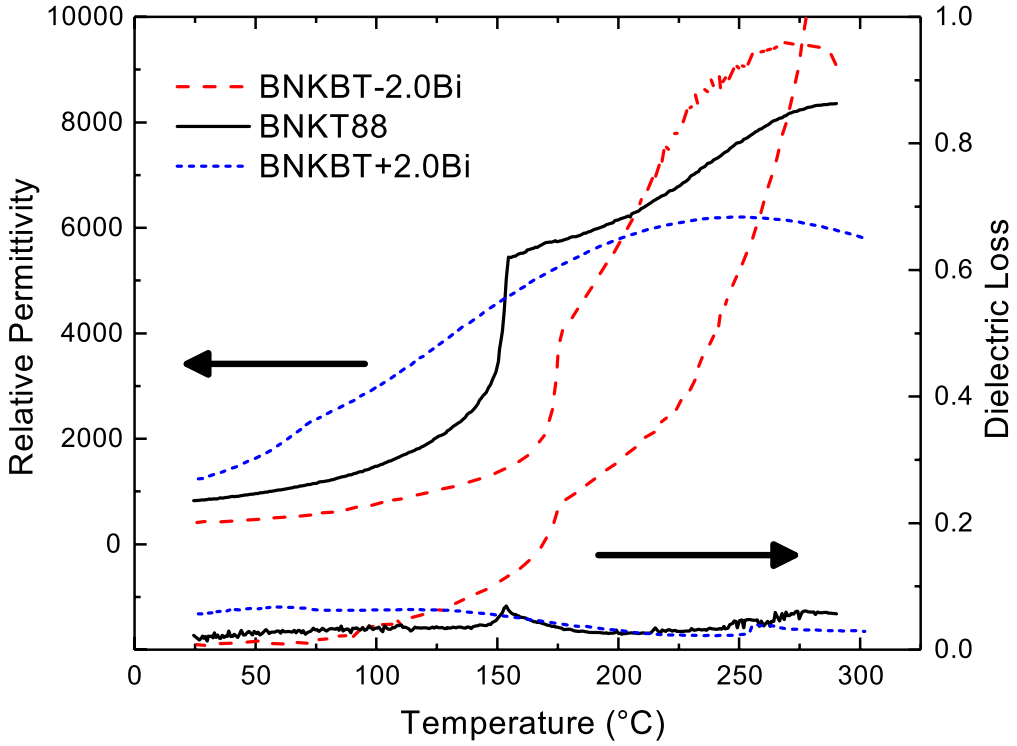

Figure 5.2. Relative permittivity and dielectric loss during heating for bismuth excess and deficient BNKBT88 compared to the unmodified BNKBT88. Depolarization occurs around 75ºC for Bi-excess composition and 170ºC for Bi-deficient.

The bismuth excess composition did not have any piezoelectric properties after poling at 90ºC. The Bi excess ceramics could be poled at 50ºC with reduced properties. A d_{33} of 170pC/N is achieved for poling at room temperatures. The measurement of the permittivity and dielectric loss during heating, shown in Figure 5.2 revealed that the depolarization temperature is about 75ºC for the Bi excess composition. Unlike unmodified BNKBT88, the bismuth excess composition depolarizes at lower temperature and over a wider temperature range. The Bi excess ceramics would begin to lose their piezoelectric properties at temperatures as low as 50ºC. Depolarization is typically

indicated by a sharp increase in permittivity and dielectric loss at T_d as is seen in the unmodified BNKBT88 and bismuth deficient composition. In bismuth excess, T_d is indicated by a slight change in permittivity and small drop in dielectric loss around 70ºC. Dielectric loss is high for the poled Bi excess composition at room temperature and decreases after poling.

The polarization-electric field hysteresis for the Bi excess composition is shown in Figure 5.3. The room temperature properties have decreased coercive field and increased saturated polarization, while the remnant polarization is similar to the unmodified BNKBT88. Similar to the effect of donor doping in PZT, bismuth excess depresses the depolarization temperature, which in turn increases room temperature properties such as d_{33} and permittivity.

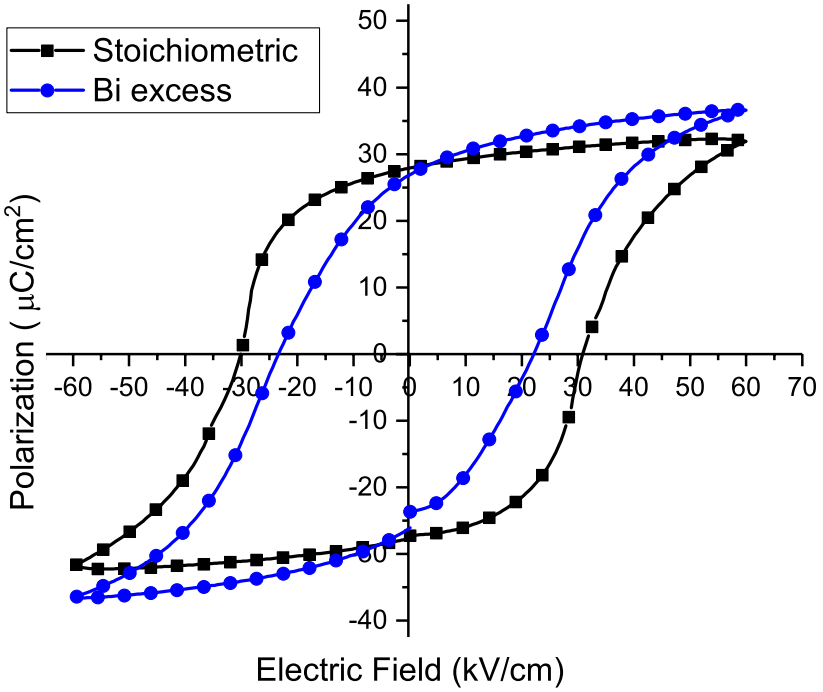

Figure 5.3. Polarization–electric field hysteresis of unmodified BNKBT88, bismuth excess, and alkali deficient compositions. Bismuth excess decreases coercive field. The alkali deficient composition becomes antiferroelectric.

The alkali deficient samples did not have any piezoelectric properties after poling at room temperature. The shape of the polarization-electric field hysteresis loops, shown in Figure 5.4, is similar to the ergodic relaxor state that occurs above T_d in some BNT-based compositions. Similar to Bi excess, the alkali deficiency depresses the depolarization temperature but to below room temperature. The alkali excess have high room temperature permittivity as result of being above the depolarization temperature. In BNT-based compositions, this state has been described as an antiferroelectric + ferroelectric [17]. The switching current, shown in Figure 5.5 for alkali deficient

composition compared to unmodified BNKBT88 suggest that the alkali deficient is in an ergodic relaxor state. In ferroelectrics, the current has a peak at the coercieve field due to the switching of domains. In the alkali deficient composition, there is a small peak when an electric field is applied that shows the domains align when an electric field is applied. Unlike the ferroelectric, the domains revert to a random orientation when the electric field is removed, causing the sharp peaks seen in Figure 5.5. Ferroelectricity is induced under the application of an electric field but does not show piezoelectric properties such as d_{33}. A result of the relaxor behavior is large positive strain under electric field due to electrostriction. A strain of 670pm/V was calculated from the displacement of the sample resulting from the application of an electric field. Induced strain due to application of bi-polar electric field in alkali deficient BNKBT88 and unmodified BNKBT88 is shown in Figure 5.6. The antiferroelectric alkali deficient composition has large electric-field induced strain only in the positive direction, compared to the “butterfly” loop in the unmodified BNKBT88. The strain in the alkali deficient is due to electrostriction and the sample only expands under the application of the electric field, compared to the unmodified BNKBT88 that expands and then contracts as the result of ferroelectric switching of domains. Large electrostriction has been reported in modified BNT-based compositions where an additive such as KNN causes the depolarization temperature to drop below room temperature and has potential to be used in an actuator application [17][18][19].

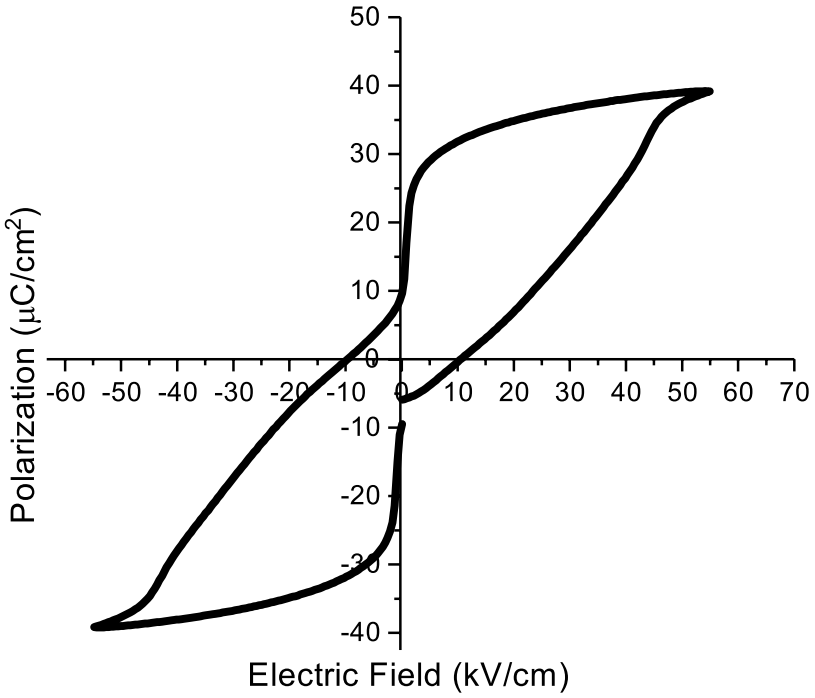

Figure 5.4. The alkali deficient composition becomes antiferroelectric at room temperature. When electric field is applied, ferroelectric phase is induced.

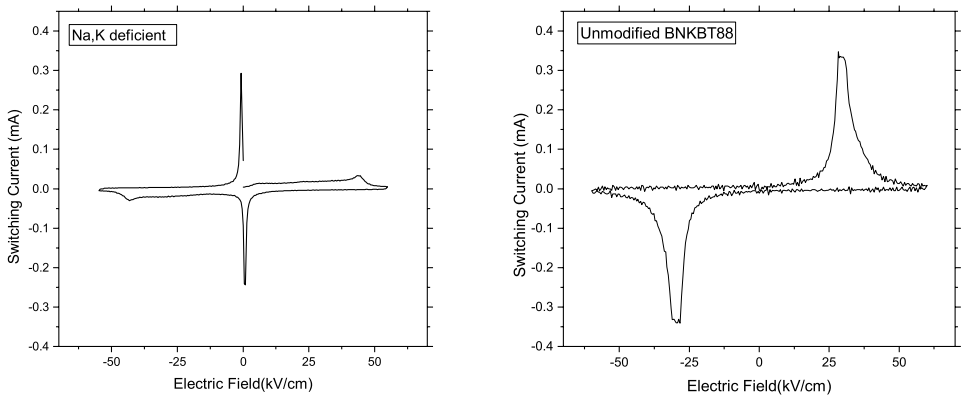

Figure 5.5. Switching current for alkali deficient BNKBT88 shows antiferroelectric behavior. The application of electric field temporarily aligns domains, however they revert to random orientation when the electric field is removed.

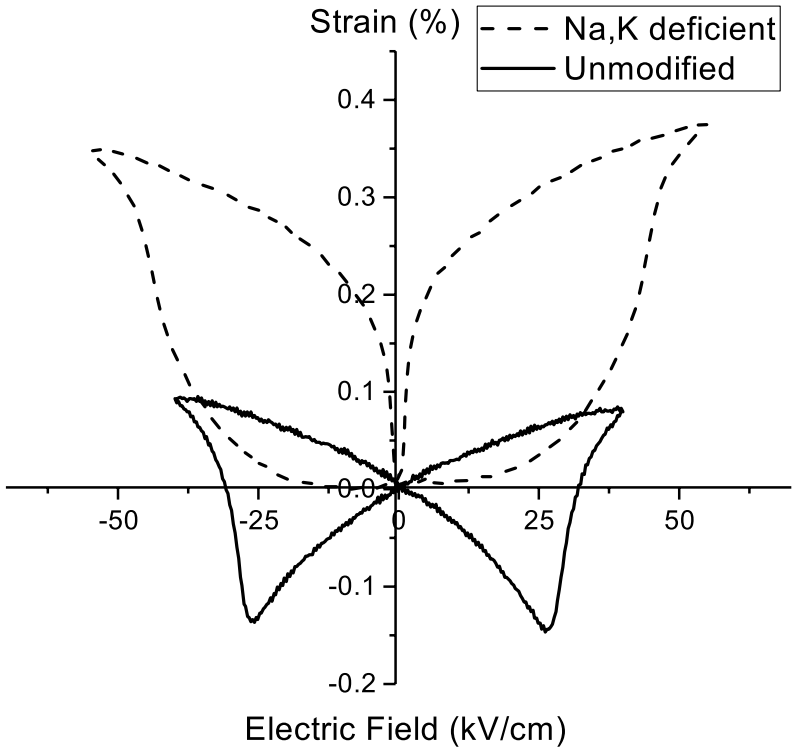

Figure 5.6. Induced strain due to application of bi-polar electric field in alkali deficient BNKBT88 compared to unmodified BNKBT88. The antiferroelectric alkali deficient composition has large electric-field induced strain only in the positive direction due to electrostriction, compared to the "butterfly" loop in the unmodified BNKBT88. The d_{33} measured by converse piezoelectric effect is 690pm/V.

The simultaneous alkali and bismuth non-stoichiometric compositions have overall lower piezoelectric properties. Both have reduced d_{33} and higher loss while the permittivity is similar to the unmodified BNKBT88. The A-site deficient ceramics did not sinter well. The polarization-electric field hysteresis for the A-site excess and deficient compositions is shown in Figure 5.7. A-site excess resulted in a slight increase in coercive field while A-site deficiency caused a slight decrease. It is difficult to determine the overall effect on properties from combined bismuth and alkali non-

stoichiometry. The increase in coercive field along with the small increase in mechanical quality factor suggests the properties become hard, however the changes in properties are too small to be concise. Overall, 2% non-stoichiometry has less effect on piezoelectric and ferroelectric properties when bismuth and alkali are modified simultaneously. The changes observed in the other non-stoichiometric compositions such as high mechanical quality factor from Bi-deficiency or large strain from alkali deficiency is caused by the change relative to the other A-site cation or the overall A-site charge.

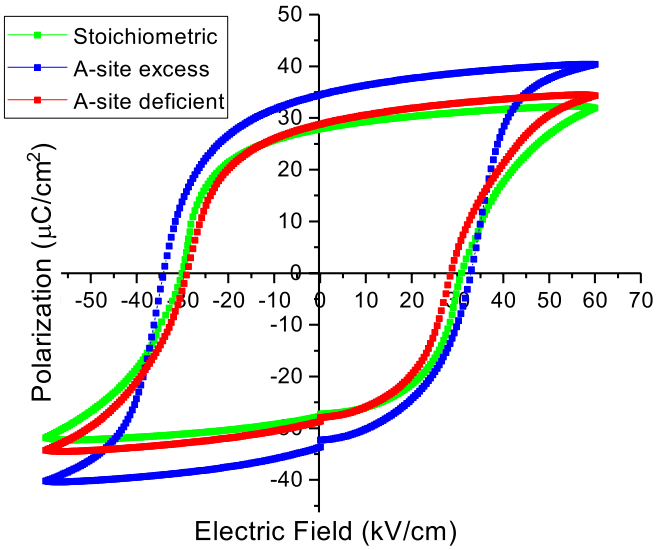

Figure 5.7. Polarization–electric field hysteresis of BNKBT88 and A-site non-stoichiometric compositions. The coercive field is slightly decreased A-site deficiency while A-site excess results in higher coercive field and higher polarization.

5.3.2 X-ray diffraction

The calculated rhombohedral and tetragonal lattice parameters for all compositions in their poled and unpoled states are given in Table 5.4. The lattice parameters were calculated using peaks that were known to be a single peak. Due to the coexistence of tetragonal and rhombohedral phases with similar lattices, reflections could occur at the same d-spacing or very close together. For poled BNKBT88, although the tetragonal phase was present, the lattice parameters could not be determined for the poled ceramic due to the overlap of rhombohedral and tetragonal phases. Crystallite size and lattice strain could not be determined due to the overlap of tetragonal and rhombohedral peaks. The diffraction patterns of unpoled ceramics are shown in Figure 5.8.

Table 5.4. Hexagonal, pseudo-cubic (rhombohedral), and tetragonal lattice parameters for poled and unpoled samples of each composition. Tetragonal lattice parameters could not be determined for poled BNKBT88 and unpoled BNKBT88+2Bi.

Composition	Poled	Hexagonal		Pseudo-cubic		Tetragonal	
		a_{hex}	c_{hex}	a_{rh}	α_{rh}	a_{tr}	c_{tr}
BNKBT88	□	5.5067	13.6150	3.9060	89.64	3.9071	3.9600
BNKBT88	☑	5.5064	13.6023	3.9047	89.68		
BNKBT88-2Bi	□	5.5015	13.5963	3.9018	89.66	3.9020	3.9513
BNKBT88-2Bi	☑	5.5054	13.6053	3.9045	89.66	3.9072	3.9506
BNKBT88+2Bi	□	5.5170	13.5236	3.9020	89.97		
BNKBT88+2Bi	☑	5.5194	13.5221	3.9030	89.99	3.9032	3.9564
BNKBT88+2(Na,K)	□	5.4994	13.6171	3.9028	89.59	3.9030	3.9631
BNKBT88+2(Na,K)	☑	5.5058	13.6057	3.9047	89.66	3.9054	3.9589
BNKBT88-2(Na,K)	□	5.5189	13.5261	3.9032	89.98	3.9045	3.9530

The base composition, BNKBT88, has both tetragonal and rhombohedral phases indicated by the splitting of peaks at the pseudo-cubic (111) and (200) reflections. The tetragonal (002) peak is broad which is typical for unpoled morphotropic phase boundary compositions and is due to the random orientation of unit cells [1]. The pseudo-cubic (111) and (200) reflections of the unpoled samples are shown in Figure 5.10. BNKBT88-2Bi and BNKBT88+2(Na,K) are similar to the base composition but have stronger orientation along the rhombohedral (202). In these compositions the $(200)_{Tr}$ and $(024)_{Rh}$ are too close together to be resolved into individual peaks and the tetragonal volume fraction could not be calculated from the intensity of these peaks. Both BNKBT88+2Bi and BNKBT88-2(Na,K) have a nearly cubic structure (α_{rh}=89.97 and 89.98 respectively), and the rhombohedral (006) and (202) peaks are very close together and combine to form a single peak. There is evidence of a tetragonal phase present in BNKBT88+2Bi, but the structure could not be determined due to the absence of any strong peaks.

Poling resulted in the growth of certain peaks and altered the unit cell. Figure 5.11 shows the pseudo-cubic (111) and (200) reflections for poled and unpoled BNKBT88-2Bi. For the (111) pseudo-cubic reflections, the diffraction pattern for the poled sample shows increased intensity for the rhombohedral (006) peak and decreased intensity for the (202). The tetragonal (002) peak increased in intensity while the (200) decreased and the rhombohedral (024) is no longer visible. Increased $(002)_{Tr}$ and decreased $(200)_{Tr}$ intensity after poling has been observed elsewhere for morphotropic phase boundary compositions [20]. The X-ray diffraction patterns of all poled samples are shown in Figure 5.9. The Na and K deficient sample, BNKBT88-2(Na,K) is not shown because it could not be poled.

Ferroelectric hysteresis measurements have determined that the composition is antiferroelectric at room temperature; it becomes polarized while an electric field is applied but polarization returns to zero when the field is removed. The lattice parameters for poled samples are also given in Table I. In most compositions, the lattice increased as a result of poling. The pseudo-cubic (111) and (200) reflections of all poled samples are shown in Figure 5.12. In BNKBT88and BNKBT88+2(Na,K), the rhombohedral angle α_{rh} decreased as a result of poling. The d-spacing of the rhombohedral (006) decreased, shifting the location of the peak closer to the tetragonal (111). In general, the effect of poling on BNKBT88, BNKBT88-2Bi, and BNKBT88+2(Na,K) was similar and increased or decreased the intensity of the same peaks.

The poor piezoelectric properties of BNKBT88+2Bi and BNKBT88-2(Na,K) can be explained by their structure determined by X-ray diffraction. Analysis of the diffraction patterns shows both compositions have a nearly cubic structure which would be expected for the antiferroelectric BNKBT88-2(Na,K). BNKBT88+2Bi has a nearly cubic structure, but poling induces tetragonal phase. The low depolarization temperature of around 50ºC indicated that this tetragonal phase would begin to disappear above room temperature. The nonstoichiometry in these two compositions results in a vertical shift in the BNBK2:1 phase diagram shown in Figure 2.13. The sodium and potassium excess composition would be located in the antiferroelectric region and the bismuth excess would be just below the transition. The X-ray diffraction patterns of BNKBT88-2Bi and BNKBT88+2(Na,K) are very similar to the stoichiometric composition BNKBT88. The crystal structure was not largely affected by the nonstoichiometry of these compositions.

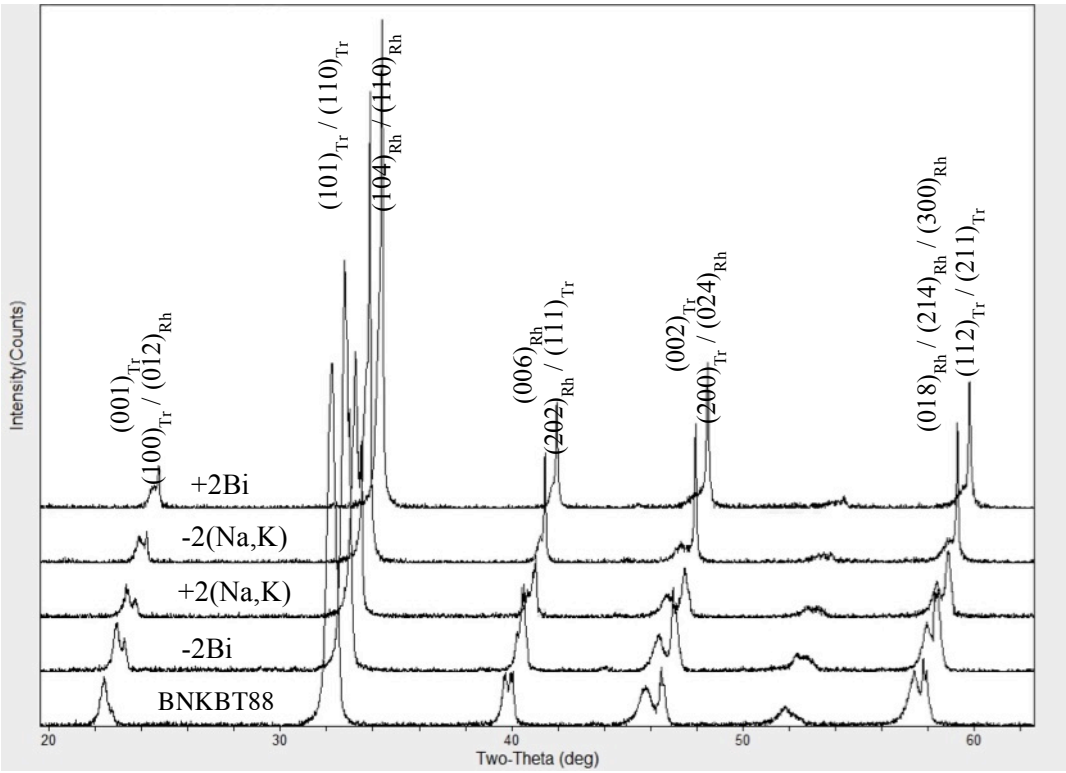

Figure 5.8. X-ray diffraction pattern of all unpoled samples.

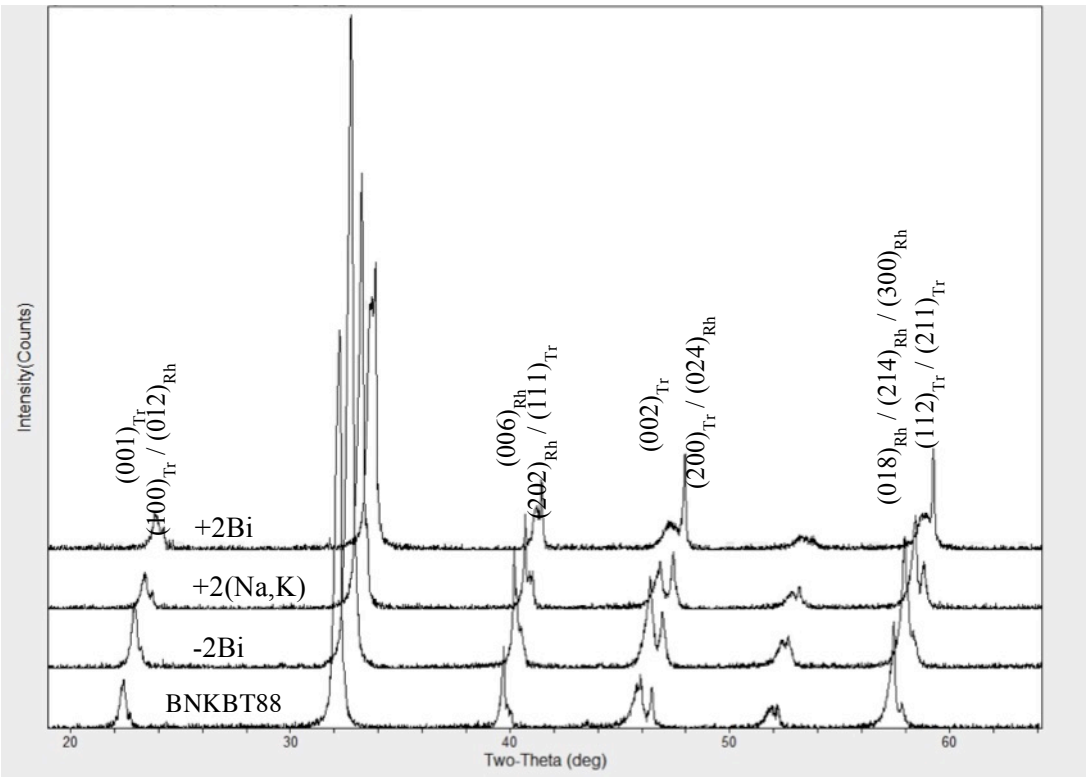

Figure 5.9. X-ray diffraction pattern of all poled samples. BNKBT88-2(Na,K) could not be poled.

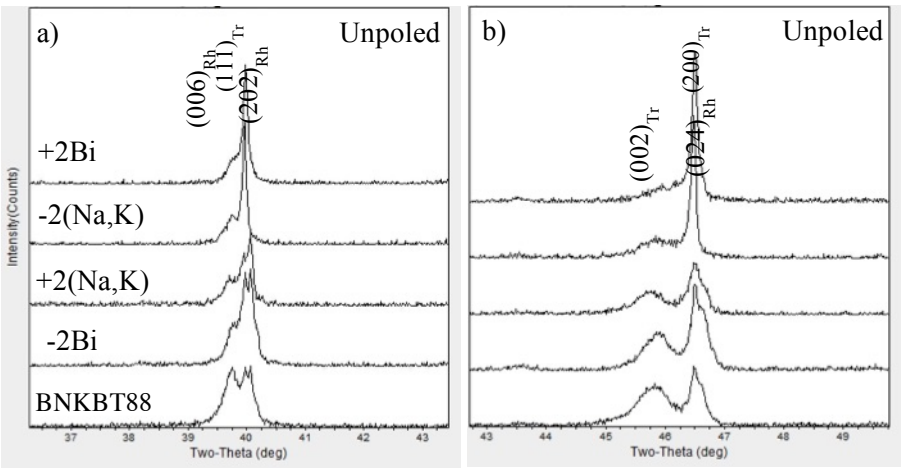

Figure 5.10. X-ray diffraction patterns of the unpoled samples showing the pseudo-cubic (111) reflections (a) and the pseudo-cubic (200) reflections (b).

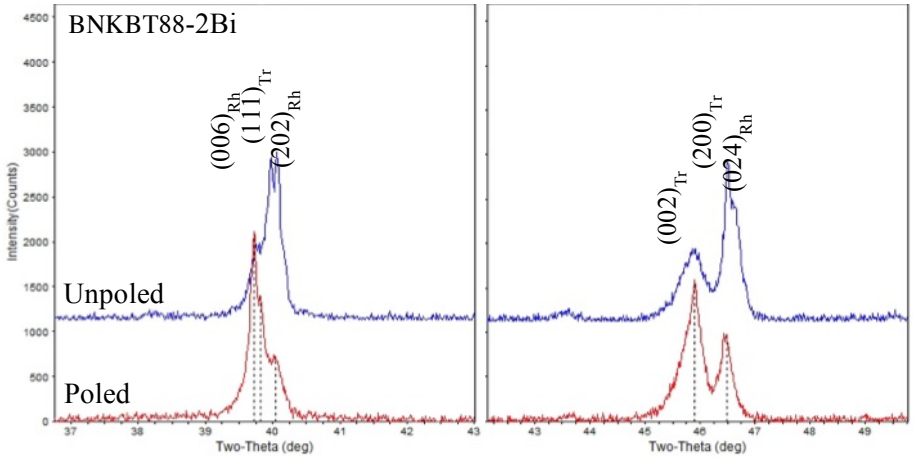

Figure 5.11. X-ray diffraction patterns of poled and unpoled BNKBT88-2Bi for the pseudo-cubic (111) reflections (a) and the pseudo-cubic (200) reflections (b).

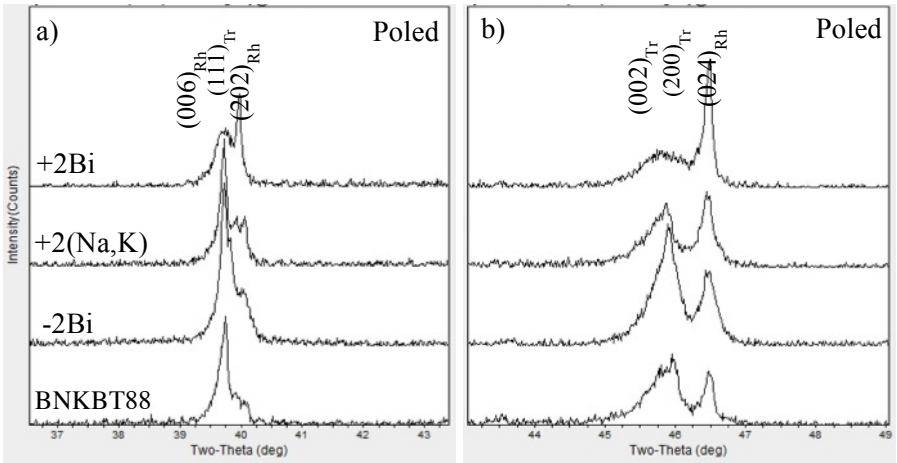

Figure 5.12. X-ray diffraction patterns of the poled ceramics showing the pseudo-cubic (111) reflections (a) and the pseudo-cubic (200) reflections (b).

5.3.3 Bismuth deficiency

The piezoelectric and ferroelectric properties of BNKBT88 become hard with increasing bismuth deficiency. The properties for different amounts of bismuth deficiency are given in Table 5.5. As the amount of deficiency increases the properties become harder; d_{33}, k_p and dielectric loss decrease while and mechanical quality factor increases. The mechanical quality factor for different amounts of Bi deficiency is shown in Figure 5.13 and Q_m increases to 1244 for 2.25% Bi deficiency. The figure of merit for high power application is $k_p^2 \cdot Q_m$, also shown in Figure 5.13, and has a maximum value of 45 for 1.5 and 2% bismuth deficient compositions. The composition with 2.25% deficiency have marginally higher mechanical quality factor but the d_{33} and coupling are reduced due to higher conductivity, which makes poling less effective an in turn reduces d_{33}. The piezoelectric coefficient, shown in Figure 5.14 for increasing Bi-deficiency, remains slightly above 100 pC/N for bismuth deficient compositions between 1-2%, and then drops to 60 pC/N when deficiency exceeds 2%. The coupling coefficient follows the same pattern as the piezoelectric coefficient, however the 1% deficient composition deviates from this behavior.

The depolarization temperature is higher for bismuth deficient BNKBT88. This may be the result of the rhombohedral distortion that was observed in poled BNKBT88-2.0Bi. In unmodified morphotropic phase boundary BNKBT88, depolarization occurs as the ferroelectric phase transitions to antiferroelectric. The rhombohedral distortion may suppress the formation of antiferroelectric phase in bismuth deficient BNKBT88.

Table 5.5. Piezoelectric properties of bismuth deficient BNKBT88 with different amount of deficiency.

BNKBT88-xBi	d_{33} (pC/N)	k_p	tanδ	ε_r	Q_m	$k_p^2 \cdot Q_m$
0	170	0.369	0.018	720	150	20
0.5	128	0.31	0.016	650	220	21
1	108	0.180	0.012	625	670	22
1.5	105	0.225	0.012	450	890	45
2	107	0.193	0.010	425	1200	45
2.25	60	0.176	0.019	340	1244	39

Bismuth deficiency induces oxygen vacancies that produce hard properties but lead to an increase in conductivity. Conduction via oxygen vacancies is a thermally activated process. At higher temperature the vacancies have greater mobility. The AC conductivity of bismuth deficient BNKBT88 is shown in Figure 5.15. On an Arrhenius plot of log conductivity and inverse temperature the slope is nearly linear. For the unmodified composition the conductivity decreases after the depolarization temperature but continues to increase in the bismuth deficient compositions. The higher conductivity leads to the high dielectric loss shown in Figure 5.2.

The temperature dependence of coercive field for bismuth deficient and unmodified BNKBT88 is shown in Figure 5.16. The coercive field decreases when heated to higher temperature. A coercive field of 48kV/cm was achieved in BNKBT88-2.0Bi at room temperature, which decreased to about 40kV/cm at 80ºC. The change in coercive field at elevated temperature was greater in 1% deficient composition. The maximum temperature for hysteresis measurements was 80ºC for the bismuth deficient compositions because conductivity was becoming too high.

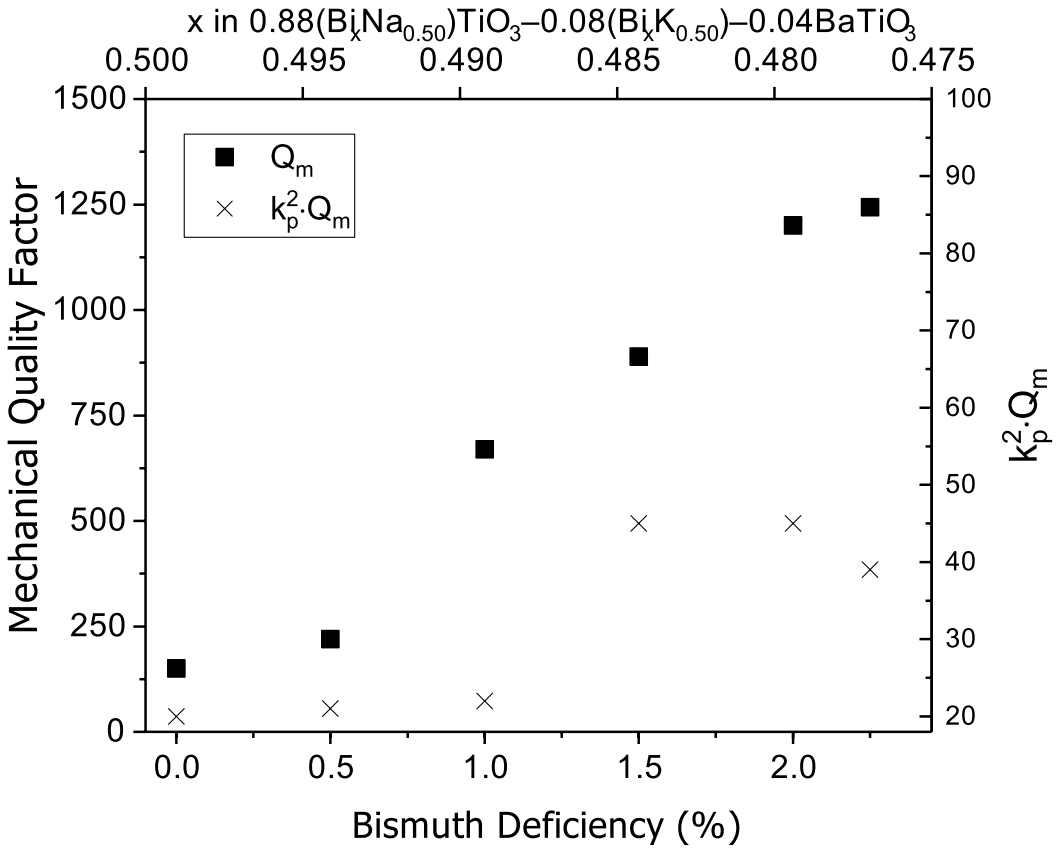

Figure 5.13. Mechanical quality factor of bismuth deficient BNKBT88 increases as the composition become more deficient. A mechanical quality factor of 1200 is achieved to 2% Bi deficiency and the figure of merit for high power application, $k_p^2 \cdot Q_m$, has a maximum value for 1.5 and 2% Bi deficiency.

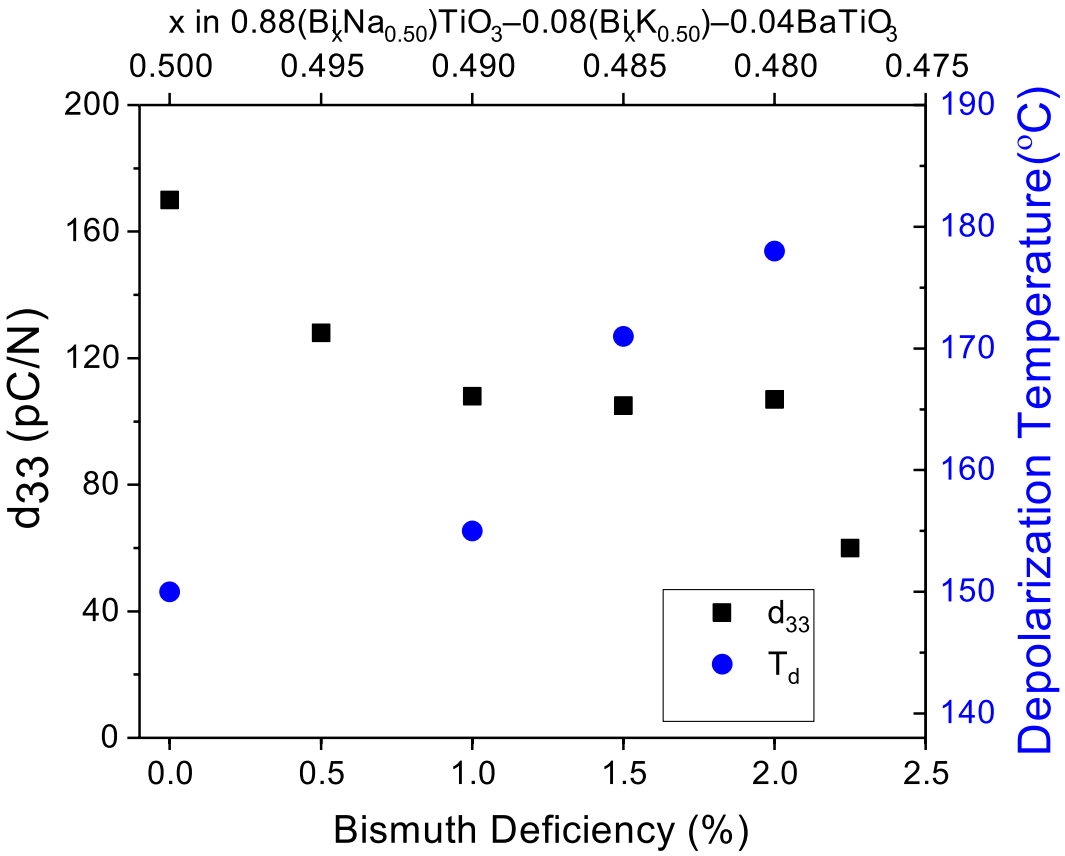

Figure 5.14. Piezoelectric coefficient and depolarization temperature for bismuth deficient BNKBT88.

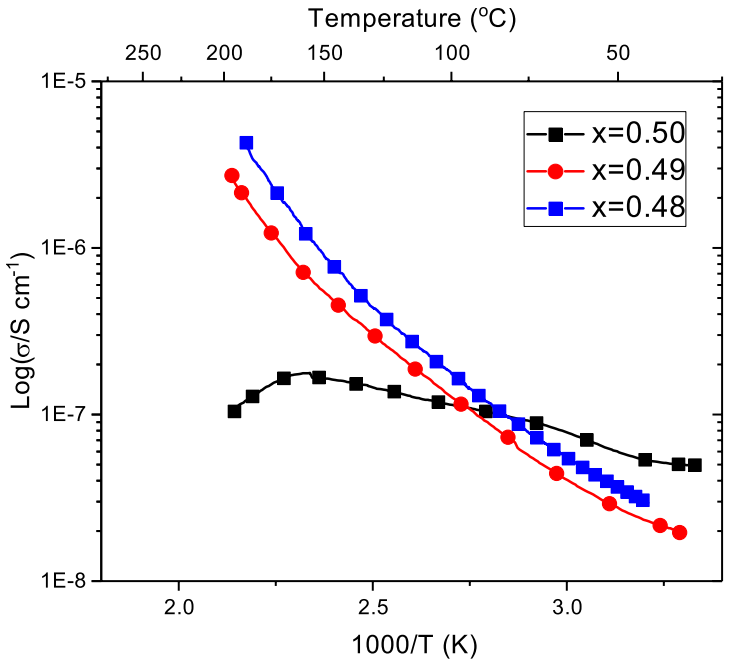

Figure 5.15. AC conductivity of bismuth deficient BNKBT88. Room temperature conductivity is higher in the unmodified composition but increases less with temperature and decreases after T_d. The conductivity rapidly rises in the bismuth deficient compositions as the temperature is increased.

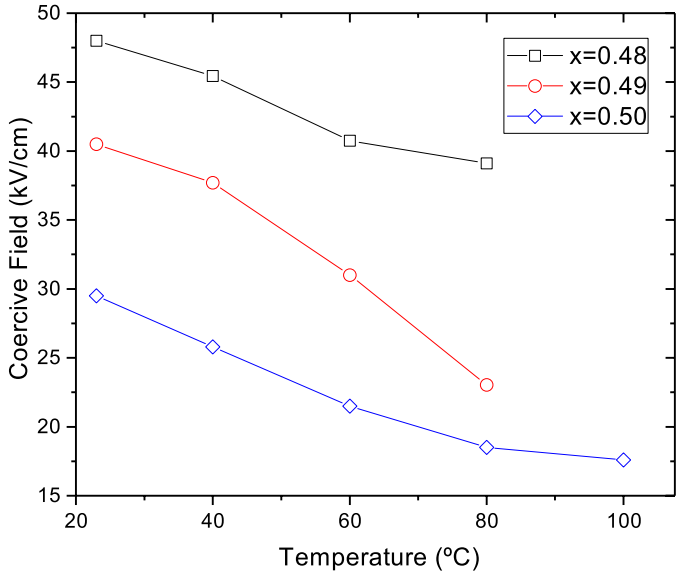

Figure 5.16. Coercive field of bismuth deficient BNKBT88.

5.3.4 Bismuth deficiency with bismuth addition

The conductivity in bismuth deficient ceramics at elevated temperature made poling difficult. The ceramics could be easily poled at room temperature, however the mechanical quality factor was significantly lower. The total time and temperature that the ceramic spends under an applied electric field affects properties. The unmodified BNKBT88 composition is normally poled at 5kV/mm at 90ºC for 10 minutes. Charged defect complexes induced by non-stoichiometry are mobile during poling and migrate towards the electrodes. The defects such as oxygen vacancies give hard piezoelectric properties but increase conductivity. Longer poling time resulted in higher conductivity, increased loss, and reduced coupling coefficient.

Bismuth oxide addition to the 2% bismuth deficient composition was able to improve resistivity while there was a small decrease in mechanical quality factor. The piezoelectric properties of bismuth deficient BNKBT88 with addition of Bi_2O_3 is given in Table 5.6. The addition of 0.2 and 0.3wt% Bi_2O_3 resulted in mechanical quality factor greater than 900. However, the planar coupling coefficient was slightly decreased, resulting in lower $k_p^2 \cdot Q_m$ value. The bismuth deficient composition with 0.5wt% Bi_2O_3 added had reduced coercive field and lower mechanical quality factor of 500. Due to higher coupling coefficient, the value of $k_p^2 \cdot Q_m$ of 58 was achieved, which is the highest among all of the modified BNKBT88 compositions studied.

Table 5.6. Piezoelectric properties of Bi-deficient BNKBT88-2.0Bi with Bi_2O_3 addition

Bi_2O_3 addition (wt%)	d_{33} (pC/N)	k_p	tanδ	Q_m	E_c(kV/cm)	$k_p^2 \cdot Q_m$
0	105	0.193	0.010	1200	48	45
0.2	105	0.172	0.009	920	46	27
0.3	110	0.186	0.010	960	46	33
0.5	110	0.341	0.008	500	36	58

The coercive field at elevated temperature for bismuth deficient BNKBT88 with Bi_2O_3 added is shown in Figure 5.17 and the hysteresis measured at room temperature and 80ºC are shown in Figure 5.18 and Figure 5.19, respectively. The addition of 0.3wt% Bi_2O_3 caused a small drop in coercive field compared to the bismuth deficient BNKBT88-2.0Bi with no Bi_2O_3 added, while the addition of 0.5wt% Bi_2O_3 further reduced coercive field. The addition of bismuth oxide has minimal effect on the polarization at room temperature and 80ºC. At elevated temperature, the top of the hysteresis loops becomes rounded due to leakage current. The addition of Bi_2O_3 improved resistivity to enable hysteresis to be measured up to 100ºC, which could not be done in BNKBT88-2.0Bi.

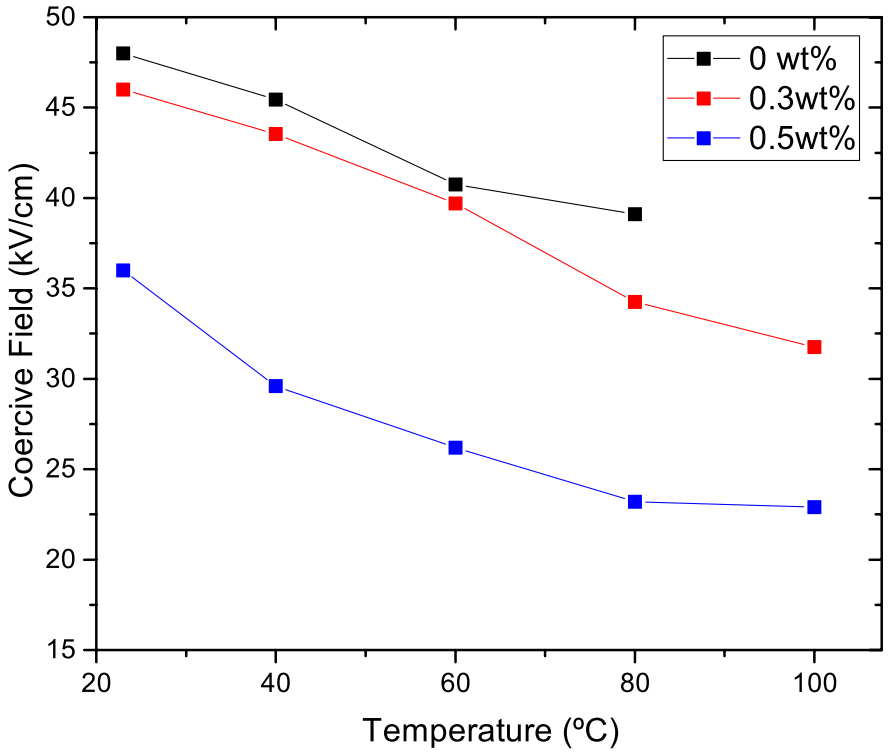

Figure 5.17. Coercive field of bismuth deficient BNKBT88 with Bi_2O_3 addition.

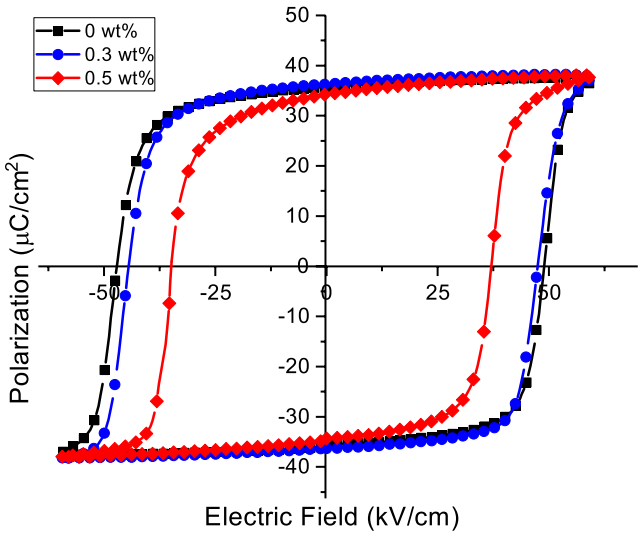

Figure 5.18. Polarization–electric field hysteresis for bismuth deficient BNKBT88 with Bi_2O_3 addition. There is a small decrease in coercive field for the addition of 0.3 wt% bismuth oxide. The addition of bismuth oxide has minimal effect on the polarization.

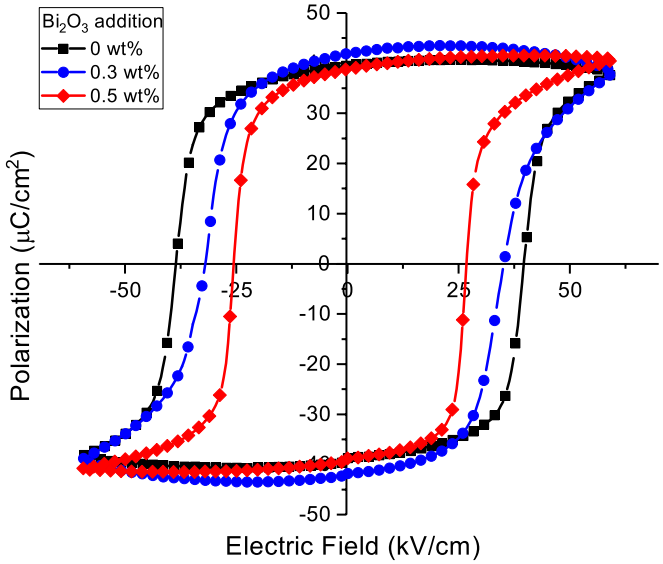

Figure 5.19. Polarization–electric field hysteresis for bismuth deficient BNKBT88 with Bi_2O_3 addition measured at 80ºC. At elevated temperature there is increased leakage current resulting in the rounding of the top of the hysteresis loop.

Permittivity and dielectric loss was measured from room temperature to 300ºC for the stoichiometric, Bi-deficient, and Bi-deficient with Bi_2O_3 added compositions, shown in Figure 5.20. The addition of bismuth oxide to the Bi-deficient compositions was able to suppress the conductivity at elevated temperature. The depolarization temperature is similar to the stoichiometric composition and the dielectric loss is lower up to 125ºC. After depolarization, the dielectric loss is flat up to 250ºC.

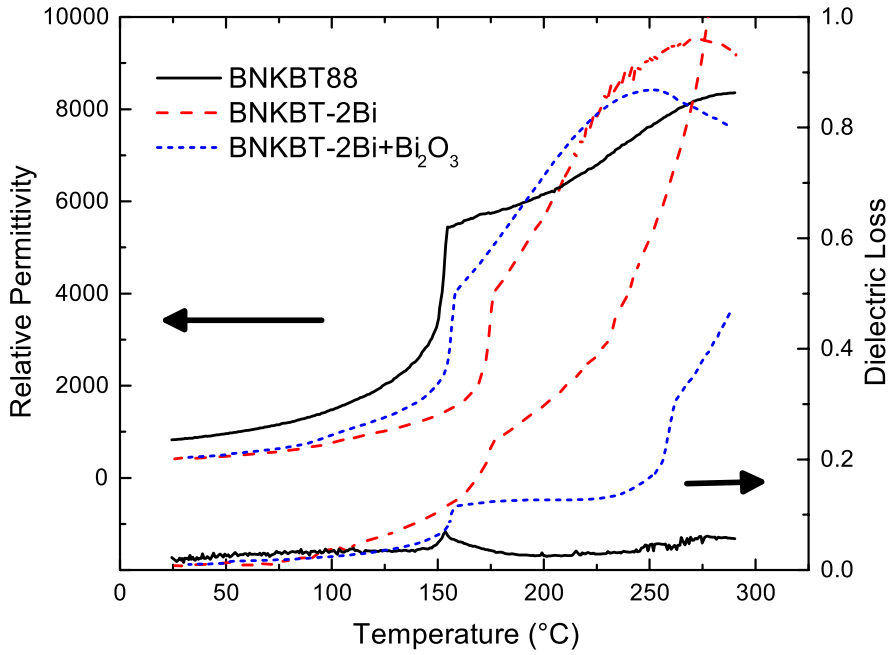

Figure 5.20. Relative permittivity and dielectric loss during heating for the stoichiometric, Bi-deficient, and Bi-deficient with Bi_2O_3 added compositions. BNKBT88-2.0Bi has the highest depolarization temperature but dielectric loss rapidly increases at high temperature.

The amount of bismuth oxide added to the Bi-deficient composition is not enough to fill all of the Bi-vacancies. An addition of 0.5 wt% Bi_2O_3 to BNKBT88-2.0Bi would have an overall formula of $0.88Bi_{0.485}Na_{0.50}TiO_3 – 0.08Bi_{0.485}K_{0.50}TiO_3 – 0.04BaTiO_3$.

The bismuth deficient composition with 1.5% Bi deficiency (without Bi_2O_3 added) has the same overall formula and is among the compositions studied in Table 5.5. The difference between properties shows that the addition of Bi_2O_3 to the bismuth deficient BNKBT88 has a unique effect that is different from the Bi-deficient composition with the same overall stoichiometry. A portion of the added bismuth oxide likely remains at the grain boundaries, improving electrical resistivity while preserving hard properties.

The samples are fully saturated by applying 100V/cm for 12 hours at 220ºC. DC conductivity was measured for Bi-deficient BNKBT88 and with Bi_2O_3 addition. The pristine samples have high resistivity; however the resistivity slowly decreases as an electric field of 100V/cm is applied. When the electric field as applied at room temperature, the current passing through the samples continues to increase for longer than 48 hours. The resistivity decreases faster when the samples are heated. A constant current could be achieved by applying the electric field at elevated temperature. Holding the samples under electric field for 12 hours at 220ºC stabilizes the current and resistivity can be calculated at any temperature. Applied electric field causes the defects to move within the sample, which increases current. The current-voltage behavior for Bi-deficient BNKBT88 with Bi_2O_3 addition is shown in Figure 5.21. There is greater current with forward bias showing diode-like behavior of a p-n junction. The resistivity in the forward direction is 2 orders of magnitude greater than with reverse bias. The application of electric field at elevated temperature turned the ceramics to a dark color due to the formation and mobility of defects.

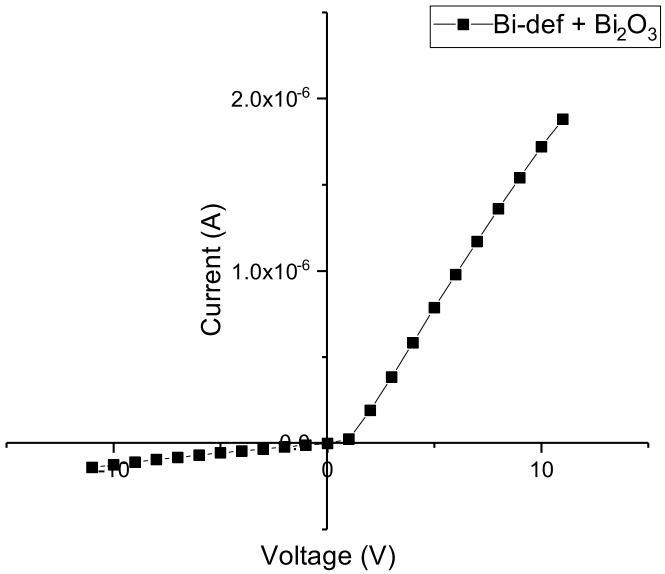

Figure 5.21. Current-voltage behavior for Bi-deficient BNKBT88 at 80ºC has higher current for forward bias. The behavior resulting from defects is similar to a diode.

The temperature dependence of DC resistivity at a forward bias field of 100V/cm for different amounts of Bi_2O_3 addition is shown in Figure 5.22. The difference in DC resistivity for forward bias between Bi-deficient and stoichiometric BNKBT88 is five orders of magnitude at room temperature. Bismuth oxide addition improved DC resistivity, but is more significant at room temperature. Above 100ºC, the resistivity of Bi-deficient BNKBT88-2.0Bi is not affected by Bi_2O_3 addition. Excess bismuth oxide is added after calcination and is not sufficient to fill in all of the vacant Bi^{3+} sites induced by non-stoichiometry. Below 100ºC, the DC resistivity may have greater influence from grain boundary while at elevated temperature is dependent on the bulk concentration of Bi-vacancies.

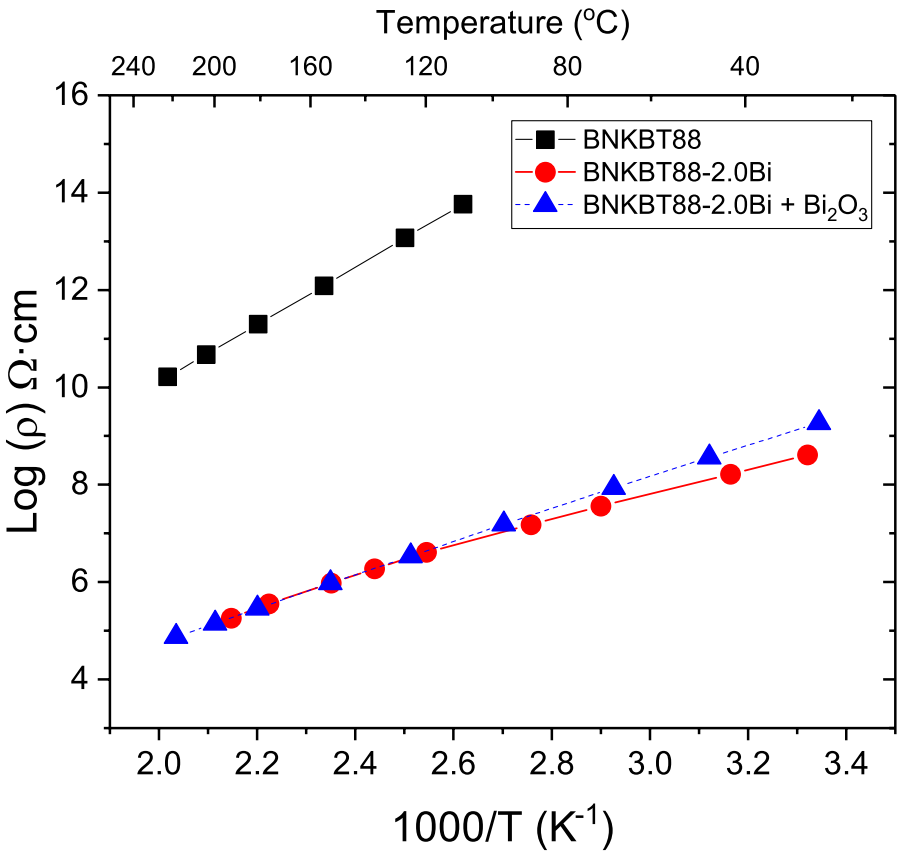

Figure 5.22. DC resistivity at 100V/cm for stoichiometric, Bi-deficient, and Bi-deficient with 0.5 wt% Bi_2O_3 addition. At temperature below 100ºC, bismuth oxide addition improves resistivity.

5.3.5 Low temperature sintering of Bi-deficient ceramics

The non-stoichiometric compositions with Bi-deficiency and alkali deficient were attempted to sinter at low temperature using the combination of additives discussed in previous chapter. At 900ºC, densification occurred rapidly in the Bi-deficient samples, which is the reason why they were used in the copper co-fired experiments. A characteristic of Bi-deficiency in BNT ceramics is large grain growth and oxygen vacancies promote diffusion. On the other hand, in BNT ceramics Na deficiency results in small grains due to defect complexes inhibiting grain growth. In the alkali deficient

BNKBT88 there was no densification and the pellets remained at their green body density of approximately 60% relative density. Mass dropped slightly after sintering, likely due to evolution of CO_2 from the sintering aids or volatilization of Bi_2O_3.

The properties of Bi-deficient BNKBT88-2.0Bi sintered at 900ºC in air and low PO_2 using the additives 0.2wt% Bi_2O_3, 0.2wt% CuO, 0.4wt% ZnO, 0.15wt% Li_2CO_3, and 0.07wt% B_2O_3 are listed in Table 5.7. The sintering aid composition contains Bi_2O_3 that is expected to influence conductivity of the ceramic. It is difficult to conclude the effect of the Bi_2O_3 because of the other components of the sintering aid composition. At 900ºC, the mechanical quality factor is 775 for air firing and drops to 480 for low PO_2.

The differences due to firing atmosphere are thought to be from the transformation of cupric oxide to cuprous oxide. Acceptor doping by the Cu^{2+} ion was not suspected to occur in the unmodified BNKBT88 when fired in air, however that may not be the case in bismuth deficient composition. The polarization-electric field hysteresis for the bismuth deficient ceramics sintered at 900ºC are shown in Figure 5.23. Coercive field is reduced compared to BNKBT88-2.0 fired at 1150ºC when fired at low temperature using sintering additives. The coercive of BNKBT88-2.0Bi sintered at 900ºC in air is slightly higher compared to firing in controlled oxygen atmosphere. The lower coercive field as well as decreased mechanical quality factor may indicate that Cu^{2+} has a hardening effect when sintered at 900ºC in air that does not occur from Cu^{1+} in controlled oxygen atmosphere. However, due to the number of components in the sintering additive and the different effect that each one could have in air or low PO_2, it is not possible to be certain of the effect of Cu oxidation on the properties.

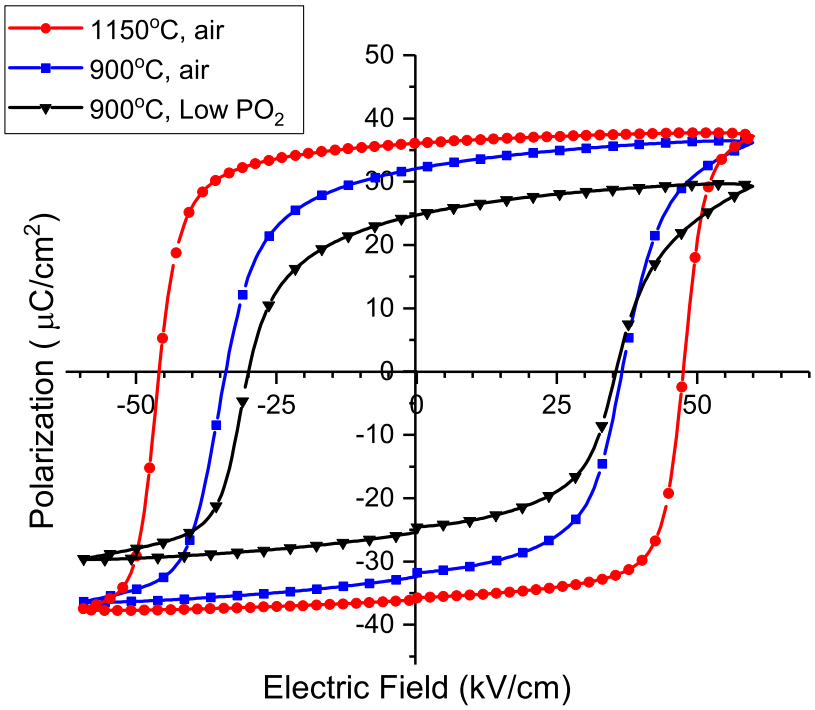

Figure 5.23. Polarization–electric field hysteresis of BNKBT88-2.0Bi sintered at different temperature and atmospheres. The coercive field decreases when sintered at 900ºC using additives.

Table 5.7. Piezoelectric properties of Bi-deficient BNKBT88 sintered at 1150 and 900ºC.

Conditions	d_{33} (pC/N)	k_p	ε_r	Q_m	T_d (ºC)
1150ºC, air	104	0.193	425	1200	178
900ºC, air	110	0.180	700	775	125
900ºC, low PO_2	105	0.200	700	480	142

5.4 Conclusion

Non-stoichiometry is a method to alter the piezoelectric properties that is unique to BNT based piezoelectric ceramics. Non-stoichiometry has been studied in BNT and the binary systems BNT-BT and BNT-BKT. In BNKBT88, bismuth deficiency makes the ceramics hard, which is desired for use in high power transducers or piezoelectric transformers. The mechanical quality factor of 1200 for BNKBT88-2.0Bi is comparable to hard PZT. Na and K deficiency decreased T_d to make the ceramic antiferroelectric at room temperature with very large strain. The oxygen vacancies induced by non-stoichiometry increase the conductivity of the ceramic making poling difficult. However, this may enable BNT based ceramics to be used as an oxygen conductor in fuel cells.

Increased conductivity due to oxygen vacancies limits the use of bismuth deficient ceramics at elevated temperature. A small addition of Bi_2O_3 to the Bi-deficient composition is able to improve resistivity and had a large effect on piezoelectric, ferroelectric, and electrical properties. Improvement to DC resistivity was greatest at lower temperature, and was effective for improving poling. However, the addition of bismuth oxide did not have an effect on DC resistivity at temperatures over 100ºC. Overall, the amount of bismuth oxide addition in this study is relatively minimal. The highest amount of Bi_2O_3 addition, 0.5 wt%, is not enough to fill the Bi-vacancies of the calcined Bi-deficient powder. Further study is needed to determine how the addition of Bi_2O_3 affects overall stoichiometry and microstructure in Bi-deficient ceramics.

X-ray diffraction was able to analyze the structure of nonstoichiometric compositions of 0.88BNT-0.08BKT-0.04BT. The composition with sodium and potassium deficiency and the composition with bismuth excess both had a nearly cubic structure, which can explain their poor piezoelectric properties. The composition with sodium and potassium excess and the composition with bismuth deficiency had similar morphotropic phase boundary structure to the stoichiometric composition BNKBT88. Overall, nonstoichiometry in BNKBT88+2Bi and BNKBT88-2(Na,K) modified their crystal structure, making them more cubic, which affected their piezoelectric properties, while the nonstoichiometry in BNKBT88-2Bi and BNKBT88+2(Na,K) induced defects that affect the piezoelectric domains and properties but did not affect crystal structure.

References

[1] Y. Hiruma, H. Nagata, and T. Takenaka, “Phase Transition Temperatures and Piezoelectric Properties of (Bi1/2Na1/2)TiO3–(Bi1/2K1/2)TiO3–BaTiO3 Lead-Free Piezoelectric Ceramics,” *Jpn. J. Appl. Phys.*, vol. 45, pp. 7409–7412, 2006.

[2] S. Zhang, T. R. Shrout, H. Nagata, Y. Hiruma, and T. Takenaka, “Piezoelectric Properties in (K0.5Bi0.5)TiO3-(Na0.5Bi0.5)TiO3-BaTiO3 Lead-Free Ceramics,” *Ieee Trans. Ultrason. Ferroelectr. Freq. Control*, vol. 54, no. 5, pp. 910–917, 2007.

[3] J.-F. Trelcat, C. Courtois, M. Rguiti, A. Leriche, P.-H. Duvigneaud, and T. Segato, “Morphotropic phase boundary in the BNT–BT–BKT system,” *Ceram. Int.*, vol. 38, pp. 2823–2827, 2012.

[4] X. X. Wang, X. G. Tang, K. W. Kwok, H. L. W. Chan, and C. L. Choy, “Effect of excess Bi2O3 on the electrical properties and microstructure of (Bi1/2Na1/2)TiO3 ceramics,” *Appl. Phys. A*, vol. 80, pp. 1071–1075, 2005.

[5] S. Prasertpalichat, W. Schmidt, and D. P. Cann, “Effects of A-site nonstoichiometry on oxide ion conduction in 0.94Bi0.5Na0.5TiO3–0.06BaTiO3 ceramics,” *J. Adv. Dielectr.*, vol. 6, no. 2, p. 1650012, 2016.

[6] Y. S. Sung and M. H. Kim, “Nonstoichiometry in (Bi0.5Na0.5)TiO3 Ceramics,” in *Lead-Free Piezoelectrics*, 2012, pp. 353–370.

[7] Y. S. Sung *et al.*, “Effects of Na nonstoichiometry in (Bi0.5Na0.5+x)TiO3 ceramics,” *Appl. Phys. Lett.*, vol. 96, p. 022901, 2010.

[8] Y. S. Sung, J. M. Kim, J. H. Cho, T. K. Song, M. H. Kim, and T. G. Park, “Effects of Bi nonstoichiometry in (Bi0.5+xNa)TiO3 ceramics,” *Appl. Phys. Lett.*, vol. 98, p. 012902, 2011.

[9] B. Jaffe, W. R. Cook, and H. Jaffe, *Piezoelectric Ceramics*. New York: Academic Press, 1971.

[10] E. Taghaddos, M. Hejazi, and A. Safari, “Electromechanical Properties of Acceptor-Doped Lead-Free Piezoelectric Ceramics,” *J. Am. Ceram. Soc.*, vol. 97, no. 6, pp. 1756–1762, 2014.

[11] M. Hejazi, E. Taghaddos, E. Gurdal, K. Uchino, and A. Safari, “High Power Performance of Manganese-Doped BNT-Based Pb-Free Piezoelectric Ceramics,” *J Am Ceram Soc*, vol. 97, no. 10, pp. 3192–3196, 2014.

[12] J. Rodel, K. G. Webber, R. Dittmer, W. Jo, M. Kimura, and D. Damjanovic, “Transferring lead-free piezoelectric ceramics into application,” *J. Eur. Ceram. Soc.*, vol. 35, pp. 1659–1681, 2015.

[13] Q. Xu, Y.-H. Huang, M. Chen, W. Chen, B.-H. Kim, and B.-K. Ahn, “Effect of bismuth deficiency on structure and electrical properties of (Na0.5Bi0.5)0.93Ba0.07TiO3 ceramics,” *J. Phys. Chem. Solids*, vol. 69, pp. 1996–2003, 2008.

[14] M. Li, H. Zhang, S. N. Cook, L. Li, J. A. Kilner, and I. M. Reaney, “Dramatic Influence of A-Site Nonstoichiometry on the Electrical Conductivity and Conduction Mechanisms in the Perovskite Oxide Na0.5Bi0.5TiO3,” *Chem. Mater.*, vol. 27, pp. 629–634, 2015.

[15] M. Li *et al.*, “A family of oxide ion conductors based on the ferroelectric perovskite Na0.5Bi0.5TiO3,” *Nat. Mater.*, vol. 13, pp. 31–35, 2014.
[16] ASTM Standard D257 − 14, “Standard Test Methods for DC Resistance or Conductance of Insulating Materials.” .
[17] S.-T. Zhang, A. B. Kounga, E. Aulbach, H. Ehrenberg, and J. Rodel, “Giant strain in lead-free piezoceramics Bi0.5Na0.5TiO3–BaTiO3–K0.5Na0.5NbO3 system,” *Appl. Phys. Lett.*, vol. 91, p. 112906, 2007.
[18] Y. Guo, M. Gu, Y. Luo, and R. L. Withers, “Composition-induced antiferroelectric phase and giant strain in lead-free (Nay,Biz)Ti1−xO3(1−x)-xBaTiO3 ceramics,” *Phys. Rev. B*, vol. 83, p. 054118, 2011.
[19] G. Dong, H. Fan, J. Shi, and M. Li, “Composition- and Temperature-Dependent Large Strain in (1 – x) (0.8Bi0.5Na0.5TiO3–0.2Bi0.5K0.5TiO3)– xNaNbO3 Ceramics,” *J Am Ceram Soc*, vol. 98, no. 4, pp. 1150–1155, 2015.
[20] G. Picht, J. Topfer, and E. Hennig, “Structural properties of (Bi0.5Na0.5)1−xBaxTiO3 lead-free piezoelectric ceramics,” *J. Eur. Ceram. Soc.*, vol. 30, pp. 3445–3453, 2010.

6. Piezoelectric energy harvesting

6.1 Introduction

Composite transducers use piezoelectric ceramics with different materials such as polymers or metals to enhance piezoelectric sensing or actuation. These devices may use a combination of d_{33} and d_{31} modes. There are many different composite transducer designs that enhance piezoelectric properties or alter mechanical properties to enable use in applications that cannot be achieved in single phase material [1]. Composite transducers may be flexible, such as piezoelectric fibers in a polymer matrix that can bend or conform to a curved surface [2][3].

Multilayer actuators (MLA) or stack actuators consist of stacked piezoelectric layers connected in parallel. The piezoelectric layers are bonded using epoxy or co-fired with internal electrodes. The conductors between the ceramic segments of the actuator are connected together in a parallel configuration. When an electric field is applied, all of the segments expand or contract in the same longitudinal direction, utilizing the d_{33} coefficient. The parallel electrode connection is made using a conductor applied to the side of the actuator. Two electrode configurations of the multilayer actuator are shown in Figure 6.1 [4]. The plate-through electrodes require an insulating layer on each electrode to prevent a short circuit. The insulating layer is not needed in the interdigital configuration because the electrodes do not fully penetrate the actuator, however this results in an inactive volume [4]. Reduced thickness of each layer requires lower driving voltage in actuator applications and the d_{33} piezoelectric coefficient of each layer is additive.

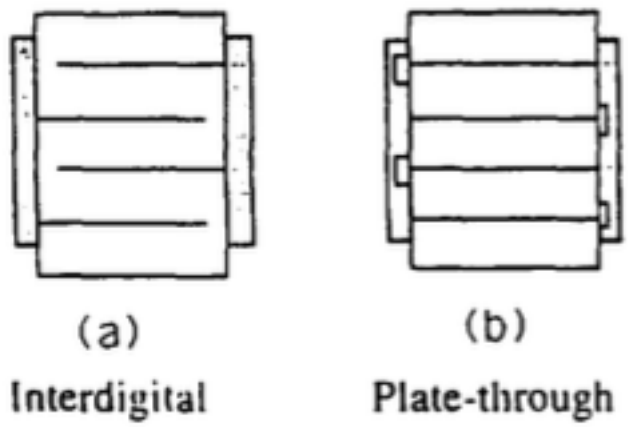

Figure 6.1. Multilayer actuators with different electrode configurations. Each section is connected in parallel on the side of the actuator. The plate-through electrode has an insulating layer on each electrode [4].

Composite transducer designs can enable enhanced energy density through pre-stress like in the THUNDER transducer. The unique design of the THUNDER allows the vertical displacement of the transducer to utilize the longitudinal piezoelectric coefficient [5][6]. The thin-layer composite uniform ferroelectric driver and sensor, or THUNDER shown in Figure 6.2, is made using a thin PZT wafer which is bonded to aluminum sheets at high temperature with a polyimide adhesive [7]. After the layers are bonded, a difference in the thermal expansion of the materials in the THUNDER warps the transducer in the 3-direction. When loaded, the THUNDER flattens, causing stress in the 1-direction of the PZT. This allows the transducer to operate in the 3-direction using the d_{31} coefficient. The THUNDER transducer was used for piezoelectric energy harvesting from walking when placed in the heel of a shoe [8]. Energy was generated from the heel strike that would flatten the transducer with each step.

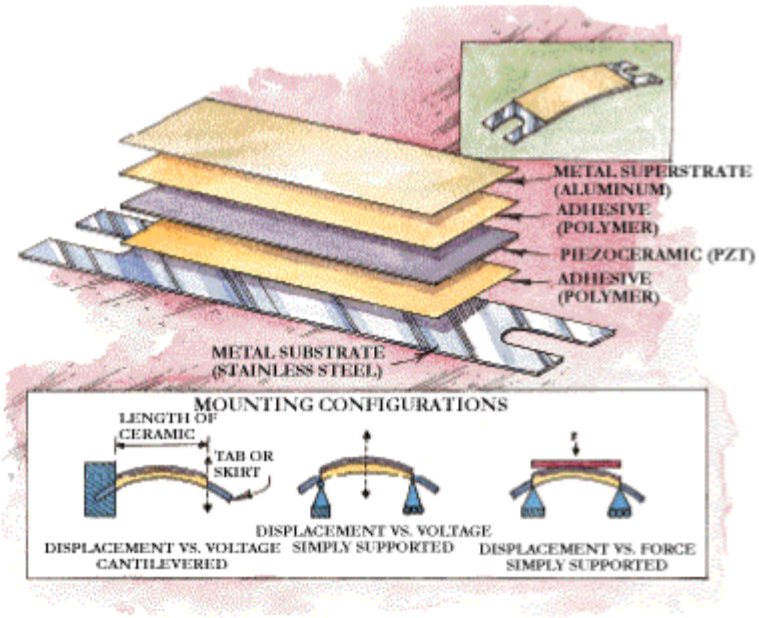

Figure 6.2. Thin-layer composite unimorph ferroelectric driver and sensor (THUNDER). The different thermal expansion of the metal layers induces pre-stress and warping in the PZT layer [6].

The cymbal transducer, or the rectangular version called a "bridge", has metal end caps that amplify the applied force and converts the stress to compression and tension in piezoelectric ceramic [9][10]. The cymbal transducer shown in Figure 6.3 has metal end caps bonded to the ceramic using epoxy. The cymbal or bridge designs use a combination of d_{33} and d_{31} piezoelectric coefficients for the applied compression and tension, respectively. Cymbal transducers have been studied for use in vibrational energy harvesting under cyclical loading and high stress [11][12].

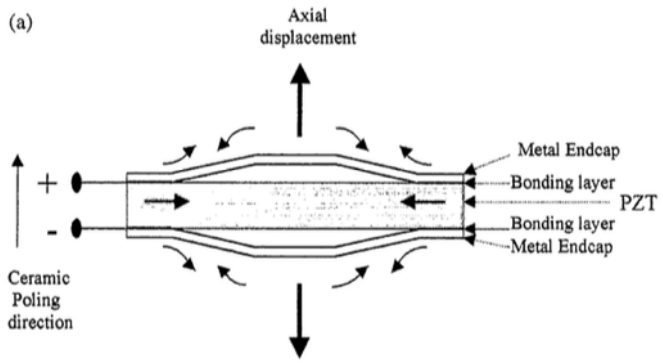

Figure 6.3. The cymbal transducer has conical metal end caps bonded to a PZT disc. The end caps amplify stress and displacement [10].

A bimorph is a composite piezoelectric transducer made from two thin piezoelectric wafers bonded to the top and bottom of a flexible metal shim [13]. The bimorph shown in Figure 6.4 is fixed at the base and a mass is placed on the end of a beam. The beam length and the mass of the counterweight determines the resonant frequency which must be matched to a vibrational energy source [14][15]. Mechanical vibrations at the resonant frequency of the bimorph can be transformed into useable electrical energy via the piezoelectric effect [16].

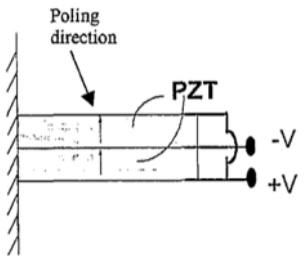

Figure 6.4. The bimorph cantilever is fixed at one end and has 2 layers of PZT bonded to a metal shim.[15]

Equipment or machinery with a known constant vibrational frequency is an excellent source of mechanical input energy for a bimorph cantilever. Energy harvesters have been developed for powering sensors and wireless nodes using vibrations [17]. Tuned energy harvesting devices are only able to operate within a narrow range near their resonant frequency. However, some designs for broadband piezoelectric energy harvesting devices use a cantilever with multiple resonant frequencies [18]. This enables use of a wide range vibrational frequencies but suffers from limited performance for low frequency and non-resonant sources such as cyclic impacts or intermittent pulses [19].

A source of unused mechanical energy is vehicle induced loading on pavement [20]. Energy which would normally be dissipated into heat from the stress and strain resulting from vehicle loading on the pavement can be harvested using piezoelectricity

[21]. The stress induced in the pavement from a truck's tire is shown in Figure 6.5 and the energy harvesting transducer would be embedded in the pavement below the surface. A study by Zhao et al compared the performance of different types piezoelectric transducers for pavement energy harvesting [22]. It was found that matching the stiffness of the transducer to the asphalt pavement was necessary to facilitate the transfer of strain energy into the transducer. The mismatch between the elastic modulus of PZT and asphalt pavement is large. The elastic modulus of PZT is as high as 130 GPa while asphalt is between 1 and 4 GPa [20]. The stiffness of a composite transducer can vary depending on the design. The transducers with the highest stiffness are monolithic ceramic and multilayer or stack actuators. The energy harvesting performance of these transducers when embedded in pavement is poor because strain is not transferred to the stiff transducer but into the surrounding and underlying pavement instead. The result is poor mechanical coupling between the pavement and the transducer. Low stiffness composite transducers like THUNDER have a high energy density due to pre-stress while macrofiber composites are flexible, with a wide range of motion. The low stiffness and flexibility of these transducers prevents them from effectively generating energy from vehicle induced loading on pavement. The strain in the pavement can only induce a small stress in the transducer due to their low stiffness and minimal energy can be generated.

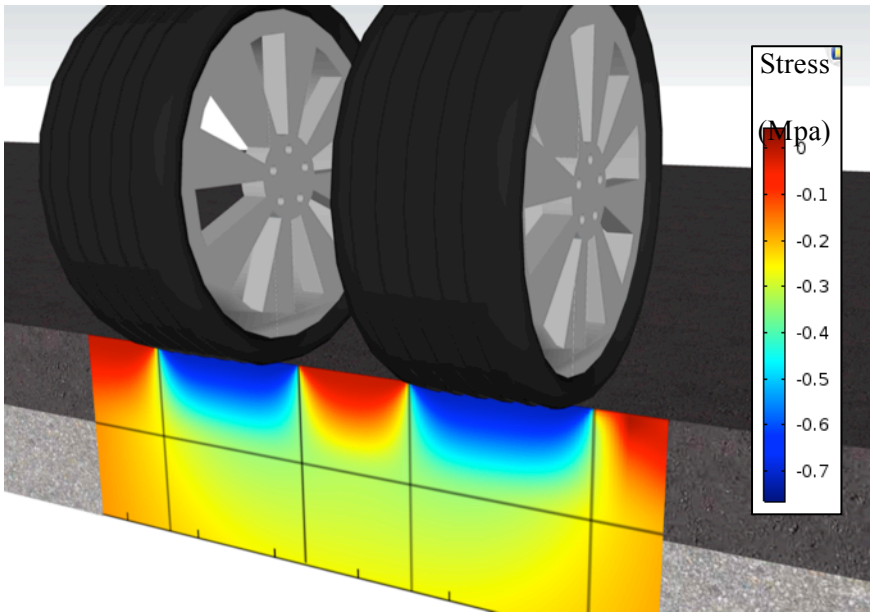

Figure 6.5. Stress in pavement resulting from a truck's dual tire load. The tires exert a pressure of 0.7MPa to the road surface.

The cymbal, and its rectangular version, the bridge transducer, can be matched to the stiffness of the asphalt pavement by the shape and material of the metal end cap [23][10][24]. When the elastic moduli of the transducer and the pavement are matched there is mechanical coupling between the pavement and the transducer and the strain developed from vehicle loading is transferred into the transducer.

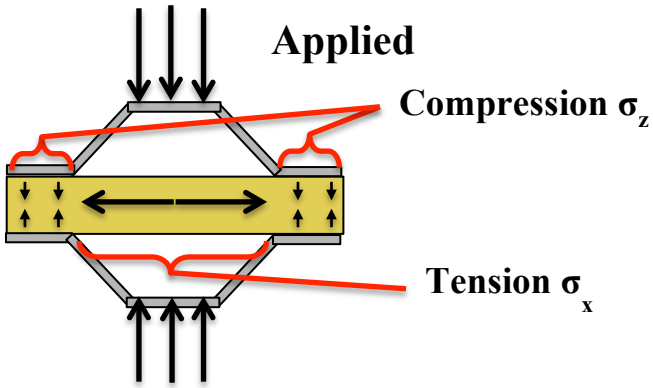

Figure 6.6. The cavity region below the end caps is in tension and the outer region is in compression due to the applied force at the end caps.

The stress acting on the ceramic on the bridge transducer can be divided into 3 regions: the outer region which is compressed, the inner region under tension, and the bonding region where the metal end caps contact the ceramic [22]. Tension and compression are distributed in the ceramic in the inner and outer regions respectively, shown in Figure 6.6. The angle between the end cap and the ceramic results in the majority of the stress acting in the horizontal direction as tension and is much larger than the compression in the outer region. The stress at the contact point between the end cap and ceramic is very large and can potentially exceed the yield stress of the ceramic, causing failure [25]. The end cap material, shape and angle should be chosen to maximize the tensile stress without exceeding the yield stress of the ceramic.

6.2 Experimental

6.2.1 Ceramic selection

In piezoelectric energy harvesting, the piezoelectric ceramic acts as a charge generator. The charge is produced via the direct piezoelectric effect. The amount of energy produced by the transducer is determined by the charge generated and the capacitance. The voltage generated is equal to the change generated divided by the capacitance shown in equation 1.

$$V = \frac{Q}{C} = \frac{F d_{33}}{\varepsilon_o \varepsilon_r} \frac{d}{A} \qquad (1)$$

The desirable piezoelectric properties for energy harvesting are high d_{33} and high permittivity. The high d_{33} means more charge will be generated for a given amount of force applied to the ceramics. A large amount of charge can be generated by the

piezoelectric ceramic, which generates voltage. The voltage is higher when the capacitance is low.

The amount of energy stored in the piezoelectric is given by the equation for energy of a capacitor. The stored electrical energy can be calculated using equation 2,

$$E = \frac{1}{2}CV_0^2 = \frac{1}{2}\frac{Q^2}{C} \quad (2)$$

where Vo is the open circuit voltage. According to equation 2, the amount of stored electrical energy is be maximized when voltage is high. Thus for a given amount of charge, more energy can be stored when capacitance is low. However, equation 2 only refers to the stored electrical energy that does not correspond to useable energy. At high output voltage, it is difficult to efficiently use the stored energy because it has high impedance. It is possible to step down the voltage, however energy is lost in the conversion. A higher capacitance will increase the useable energy.

The output energy of the transducer is related to the electrical load in the circuit. In Figure 6.7, the relationship between charge, voltage, and output electrical energy is shown assuming a linear relationship [22]. The area beneath the curve represents the stored electrical energy, while the area of the shaded region is the useable, or output electrical energy. The maximum output energy occurs when voltage is equal to half of the open circuit voltage, which is determined by the impedance of the circuit. Here V_{oc} is the open circuit voltage and Q_s is the short circuit charge. The output electrical energy, U_{out}=1/2QV is shown as the shaded rectangular region beneath the line connecting V_{oc} and Q_s. There are 2 points where the output electrical energy is zero: V_{oc} and Q_s. At V_{oc} there is voltage but no current and for Q_s there is charge but no voltage to move the

charge. The maximum output energy occurs where the shaded area is largest: at $Q=1/2Q_s$ and $V=1/2V_{oc}$. Maximum useable energy is

$$U = (0.5)(0.5)Q_s V_{OC} \quad (3)$$

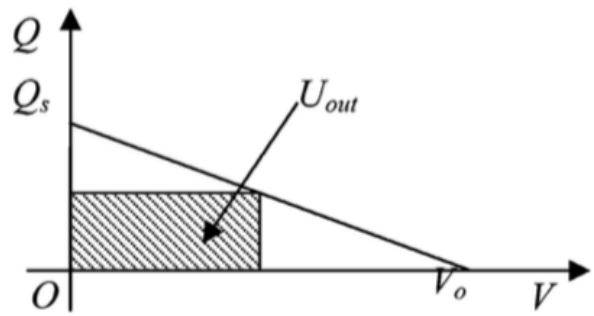

Figure 6.7. Relationship between charge, voltage, and output electrical energy [22].

The energy generated by the transducer is efficiently used when the electrical load results in the circuit operating at half of the open circuit voltage. The open circuit voltage is determined by the charge generated via the piezoelectric effect and the capacitance of the transducer, as given by the equation:

$$V = \frac{Q}{C} = \frac{A_{inner}\sigma_x d_{33} + A_{outer}\sigma_z d_{31}}{C} \quad (4)$$

Increasing the generated charge with no increase in capacitance causes the voltage to surge because the transducer lacks the capacitance necessary to store the charge. The amount of stored energy is high but cannot be used it efficiently without the loss of a large amount of energy. Efficient use of the output energy can be achieved by using impedance matching circuits or inverters but these reduce efficiency through losses in the circuits. Increasing the capacitance or permittivity of the transducers is the best way to efficiently use the output energy.

In order to use the electrical output at lower resistive load, the voltage can be stepped down using a transformer. An AC transformer, such as the devices used to step down high voltage power lines to for residential use, have primary and secondary coils of wire wrapped around an iron core. AC-AC transformers that convert an AC input to AC output at a lower voltage are not suitable for small-scale energy harvesting due to the high loss because the frequency is too low for efficient conversion. DC-DC step down converters with greater efficiency can be used instead [26].

Table 6.1. d_{33} and permittivity for various piezoelectric ceramics. The capacitance, voltage, and stored electrical energy E for a 32x32x2mm plate are calculated.

Material	ε_r	d_{33}(pC/N)	C (nF)	V	E (mJ)
PZT-5X[1]	4500	750	20.4	83	0.07
PZT5H[2]	3400	620	15.4	86	0.06
PZT5A[2]	1800	410	8.2	114	0.05
PZT4[2]	1400	315	6.3	109	0.04
$BaTiO_3$ [27]	1420	135	6.4	45	0.01
BNT based [27]	1000	180	4.5	72	0.01
Textured KNN-LT-LS [28]	1570	416	7.1	115	0.05

[1]Sinocera (College Park, PA), [2]Morgan Technical Ceramics

Table 6.1 lists d_{33} and relative permittivity for various piezoelectric ceramic compositions and the calculated capacitance, voltage, and stored electrical energy for a 32x32x2mm square plate with the top and bottom electrode. Among all PZT compositions, PZT-5X and PZT5H have high piezoelectric coefficient and high permittivity. PMN-PT has the highest d_{33} and permittivity among the ceramics considered but it has lower mechanical strength. Compared to lead based piezoceramics, the lead free compositions have significantly lowered properties. Barium titanate as well as BNT based ceramics have significantly lower d_{33} and permittivity that limits the amount of

energy that can be generated. The textured KNN-LT-LS would be an excellent lead-free alternative to be used in the transducer due to its similar permittivity and d_{33} as PZT5A. However, all KNN-LT-LS are not available commercially and the results of their study have not been reproduced as of today by any other researcher.

6.2.2 Electrode pattern and poling

In a disc ceramic, the top and bottom surfaces of the ceramic disc or plate are electroded as shown in Figure 6.8a. The ceramic is then poled under a high electric field at elevated temperature in a silicone oil bath to prevent electrical arcing. The magnitude of the applied electric field required for poling is specific to each piezoelectric composition but 2 kV/mm is sufficient for soft PZT. For example, a 2 mm thick ceramic placed in an oil bath at 90ºC would require 4 kV. Figure 6.8a represents a schematic drawing of poling a ceramic plate or disc through a thickness of a few millimeters, which is easily accomplished. However, it is difficult to polarize along the length of the ceramic (Figure 6.8b). Poling a 32 mm ceramic along its length with an electric field of 2 kV/mm would require an applied 64 kV. At very high voltage, the presence of defects in the ceramic such as inhomogeneity, porosity, internal cracks in the ceramic can lead to dielectric breakdown and failure. The effect is multiplied by the thickness and length of the samples. The ceramic can be effectively poled by horizontally continuous poling or by sectioning the ceramic into multiple smaller segments as shown in Figure 6.8c [29]. The segments can be poled simultaneously at lower voltage using a parallel connection.

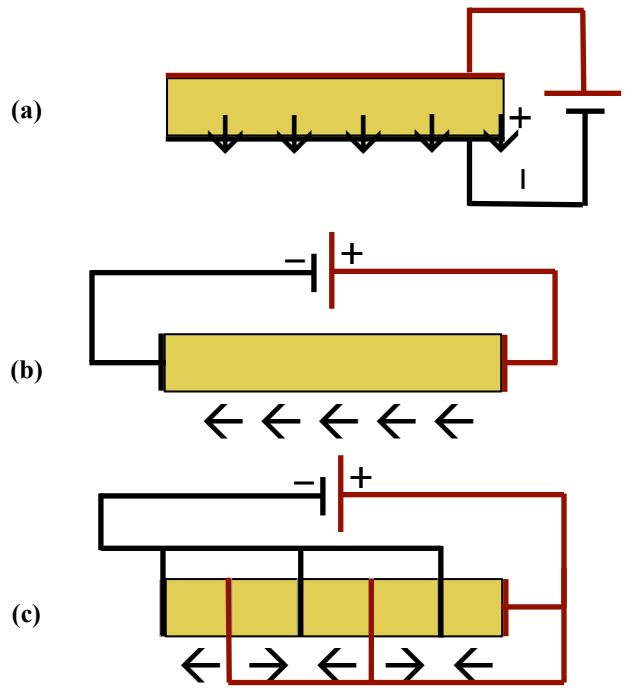

Figure 6.8. Polarization direction and electrode connections of the ceramic in a cymbal or bridge transducer. (a) Conventional poling direction, (b) horizontal poling direction, and (c) horizontal segment poling.

Poling of the segments of the ceramic can be accomplished using surface electrodes for thinner samples. To effectively polarize the electroded ceramic along the length, the internal electric field resulting from the applied electric field at the surface has been analyzed for PZT ribbons and fibers [29]. A PZT ribbon or fiber is drawn through slits in two copper conductors connected to a high voltage power supply. The electric field inside the ceramic can be calculated based on inter-electrode spacing and depth as shown in Figure 6.9. The equation 5 gives the magnitude of the local internal electric field E′ as a function of the inter-electrode spacing 2a and depth r, where E is the applied electric field at the surface [29].

$$E'(a,r) = E\frac{a^3}{(a^2+r^2)^{3/2}} \quad (5)$$

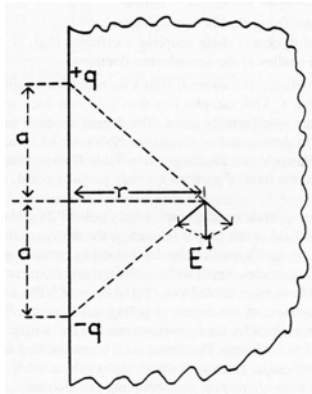

Figure 6.9. The model used for calculating the internal electric field at a depth of r resulting from an electric field applied to the surface. [29]

By utilizing surface electrodes, a single ceramic to be poled along its length while separated electrically into multiple segments, and the thinner segments are easier to pole. This is the method used for poling thin PZT fibers in macrofiber composites using an interdigitated electrode pattern shown in Figure 6.10 [3]. The fiber is poled by the electrodes applied to the surface. The poling direction of the PZT fiber alternates between the electrodes but is always in the horizontal direction. The longitudinal piezoelectric coefficient d_{33} is used along the length of the sample rather than the transverse d_{31} coefficient because poling would be in the same direction as the applied stress for the cymbal design.

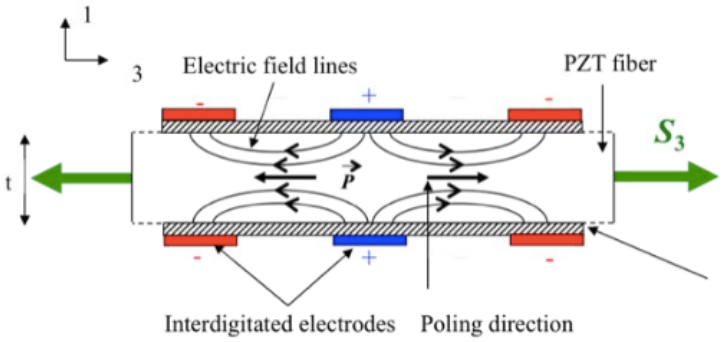

Figure 6.10. Electrode configuration used to pole PZT fibers along their length to utilize the d_{33} coefficient. The electric field penetrates vertically into the fiber to pole in the same direction as the stress, applied along the length of the fiber [3].

Increasing the number of poled segments increases the d_{33} and capacitance of the transducer. The spacing between the surface electrodes and the relative capacitance for a given number of electroded segments on ceramic with the 32mm length are given in

Table 6.2. Because of the parallel connection of the electrodes, the piezoelectric coefficient of each segment is additive so d_{33} is proportional to the number of segments. The capacitance is relative the number of segments squared. Therefore a greater number of segments will have huge benefit in an energy generation due to higher d_{33} and capacitance. However, the ceramic has fixed dimensions and the increasing number of sections causes the inter-electrode spacing to decrease, hence the effective electric field at the center of the ceramic decreases making poling inefficient along the lengths of the segments. However, the capacitance of each segment increases as the inter-electrode spacing decreases, and as the spacing decreases more segment can be added in parallel for further increase of d_{33}.

Table 6.2. Electrode spacing, capacitance, and electric field strength at the central ling along the length of the 32mm length sample.

Number of segments	Number of surface electrodes	Interelectrode Spacing (mm)	Relative Capacitance	Calculated electric field strength at center line along length
1	0	32	1	99%
3	2	10	9	94%
5	4	5.6	25	84%
7	6	3.7	49	68%
9	8	2.7	81	51%
11	10	2	121	35%

The limitation in increasing the number of segments is due to manual application and working space between electrodes. An interelectrode spacing of 5.6mm with 5 is earier to work and may result in more effective poling than a spacing of 2mm with 11 segments. When the interelectrode spacing is small, the electric field does not penetrate as far vertically into the ceramic. The middle section of the ceramic only has a fraction of the electric field applied at the surface. A 32mm ceramic with 10 electrodes (electrode spacing of 2mm) will result to an effective electric field of 0.35E along the centerline. To compensate for the reduced local electric field, the applied field would need to be increased by a factor of 2.8, or approximately 6kV/cm, to effectively polarize the ceramic slab along the length. However, higher applied electric field may cause electric breakdown of the ceramic during poling.

In this work, the number of electrodes and segments for the 32mm length PZT plates was chosen to be 6 and 7 respectively, with an inter-electrode spacing of 3.7mm. With this inter-electrode spacing, the electric field applied in the middle of the ceramic is 68% of the applied electric field applied to the surface.

Poling of the ceramic was first demonstrated using 24mm long bars of PZT. The electrodes were applied to the ceramic using air-dry silver paint. The electrodes are connected in parallel configuration with 22 gauge copper wire that is wrapped securely around the electrode. The first sample is shown in Figure 6.11 with the Berlincourt d_{33} meter during measurement. The PZT was poled along the length of the bar using the copper wires are in a parallel configuration connected to the supply voltage and ground. Measurement of a thin ceramic plate of PZT showed that is has a d_{33} of 350pC/N, while the PZT bar with 3 electroded segments connected in parallel showed a d_{33} of 990pC/N. This method effectively poled the 24mm PZT bar with 3 segments, with an average of 330pC/N per segment.

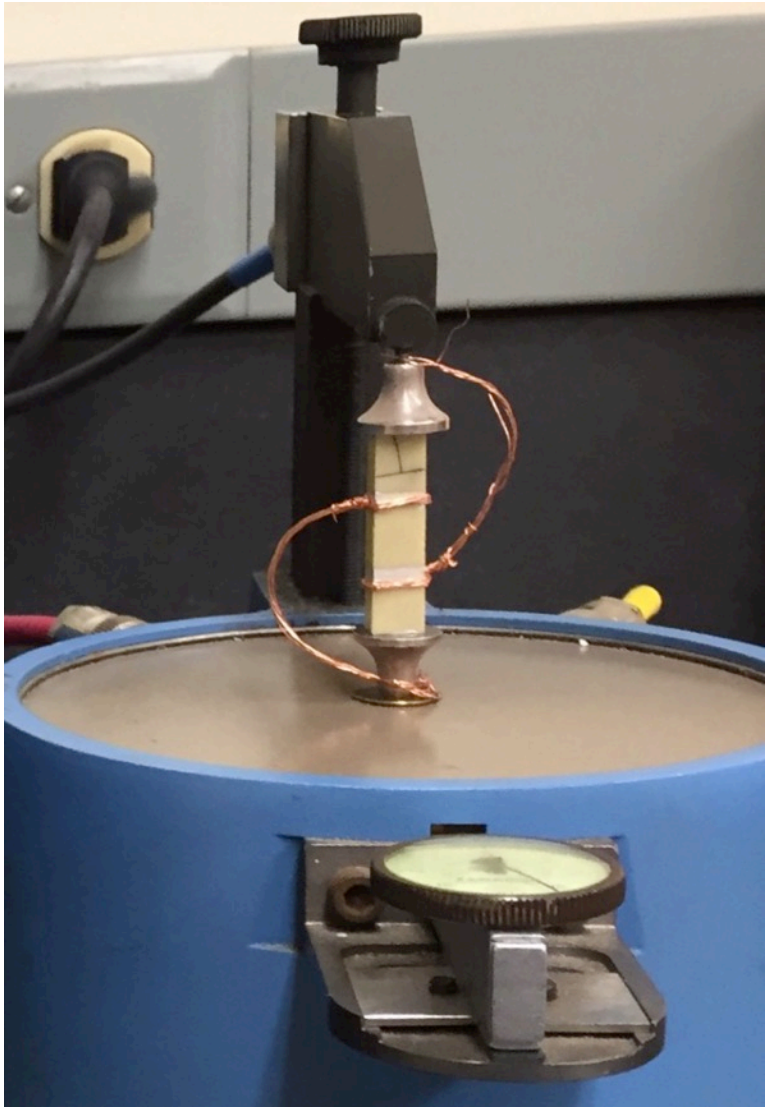

Figure 6.11. Test bar of PZT with 4 electrodes connected in parallel during d_{33} measurement. The copper wires are used to connect the electrodes in parallel.

An alternative electrode pattern shown in Figure 6.12 was tested. The electrodes are connected in parallel using a conductor applied to the edges of the ceramic. A gap is left between the repeating electrodes so that they are separated from the conductor on the edge. This pattern is similar to the pattern of a multilayer actuator where the electrode terminates; leaving an un-polarized section near the edge of the material.

This electrode pattern was carefully applied using air-dry silver paint. Ink was used as a guide to outline the pattern. It was evaluated that the ink does not have any effect on poling. The measured d_{33} was very low utilizing this configuration. It was determined that the conductor on the edge of the ceramic limited the polarization of the ceramic. Samples were poled effectively by removing the conductor from the side and parallel connections were made using wires as show in Figure 6.13.

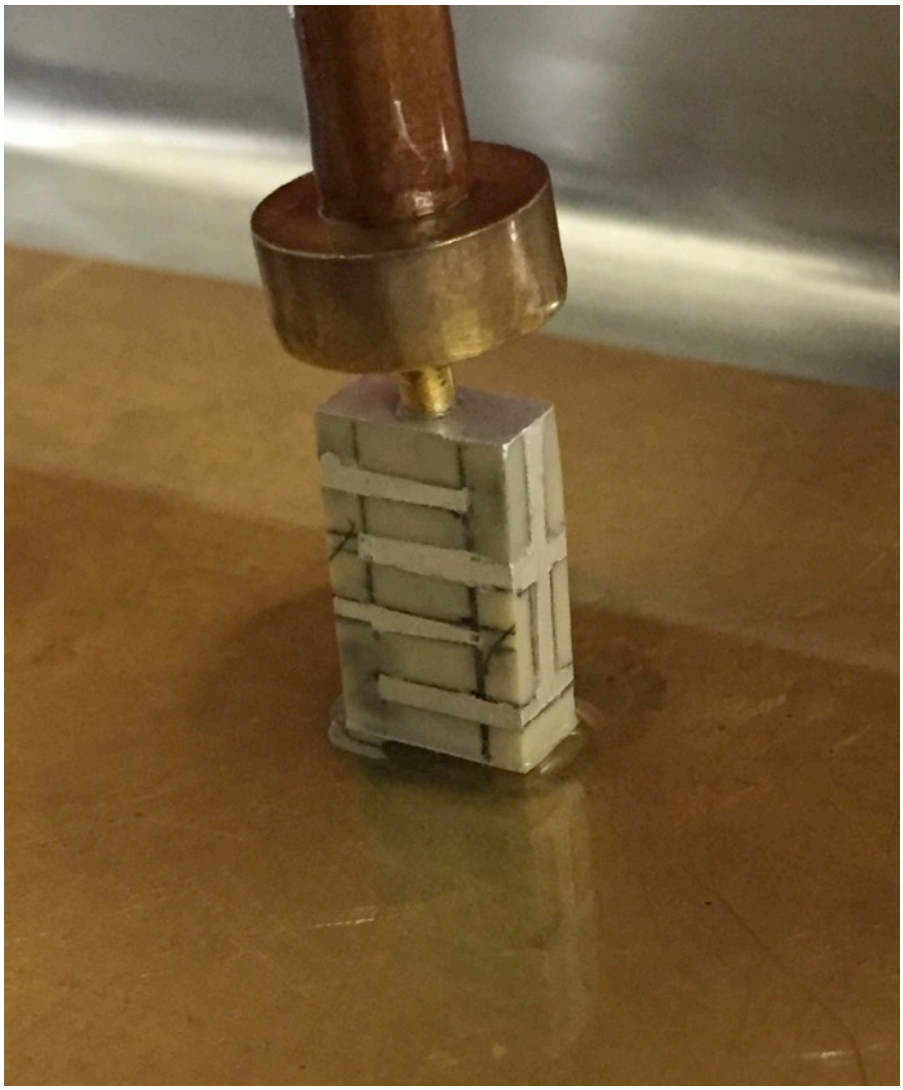

Figure 6.12. Test bar of PZT with an alternative electrode pattern where the electrodes are connected in parallel using air-dry silver paint on the sides. The electrodes do not extend around the ceramic. The PZT did not pole when this pattern was used. The black ink was used as a guide for painting the pattern and did not affect poling.

In another experiment, a larger PZT plate with thickness of 2mm was patterned with 4 surface electrodes and 5 segments with a spacing of about 3.5mm, shown in Figure 6.13. Fired-on silver paint was used and the copper wires are soldered to the electrodes to create a parallel connection. This sample was successfully poled and had an effective d_{33} of 1500pC/N when measured in the parallel configuration. The copper wires were cut to measure the d_{33} of each segment. The d_{33} of each segment varied from 270 to 340pC/N due to the non-uniform inter-electrode spacing.

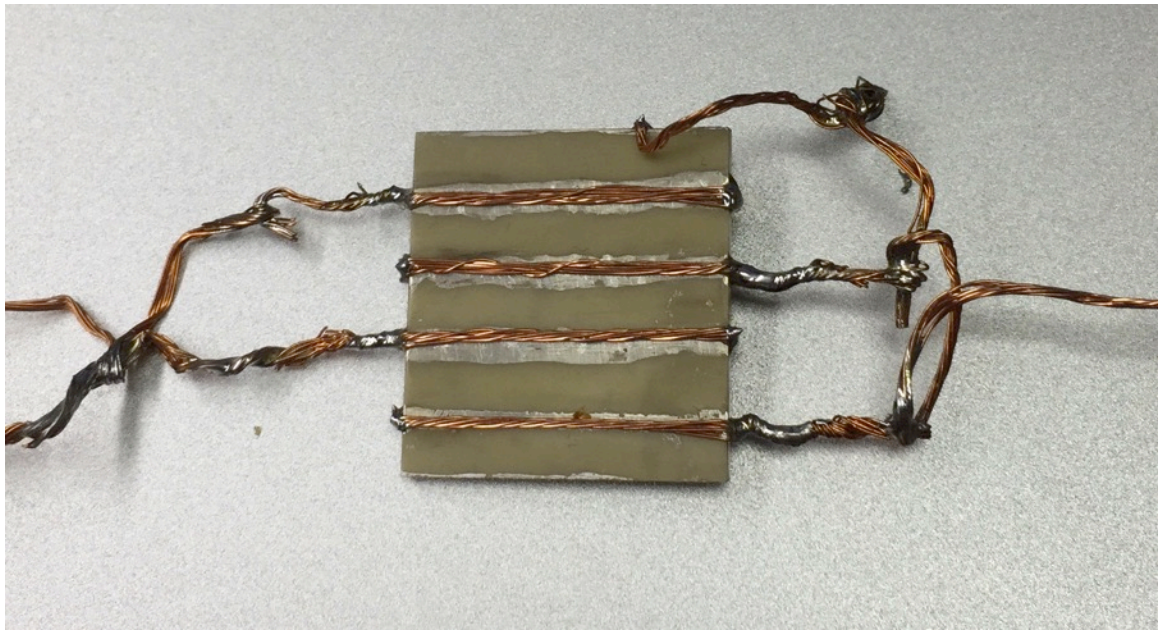

Figure 6.13. Test sample for poling using surface electrodes in parallel. Air-fired silver paint is used and the copper wires are soldered to the electrodes and connected in parallel.

After the d_{33} measurement of each segment, all copper wires were removed and air-dry silver paint was applied to the edge of the ceramic and used to connect the electrodes in parallel in the same way shown previously in Figure 6.12. The d_{33} could not be measured when the conductor was applied to the surface. The piezoelectric coefficient of the poled ceramic could not be measured in this method, although the reason for this is

not completely understood. From this experiment it was determined that an insulating layer would be needed in order to have successful parallel connection on the side of the ceramic. It is necessary to have the conductor for parallel connection be insulated from the edge of the ceramic and not directly on the surface.

Two methods were developed for applying the fired-on silver paste to the ceramics. The first method used painter's tape to outline the electrode. The tape was applied to the ceramic using a 3D printed guide, shown in Figure 6.14 that helped to align the tape to the electrode. This method could reliably reproduce the identical electrode pattern with consistent width and spacing. The other method used for applying the electrodes was a thin brass mask with the desired electrode patterns. The brass mask was placed on top of the ceramic and a fine tipped paintbrush was used to apply the electrode through the slots in the mask. This method proved to be difficult as the electrode paste would run underneath of the mask. Additional attempts have to be made to remove the unwanted prior to firing or it would bond to the surface.

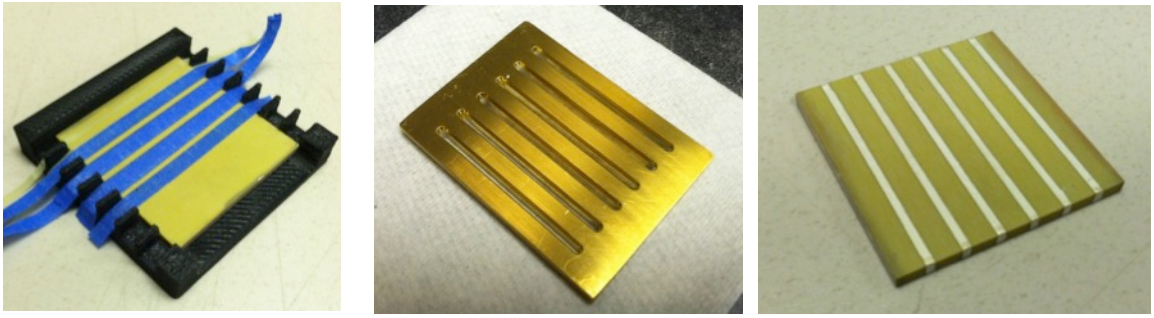

Figure 6.14. The electrodes were applied to the ceramics using tape (left) or applying through a brass mask (middle). The electrode pattern (right) could be reproduced with precision.

After the electrodes had been applied to the ceramic, it was fired at 550ºC for 15 minutes. The ceramics were placed on top of zircon sand, shown in Figure 6.15. Once the top and bottom surfaces of the ceramic had been electroded and fired the conductor was

applied to the edges carefully by hand using a paintbrush and fired at 550ºC for 15 min. After firing, all electrodes were inspected visually and with a digital multimeter as well as a capacitance bridge to ensure a resistance of less than 5Ω as well as continuity across all 4 corners of each electrode. Continuity can only be determined done when 3 sides have been painted. A lower capacitance reading during inspection would indicate that a section of the electrode is not connected and any anomaly or region with resistance greater than 5Ω was identified and corrected.

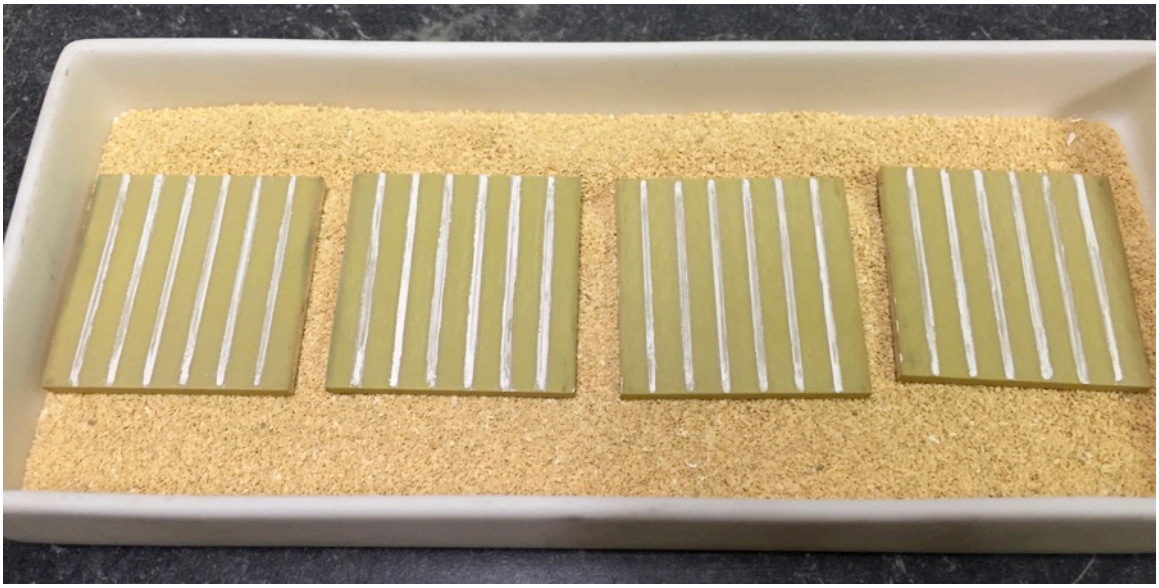

Figure 6.15. The silver paste is fired in air at 550ºC. The ceramics are placed on top of zircon sand to allow the organic components of the paste to be removed.

The novel transducer is a 32x32x2 mm PZT-5X (Sinocera, State College, PA) ceramic divided into seven segments separated with 3.7mm length. The 1 mm thick electrodes are applied around the sample using DuPont 7095 air fired silver paste. The

electrodes are continuous around the surface of the ceramic as shown in Figure 6.16a. The external parallel connections required for poling the ceramics are shown schematically in Figure 6.16b. Electroded samples were placed in an 80ºC silicon oil bath. The electric field of 2.15 kV/cm was applied to effectively polarize the 3.7mm segments.

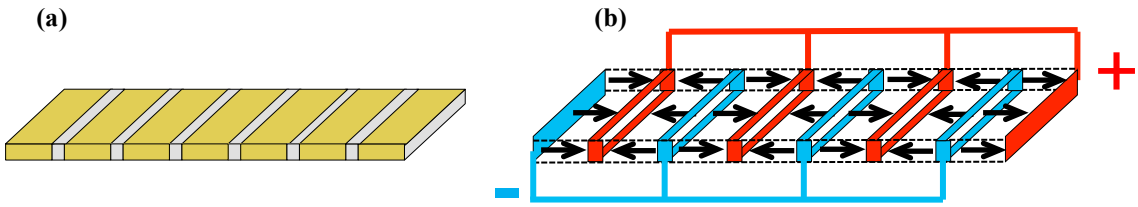

Figure 6.16. (a) Electrode configuration and (b) parallel electrode connectivity and poling direction

Two initial designs for poling fixtures designs were made by 3D printing as shown in Figure 6.17. The ceramic is placed in the plastic fixture and copper tape or wires were used connect the electrodes in parallel. The copper tape was able to establish excellent electrical connection to the electrodes on the edges of the ceramic. However after exposure to the silicon oil the adhesive became ineffective. The ceramic was successfully poled at 50ºC. When the temperature was increased to 80ºC, the plastic became soft and deformed.

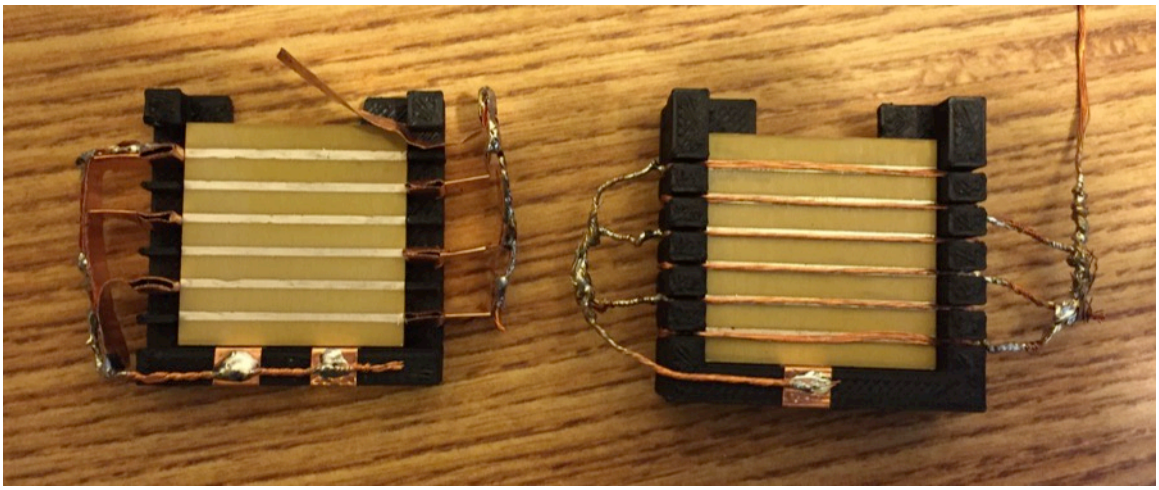

Figure 6.17. 3D printed poling fixtures. The copper tape did not adhere well after exposure to silicon oil. The copper wires made good contact with the electrodes. The fixtures were unusable after use at 80ºC because the 3D printed plastic softened and bent.

6.2.3 Poling fixture

A new fixture to hold the ceramics during poling and allow the electrodes to be connected to the power supply in a parallel configuration was designed. Teflon was chosen as the material to use due to its electrical insulation and ability to withstand high temperature. The base of the poling fixture is made from a 3x2x1" Teflon block, shown schematically in Figure 6.18. Slots were cut into the Teflon to hold the ceramics. A total of 5 ceramics could be poled simultaneously in the fixture, shown in Figure 6.19. The width of the slots was chosen to hold the ceramics in place securely without constraining or compressing them. However, it was difficult to machine Teflon to exact specifications and the fixture had narrower slots that specified and will apply additional stress during poling, causing electrical breakdown. The slots were widened by hand using a file to achieve the correct specifications of slot width.

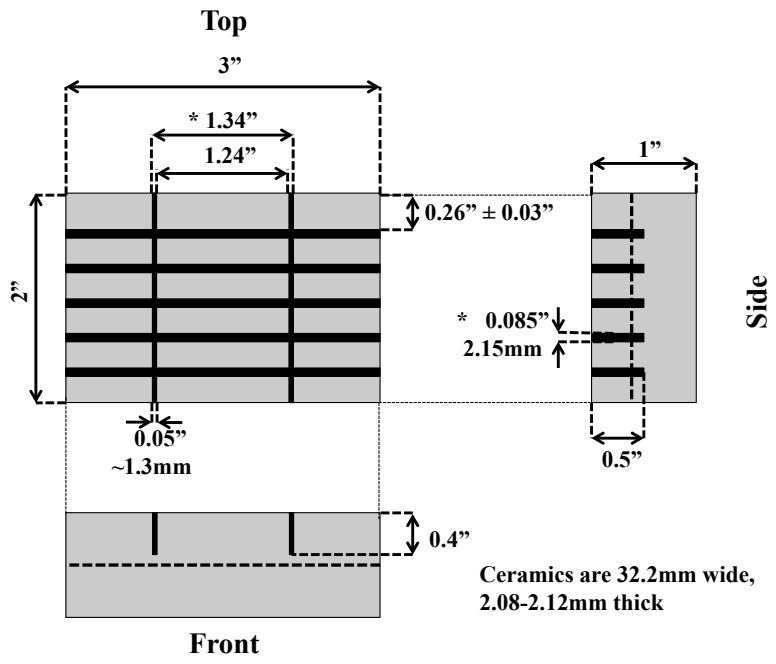

Figure 6.18. Schematic diagram of the base of the poling fixture. Slots cut into the Teflon block hold the ceramics during poling.

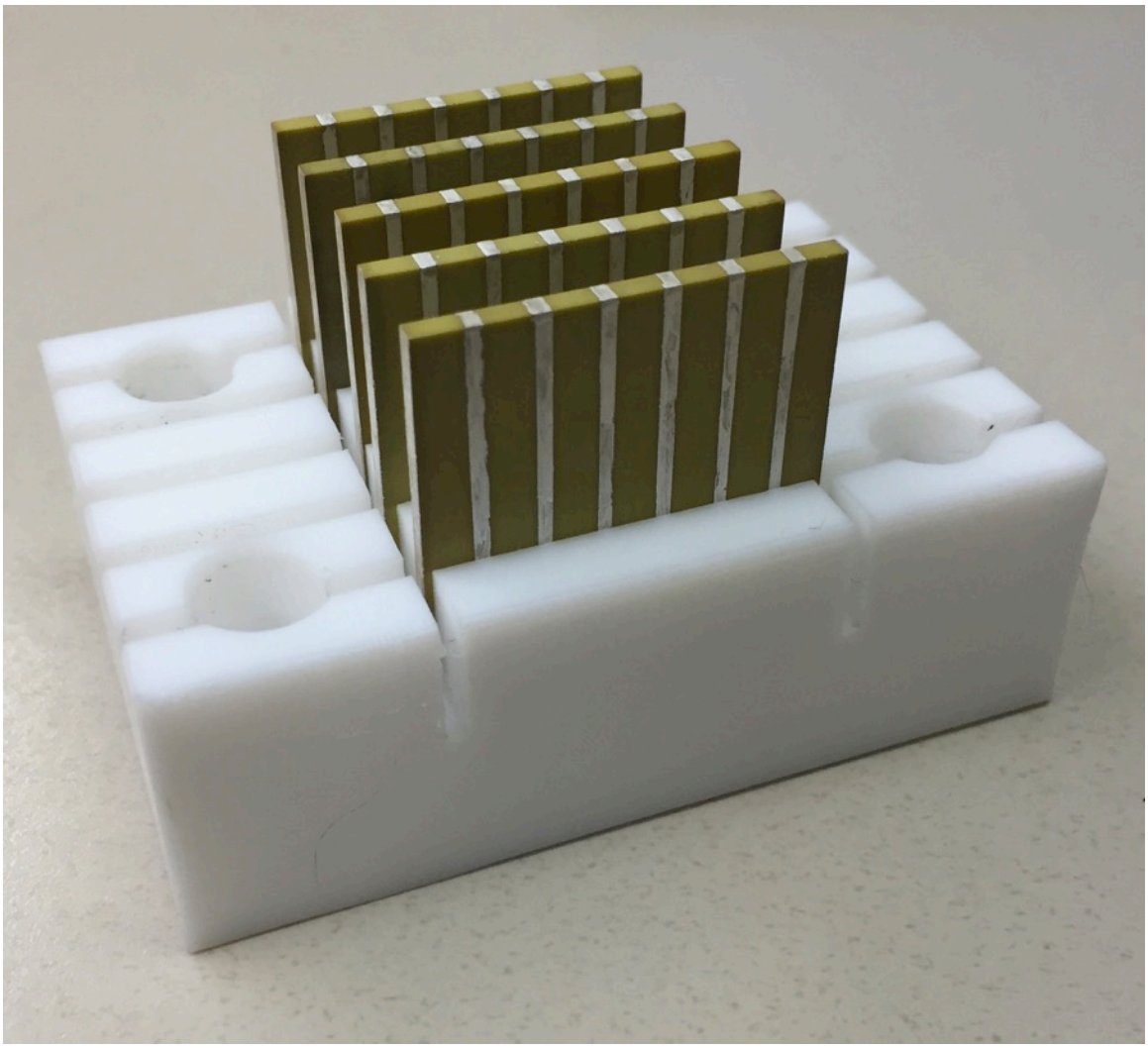

Figure 6.19. The base of the poling fixture with slots to hold up to 5 ceramics in place during poling. The fixture is made of Teflon to withstand high electric field and high temperature of poling.

Copper wires in the top part of the poling fixture make an electrical connection to the electrodes on the edge of the ceramics and connect them in parallel. Six copper wires were placed tightly and then soldered in a parallel configuration. The whole poling fixture is shown in Figure 6.20. An additional 2 wires were used to connect the electroded sides of the ceramic and were attached in parallel. The wires were connected to alligator clips that attach to the high voltage power supply and ground.

The top part of the poling fixture is secured onto the ceramics using Teflon bolts, nuts, and washers for a gentle contact with the six electrodes. The bolts are countersunk into the base and the nuts are tightened by hand. Connectivity to all of the electrodes was tested before poling using a digital multimeter and a capacitance bridge. The top of the fixture was adjusted if all of the connections were not made. The ceramics would break during poling if they were mechanically constrained by the fixture, which added more difficulty in preparing the ceramics for poling. This was especially difficult to accomplish due to the tendency of the Teflon sheet to bend when the nuts were tightened.

The wires shown in Figure 6.20 were wound by hand using 32ga copper wire. A different number of strands of the 32ga wire were used for each wire. The two wires at the center needed to have the largest diameter to fill the gap between the electrodes resulting from the upward flexing of the Teflon sheet. The wires at the edges use 7 strands, followed by 9 stands in the adjacent wires and then 11 strands for the two middle wires.

Due to the difficulty of connecting all of the electrodes without constraint, approximately 20% of the ceramics failed during poling where clamping lead to crack formation, which is shown in Figure 6.21. Modifications to the poling procedure were developed and a new fixture was designed to alleviate mechanical clamping of the transducers but was not built.

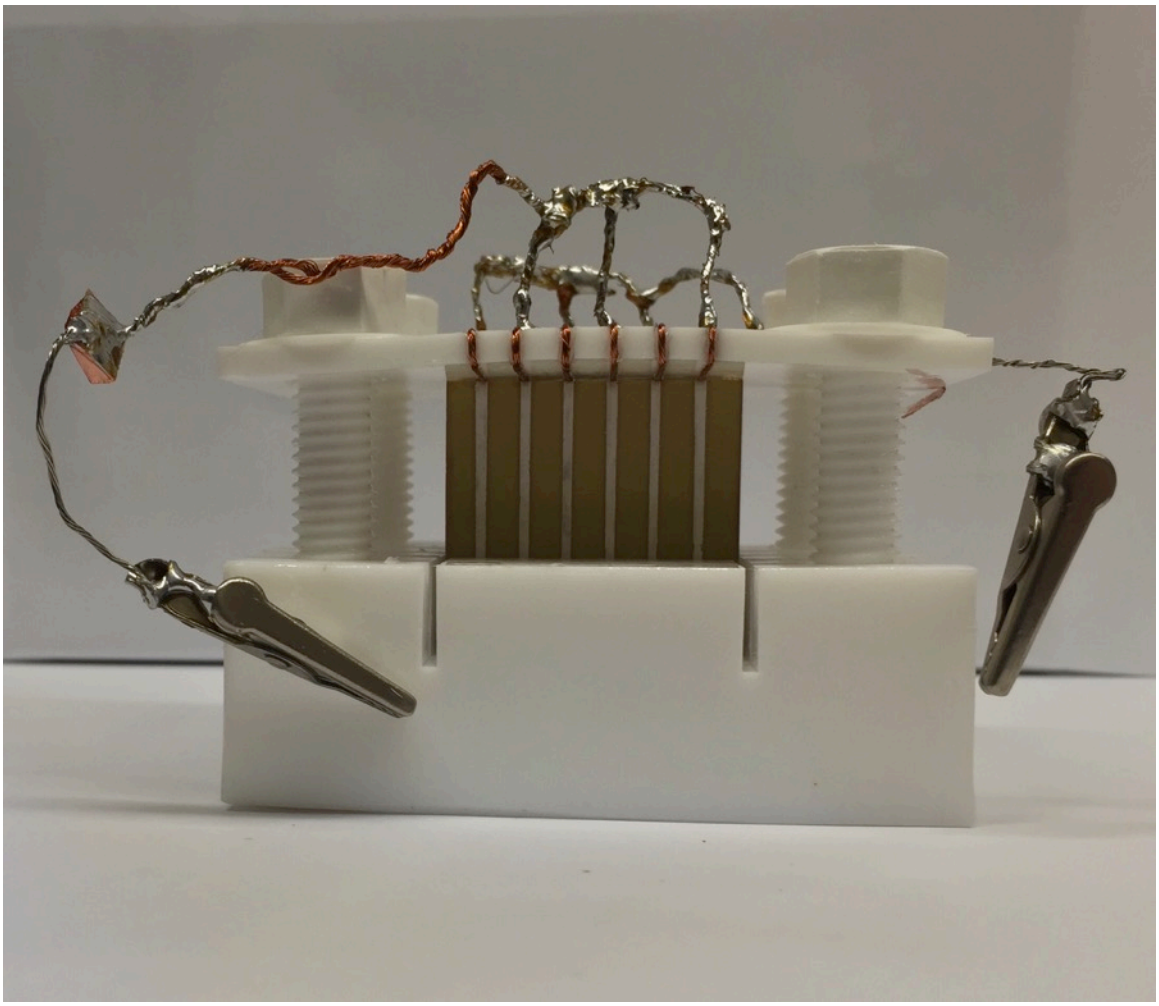

Figure 6.20. Poling fixture holds the ceramics securely and copper wires contact the electrodes on each ceramic. The wires are connected in a parallel configuration and alligator clips connect to the high voltage power supply and ground.

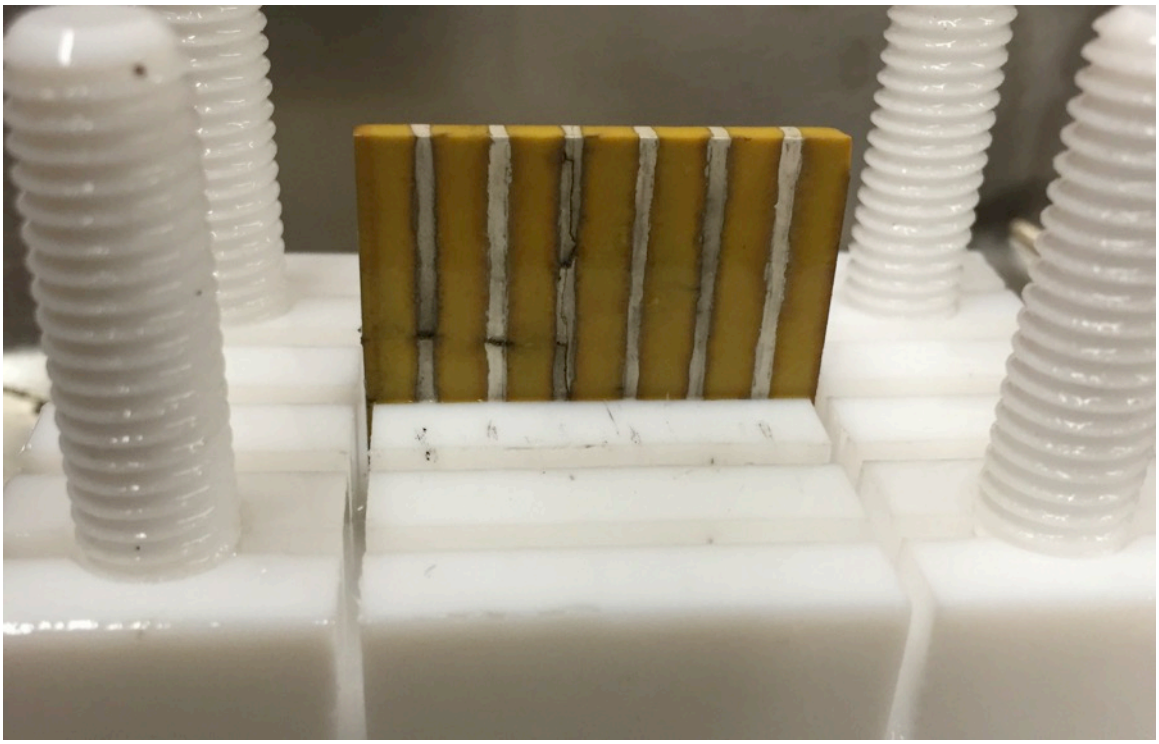

Figure 6.21. Fracture of the ceramic during poling to clamping from the fixture.

The electric field inside of the ceramic was simulated to determine the magnitude and direction of the electric field during poling. The magnitude of the horizontal and vertical electric field inside of the ceramic for a single segment under poling conditions of 8 kV was simulated by Abbas Jasim using the software COMSOL and is shown in Figure 6.22 [30]. The volume of the ceramic below the electrodes is inactive. The electric field between the electrodes is horizontal and strongest at the surface. The strength of the electric field at the center of the ceramic is reduced to 80% of the applied electric field at the surface, or 1.7 kV/mm. The direction of the electric field is uniform along the length of the sample.

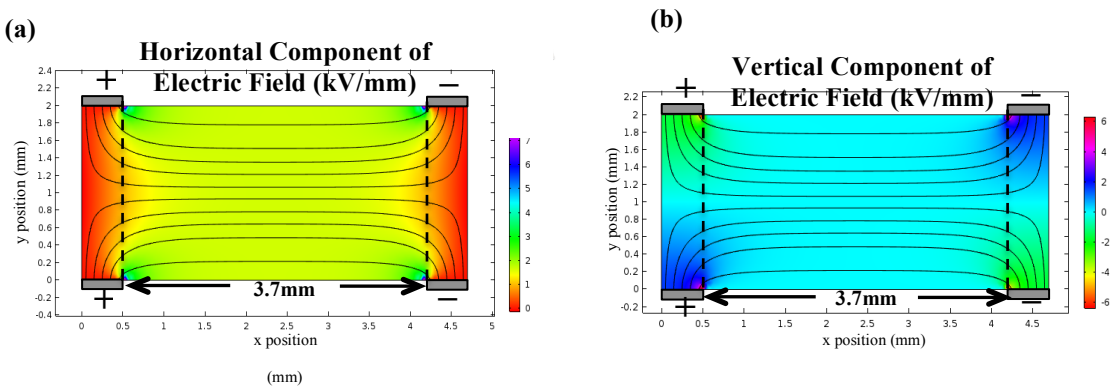

Figure 6.22. Modeled horizontal and vertical components of electric field inside a segment of the ceramic during poling. The direction of the electric field is parallel with the surface of the samples.

The measured value of the d_{33} of each segment is 550 pC/N, compared to 700pC/N measured for the conventionally poled ceramics. The lower d_{33} is likely lower due to the 20% in the middle section of the ceramics resulting from surface poling.

The d_{33} and capacitance of each section are additive when the segments are connected in parallel and was confirmed by measurements with the Berlincourt d_{33} meter and LCR meter. The Berlincourt meter can measure the piezoelectric coefficient up to a maximum of 2000pC/N. The d_{33} of the ceramic with the sections connected in parallel exceeds the measureable range of the meter so each section is measured individually and added together to determine the value when connected in parallel. The d_{33} of the ceramic with 7 segments and 6 surface electrodes in parallel connections exceeds 4000pC/N.

6.2.4 Transducer Fabrication

The ceramics are cleaned with isopropyl alcohol to remove the silicon oil after poling. The oil adheres to skin and nitrile gloves so special care was taken when handling the ceramics in order to prevent contamination from dirty hands or gloves. As a

precaution, the surface of the ceramics is cleaned again with isopropyl alcohol before each step of fabrication.

After the first batch of transducer was completed, multiple transducers failed due to the ceramic cracking at low loading. It was discovered that the ceramics contained micro-cracks visible under microscope along the edges of electrodes that occurred during poling. These cracks cannot be seen on the surface until fracture has occurred. The flawed ceramics fail immediately under loading and need to be identified and discarded. A simple yet effective proof testing method was developed to quickly identify the damaged ceramics. The ceramic is held between the index finger and thumb with both hands while trying bend the ceramic. The undamaged ceramics are too strong to be broken by maximum bending force by hand, however the flawed ceramics would easily break during bending.

Previous testing demonstrated that the conductor couldn't be applied directly to the side of the ceramic, so an insulating layer is needed. The insulating layer is eccobond 45LV (Henkel Ablestik 45LV) epoxy. The epoxy is applied to the side of the ceramic leaving alternating electrodes exposed as shown in Figure 6.23. First, the blue painters tape is wrapped around the ceramic to prevent overflow of the epoxy. Thin tape is stretched until it is approximately the width of the electrode and it used to cover alternating electrodes. The insulating epoxy is dispensed onto the side of the ceramic using a syringe. Then the tape is pulled off exposing three electrodes on each side. Different stages of this process are shown in Figure 6.23. The ceramics on the left side have been taped in preparation of dispensing the epoxy. The ceramic on the back right has been coated in the layer of epoxy and the 2 remaining ceramics on the right have had

the tape removed to expose the alternating electrodes. The epoxy is allowed to sit for 30 to 60 minutes to thicken before placing in an oven at 90ºC to cure. It is important for the epoxy to begin to harden at room temperature; otherwise the epoxy will flow and cover the exposed electrodes.

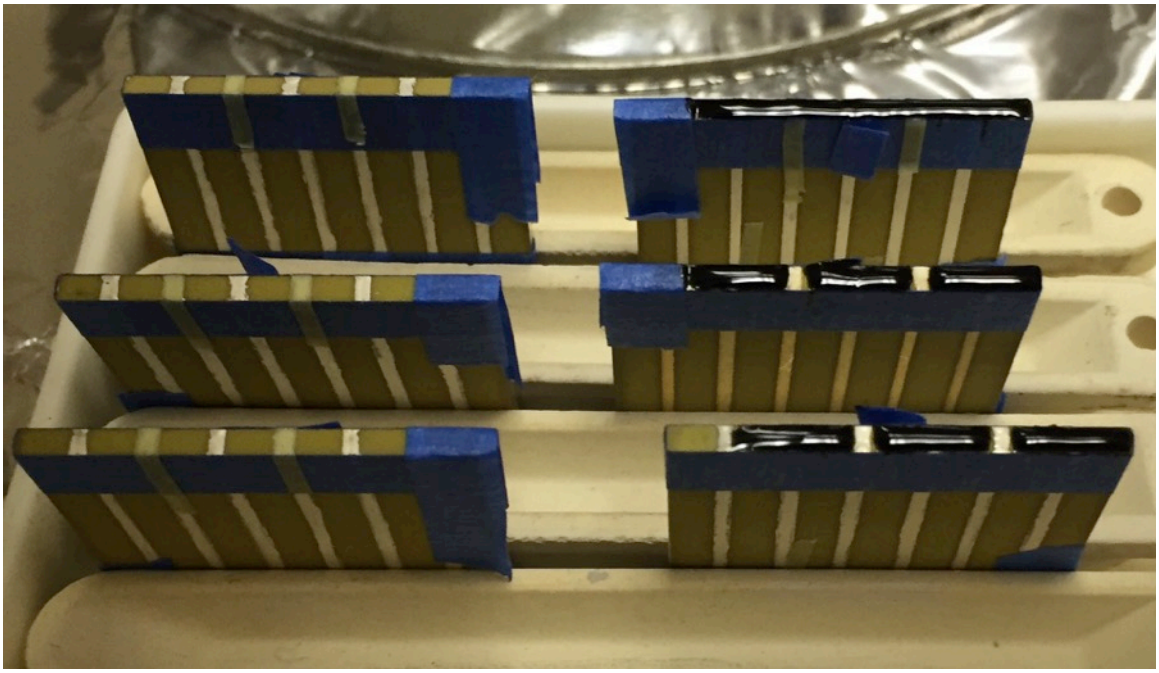

Figure 6.23. Process for applying insulating epoxy layer to the side of the ceramic. Tape is used to cover alternating electrodes. After the insulating epoxy is applied, the tape is removed to expose the electrodes.

The conductor for the parallel connection is applied on top of the insulating layer shown in Figure 6.24. Different types of conductors were used to connect the electrodes in parallel, however there were multiple issues that appeared with each type of conductor that prevent a good electrical connection. The first conductor used is air-dry silver paint. The air-dry silver paint has low resistance of 5-10Ω and is easy to apply using a paintbrush. However, it is acetone based and does not harden when applied on top of insulating epoxy. After the paint had dried, the silver conductor could be easily smudged

during handling and was not suitable to be used since the electrical connection could be easily broken.

The next conductor used was a Chemtronics CW2200 conductive pen. The air-dry silver paint from the pen uses the solvent butyl acetate, which dries better than the acetone on top of the insulating epoxy. It was difficult to apply to the sides of the ceramic and any small mistakes could cause an electrical short.

Another conductor that was considered is Chemtronics CW2400 conductive epoxy. However, the 2-part epoxy is too viscous to be applied to the sides of the ceramic. The epoxy has a pot life of 10 minutes that makes it impractical to be used for large batches of transducers.

A different conductive epoxy, Epotek H20E epoxy is a 2-part epoxy with good electrical conductivity, low viscosity, and long pot life of 60hr. The thixotropic rheology of the epoxy made it especially easy to apply with a fine paintbrush. The epoxy was cured at 80ºC for 3hr in an oven. Although the resistance along the conductive epoxy is 20-50Ω, there were discontinuities in the connection after curing. Cracks formed in the silver epoxy during cool down due to thermal expansion mismatch with the underlying insulating layer creating discontinuity in the electrical connection. The Epotek H20 epoxy could not create a reliable parallel connection to the electrodes.

Applying the air-dry silver paint on top of the silver epoxy solved the issues with the conductor. The silver epoxy layer, shown in Figure 6.24, has a rough and porous surface after curing. The air-dry silver paint adheres to the rough surface and fills in the voids of the silver epoxy. The combination of Epotek H20 epoxy and the air-dry silver paint fixes the electrical discontinuity and improves the conductivity of the epoxy. The

hard, rough epoxy surface prevents the dried silver paint from scratching or rubbing off. The conductor connection was tested using a digital multimeter. If the resistance between electrodes was greater than 5Ω, silver paint was reapplied to the conductor

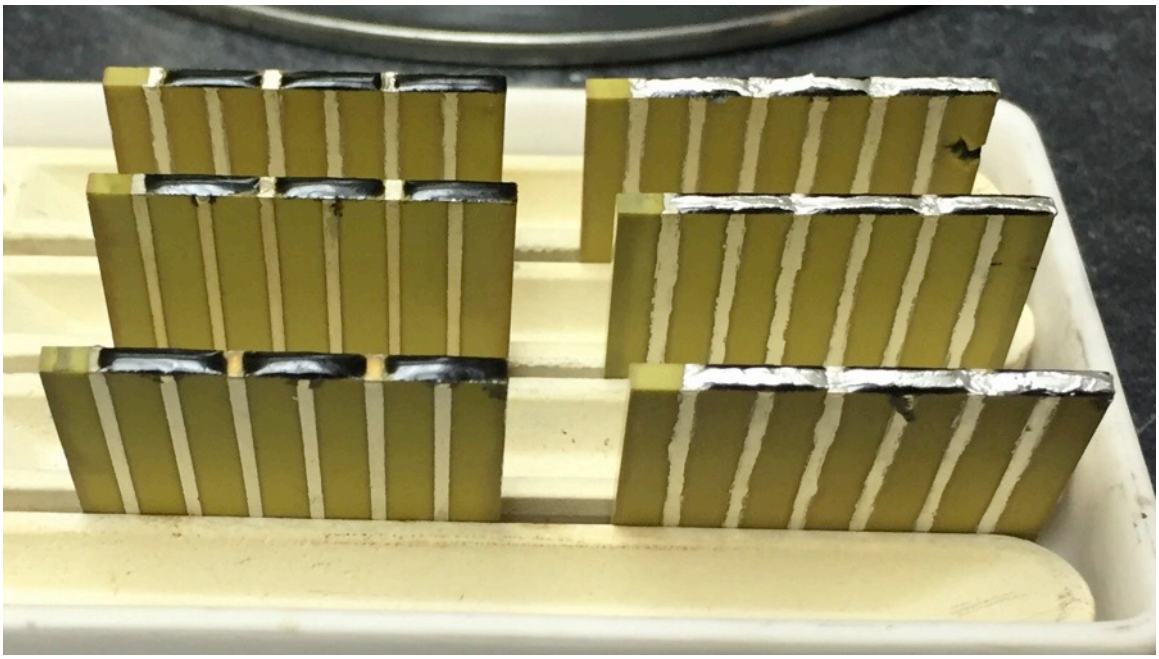

Figure 6.24. Conductor is applied on top of the insulating epoxy layer. Silver epoxy was cured at 90ºC and air-dry silver paint was applied on to of it.

6.2.5 Transducer end caps

The end cap shape was determined by simulation to maximize the tensile stress without causing fracture of the ceramic at the contact point with the end cap [30]. The shape and dimensions of the end cap is shown in Figure 6.25. The maximum stress was limited to 45MPa in the simulation, which was considered to be a safe upper limit. Data on the mechanical strength of PZT-5X was not available from the manufacturer so the

data on the probability of failure under stress from PZT-5H was used [31]. Analysis of the data using a Weibul distribution determined the probability of failure from a stress of 45MPa is 2%.

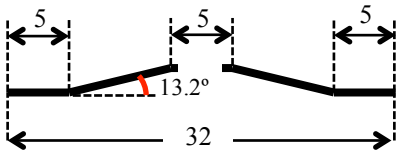

Figure 6.25. Dimensions of the steel end cap in mm.

Steel was chosen as the end cap material due to its strength, which is necessary for operation under heavy loading, and the ability to perform heat treatment after forming. The end caps are stamped from 4130 alloy steel sheets by Small Quantities NJ (Edison, NJ). The alloy steel has a high hardenability, which is a measure of how much hardness increases during heat treatment. The annealed 0.025" thick sheets are soft and can be stamped into the desired shape of the end cap. The stamped end caps are then heat treated to a hardness of Rc36 by quenching in oil followed by tempering. Some of the end caps warped during the heat treatment and were discarded.

Before the end caps were attached to the ceramics using epoxy, the ceramics and the steel end caps were cleaned with alcohol to remove any oil or debris in order to have a clean bonding surface. The epoxy was dispensed with a syringe through a short bevel 20-gauge needle. A fixture was used to apply pressure to the end caps while the epoxy cured. The fixture is able to hold five transducers at a time and is show in Figure 6.26. The epoxy was partially cured at room temperature overnight and then fully cured at 90ºC for 2 hr.

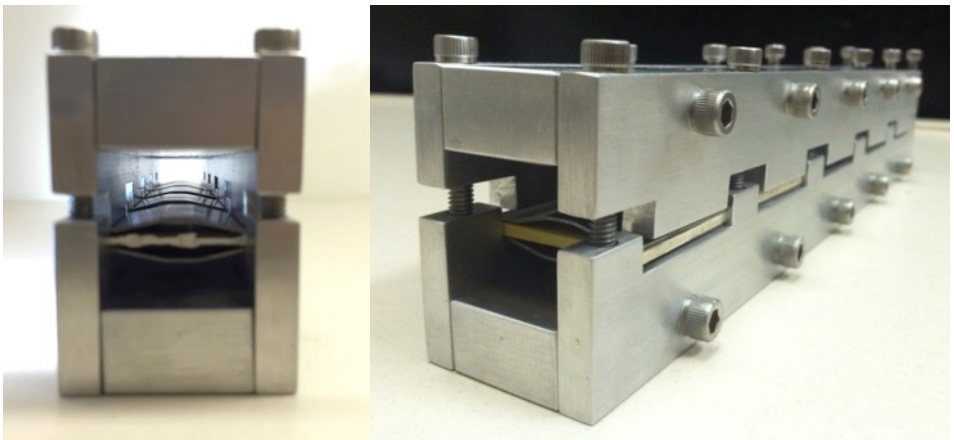

Figure 6.26. The fixture used to hold the end caps to the ceramics while the epoxy cures.

6.2.6 Module fabrication

The energy harvesting module is designed to hold 64 transducers in four layers. It was built at the Physics machine shop to the specifications of the schematic shown in Figure 6.27. The casing is made from 0.5” aluminum and copper sheets separate each layer. There are 16 transducers in each layer are arranged in a 4x4 configuration.

A layer of the module can be seen in Figure 6.28. Nylon sheets line the sidewalls to insulate the from the aluminum casing. Nylon strips arranged into a grid separate the transducers in the layer. The strips are shorter than the transducers and do not support any load. The transducers have various markings indicating polarity, height, capacitance, and batch number. All of the transducers in a layer are arranged in the same poling direction, and the poling direction alternates in the adjacent layer.

The transducers placed on top of copper plates that divide the layers and act as current collectors. Wires are soldered to the copper plates to connect them in parallel and go through the nylon-lined sidewall, which can be seen in Figure 6.28. A channel is cut into the aluminum wall to hold the wires and exit through a drilled hole. The transducers

are insulated from the metal case by nylon-lined sidewalls and a spray-on insulating epoxy (Aervoe Industries inc.). A layer of insulating epoxy is sprayed between the copper plates and the aluminum base and cover plates on the top and bottom of the module.

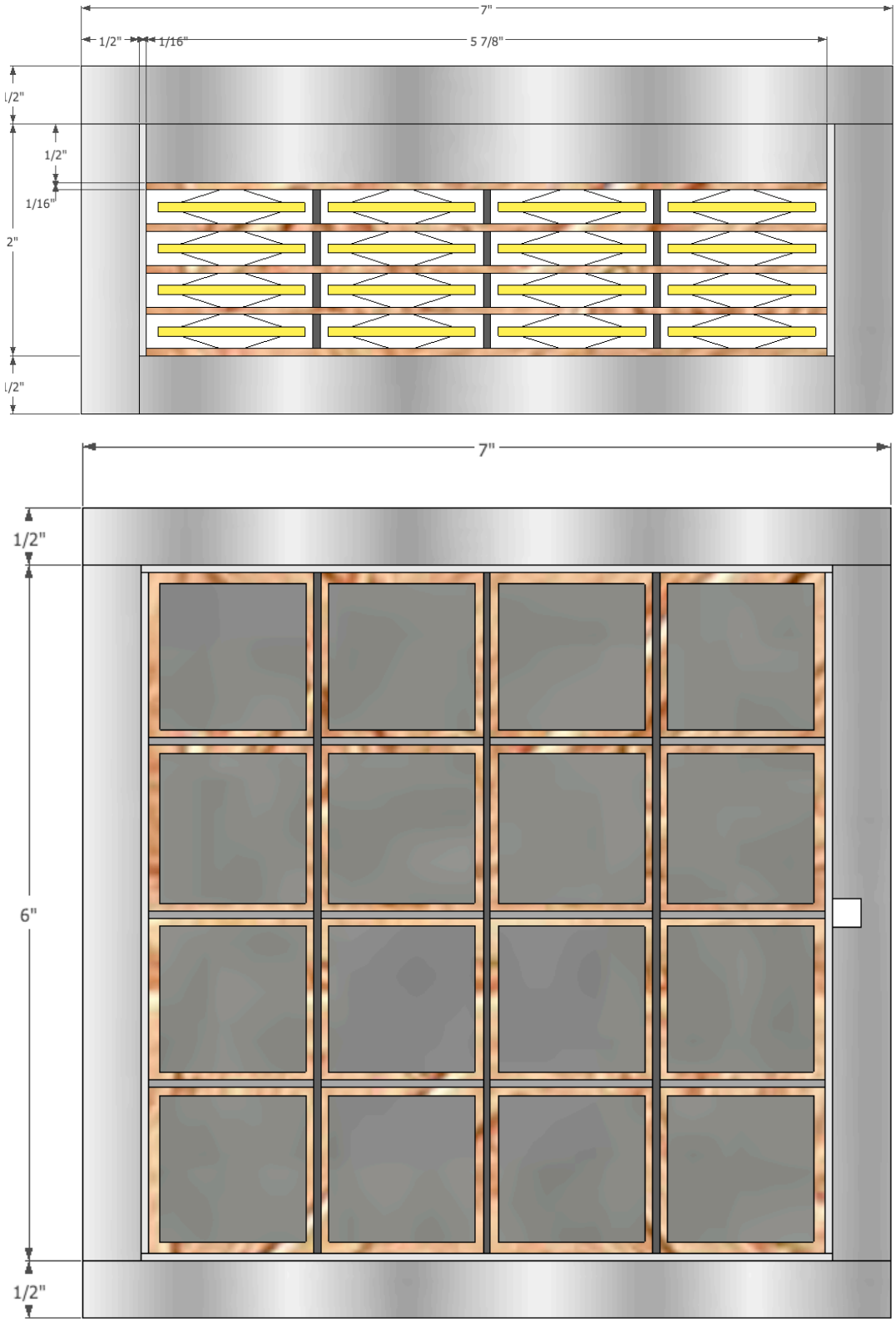

Figure 6.27. Schematic drawing of the energy harvesting module. The casing is made of 0.5” thick aluminum and 5 copper sheets separate 4 layers of transducers.

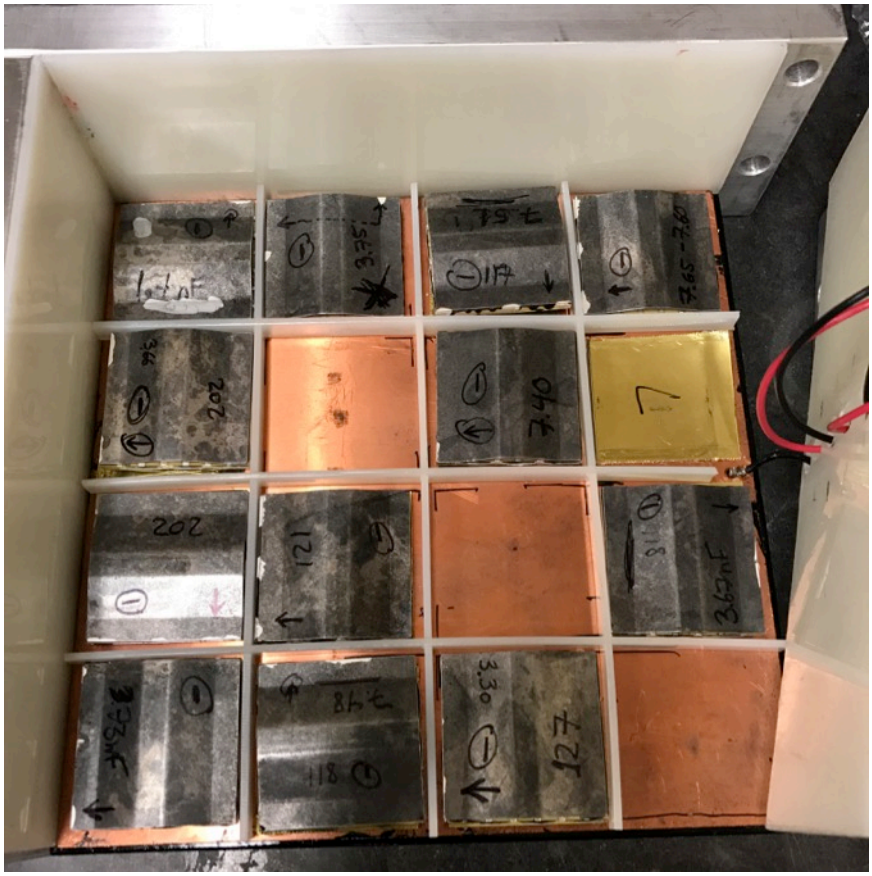

Figure 6.28. Disassembled module showing a layer of transducers. Nylon sheets line the walls and nylon strips separate the transducers. On the right side, a wire can be seen attached to the copper plate. The transducers have various markings to identify polarity, batch number, height, and capacitance.

The design of the module requires that each layer have a uniform height to spread out the load and effectively transfer force to the next layer. Although the transducers were designed to have a nominal height of 7.50mm, due to the bending of the steel end caps during heat treatment the height of the transducers ranged from 7.21mm to 7.60mm. The majority of transducers have height between 7.30 and 7.40mm. To achieve a uniform layer thickness the position of each transducer had to be carefully selected and the transducers with similar height were grouped together. A uniform layer thickness is achieved using brass shims to increase the height of smaller transducers. The shims have thickness in the range of 0.001-0.007" (0.025-0.18mm) and are cut to match the height of individual transducers. The shims are used to get a uniform height of 7.45mm in the layer and are attached to the copper plates as shown in Figure 6.29. The brass shims provide a good electrical connection and are attached to the copper plates using a hot-melt adhesive. The adhesive is applied to the edges of the shim and then melted between the brass shim and copper plate using a soldering iron so the center of the shim in in direct contact with the copper plate.

A safety feature of the case is the gap between the cover plate and the sidewall, which can be seen in Figure 6.30. The transducers are compressed under loading and the cover plate is displaced downward. The gap is adjusted so that the cover plate will impact the sidewall at maximum loading. If the module is loaded excessively, the additional force is transferred to the module casing to prevent damage to the transducers. The maximum force transferred to the transducers can be adjusted by changing the height of the gap using setscrews in the cover plate. Aluminum shims are stacked between the two

pieces of the cover and then screwed together. The gap can be adjusted in increments of 0.001” by increasing the number of shims.

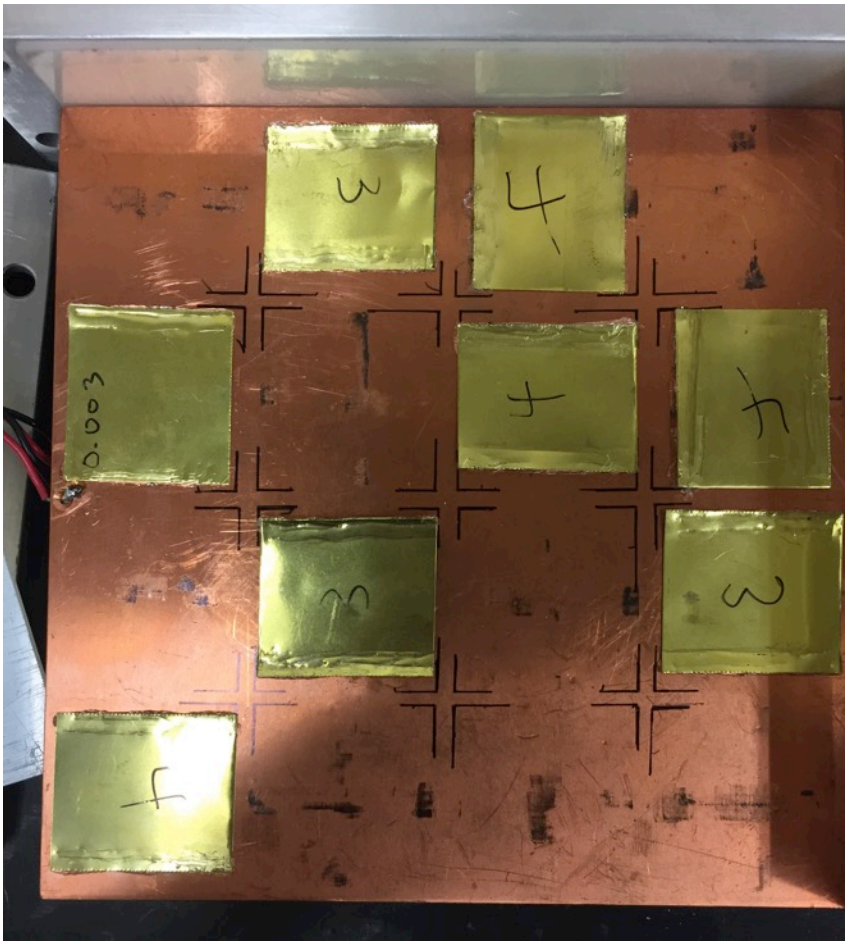

Figure 6.29. Brass shims are used to obtain a uniform layer height by placing them beneath shorter transducers. The shims are labeled according to their thickness and are 0.003” or 0.004” shown in this layer.

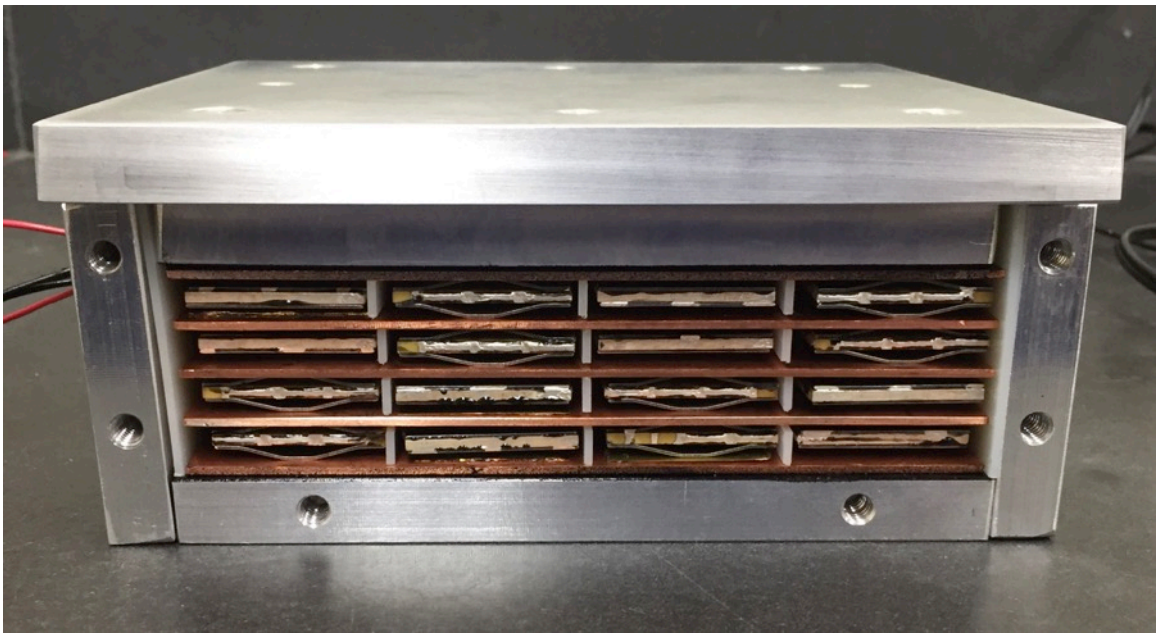

Figure 6.30. Module with the side removed showing the 4 layers of transducer between copper plates. Nylon sheets insulate the transducer from the walls and a layer of insulating epoxy can be seen above and below the top and bottom copper plates, respectively.

6.2.7 Impact testing

The loading of a vehicle on a road surface was simulated using a pneumatic loading system. The system was designed and built by Professor B. Basily of the Civil and Environmental Engineering department at Rutgers University to test the energy harvesting module. It is built from a 20-ton hydraulic press frame to withstand high levels of impact forces. A pneumatic piston, electronic control unit, and pressurized air tanks are mounted to the frame shown in Figure 6.31.

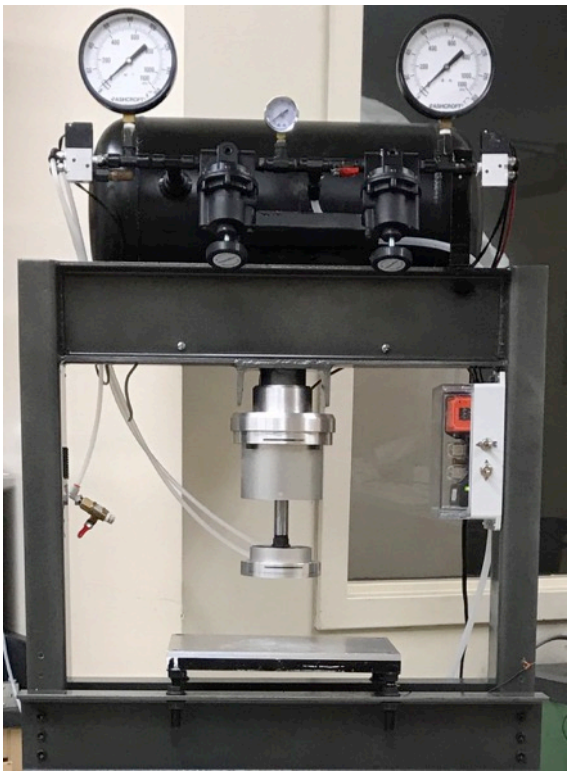

Figure 6.31. Pneumatic system used to simulate vehicle loading. Pressurized air tanks are mounted to a 20-ton hydraulic press frame. The impact force and frequency can be adjusted with a maximum of 700lb of force up to 5Hz.

An air compressor fills two reserve tanks mounted to the base of the frame. An inline regulator is used to control the pressure in the tank mounted to the top of the frame that supplies air to the piston. This configuration prevents pressure drop in the air supplied to the piston to allow constant load to be applied repeatedly. The air pressure in the loading system was kept below 100psi as a safety factor, however the maximum allowable pressure is 150psi. The 3” diameter piston exerts a force of 700lbs at 100psi.

The electronic control unit operates a valve to release the pressure in the piston and can be set to operate at different frequency. The maximum frequency of the electronic control unit is 50Hz. However, at high frequency there is not enough time for

air to completely fill the piston. In actual use the maximum frequency achieved by the pneumatic loading system is 5Hz.

The energy-harvesting module sits on a stage mounted to the frame shown in Figure 6.32. The height of the stage is adjusted so the module sits just below the piston. The piston travels a distance of less than ¼ inch.

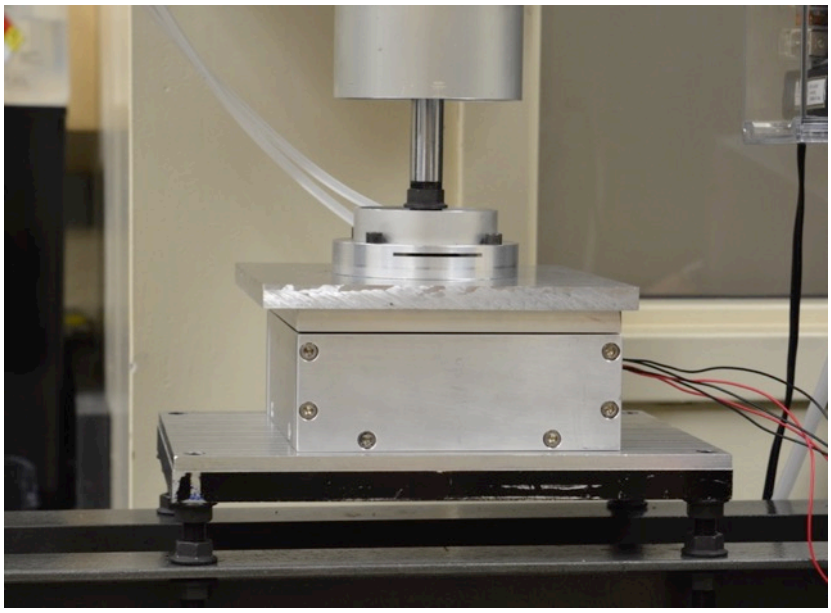

Figure 6.32. Energy harvesting module inside of the vehicle impact simulator. The module sits on top of an adjustable stage and is loaded above by the piston.

6.2.8 Impedance matching

The transducer produces AC pulses when loaded and unloaded. A positive pulse is generated when loaded, and a negative pulse when unloaded. The charge from the AC output cannot be stored on a capacitor because the charge generated during loading is neutralized when unloaded.

The output of the transducers need to be converted into a form that is useable in order to power electronic circuits or LEDs that require a constant supply of voltage and current to operate. To use the energy generated by the piezoelectric transducers, the

output must first be rectified and then stored on a capacitor. A rectifier is set of four diodes that take an AC input and transforms negative voltage into positive. The rectified transducer output is a series of positive voltage pulses produced during loading and unloading of the transducers.

The piezoelectric transducers generate a high open circuit voltage due to the large amount of charge produced when loaded relative to their capacitance. The voltage is proportional to the charge divided by capacitance $V=Q/C$. After rectification, the charge generated by the piezoelectric transducer can be stored on a capacitor C which is placed in parallel connection with the resistor R. This circuit is shown schematically in Figure 6.33. Voltage is measured across a resistor R that is in parallel with the capacitor. The charge and the stored electrical energy are calculated by the measured voltage and capacitance using equation $Q=CV$ and $E=\frac{1}{2}CV^2$, respectively. This measurement is made in open circuit conditions where the resistor R is assumed to be infinite. In reality, losses in the capacitor as well as the impedance of the probes used to measure voltage affect the resistance in the circuit. The impedance of the LeCroy 9310A oscilloscope is 1MΩ. It is necessary to use LeCroy PP002 high impedance 10:1 probes with 10MΩ impedance in order to accurately measure the voltage in the circuit.

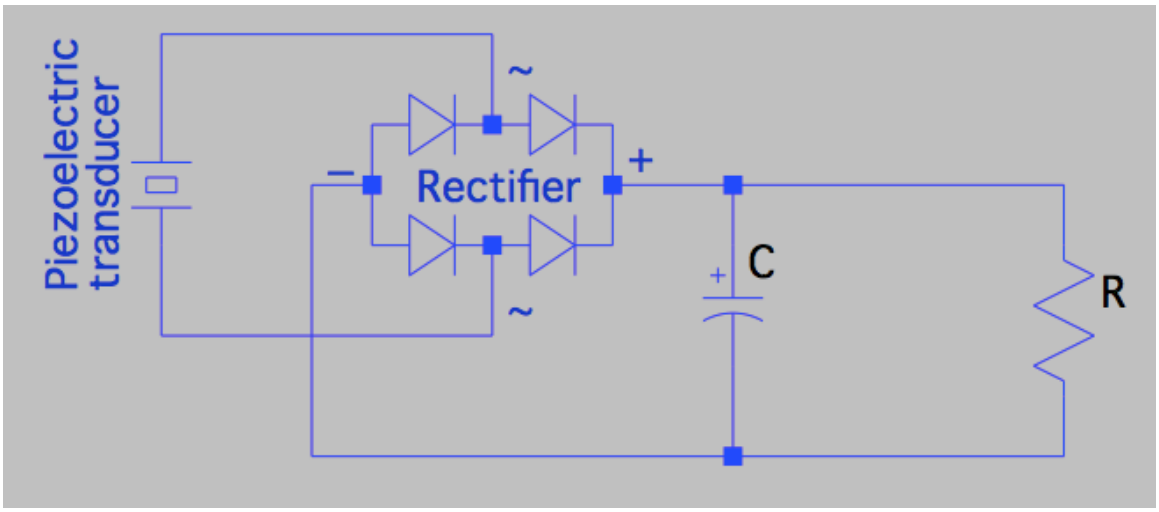

Figure 6.33. Circuit used to measure the energy generated by the piezoelectric transducer. The AC output of the transducer is rectified and filtered across a capacitor. Voltage is measured across the resistor, which is in parallel with the capacitor. The circuit is used to measure the charge generated by the transducers.

Power is measured under repeated loading of the transducers using the same circuit shown in Figure 6.33. The power is measured by the current that flows through the resistor. The current that flows through the resistor R is calculated I=V/R and the electrical power dissipated by the resistive load is $P=VI=V^2/R$.

As the transducer is repeatedly loaded, the charge generated is rectified and stored on the capacitor. When the resistive load is small, the current that flows through the resistor is large. However, due to the limited amount of charge stored on the capacitor, the voltage is quickly depleted. The charge generated by the transducer can produce very little power at low voltage. In this situation the transducer output is not utilized efficiently at the low resistive load due to mismatched impedance. On the other hand, if the resistive load is large the current is restricted. Charge will accumulate in the capacitor and result in higher voltage but electrical losses that occur in the capacitor are greater and power is dissipated and hence, the generated energy is not efficiently used due to low current through the resistive load. Therefore there is an optimal value of resistance that

maximizes the electrical output power. The optimal impedance is determined experimentally by measuring the voltage and current for different resistive load to find the maximum power. The impedance is influenced by the many aspects of the transducer such as capacitance, leakage current, internal losses and resistivity, as well as loading conditions such as impact force and frequency [32].

The high output impedance of the transducer limits how the output power can be utilized. Electronic circuits and LEDs have low impedance and require a minimum sustained voltage for operation. LEDs have little resistance in the forward direction. When the resistor in the circuit is replaced with an LED, all of the charge generated by the piezoelectric transducer passes through the LED instantaneously, briefly illuminating the LED, and depleting the charge stored in the capacitor. A flash can be seen on the LED each time the transducers are loaded and unloaded. Due to the low impedance of the LED, the voltage is low and lower power is utilized.

In order to utilize the high impedance output of the piezoelectric transducer a converter such as a step down DC-DC switch mode converter (also known as a “buck” converter) can be used. The converter reduces voltage while increasing current, which is more effective for supplying power for low impedance loads. The circuit can be used to convert the transducer electrical output into continuous power for LEDs or electronic devices.

A simplified schematic of the DC-DC converter circuit is shown in Figure 6.35. First, the output of the transducer is rectified and filtered across a capacitor. A metal oxide semiconducting field effect transistor, or MOSFET, is used to control the flow of current into the circuit. The MOSFET M1 allows current to pass when voltage is applied

to the gate. When open, current flows from capacitor C1 through inductor L and resistor R while charging capacitor C2. The inductor L generates a magnetic field as the current flows through it. When the gate is closed, the magnetic field in the inductor collapses, creating positive voltage. Capacitor C2 discharges and the current flows through resistor. The diode D allows the circuit to be completed. A constant flow of current through a resistive load can be achieved when the MOSFET is switched repeatedly.

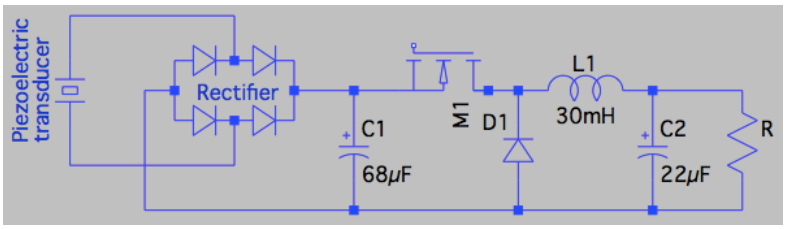

Figure 6.34. DC-DC step down converter. The converter reduces voltage while increasing current, which is more effective for supplying power for low impedance loads. The circuit can be used to convert the transducer electrical output into continuous power for LEDs or electronic devices.

The gate of the MOSFET is driven by a square waveform. The periodic switching of the transistor prevents the capacitor C1 from continuous drain, allowing voltage to build up in the capacitor. The ratio of the time the switch is open to closed is called the duty cycle and is expressed as a percentage. In a switch mode converter, the duty cycle determines the step down ratio between the input and output voltage. The output voltage of the circuit is given by the equation $V_{out} = V_{in}\frac{t_{on}}{t_{cyc}}$, where t_{on} is the time the switch is open and t_{cyc} is the cycle length. As can be seen from the equation, the input voltage is equal to the output voltage when the duty cycle is 100%, i.e. the switch is always open. A step down ratio of 10:1 would be achieved for a duty cycle of 10%. The frequency of the switch is determined by the values of inductor L1 and capacitor C2. The fabricated circuit used a frequency of 2kHz.

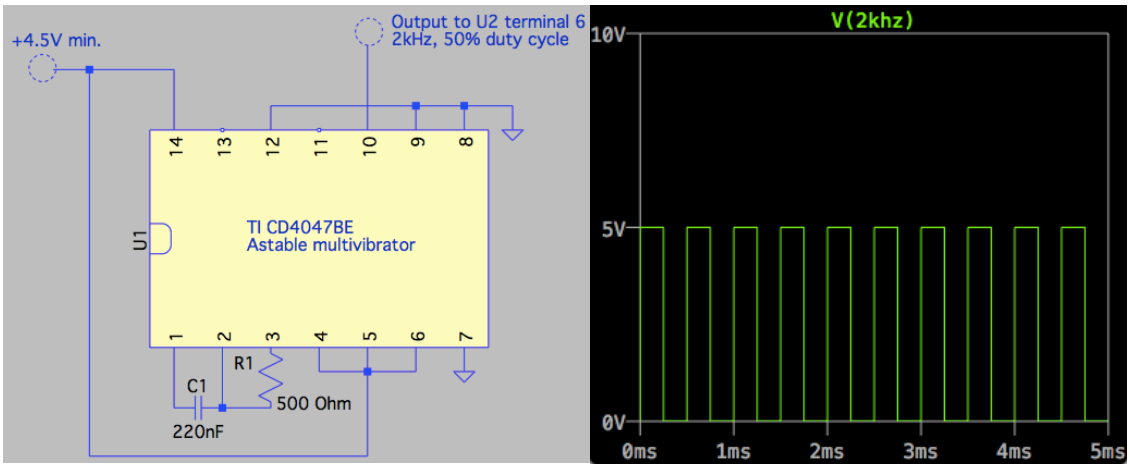

Figure 6.35. Output of vibrator U1. U1 produces a continuous square wave pattern with frequency controlled by R1. A 220nF capacitor and 500Ω resistor produces a continuous 2kHz square wave with duty cycle of 50%.

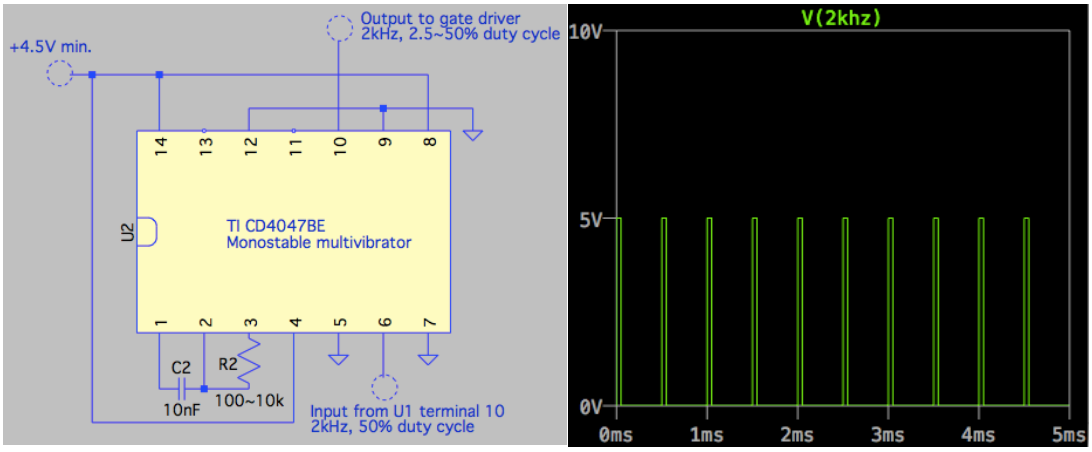

Figure 6.36. Output of vibrator U2. Vibrator U2 controls the duty cycle. U2 is triggered by the 2kHz output of U1 and produces a pulse, which length is controlled by C2 and R2. Using the variable resistor R2, a 2kHz square waveform with a duty cycle of between 2.5 and 50% can be achieved. The square wave pattern shown has a duty cycle of 10%.

The waveform for driving the MOSFET is generated using two vibrators. The frequency is controlled using the vibrator U1 and is shown schematically in Figure 6.35.

U1 is an astable multivibrator in a free running configuration, which produces a continuous square wave pattern with 50% duty cycle shown in Figure 6.35. A 220nF capacitor and a variable resistor control the frequency within the range of 100Hz to 10kHz. A 500Ω resistance produces a continuous 2kHz square waveform. The vibrator U2, shown in Figure 6.37, is in a negative-edge trigger configuration and controls the duty cycle. U2 is triggered by the output of U1 and produces a pulse, which length is controlled by C2 and R2. Using the 2kHz waveform along with the variable resistor R2 and a 10nF capacitor, a duty cycle between 2.5 and 50% can be achieved. The minimum duty cycle at 2kHz is limited by the amount of time needed for voltage rise in the square waveform. Together, the two vibrators are used to generate a square waveform with adjustable frequency and duty cycle for operating the MOSFET.

The vibrator output waveform is passed to a gate driver U3 to charge and discharge the MOSFET. The vibrators and the gate driver require an external power source of 4.5V minimum. A 9V battery was incorporated to power the integrated circuits. The battery is used in a floating configuration. The entire circuit is shown in Figure 37 and the parts are listed in Table 6.3. The battery-powered section of the circuit, shown in Figure 6.38, is isolated from the step down converter. Power from the battery-powered part of the circuit is not transferred through the gate driver. A self-powered step down converter is possible with sufficient power generation as the circuit consumes less than 4mW. However, the power consumption does not consider a voltage regulator that would need to be incorporated to obtain the startup power directly from the transducer output. Similar circuits are commercially available but consume more power as they are primarily designed to powering LEDs from 120VAC source.

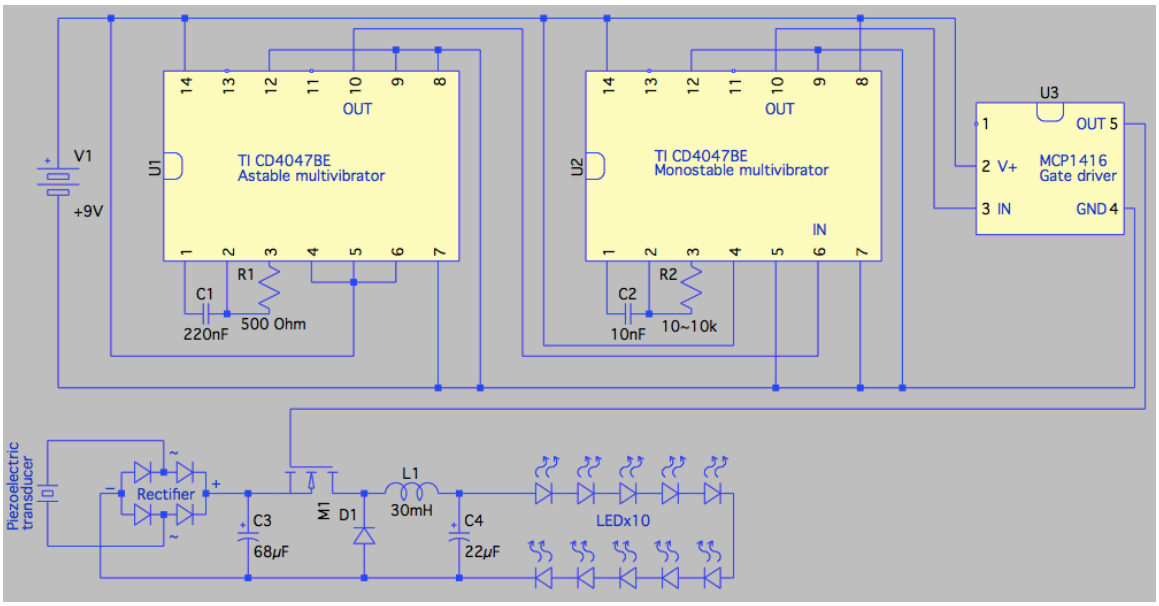

Figure 6.37. Step down DC-DC "buck converter" for using the high impedance output of the transducer to power LEDs.

Table 6.3. Parts list for step down DC-DC "buck converter" circuit.

Symbol	Type	Value	Manufacturer	Part Number
D1	Diode	100V	Fairchild Semiconductor	1N914TR
Rectifier	Rectifier Bridge	1A, 600V	Micro Commercial Co	DB105-BP
M1	MOSFET	400V	Vishay	IRFD320PBF
U1,U2	Astable/monostable vibrator		Texas Instruments	CD4047BE
U3	MOSFET gate driver		Microchip Technology	MCP1416
C1	Capacitor, film	220nF	Panasonic	ECQ-E2224KF
C2	Capacitor, ceramic	10nF	Vishay	K103K10X7RF5UH5
C3	Capacitor, electrolytic	68µF	Nichion	UKL1H680MPD1TD
C4	Capacitor, electrolytic	22µF	Nichion	UKL2A220MPD1TD
R1, R2	Variable resistor, linear	0-10kΩ		
L1	Inductor	33mH		
LED	LED	V_f=2.65V	Kingbright	WP7113LZGCK

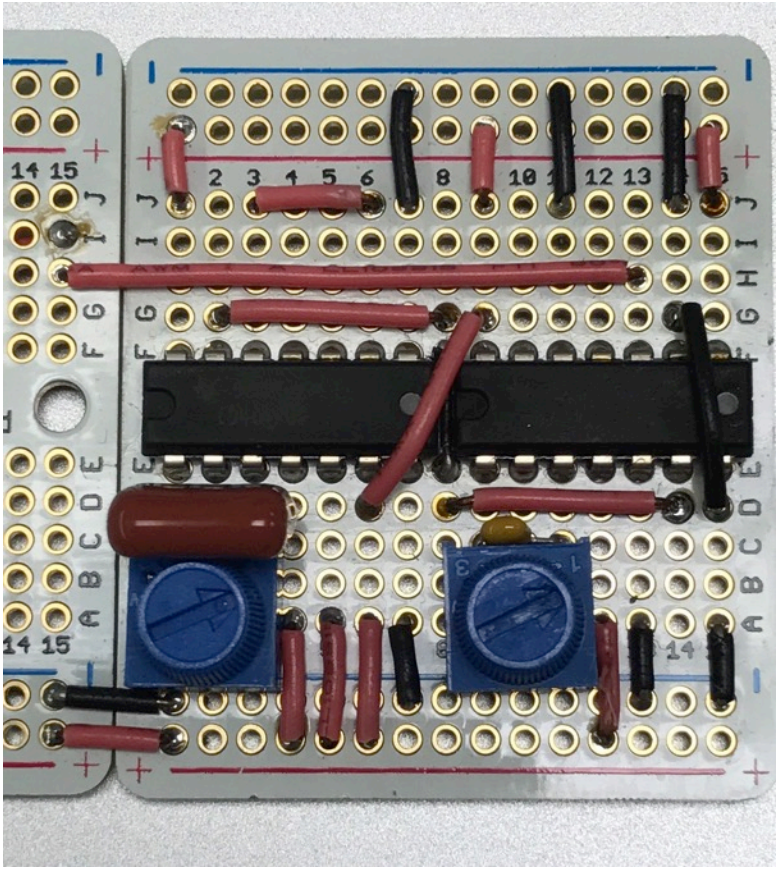

Figure 6.38. Vibrator circuit on solder-able breadboard. The circuit produces a square waveform. The frequency and duty cycle can be adjusted using the variable resistors. The duty cycle can be from 2.5-50% and the minimum frequency is 100Hz.

Low leakage current electrolytic capacitors (Nichion, UKL series) are used to reduce the losses in the circuit. Low current green LEDs with a forward voltage drop of 2.65V are used in series. The low current LEDs have a nominal forward current of 2mA but can be illuminated with less than 0.1mA. A series of 10 LEDs requires a 26.5V to operate.

6.2.9 Effective piezoelectric coefficient

The piezoelectric coefficient can be measured using the direct and converse piezoelectric effect. The direct piezoelectric effect is the same method used by the Berlincourt meter. The piezoelectric ceramic is placed on top of a known reference piezoelectric standard and force is applied. The unknown and reference ceramics receive the same force. The piezoelectric coefficient is calculated based on the response of the unknown compared to the reference. The Berlincourt meter clamps the ceramics and applies an oscillating load generated by an electromagnetic shaker inside of the base unit. The standard measurement is conducted at a frequency of 100Hz.

The converse piezoelectric effect is measured from the strain resulting from an applied electric field. The measured units are pm/V, which are equivalent to pC/N. A laser interferometer or fiber optic sensor is used to measure the displacement of the sample [33]. The effective piezoelectric coefficient was measured by the converse piezoelectric effect using Radiant Technologies Precision LC, high voltage interface (HVI), high voltage test fixture (HVTF), and an MTI-2000 Photonic senor.

The effective piezoelectric coefficient may not be consistent for composite transducers when measured using the direct and converse effects. A. Dogan observed that moonie transducers with Lucite end caps had lower d_{33} when measured by the direct piezoelectric effect [34]. The low stiffness of the Lucite prevented the applied stress from transferring to the PZT. On the other hand, PZT can easily drive the compliant Lucite end caps and shows a greater piezoelectric coefficient when measured using the converse effect [34].

Measurement of the effective piezoelectric coefficient could not be done using the Berlincourt d_{33}. The effective d_{33} of the transducer exceeds the 2000pC/N limit on the Berlincourt meter. Individual segments could be measured if the parallel connection was broken.

A modified method was developed to measure the effective piezoelectric coefficient using the direct piezoelectric effect. The piston used for impact testing of the energy harvesting module is used to apply force to an individual transducer. The transducer is placed on top of a PZT disc with known d_{33} and measured capacitance. The transducer is stacked on top of the PZT disc as a reference, shown in Figure 1. When loaded, the transducer and the reference PZT disc receive the same force.

The piezoelectric coefficient is calculated using the piezoelectric voltage coefficient and the capacitance. The piezoelectric voltage coefficient g_{33} is the electric field generated from the applied pressure. The units are expressed as Vm/N, which come from the equation of electric field divided by pressure.

$$g_{33} = \frac{electric\ field}{applied\ stress} = \frac{V\ /\ t}{F\ /\ A}$$

$$g = {}^{E}/_{\sigma} = \frac{\frac{V}{m}}{\frac{N}{m^2}} = \frac{Vm}{N}$$

The piezoelectric coefficient is equal to the piezoelectric coefficient times the permittivity.

$$d_{33} = g_{33}\varepsilon_o\varepsilon_r$$

The expression for the piezoelectric voltage coefficient can be substituted into the equation:

$$d_{33} = \frac{V}{F}\frac{A}{t} \times \varepsilon_0 \varepsilon_r = \frac{V}{F} \cdot C$$

When rearranged, the permittivity combined with the dimensional terms becomes capacitance:

$$C = \varepsilon_o \varepsilon_r \frac{A}{t}$$

The equation for piezoelectric coefficient is calculated using the capacitance, voltage, and force applied:

$$d_{33} = C \cdot \frac{V}{F}$$

A capacitance bridge can easily measure the capacitance of the transducer. The voltage can be monitored on an oscilloscope. The force applied to the transducer is difficult to measure for a pneumatic system. The pressure inside the piston is not easily measured with the same precision as voltage. By stacking the transducer on top of a known reference, both receive the same amount of force when loaded.

$$d_{33} \Big/ d_{33}^{ref} = C \cdot \frac{V}{F} \Big/ C^{ref} \cdot \frac{V^{ref}}{F}$$

Which simplifies to:

$$d_{33} = \frac{C}{C^{ref}} \frac{V}{V^{ref}} \cdot d_{33}^{ref}$$

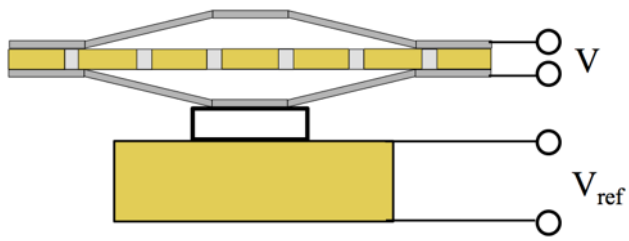

Figure 6.39. Experimental setup for measuring the effective d_{33} of the piezoelectric transducer. The transducer is placed on top of a disc of PZT with a known d_{33}. The effective d_{33} is calculated by the voltage generated under loading and the measured capacitance.

6.3 Results and discussion

6.3.1 Energy generation

Each loading cycle of the module produces a positive voltage during loading and negative voltage for unloading. Transducer output voltage from loading at 220lb and 1Hz is shown in Figure 6.40. When compressive load is applied, electrons leave the PZT generating voltage. Initially there is a rapid accumulation of charge at the electrode surface and the voltage rises to the open circuit voltage, V_{oc}. After the initial rise in voltage rise, the voltage drops as the charge dissipates according to the equation $V=V_{oc}(1-e^{-t/RC})$, where C is the capacitance of the transducer, R is the circuit resistance, and t is time. The time required for the voltage to drop can be calculated.

When the compressive load is released, electrons flow back into the piezoelectric ceramic generating negative voltage. At 1Hz there is enough time for the generated voltage to dissipate before the load is removed. The negative voltage produced during unloading can be transformed into positive voltage using a rectifier. The rectified output of the transducer loaded with 220lb and 1Hz is shown in Figure 6.41. Greater voltage is generated during unloading compared to loading. When the air pressure is removed from the piston and all of the transducers are unloaded simultaneously and the metal end caps

spring back to their initial shape. All of the charge generated during unloading is produced in 20ms. During loading all four layers of the module are compressed and the force must be transferred from the top layer to each underlying layer. Similar to unloading, the initial rise in voltage takes 20ms. Over the next 20ms the load is transferred to the remaining transducers and two peaks can be seen in Figure 6.41.

Under higher frequency loading, charge generated from loading remains in the circuit when the load is removed. If the compressive load is removed, the generated charge flows back into the PZT and neutralizes a portion of the charge. The charge remaining in the circuit is lost because the voltage is reversed and the electrons flow back into the piezoelectric ceramic. This effect is called voltage “switch back” and can be seen in Figure 6.42 for the transducer output at a loading frequency of 2.3Hz. In Figure 6.42 there is approximately 5V prior to unloading. When unloaded, this charge goes back into the PZT and decreases the negative voltage that is produced. The rectifier does not save the voltage lost due to switch back. It can be seen in Figure 6.42 for the rectified output that the voltage first drops to zero when unloaded. In order to efficiently generate energy at higher loading frequency, the generated charge must be removed from the piezoelectric ceramic before the load is removed.

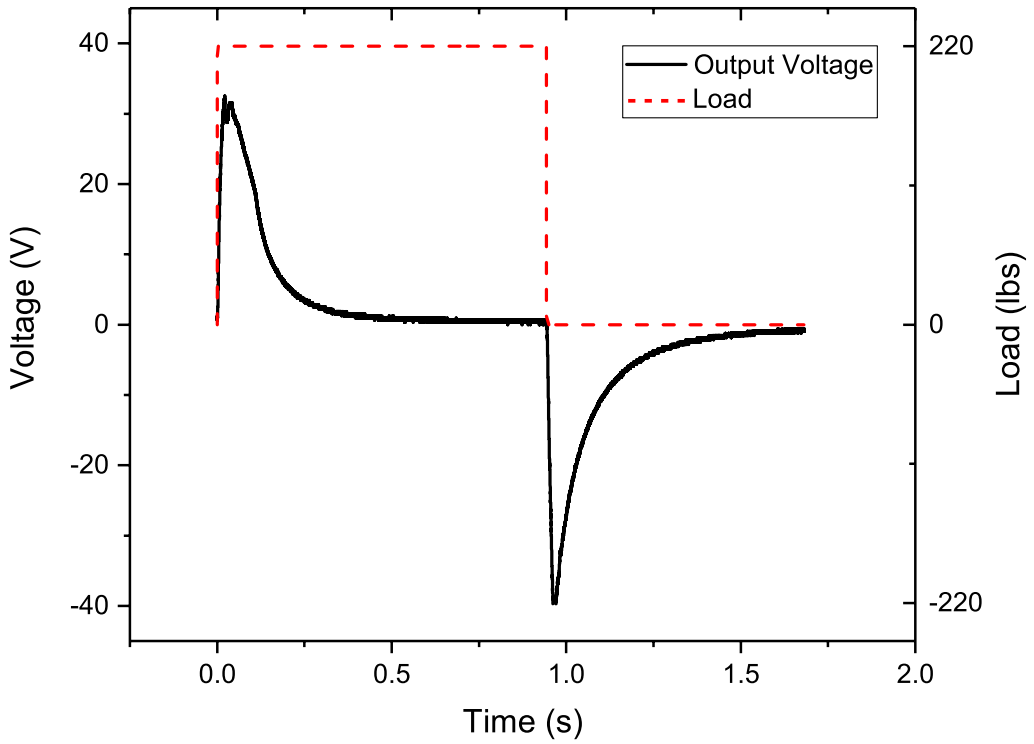

Figure 6.40. Transducer output voltage from loading at 1Hz. When compressive load is applied, electrons leave the PZT generating voltage. The Charge dissipates. When the compressive load is removed, electrons flow back into the PZT creating negative voltage. The voltage generated from the removal of the compression is sharper because the load is released instantaneously.

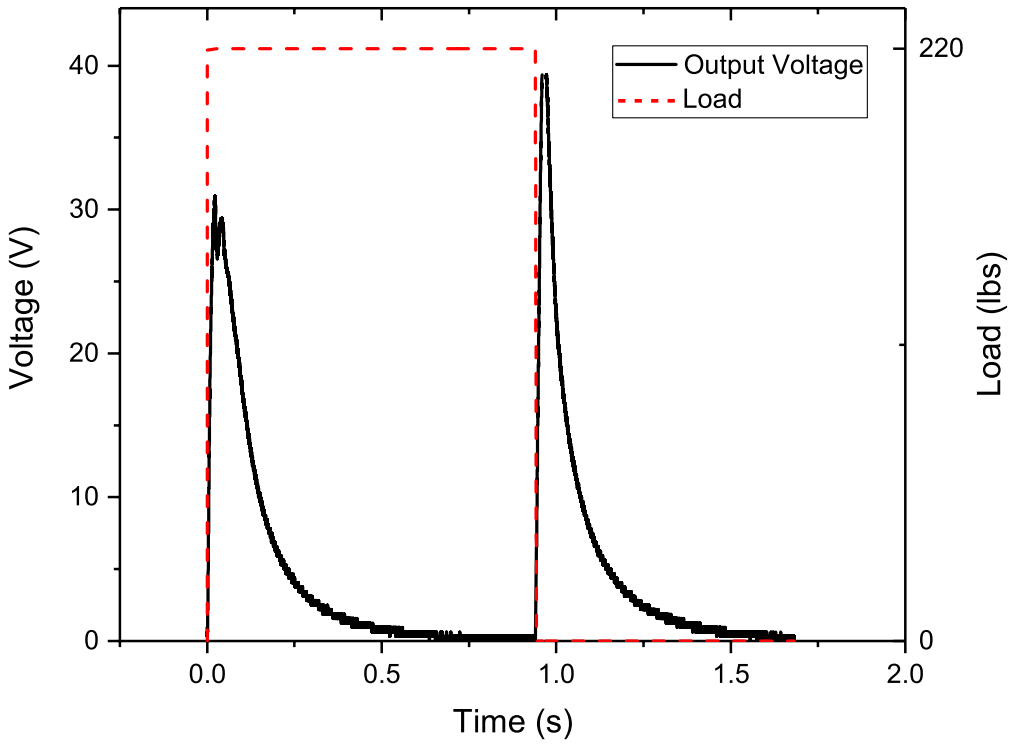

Figure 6.41. Rectified transducer output voltage from loading at 1Hz. The rectifier transform the negative voltage produced during unloading into positive voltage.

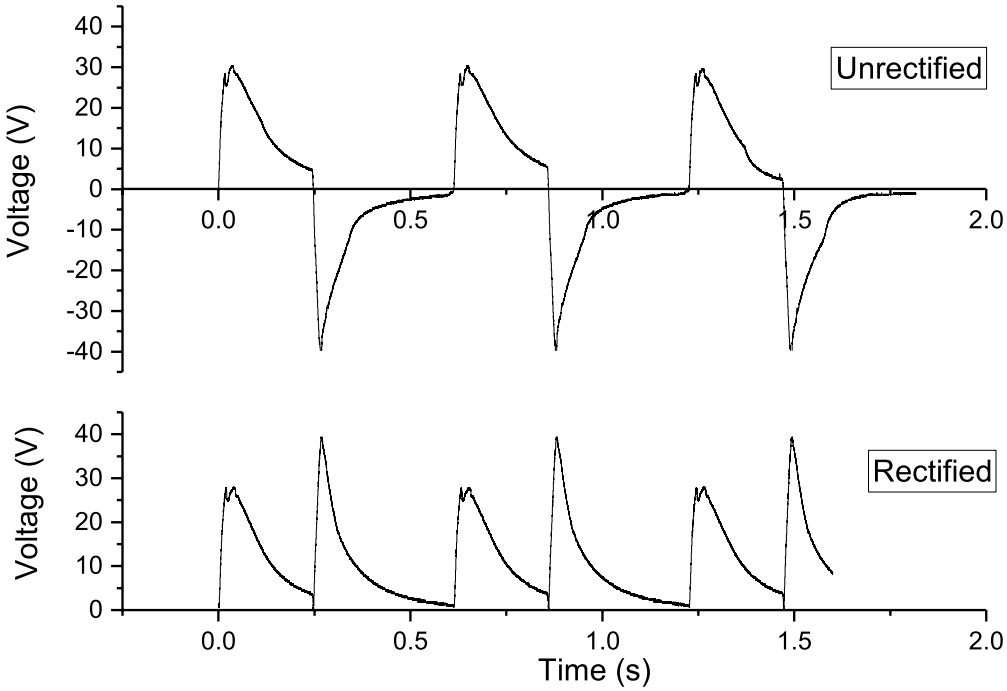

Figure 6.42. Unrectified and rectified transducer output at loading frequency of 2.3Hz. At higher frequency there is voltage "switch back". At higher loading frequency, charge remains on the transducer when it is unloaded. The remaining charge is wasted as it flows back into the PZT.

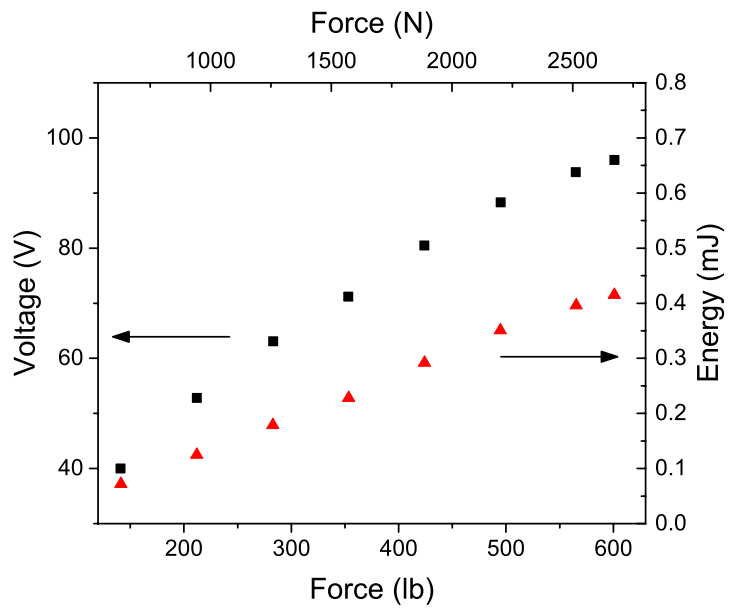

Figure 6.43. Voltage and energy generated during unloading of the transducer. The voltage from loading was shorted to remove the effects of switch back.

The voltage generated from unloading was measured across an 88nF capacitor. The rectified output from the unloading was used for the measurement. To measure the energy generated from a single loading, the voltage is measured across the capacitor in an open circuit. The circuit was shorted after the transducers were loaded to completely remove the effect of switch back. The voltage ranged from 40V at a load of 140lb to 100V at 600lb, and is shown in Figure 6.43. The energy stored on the capacitor was calculated using the equation $E=1/2CV^2$. It was found that the energy generated had a linear relationship with load applied to the transducers. A loading cycle at 600lb produces 0.7mJ of energy.

The transducers are loaded with 500lb at 5Hz until a constant voltage is achieved. The measurement is repeated using different resistive loads ranging from 50kOhm to 1MOhm. The calculated power measured for each resistive load is shown in Figure 6.44. The maximum power of 2.1mW occurred at a resistive load of 330kOhm. This resistive

load is very large and most electronic devices, which have impedance of less than 10kOhm, cannot efficiently utilize the transducer output. Therefore, it is necessary to step down the output in order to efficiently power electronic devices with lower impedance such as LEDs.

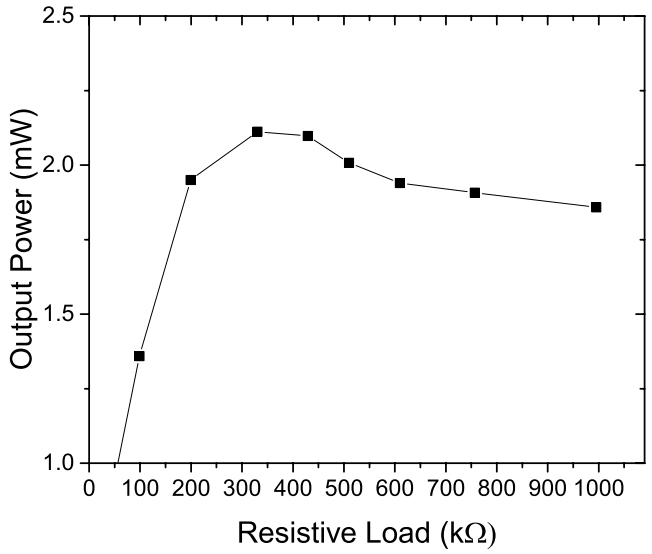

Figure 6.44. Output power for 500lb loading at 5Hz. The maximum power of 2.1mW occurs at a resistive load of 330kΩ.

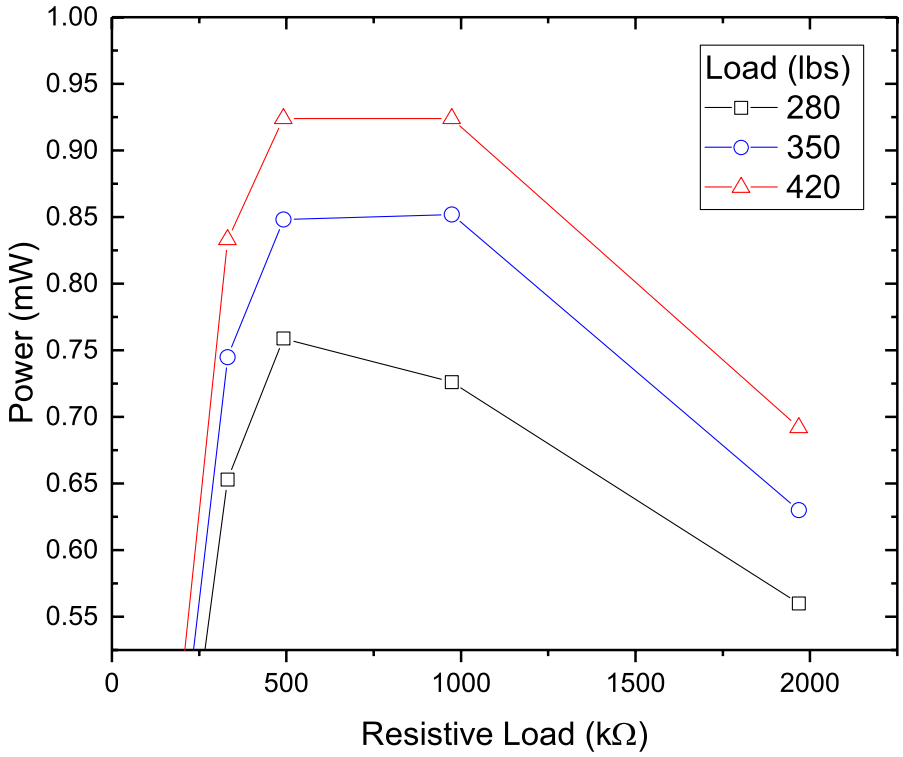

Figure 6.45. Output power of the piezoelectric energy harvesting module for different loading force. The maximum power at each of the different loads occurred at 500kΩ.

The power was expected to be proportional to load due to the linear relationship between energy and load. However the impedance must be considered for power generation. The transducers received different amount of load at 5Hz and power was measured using resistive load from 330kΩ-2MΩ, shown in Figure 6.45. Due to the lower amount of charge generated at reduced loading, the maximum power output is expected to be decreased and occur at higher impedance. The maximum power was generated at a resistive load of 500kΩ for each of the different loading amount. The power output at 500kΩ is proportional to the load.

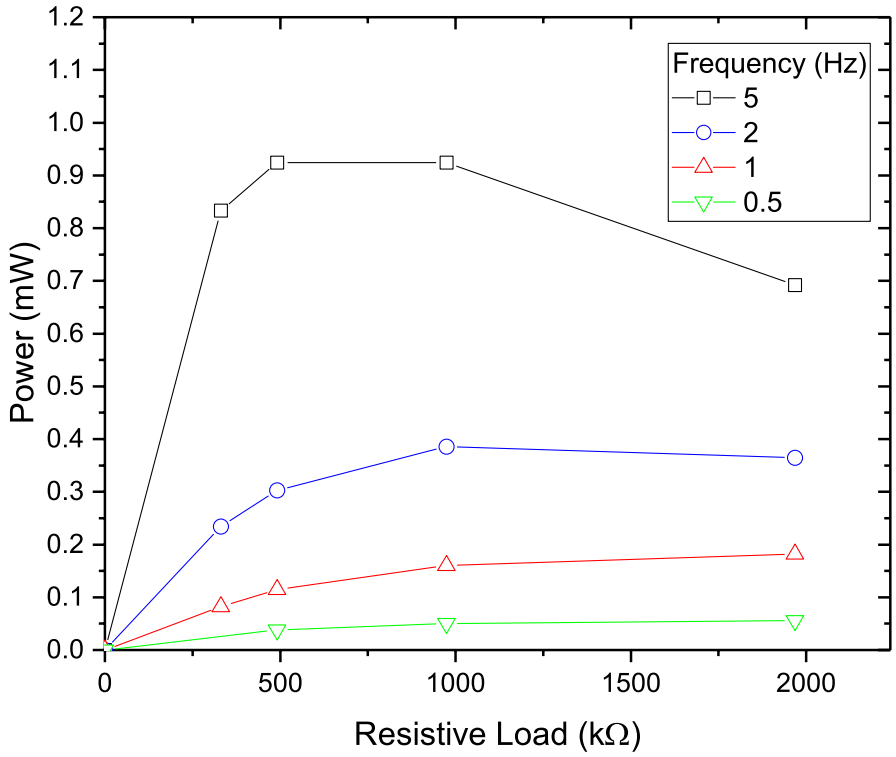

Figure 6.46. Output power of the piezoelectric energy harvesting module for loaded at 420lb at different frequency. The maximum power occurs at higher resistive load for less frequency.

The transducers were loaded with 420lb at frequency between 0.5 to 5Hz and power was measured for resistive load from 330kΩ-2MΩ, shown in Figure 6.46. The resistive load where the maximum power is generated was significantly affected by the frequency. At 5Hz, the most power was generated and the maximum occurred at 500kΩ. Above 1MΩ, to power is considerably reduced. For loading at 1Hz and 2Hz, the less power is generated and the maximum occurs at 2MΩ and 1MΩ, respectively. However in both cases the differences in maximum power generated between 1MΩ-2MΩ are minimal.

The maximum power generated at any resistance at 420lb for different loading frequency is shown in Figure 6.47. The power output at 1, 2, and 5Hz are proportional to their loading frequency. For 0.5Hz loading, the maximum output power continued to increase up to the highest resistive load used to measure. It is possible that the maximum output power occurs at a resistive load greater than 2MΩ. There are also losses in the circuit that would be amplified in this case. Leakage current in the capacitor is always present but there is forward voltages drop across the rectifying diode that blocks voltage from the transducers that is less than 0.6V. The amplified losses in the circuit as well as the high impedance limit the useable energy for loading less than 1Hz.

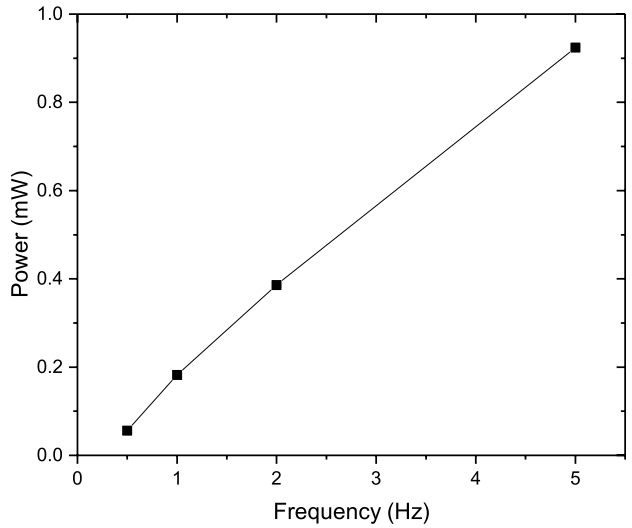

Figure 6.47. Maximum power output for 420lb loading at different frequency. The maximum power was measured using resistive load ranging from 330kΩ-2MΩ.

The DC-DC step down "buck" converter was used to reduce the output impedance of the transducers. As described previously, the circuit has an adjustable frequency and duty cycle that is controlled by variable resistors. The goal of the circuit is

to provide continuous current and voltage. The output power is determined by the amount of current that can be drawn from the circuit without depleting the charge stored on the capacitor. For a given resistive load, the duty cycle adjusted to find where there is no drop in voltage. At loading of 500lb at 5Hz, the circuit was able to produce a maximum continuous current of 0.12mA. Supplying power to LEDs is difficult because voltage must be high enough to overcome the forward voltage drop. A string of LEDs are ideally connected in series where the to voltage drop is additive. Often step up converters are used when powered by battery. A string of 10 LEDs requires a minimum of 26.5V and the buck converter was able to supply 0.08mA continuously to a string of LEDs. The power dissipated by the LEDs is 2.1mW.

Under loading of 500lb at 5Hz, the transducer were able to produce the same quantity of power; 2.1mW at 330kΩ or 0.08mA through a voltage drop of 26.5V using the step down converter. Since the gate driver and MOSFET of the circuit were powered externally, similar losses are expected in both of the circuits used to measure power. The amount of energy generated for a single loading cycle at 500lb without switch back is 0.65mJ; 5 cycles per second would generate 3.25mW. As the voltage rises in the circuit, less of the charge generated by the piezoelectric transducers can be used and 35% of the energy is lost due to switch back.

6.3.2 Effective piezoelectric coefficient

The effective piezoelectric coefficient and voltage constant of each individual transducer are 19,000 pC/N and 2150 x 10^{-3} Vm/N, respectively when measured using the direct piezoelectric effect. The wide inter-electrode spacing decreases capacitance,

and combined with the high d_{33}, the resulting g_{33} coefficient is extremely large. Higher d_{33} would be expected for the same transducer with thinner steel or bronze end caps [26]. Bronze is more compliant than steel and the end cap would flex under loading, creating additional stress.

This method provides an estimate of the piezoelectric coefficient of the transducer. Unlike the Berlincourt meter, the force is applied instead of vibration. The impact of the piston on the end cap would cause the stress transferred to the ceramic to be amplified. With this setup, it is possible that the piezoelectric coefficient will be higher due to the amplification of stress caused by the design of the transducer. However, this method of loading is similar to the impact loading that it would receive under normal operation and would give a better characterization of the transducer than the Berlincourt meter.

The converse piezoelectric effect is defined when strain results from the application of an electric field. The displacement of the piezoelectric ceramic is in the range of a few microns but can be accurately measured using laser interferometry of fiber optic sensors. The effective d_{33} is calculated by the displacement of the sample and the applied electric field.

When an electric field is applied to the transducer, the ceramic expands or contracts horizontally. The strain in the ceramic is transferred to the steel end caps, as shown in Figure 6.48. In this method, the PZT causes the steel end cap to bend. The maximum displacement is at the top center of the end cap.

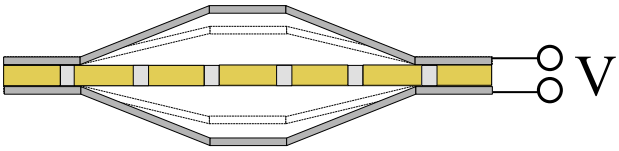

Figure 6.48. Displacement of the end caps due to applied electric field. A displacement of 7.5µm was measured with the photonic sensor for an applied electric field of 3kV/cm.

The displacement of the transducer and the PZT5X ceramic is shown in Figure 6.49. The displacement of the end caps of the transducer is about 7.5µm under an electric field of 3kV/cm. The effective d_{33} is calculated to be 7500pm/V, compared to 1150pm/V measured for the PZT5X ceramic.

In the transducer, the PZT is not able to effectively drive the steel end caps resulting in smaller effective piezoelectric coefficient measured using the converse effect. The impact of the piston causes the end caps to flex, which amplifies the stress. The stress is able to effectively transfer to the ceramic through the epoxy-bonding layer and the effective piezoelectric coefficient is larger. The direct piezoelectric effect is more representative of an energy harvesting application.

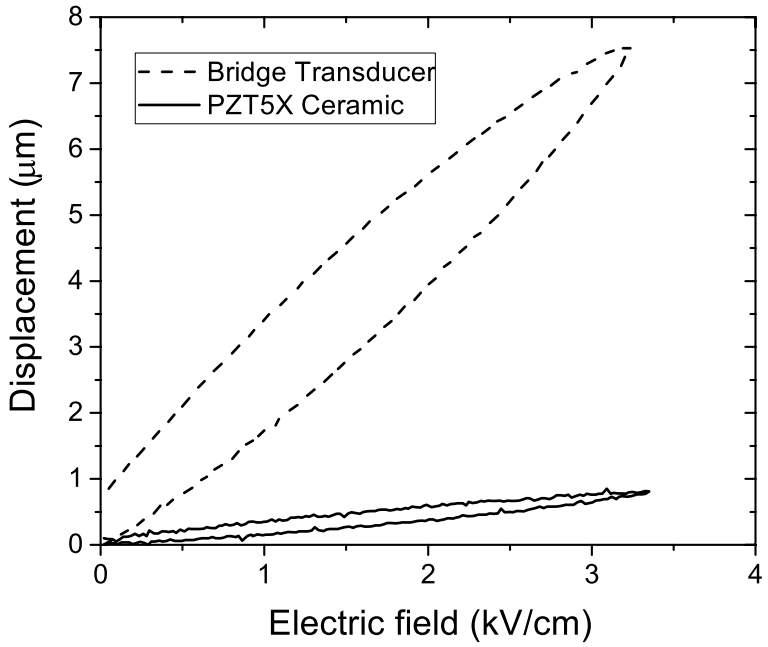

Figure 6.49. Displacement of the piezoelectric transducer compared to the PZT5X ceramic. Using the converse piezoelectric effect, the transducer has an effective d_{33} of 7500pm/V compared to 1150pm/V for the ceramic.

6.3.3 Fatigue

After 50,000 loading cycles, the output energy and power of the piezoelectric generator decreased. Analysis of the individual transducers revealed that 12 transducers were no longer functioning. These transducers failed from a combination of de-bonding of the ceramic from the epoxy and fracture of the ceramic. None of the failed transducers caused short-circuiting, which would have completely eliminated the electrical output of the piezoelectric generator.

Of the 12 failed transducers, 8 had the same characteristics, shown schematically in Figure 6.50: the epoxy bond between the end cap and the ceramic had separated and the ceramic was fractured on the opposite side. The typical epoxy bonding layer thickness

was measured to be 90-120 microns. However, the epoxy thickness where separation of the end cap occurred was about 30 microns.

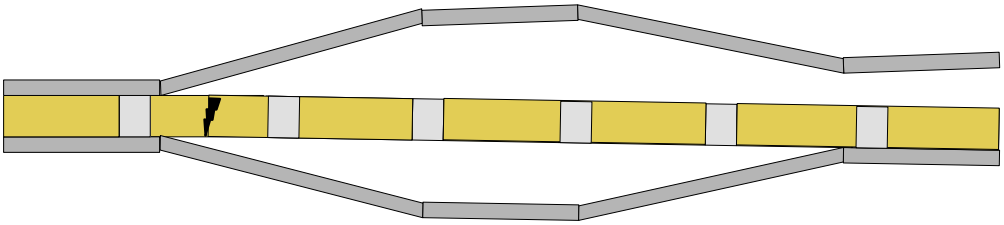

Figure 6.50. Failure of the transducer was caused by insufficient thickness of the epoxy layer. The ceramic would break shortly after de-bonding from the end cap.

When the transducer was simulated with one of the bonding layers having a thickness of 30 microns, failure occurred after 18,000 cycles at 800 lb loading. Further analysis by simulation identified the inter-electrode area where fracture of the ceramic occurred as being susceptible to fatigue, shown in Figure 6.51. After separation of the end cap from the ceramic, increased stress in the led to failure at this region. According to the simulation, the cycles to failure of the transducer is correlated to the epoxy layer thickness shown in Figure 6.52. The optimal epoxy thickness is 120 micron and the lifetime of a transducer where all four bonding regions have the same epoxy thickness is 350,000 cycles.

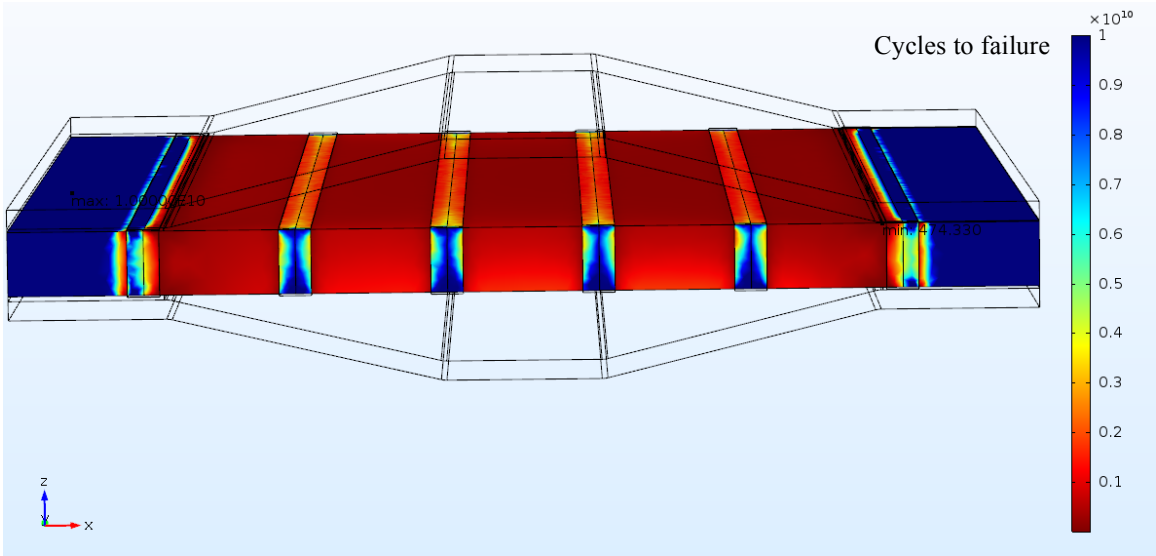

Figure 6.51. Lifetime cycles for transducer with a 30-micron epoxy layer. The thin epoxy layer will cause failure of the transducer.

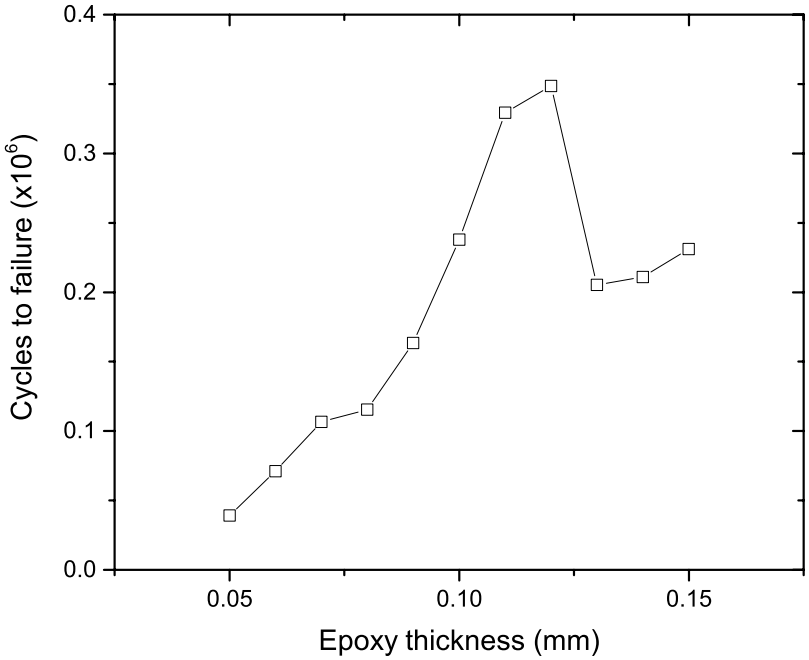

Figure 6.52. Simulated lifetime of the transducer as a function of epoxy bonding layer thickness. Maximum lifetime occurs at an epoxy thickness of 120µm.

6.4 Conclusion

Testing of the prototype novel transducers revealed that uniform epoxy thickness is an important factor that must be carefully controlled during fabrication. If the epoxy layer is too thin, it decreases the lifetime of the transducers. The transducer shape can also be modified to increase the lifetime and will be determined using simulation in the future.

The effective piezoelectric coefficient of the transducers was measured using the direct and converse piezoelectric effects and higher d_{33} was measured using the direct piezoelectric effect. The high piezoelectric voltage constant is an attractive feature of the novel bridge transducer design. The decreased capacitance enhances voltage sensitivity

and makes the transducer suitable for sensor application. However, for energy harvesting higher capacitance is preferred to decrease the impedance of the electrical output.

The novel bridge transducers were designed for high strength in order to support vehicle loading and thick steel end caps were chosen. However, the steel end caps used in the current design are too stiff to be displaced by the PZT ceramic, causing the effective piezoelectric strain coefficient to be lower. Thinner steel or bronze end caps would be preferred for actuator application.

References

[1] K. Uchino and T. Ishii, "Energy Flow Analysis in Piezoelectric Energy Harvesting Systems," *Ferroelectrics*, vol. 400, pp. 305–320, 2010.

[2] L. M. Swallow, J. K. Luo, E. Siores, I. Patel, and D. Dodds, "A piezoelectric fibre composite based energy harvesting device for potential wearable applications," *Smart Mater. Struct.*, vol. 17, p. 25017, 2008.

[3] F. M. Guillot, H. W. Beckham, and J. Leisen, "Hollow Piezoelectric Ceramic Fibers for Energy Harvesting Fabrics," *J. Eng. Fibers Fabr.*, vol. 8, no. 1, pp. 75–81, 2013.

[4] K. Uchino and S. Takahashi, "Multilayer ceramic actuators," *Curr. Opin. Solid State Mater. Sci.*, vol. 1, no. 5, pp. 698–705.

[5] J. Palosaari, M. Leinonen, J. Hannu, J. Juuti, and H. Jantunen, "Energy harvesting with a cymbal type piezoelectric transducer from low frequency compression," *J. Electroceramics*, vol. 28, pp. 214–219, 2012.

[6] K. M. Mossi, R. P. Bishop, R. C. Smith, and H. T. Banks, "Evaluation criteria for THUNDER actuators," *Proc SPIE 3667 Smart Struct. Mater. 1999 Math. Control Smart Struct.*, 1999.

[7] K. M. Mossi, G. V. Selby, and R. G. Bryant, "Thin-layer composite unimorph ferroelectric driver and sensor properties," *Mater. Lett.*, vol. 35, pp. 39–49, 1998.

[8] N. S. Shenck and J. A. Paradiso, "Energy Scavenging with Shoe-Mounted Piezoelectrics," *IEEE Micro*, vol. 21, no. 3, pp. 30–42, 2001.

[9] R. E. Newnham and A. Dogan, "Metal-electroactive ceramic composite transducer," US5729077, 17-Mar-1995.

[10] J. F. Fernandez, A. Dogan, J. T. Fielding, K. Uchino, and R. E. Newnham, "Tailoring the performance of ceramic-metal piezocomposite actuators, 'cymbals,'" *Sens. Actuators A*, vol. 65, pp. 228–237, 1998.

[11] H. Kim, S. Priya, and K. Uchino, "Modeling of Piezoelectric Energy Harvesting Using Cymbal Transducers," *Jpn. J. Appl. Phys.*, vol. 45, no. 7, pp. 5836–5840, 2006.

[12] C. Mo, D. Arnold, W. C. Kinsel, and W. W. Clark, "Modeling and experimental validation of unimorph piezoelectric cymbal design in energy harvesting," *J. Intell. Mater. Syst. Struct.*, vol. 24, no. 7, pp. 828–836, 2013.

[13] Q.-M. Wang, X.-H. Du, B. Xu, and E. L. Cross, "Electromechanical Coupling and Output Efficiency of Piezoelectric Bending Actuators," *IEEE Trans. Ultrason. Ferroelectr. Freq. Control*, vol. 46, no. 3, pp. 638–646, 1999.

[14] V. Bedekar, J. Oliver, and S. Priya, "Design and Fabrication of Bimorph Transducer for Optimal Vibration Energy Harvesting," *IEEE Trans. Ultrason. Ferroelectr. Freq. Control*, vol. 57, no. 7, pp. 1513–1523, 2010.

[15] I. Jung and Y. Roh, "Design and fabrication of piezoceramic bimorph vibration sensors," *Sens. Actuators A*, vol. 69, pp. 259–266, 1998.

[16] S. R. Anton and H. A. Sodano, "A review of power harvesting using piezoelectric materials (2003–2006)," *Smart Mater. Struct.*, vol. 16, no. 3, pp. R1–R21, 2007.

[17] S. Roundy, P. K. Wright, and J. Rabaey, "A study of low level vibrations as a power source for wireless sensor nodes," *Comput. Commun.*, vol. 26, pp. 1131–1144, 2003.

[18] S. Qi, R. Shuttleworth, S. O. Oyadiji, and J. Wright, "Design of a multiresonant beam for broadband piezoelectric energy harvesting," *Smart Mater. Struct.*, vol. 19, p. 94009, 2010.
[19] R. Dauksevicius *et al.*, "Frequency up-converting vibration energy harvester with multiple impacting beams for enhanced wideband operation at low frequencies," *Procedia Eng.*, vol. 87, pp. 1517–1520, 2014.
[20] H. Zhao, Y. Tao, Y. Nui, and J. Ling, "Harvesting Energy from Asphalt Pavement by Piezoelectric Generator," *J. Wuhan Univ. Technol. Mater Sci Ed*, vol. 29, no. 5, pp. 933–937, 2014.
[21] H. J. Xiang, J. J. Wang, Z. F. Shi, and Z. W. Zhang, "Theoretical analysis of piezoelectric energy harvesting from traffic induced deformation of pavements," *Smart Mater. Struct.*, vol. 22, p. 95024, 2013.
[22] H. Zhao, J. Ling, and J. Yu, "A comparative analysis of piezoelectric transducers for harvesting energy from asphalt pavement," *J. Ceram. Soc. Jpn.*, vol. 120, no. 8, pp. 317–323, 2012.
[23] H. Zhao, J. Yu, and J. Ling, "Finite element analysis of Cymbal piezoelectric transducers for harvesting energy from asphalt pavement," *J. Ceram. Soc. Jpn.*, vol. 118, no. 10, pp. 909–915, 2010.
[24] C.-L. Sun, S. S. Guo, W. P. Li, Z. B. Xing, G. C. Lui, and X. Z. Zhao, "Displacement amplification and resonance characteristics of the cymbal transducers," *Sens. Actuators A*, vol. 121, pp. 213–220, 2005.
[25] P. Ochoa, J. L. Pons, M. Villegas, and J. F. Fernandez, "Advantages and limitations of cymbals for sensor and actuator applications," *Sens. Actuators A*, vol. 132, pp. 63–69, 2006.
[26] H. Kim, S. Priya, H. Stephanou, and K. Uchino, "Consideration of Impedance Matching Techniques for Efficient Piezoelectric Energy Harvesting," *IEEE Trans. Ultrason. Ferroelectr. Freq. Control*, vol. 54, no. 9, pp. 1851–1859, 2007.
[27] H. Nagata, M. Yoshida, Y. Makiuchi, and T. Takenaka, "Large Piezoelectric Constant and High Curie Temperature of Lead-Free Piezoelectric Ceramic Ternary System Based on Bismuth Sodium Titanate-Bismuth Potassium Titanate-Barium Titanate near the Morphotropic Phase Boundary," *Jpn. J. Appl. Phys.*, vol. 42, pp. 7401–7403, 2003.
[28] Y. Saito *et al.*, "Lead-free piezoceramics," *Nature*, vol. 432, pp. 84–87, 2004.
[29] T. R. Gururaja, D. Christopher, R. E. Newnham, and W. A. Schulze, "Continuous Poling of PZT Fibers and Ribbons and its Application to New Devices," *Ferroelectrics*, vol. 47, pp. 193–200, 1983.
[30] A. Jasim, "unpublished work."
[31] H. Nagata and T. Takenaka, "Mechanical Strength of Some Lead-Free Piezoelectric Ceramics," in *16th US-Japan Seminar on Dielectric and Piezoelectric Materials*, Raleigh, NC, 2013, pp. 194–195.
[32] M. Okayasu and K. Watanabe, "The electric power generation characteristics of a lead zirconate titanate piezoelectric ceramic under various cyclic loading conditions," *Ceram. Int.*, vol. 41, pp. 15097–15102, 2015.
[33] T.-B. Xu *et al.*, "Energy harvesting using a PZT ceramic multilayer stack," *Smart Mater. Struct.*, vol. 22, p. 65015, 2013.

[34] A. Dogan, “Flextensional ‘Moonie and Cymbal’ Actuators,” Pennsylvania State University, 1994.

Summary and Conclusions

The lead-free, morphotropic phase boundary composition $0.88Bi_{1/2}Na_{1/2}TiO_3 – 0.08Bi_{1/2}K_{1/2}TiO_3 – 0.04BaTiO_3$ can be sintered at 900ºC with minimal change in the piezoelectric properties compared to sintering at 1150ºC. The combination of additives Bi_2O_3, CuO, Li_2CO_3, ZnO, and B_2O_3 are used for liquid phase sintering to lower the firing temperature by 250ºC. While the piezoelectric properties are similar, the depolarization temperature is reduced from 155ºC for BNKBT sintered at 1150ºC to approximately 130ºC when sintered at 900ºC with additives. Overall, it is difficult to determine the individual effect of each component of the additives on the densification and piezoelectric properties.

The additives were modified by the addition of ZnO for sintering in controlled oxygen atmosphere. Bismuth-based ceramics can be sintered at 900ºC in controlled atmosphere with an oxygen partial pressure of 10^{-8} atm for 2-4hr. The reduction of the sintering temperature and compatibility in low oxygen conditions enables development of cost effective BNKBT88 ceramics with copper internal and external electrodes to be developed.

The reduction of the sintering temperature to 900ºC and compatibility of the additives for firing in controlled oxygen atmosphere allowed the development co-fired copper base metal electrodes. Control of the atmosphere is the greatest challenge for co-firing a copper metal electrode and Bi-based ceramic. An in-situ oxygen sensor and mixing CO_2 and H_2 gases provides the precise control of oxygen inside the tube furnace necessary to avoid reaction of the copper or reduction of the bismuth oxide. The presence

of a mixture of Cu metal and Cu_2O next to the samples inside of a covered alumina boat was able to keep the Cu/Cu_2O equilibrium oxygen partial pressure needed to co-fire the ceramic.

Co-fired BNKBT88 with internal and external copper electrodes were successfully fired. An internal electrode of 125μm was prepared using pressed copper power, while a copper paste was used as an internal as well as surface electrode. The piezoelectric ceramic could be poled using the co-fired copper electrode.

Non-stoichiometry has a unique effect on the piezoelectric properties of BNT-based ceramics. Previous studies in BNT and the binary systems BNT-BT and BNT-BKT demonstrated sensitivity to the stoichiometry of the composition. In the ternary morphotropic phase boundary composition BNKBT88, the effects of non-stoichiometry are larger. Bismuth deficiency makes the ceramics hard, which is desired for use in high power transducers or piezoelectric transformers. The mechanical quality factor of 1200 for BNKBT88-2.0Bi is comparable to hard PZT. Na and K deficiency decreased T_d to make the ceramic antiferroelectric at room temperature with very large strain. The oxygen vacancies induced by non-stoichiometry increase the conductivity of the ceramic making poling difficult. However, this may enable BNT based ceramics to be used as an oxygen conductor in fuel cells.

Increased conductivity due to oxygen vacancies makes the ceramic difficult to pole and increases dielectric loss at elevated temperature, limiting the use of bismuth deficient ceramics. A small addition of Bi_2O_3 to the Bi-deficient composition is able to improve resistivity and had a large effect on piezoelectric, ferroelectric, and electrical properties. Improvement to DC resistivity was greatest at lower temperature, and was

effective for improving poling. However, the addition of bismuth oxide did not have an effect on DC resistivity at temperatures over 150ºC.

A prototype piezoelectric transducer was fabricated for a pavement-based energy harvesting application. Using a unique surface electrode pattern, the ceramic is poled horizontally to enhance the contribution of the piezoelectric d_{33} coefficient. Testing of the prototype bridge transducers under simulated vehicle loading produced 2.1mW at an impedance of 330kΩ. The output voltage was passed through a step down converter to reduce the output impedance, to provide power to illuminate LEDs. This demonstrates that the energy produced by the piezoelectric generators can be used as a power source for electronic devices.

The effective piezoelectric coefficient of the transducers was measured using the direct and converse piezoelectric effects. The high piezoelectric g_{33} voltage constant of 2150×10^{-3} Vm/N is an attractive feature of the novel bridge transducer design. The decreased capacitance enhances voltage sensitivity and makes the transducer suitable for sensor application.

Suggestions for future work

This research accomplished sintering BNKBT88 at 900ºC in air or controlled oxygen atmosphere with minimal effect on the piezoelectric properties. At this time, there is little benefit to further decrease the sintering temperature, as 900ºC is sufficient for co-firing with an electrode. Future work should focus on understanding the effect of each component on the piezoelectric properties, especially the cause of decreased T_d.

The challenges of co-firing Bi-based ceramics with copper base metal electrodes can be overcome; however further research is limited due to safety concerns and limitations of the laboratory equipment. Control of the atmosphere during cool down can be accomplished by switching the furnace gas to wet hydrogen, $H_2 + H_2O$, which reacts at a lower temperature than the carbon dioxide and hydrogen. A secondary oxygen sensor, such as a fiber optic sensor, could be used to monitor the furnace atmosphere below the operational temperature range of the zirconia sensor.

Future work of co-firing lead-free ceramics with copper metal electrodes would involve the fabrication of a multilayer actuator using tape casting. Additives such as surfactants, plasticizer, and binders would be added the ceramic and electrode composition. After tape casting, layering, and laminating, the organics would be removed under a wet hydrogen atmosphere to avoid oxidizing the copper electrode. These organic additives would decompose in the limited oxygen atmosphere rather than be burned off. The flammable organic residues can clog the furnace's exhaust and be ignited by flammable vapors from the organic binders as well as the H_2 gas. The furnace exhaust

cannot be safely vented with the current laboratory exhaust systems and further research cannot be conducted due to fire hazard.

The conductivity in Bi-deficient BNKBT88-2.0Bi can be suppressed by the addition of Bi_2O_3 after calcination, although the improvement in resistivity is small. Bismuth deficient BNKBT88 with Bi_2O_3 added still has semiconductor behavior due to the formation and mobility of defects. Additional additives may further suppress conductivity and limit the mobility of defects and vacancies.

Many lessons were learned during the fabrication of the novel transducer and the prototype energy harvester. The poling fixture constrained the ceramics and led to failure during poling. A new fixture was designed to allow the electrodes to be connected in parallel without any mechanical constraint but it was not built. The new fixture should be built to determine if it can reduce the number of broken ceramics during poling. The electrode was applied to the ceramic by hand using a paintbrush and it was not possible to decrease the electrode spacing. Using a screen printer, different electrode patterns could be printed on the ceramic to determine the optimal electrode spacing, which would maximize the effective d_{33} and capacitance.

Fatigue, exacerbated by uneven epoxy bonding layer thickness, led to the failure of many transducers. The fixture for holding the transducer while the end caps were bonded is likely responsible for clamping some of the ceramics too tightly, squeezing the uncured epoxy out of the bonding region. Overall, the fabrication process needs to be refined to achieve consistency, as it is crucial to the lifetime reliability of the transducers.

Publications

2017

G. Yesner, A. Safari, A. Jasim, H. Wang, B. Basily, and A. Maher, "Energy Harvesting and Evaluation of a Novel Piezoelectric Bridge Transducer", 2017, in preparation.

G. Yesner and A. Safari, "Development of a lead-free copper co-fired BNT-based ceramic", 2017, in preparation.

A. Jasim, H. Wang, G. Yesner, A. Safari, and A. Maher, "Optimized design of layered bridge transducer for piezoelectric energy harvesting from roadway," *Energy*, 141, pp. 1133-1145.

A. Safari, G. Yesner, M. Kuciej, and M. Maher, "Enhanced Cymbal Piezoelectric Transducer," provisional US patent application 62/517,502 filed on June 9, 2017.

G. Yesner and A. Safari, "Improvement in Electrical Resistivity and Mechanical Quality Factor in BNT Based Ceramics for High Power Application" 18th US–Japan Seminar on Dielectric and Piezoelectric Materials. 2017.

G. Yesner, A. Safari, A. Jasim, H. Wang, B. Basily, and A. Maher, "Evaluation of a Novel Piezoelectric Bridge Transducer," *2017 Joint IEEE ISAF-ECAPD-PFM,* Atlanta, 2017, pp. 113-115.

G. Yesner and A. Safari, "Improved Resistivity in Bismuth Deficient Morphotropic Phase Boundary 0.88BNT-0.08BKT-0.04BT Ceramics, " *2017 Joint IEEE ISAF-ECAPD-PFM,* Atlanta, 2017, pp. 110-113.

2016

G. Yesner, M. Kuciej, A. Safari, A Jasim, H. Wang, and M. Maher, "Piezoelectric Energy Harvesting Using a Novel Cymbal Transducer Design," *2016 Joint IEEE ISAF-ECAPD-PFM,* Darmstadt, 2016, pp. 1-4.

2015

G. Yesner, M. Kuciej, and A. Safari, "Bismuth Deficiency and Low Temperature Sintering in Morphotropic Phase Boundary BNT–BKT–BT Ceramics," 17th US-Japan Seminar on Dielectric and Piezoelectric Materials, Matsumoto, Japan, 2015.

G. Yesner, M. Kuciej, A. Safari,"Low temperature sintering of $Bi_{0.5}Na_{0.5}TiO_3$ based ceramics," *2015 Joint IEEE ISAF-ISIF-PFM*, Singapore, 2015, pp. 21-23.

2013

G. Yesner and A. Safari, "Multiferroic bismuth ferrite based thin films," *2013 Joint IEEE ISAF-PFM*, Prague, 2013, pp. 122-123.

Posters/presentations

2017

G. Yesner, A. Safari, A. Jasim, H. Wang, B. Basily, and A. Maher, "Evaluation of a Novel Piezoelectric Bridge Transducer," *2017 Joint IEEE ISAF-ECAPD-PFM,* Atlanta, 2017, pp. 113-115.

G. Yesner and A. Safari, "Improved Resistivity in Bismuth Deficient Morphotropic Phase Boundary 0.88BNT-0.08BKT-0.04BT Ceramics, " *2017 Joint IEEE ISAF-ECAPD-PFM,* Atlanta, 2017, pp. 110-113.

G. Yesner and A. Safari, "Novel Electrode Design and Piezoelectric Energy Harvesting Using Modified Cymbal Transducer," Electronic Materials and Applications, Orlando, FL, 2017.

G. Yesner and A. Safari, "Low Temperature Sintering and Non-Stoichiometry in Morphotropic Phase Boundary BNT-BKT-BT Ceramics" Electronic Materials and Applications, Orlando, FL, 2017.

2016

G. Yesner, M. Kuciej, A. Safari, A. Maher, B. Basily, A. Jasim, and H. Wang, "Piezoelectric Energy Harvesting Using a Novel Cymbal Transducer Design, " 2016 International Workshop on Acoustic Transduction Materials and Devices, State College, Pa, 2016.

G. Yesner, M. Kuciej, and A. Safari, "Low Temperature Sintering, Atmospheric Control, and Bismuth Deficiency in Morphotropic Phase Boundary 0.88BNT-0.08BKT-0.04BT Ceramics" 2016 International Workshop on Acoustic Transduction Materials and Devices, State College, Pa, 2016.

2015

G. Yesner, M. Kuciej, and A. Safari, "Low Temperature Sintering of $Bi_{0.5}Na_{0.5}TiO_3$ Based Ceramics," 7th International Conference on Electroceramics, State College, Pa, 2015.

2014

G. Yesner, P. Urbankowski, and A. Safari, "Piezoelectric Properties of BiNT Based Ceramics Doped with Sn" *2014 Joint IEEE ISAF-ISIF-PFM*. State College, Pa, 2014.

2013

G. Yesner and A. Safari, "Multiferroic bismuth ferrite based thin films," *2013 Joint IEEE ISAF-PFM*, Prague, 2013, pp. 122-123.